Institut für Wasserbau · Universität Stuttgart

# Mitteilungen

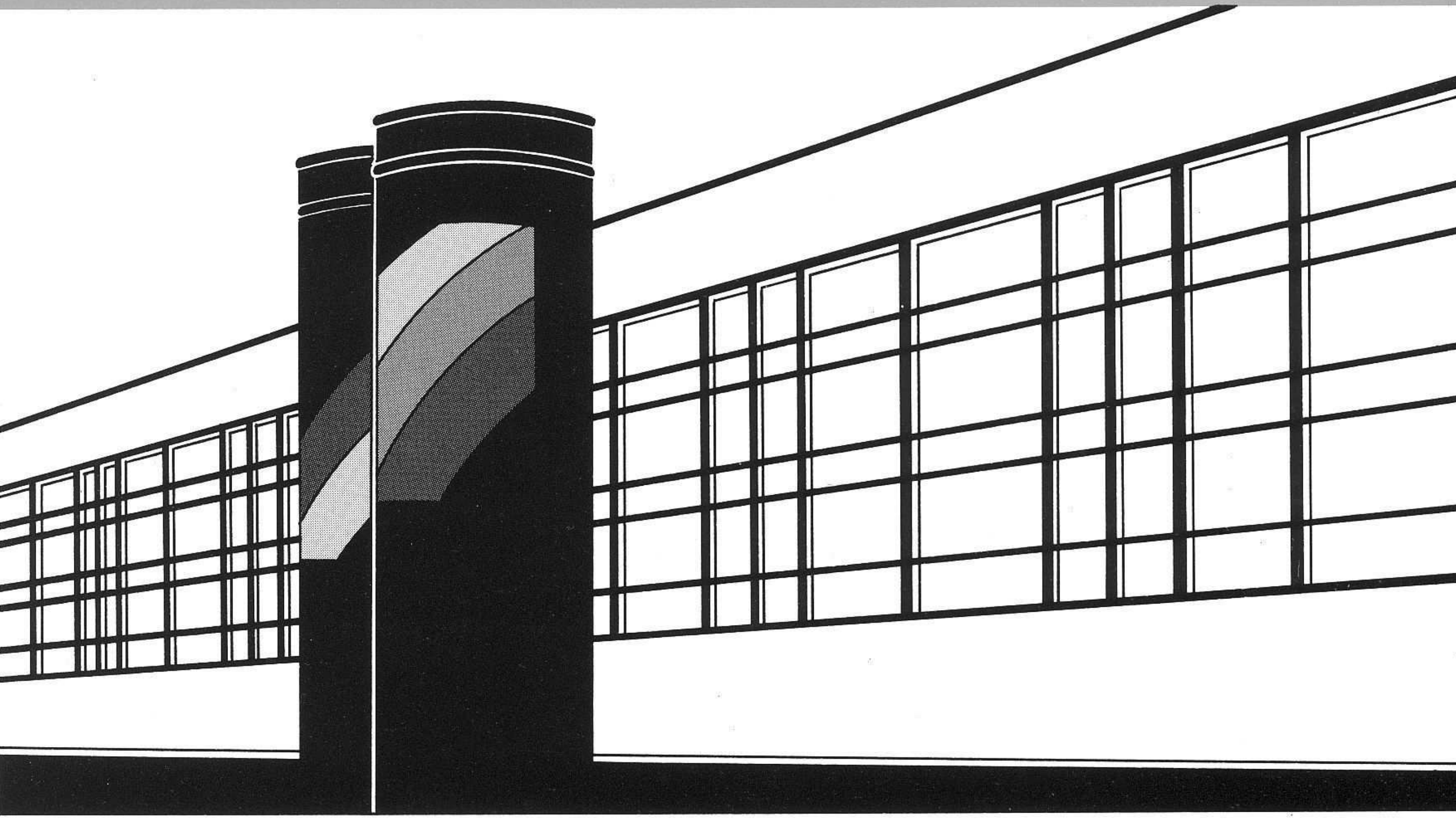

Heft 169

Ianina Kopecki

# Calculational Approach to FST-Hemispheres for Multiparametrical Benthos Habitat Modelling

# Calculational Approach to FST-Hemispheres for Multiparametrical Benthos Habitat Modelling

Von der Fakultät Bau- und Umweltingenieurwissenschaften der
Universität Stuttgart zur Erlangung der Würde eines
Doktor-Ingenieurs (Dr.-Ing.) genehmigte Abhandlung

Vorgelegt von

**Ianina Kopecki**

aus Leningrad

| | |
|---|---|
| Hauptberichter: | Prof. Dr.-Ing. habil. Dr.-Ing. E.h. Jürgen Giesecke |
| Mitberichter: | Prof. Dr.-Ing. Silke Wieprecht |
| | Prof. Dr.-Ing. habil., Prof. h.c. Ulrich C.E. Zanke |
| Tag der mündlichen Prüfung: | 18. Januar 2008 |

Institut für Wasserbau der Universität Stuttgart
2008

Heft 169

# Calculational Approach to FST-Hemispheres for Multiparametrical Benthos Habitat Modelling

von
Dr.-Ing.
Ianina Kopecki

Eigenverlag des Instituts für Wasserbau der Universität Stuttgart

# D93 Calculational Approach to FST-Hemispheres for Multiparametrical Benthos Habitat Modelling

Titelaufnahme der Deutschen Bibliothek

Kopecki, Ianina:
Calculational Approach to FST-Hemispheres for Multiparametrical Benthos Habitat Modelling / von Ianina Kopecki. Institut für Wasserbau, Universität Stuttgart. - Stuttgart: Inst. für Wasserbau, 2008

(Mitteilungen / Institut für Wasserbau, Universität Stuttgart: H. 169)
Zugl.: Stuttgart, Univ., Diss., 2008)
ISBN 3-933761-73-5
NE: Institut für Wasserbau <Stuttgart>: Mitteilungen

Herausgegeben 2008 vom Eigenverlag des Instituts für Wasserbau
Druck: Document Center S. Kästl, Ostfildern

# Vorwort

## Veranlassung

### Der Lebensraum Fließgewässer

Gewässer sind ein prägender Bestandteil des Naturhaushaltes. Die fließende Welle, das Gewässerbett, die Flussniederungen, das Lückensystem unter und neben der Gewässersohle als Lebens- und Schutzraum, das sog. Interstitial, ferner die Auezonen und das Grundwasser – diese alle bilden eine Einheit. Menschliche Einflüsse bedingen deren Veränderungen. Daher steht der Zustand eines Gewässers in enger Wechselbeziehung zu sozialen und wirtschaftlichen Strukturen. Deren Verbindung mit ökologischen Erfordernissen legen umsetzbare Entwicklungskonzepte nahe.

Diesbezügliche Strategien stellen die begrenzten Nutzungsmöglichkeiten des betrachteten Lebensraumes den anzupassenden, gesellschaftlichen und ökonomischen Zielsetzungen gegenüber. Neue Verhaltens- und Lebensweisen sollen ebenso zu nachhaltigen, d. h. dauerhaften umweltgerechten Nutzungen eines Gewässerlaufes unter Ausgewogenheit von Ökologie und Ökonomie führen. Derartige Entwicklungskonzepte lassen sich durch die Verflechtung von Natur- und Ingenieurwissenschaften erarbeiten.

Die Vorgehensweise ergibt sich aus dem im Wasserhaushaltgesetz verankerten Leitgedanken: “Die Gewässer sind als Bestandteil des Naturhaushaltes so zu bewirtschaften, dass sie dem Wohl der Allgemeinheit dienen und im Einklang mit ihm auch dem Nutzen Einzelner entsprechen sowie jede vermeidbare Beeinträchtigung unterbleibt.” Und die 2002 erlassene Europäische Wasserrahmenrichtlinie führt hinsichtlich der unabdingbaren Bewahrung aquatischer Ökosysteme aus, dass Wasser kein Handelsprodukt wie jedes andere ist sondern vielmehr ein Lebensgut, welches geschützt, verteidigt und als solches behandelt werden muss.

### Gewässer als Lebensader

Grundlage allen Lebens ist das Wasser. Es gibt hierfür keinen Ersatz. Der mit der geschichtlichen Entwicklung des Menschen gewachsene Instinkt lässt die überragende Bedeutung des Umweltfaktors Wasser jedem einzelnen bewusst werden. Die Eingriffe des Menschen in den natürlichen Kreislauf des Wassers, die durch die enge Verflechtung des Wassers mit der Vielzahl an Lebensvorgängen bedingt sind, bedürfen der Ordnung.

In allen Phasen der Menschheitsgeschichte waren Kreativität, Erfindungsgeist und technische Kunst gefordert, die Existenz zu sichern und die Lebensqualität zu verbessern. Heute ist mehr denn je die Abstimmung der Lebensbelange des Menschen mit dem Ökosystem Natur notwendig. Die Natur inklusive des Menschen mit seinen sozialen, psychischen und kulturellen Forderungen ist hierbei als Umwelt zu verstehen. Ein Ökosystem umfasst die Schutzgüter der Natur, die die Pflanzen- und Tierwelt mit ihren terrestrischen und aquatischen Umgebungen enthalten.

## Typische Strömungsmuster eines Fließgewässers

Jeder wesentliche Eingriff in den Flussquerschnitt oder in den natürlichen Abfluss bedeutet eine Veränderung der ursprünglichen Strömungsverhältnisse. Beispielsweise erfolgt in Staubereichen vor allem eine Verminderung und Vergleichmäßigung der Strömung. In Ausleitungsstrecken bei Wasserentnahme z. B. für Bewässerungsflächen oder Wasserkraftnutzung bewirkt die Abflussreduzierung eine Verringerung des Wasservolumens und damit des aquatischen Lebensraumes, der überströmten Sohlfläche, der Wassertiefen und der mittleren Fließgeschwindigkeiten.

Diese Einflüsse haben gleichzeitig zur Folge, dass sich die Charakteristik der sohlnahen Strömungsbedingungen, d. h. der Sohlschubspannungen, Auftriebskräfte und Turbulenzen teilweise erheblich verändert. Die Veränderungen hängen von der Wassertiefe, dem Wasserspiegel- und Sohlgefälle sowie der Substratrauheit ab, auch von der Fließgeschwindigkeit in Sohlennähe. Sie geben den Ausschlag für Geschiebetrieb, Erosion und Sedimentation, ferner für die Umformung des Gewässerbettes und des als Lebensraum genutzten Substrates, der sogenannten, einem bestimmten Struktursediment zugeordneten Choriotope.

## Einflüsse auf das biologische System eines Fließgewässers

Die vorgenannten wesentlichen Faktoren eines Strömungsmusters haben für die wassergebundenen Organismen eine ausschlaggebende Bedeutung bezüglich der Eignung der örtlichen Gewässersohle, d. h. des den Lebensraum bildenden Benthals. Sie kennzeichnen mit ihrer räumlichen und zeitlichen Heterogenität das hydraulisch-morphologische Habitatangebot, wonach sich das Benthos als Lebensgemeinschaft ausrichtet.

Die Flora und Fauna von Gewässern stellen ein sehr komplexes System dar. Mit der Wasserbewegung stehen das Vorkommen von Arten, die Lebensweisen und die spezifische Umwelt in Zusammenhang. Kaum besiedelt ist die frei fließende Welle. Unter dieser, oberhalb der Gewässersohle, befindet sich jene Wasserschicht, die bereits durch die Rauheit der Sohle beeinflusst wird. Sie weist zur Sohle hin stark veränderliche mittlere Geschwindigkeiten auf. Hydraulisch betrachtet ist dies die raue Grenzschicht. Unterhalb dieser Zone schließt sich das turbulente Totwasser im Bereich größerer Substratkörper an. Darunter folgt innerhalb des Interstitiales der Lebensraum der wassergefüllten und ganz schwach durchströmten Kieslücken.

Jede Umbildung des Strömungsmusters im Freiwasserraum sowie an der Gewässersohle, verbunden mit den veränderlichen Substratgrößen, bewirkt Veränderungen bei den Tier- und Pflanzengemeinschaften, die die erwähnten Lebensräume besiedeln. Viele Fischarten, benthische Organismen (Kleinkrebse, Insektenlarven, Weichtiere usw.) und Makrophyten (Wasserpflanzen) sind auf ganz bestimmte Strömungsgeschwindigkeiten oder Strömungskräfte sowie auf geeignete Substrate, die Choriotope, angewiesen.

## Erfassung des hydraulischen Habitatangebotes

Der geschilderte Lebensraum der benthischen Organismen wird in erster Linie durch das Substrat und die sohlnahen Strömungsbedingungen charakterisiert. Dieser Lebensraum kann anhand hochsignifikanter Referenzen sowohl für strömungsliebende (rheophile) als auch für stillwasserliebende (stagnophile) Arten beschrieben werden. Über stabilen Habitatstrukturen ergibt sich die wirksame hydraulische Variabilität der sohlnahen Strömungsbedingungen aus Veränderung der Dicke der Prandtl´schen Grenzschicht, der Sohlschubspannungen, der Froude-Zahl und der Reynolds-Zahl. Darüber hinaus spielen Störungen, die bestehende physikalische Eigenschaften der Gewässersohle verändern, eine wichtige Rolle für die Entwicklung fließgewässertypischer benthischer Lebensgemeinschaften.

Für die Erfassung und Simulation des hydraulischen Habitatangebotes für die Bewohner der Gewässersohle bietet sich an, ein derartiges hydraulisches Habitatangebot als eine Kombination unterschiedlicher physikalischer Faktoren zu betrachten. Sind diese Muster ermittelt, werden sie anschließend mit den diesbezüglichen Ansprüchen unterschiedlicher Tier- oder Pflanzenarten bzw. -gesellschaften verglichen. Beispielsweise wird mit Hilfe der sog. FST-Halbkugel-Methode das örtliche hydraulische Muster an der Gewässersohle bei veränderlichen Abflüssen gemessen und anschließend mittels statistischer Verfahren die Verteilung der sohlnahen Strömungskräfte als Funktion des Abflusses formuliert. Die Verknüpfung der Muster mit Abflussganglinien und anschließend mit standardisierten Präferenzfunktionen ausgewählter benthischer Organismen ermöglicht die Einbeziehung der räumlichen Heterogenität und der zeitlichen Dynamik ökologisch relevanter Faktoren. Dabei wird erkennbar, wie sich die Gewässerbettmorphologie, hydrologisch unterschiedliche Jahre und verschiedene Wasserführungen tatsächlich auf das hydraulische Habitatangebot auswirken. Die Komplexität der maßgebenden Einflussgrößen erfordert computergestützte Simulationsmodelle.

## Zielsetzung der Dissertation

Am Institut für Wasserbau, Lehrstuhl für Wasserbau und Wasserwirtschaft der Universität Stuttgart, wurde Anfang der 90er Jahre eine bundesweite Forschergruppe aufgebaut, die sich zunächst mit Entscheidungsgrundlagen für Mindestwasserregelungen in Ausleitungsstrecken von Wasserkraftanlagen befasste, um effektive Lösungsansätze für Konfliktsituationen zwischen den Interessen der Wassernutzung auf der einen Seite und den Anforderungen der Gewässerökologie auf der anderen Seite zu entwickeln. Hieraus entstanden Simulationsmodelle für die Verknüpfung von Hydraulik und Morphologie, die dank des modularartigen Aufbaus die Einbindung wasser- und energiewirtschaftlicher Kennwerte einerseits und von Flora und Fauna einschließlich zugehöriger Präferenzfunktionen andererseits mehr und mehr erlaubten. Die entwickelten Modelle sind vor allem CASIMIR (Computer Aided Simulation Model for Instream Flow Requirements), BHABIM (Benthos Habitat Model) und das Fischhabitate einschließende SORAS (Structure Oriented River Analysing System). Sie alle fanden weltweite Verbreitung.

Ausgangspunkt waren die FST-Halbkugel-Messungen, die von Statzner und Müller an der Universität Karlsruhe 1989 als aussagekräftige Indikatoren für die Sohlschubspannung und die davon abgeleiteten Benthos-Charakteristika mittels standardisierter 24 Halbkugeln unterschiedlicher Dichte begründet worden sind. Der Name FST rührt aus den Anfangsbuchstaben der zwei Substantive Fließwasser und Stammtisch her.

Nach wie vor ist diese mehr qualitativ, empirisch und statistisch geprägte Methode von hohem Wert, jedoch lag es nahe, angesichts der in den zurückliegenden zwei Jahrzehnten gewonnenen vielfältigen Messergebnisse und der so ständig erweiterten Datenbanken für das FST-Verfahren die physikalischen Grundlagen zu klären, eventuell einen numerischen Hintergrund zu schaffen, schließlich anhand von Felddaten zu verifizieren und die Aussagekraft aufgrund von Fließgerinnedaten auszudehnen.

Für Ziele der Gewässerrevitalisierung bedeutet der hierdurch vorgegebene einparametrige Ansatz einen Mangel. Die Standardpräferenzen decken hauptsächlich jene Benthosorganismen ab, welche auf den Steinen des Flussbettes sitzen. Auch dürften die FST-Halbkugeln nicht jene Kräfte erfassen, die auf die Tiere selbst wirken, sondern repräsentieren ein Objekt auf der Gewässersohle. Dagegen sind die Bedingungen, die an der Oberfläche der Halbkugel bei bestimmten Strömungsverhältnissen zu verzeichnen sind, mit jenen vergleichbar, welche auf die auf den Steinen sitzenden Benthosorganismen wirken. Das heißt jedoch, dass für Tiergemeinschaften, die aus Nahrungsgründen ein Habitat hinter großen Steinen bevorzugen, die Methode nicht zu überzeugenden Ergebnissen führen könnte, obwohl die Strömungskräfte dieselben sein werden. Daher ist eher ein mehrparametriger Ansatz zu verfolgen, da die gleichen Strömungskräfte auf eine Gewässersohle aus grobem Substrat und ebenso auf eine feinkörnige, stark kolmatierte Sohle wirken können.

Die Fülle an Organismen wird im ersten Fall größer sein, da das grobkörnigere Substrat mehr Lebensraum und auch mehr Schutz bietet.

Ein weiterer Mangel der FST-Methode ist darin zu sehen, dass jeweils sehr viele Messungen bei unterschiedlichen Abflüssen anfallen, die zeit- und kostenaufwändig sind. Primär ist die Aufgabenstellung, nach Möglichkeit eine dreidimensionale, numerische Strömungsmodellierung der Halbkugel im Geschwindigkeitsprofil zur Ermittlung der nötigen Koeffizienten zu erreichen, mit der dann das Kräftegleichgewicht zwischen Schleppkraft, Auftrieb und Reibung an der Halbkugel zu definieren ist. Des Weiteren ist eine Untersuchung der Auswirkung verschiedener physikalischer Parameter auf das Strömungsbild im Umfeld der Halbkugel anzustellen. Schließlich sollten Vergleiche der rechnerisch ermittelten Halbkugeldichten mit Felddaten aus entsprechenden Messkampagnen im Labor und in Gewässerläufen den Grad der Übereinstimmung klären.

## Zum Inhalt

Die von Frau Kopecki eingereichte Promotionsschrift umfasst in acht Hauptkapiteln 197 Textseiten in englischer Sprache. Der für die gewählten Berechnungsbeispiele zusätzliche 57-seitige Anhang mit Zahlentafeln wird getrennt hinterlegt. Die der Dissertation vorangestellte, in deutscher Sprache abgefasste Zusammenfassung zählt zehn Seiten. Die hinzugezogene Fachliteratur weist im Schriftenverzeichnis 102 Publikationen aus.

Die Autorin stellt im 1. Kapitel einführend die Problemkreise, die Zielsetzungen und die ins Auge gefassten Lösungswege dar. Deutlich wird die Überlagerung mehrerer anzusprechender Fachdisziplinen, die sich in die Schwerpunkte Wasserwirtschaft, Hydraulik, Fauna, physikalische und messtechnische Grundlagen bis hin zu numerischen Simulationsverfahren und Rechenmodellen aufteilen.

Das 2. Kapitel gibt Aufschluss über die für die aquatischen Organismen in Fließgewässern maßgebenden Parameter sowie über die Möglichkeiten zur Nachbildung des von Wasserabfluss, Wassertiefe, Strömungsgeschwindigkeit, Beschaffenheit der Gewässersohle mit Substrat und Lückensystem abhängigen Benthos, worunter die für den Fischbestand und die zugehörigen Lebensvorgänge ausschlaggebenden Lebensgemeinschaften zu verstehen sind.

Aquatische Habitatmodelle, die den Lebensraum von kennzeichnenden Organismen beschreiben, sind die Grundlage für den ökologischen Bezug von Gewässerlauf, wobei die wasserwirtschaftliche Nutzung hiermit in Einklang stehen muss. Die ersten Vorgaben für eine aufrecht zu haltende Wasserführung im Gewässerbett, die zur Erhaltung natürlicher Lebensabläufe für Fauna und Flora im Flusslauf individuell zu beachten ist, wurden in den USA vor rund vier Jahrzehnten definiert. Sie sind die Voraussetzung für die Bewahrung des örtlichen Ökosystems Fließgewässer, das eine funktionelle Einheit von Lebewesen oder gar die Gesamtheit der Gesellschaft aus Tieren und Pflanzen (Biozönose), die einen gemeinsamen Lebensraum (Biotop) besiedeln, darstellt. Bis heute sind etwa 200 derartige Habitatmodelle weltweit bekannt geworden, deren Eingrenzung auf möglichst ebenso physikalisch begründete Verfahren ein Gebot der Stunde je nach geografischer Region geworden ist.

Sehr gründlich behandelt Frau Kopecki das Für und Wider einer aussagekräftigen Modellbildung zur Erfassung eines Benthos unter Einbeziehung von Ökologie, Physiologie, Morphologie, von Strömungssystem, Lichteinfall und Gewässerausbildung längs einzelner Flussabschnitte. Die zugehörigen Kennwerte werden ebenso herausgestellt wie der grundsätzliche Zusammenhang von Strömungsverhalten, Nahrungsketten und Verteilungsformen für Macro- und Micro-Invertebraten (wirbellose Tierarten).

Unter den im Einzelnen bewerteten Verfahren zur Nachbildung von Hydraulik und Morphologie nimmt die FST-Halbkugelmethode eine herausragende Stellung ein. Diesem Ende der 80er Jahre von Statzner and Müller [88] entwickelten Verfahren liegt die Annahme zugrunde, dass die aus der örtlichen und zeitlichen an der Gewässersohle herrschende Wasserströmung die Größenverteilung des stark durchströmten Macrozoobenthos vorzeichnet. Letzteres ist die Sammelbezeichnung der Tiere, die den Gewässerboden bewohnen und zumindest in einem Lebensstadium mit bloßem Auge sichtbar sind. Diese FST-Messmethode soll als hydraulische Parameter sowohl die Froude-Zahl als auch die Reynoldszahl vereinen und weniger die Organismenverteilung abhängig von einzelnen Parametern wie Strömungsgeschwindigkeit, Wassertiefe und Substratbeschaffenheit erscheinen lassen. Daher sprechen auch die Autoren von einem integrierenden Indikator der hydraulischen Charakteristika wie Turbulenzen und Schubspannungen. Tatsächlich zeigte sich mit der Fülle nachfolgender Messkampagnen bei unterschiedlichen Randbedingungen eine sehr gute Korrelation zwischen den mit 24 Halbkugeln - gleicher Größe (Radius 3,9 cm), unterschiedlicher Dichte und sich auf einer Bodenplatte je nach der Strömung bewegend - erzielten Ergebnissen und den tatsächlich aufgetretenen Sohlschubspannungen. Diese führen zu einer Aussage über die vorherrschenden Organismen des Benthos.

Doch stellte sich ebenso im Laufe der Zeit heraus, dass diese Korrelation nicht einheitlich ausfällt und vor allem vom Sohlensubstrat abhängig ist. Auch sind der große Zeit- und Kostenaufwand sowie die nicht immer leichte Durchführbarkeit der FST-Halbkugelmessungen von erheblichem Nachteil.

Neben der FST-Methode findet das PHABSIM-Modell (Physical Habitat Simulation System) häufigere Anwendung. Ihm liegen die Messungen von Wassertiefe, mittlerer Geschwindigkeit und Substratklasse an verschiedenen Messpunkten von Flussquerschnitten zugrunde. Doch stehen hier gleichfalls eine Reihe von Bedenken bezüglich der tatsächlichen Aussagekraft und der Übertragbarkeit der Messergebnisse entgegen.

Für die Weiterverfolgung der sich am ehesten anbietenden FST-Halbkugelmessmethode ist die vorliegende Dissertation auf die drei Fragestellungen ausgerichtet:

- Welcher Messwert folgt tatsächlich aus dem Einsatz der Halbkugeln?
- Sind die hohen Kosten der Messung zu rechtfertigen (z. B. 100 Messungen bei einem Strömungszustand)?
- Lassen sich tatsächlich zusätzliche Parameter des Fließgewässers auf statistischem Wege zuordnen?

Im 3. Kapitel setzt sich die Doktorandin mit den Erscheinungsformen der Strömungsabläufe relativ dünner Wasserschichten entlang der durch Geschiebe und Sedimente geprägten rauen Gewässersohle auseinander. Die Vertikalverteilung der durch die Turbulenz signifikanten Sohlschubspannungen weicht deutlich von der bei höherer Wasserüberdeckung vorhandenen linearen Verteilung ab. Es liegt auf der Hand, dass die örtlichen Wasserströmungsverhältnisse die kleinskalige Verteilung der Benthos-Organismen besser bestimmen, woraus letzten Endes sich das qualitative Messverfahren der FST-Halbkugelmethode erklärt.

Die physikalischen Grundlagen der FST-Messmethode lassen sich daher am ehesten durch die Betrachtung der hydrodynamischen Kräfte, des Auftriebes, der Schleppspannung und der Dichte der jeweils in Bewegung geratenen Halbkugeln angehen. Ansatzpunkte bieten hierfür die bekannten, für den Fischbestand entwickelten, ein- und mehrdimensionalen Modelle, hierunter am ehesten die zweidimensionalen Betrachtungsweisen. Ferner eignet sich für die Weiterverfolgung die logarithmische Geschwindigkeitsverteilung in Anlehnung an das Nikuradse-Diagramm für Fließbewegungen in rauen Gerinnen.

Zunächst konzentrieren sich die Einzelbetrachtungen auf die variierenden Strömungsverhältnisse in Flussläufen vom Quellgebiet bis zur Meeresmündung hinsichtlich Gefälle, Flussbett, Flusskrümmung und Flusssohle sowie Rauheit, Hydrologie und Wasserführung. Es folgen die eingehenden Darlegungen der für turbulente Wasserströmungen zu beachtenden Grundgleichungen von Navier-Stokes nach den Formulierungen von Reynolds und Boussinesq, ferner nach Prandtl und von Kármán, mit dem Ziel der Berechnung von Sohlschubspannungen, die sich bei unterschiedlichen Rauheitskennwerten der Gewässersohle und Turbulenzgrad einstellen.

Da die Navier-Stokes-Gleichungen für hochgradig 3-dimensionale, instationäre, turbulente Bewegungsabläufe nur auf vereinfachtem Wege gelöst werden können, erfolgt in der Wasserbaupraxis die Minderung des numerischen Aufwandes durch Einbringung der Reynolds-Averaged-Navier-Stokes-Gleichungen (RANS-Gleichungen), bei denen die ursprünglichen Beziehungen über einen langen Zeitraum analysiert und schließlich die turbulenten Prozesse statistisch gemittelt werden. Der aus einer derartigen Mittelung über ein Turbulenzmodell folgende Reynolds-Spannungsterm beschreibt den Einfluss der Turbulenz auf die mittlere Strömung. Das weithin bekannteste Turbulenzmodell ist das $k-\epsilon$-Modell, das den Transport der turbulenten kinetischen Energie $k$ und der Dissipationsrate $\epsilon$ ausweist. Es erlaubt die Beschreibung von Wasserspiegellagen, Strömungsgeschwindigkeiten und Sohlschubspannungen in Fließgewässern.

Es zeigt sich, dass die Sohlschubspannungen bei kleiner Wasserüberdeckung der Gewässersohle eher durch die Einzelelemente des Flussbodens, d. h. durch die Bodenkorngruppen, deren Lagerungsdichte und Rauheit bestimmt werden. Damit ist die Dicke dieser rauen Unterschicht der zusätzliche Parameter für die weiter reduzierte Strömungsgeschwindigkeit. Der hierdurch bedingte Dämpfungseffekt für die bodennahe Geschwindigkeitsverteilung ist durch die innerhalb des Kornhaufwerkes auftretenden turbulenten Sekundärströmungen mit den der bodennahen Hauptströmung entgegen gesetzten Auswirkungen zu erklären. Diese Vorgänge spiegeln sich in der von Bezzola 2002 aufgestellten Gleichung für die mittlere, auf die Schergeschwindigkeit bezogene Geschwindigkeit wider, die einer normalen Logarithmusverteilung bezogener Schichtdicken (Wandgesetz für Rauheitstypen) und einem Rauheitsmaß folgt.

Im 4. Kapitel wird die FST-Halbkugelmethode in vielen Details analysiert. Dieses 1989 veröffentlichte Messverfahren für die Bestimmung der durch das Benthal und das Benthos gekennzeichneten Sohlschubspannungen fand eine große Verbreitung. Zwischenzeitlich liegen nach umfangreichen Messprogrammen über 50 standardisierte, d. h. von individuellen Flussabschnitten unabhängige Präferenzkurven für die im Makrozoobenthos anzutreffenden Tierarten vor. Doch stellten sich ebenso in der Fachwelt mehr und mehr Zweifel über die tatsächliche Aussagekraft ein, da die abgeleiteten Kennwerte um eine bis zwei Größenordnungen über den tatsächlich anzutreffenden benthischen Organismen liegen. Darüber hinaus führt der jeweilige Umfang der Messkampagnen zu extrem hohen Kosten. Umso mehr schien es angebracht, in der vorliegenden Promotionsschrift die Hintergründe zu erforschen und nach einem gangbaren Lösungsweg für realistischere Ergebnisse zu suchen.

Der Schwerpunkt dieser Analysen liegt in der Entwicklung der möglichen Korrelation zwischen den durch Strömungskräfte bewegten Halbkugeln verschiedener Dichte und den Sohlschubspannungen. Die leichteste Halbkugel von 3,9 cm Größe (Nr. 1) hat eine Dichte von 1,015 $g/cm^3$, die schwerste Halbkugel (Nr. 24) mit 10,009 $g/cm^3$ etwa das Zehnfache. Die Halbkugeln werden der Reihe nach bis zu einem Abdriften auf eine 13 x 18 cm große Grundplatte mit zwei eingebauten Libellen aufgelegt, die bis zur Oberkante in dem Sohlesubstrat einzubetten ist. Die Nummer jener schwersten Halbkugel, die gerade noch durch die bodennahe Strömung abgetrieben wird, repräsentiert die in Hauptströmungsrichtung an Ort und Stelle vorhandene Strömungskraft, die über die Hydraulik bei bestimmten Substratverhältnissen mit zugehörigen Organismen Auskunft gibt. Die Vervielfachung derartiger Messfolgen führt zu Vergleichswerten mit das Benthos beschreibenden Präferenzkurven.

Offensichtlich ist die Aussagekraft derartiger Messkampagnen stark davon abhängig, welcher Qualität die Verlegung der Grundplatte, die Oberflächenbeschaffenheit (Rauheit, Wasserfilm), das jeweilige Aufsetzen der Halbkugel auf die Platte (Kippen, Drücken, Pressen) und zusätzlich die Kornstruktur der Gewässersohle sind. Hierüber folgten in jüngster Zeit sorgfältige Labor- und Felduntersuchungen durch eine ganze Reihe von Forschungsstätten, woraus sich eine Vielfalt von Verbesserungsvorschlägen in der praktischen Handhabung ergeben haben.

Frau Kopecki analysierte diese detailliert und ging neue Wege auf Basis vertiefter strömungstheoretischer, vor allem hydrodynamischer Betrachtungen. Sie führten zu maßgebenden Beziehungen für die durch Kennwerte gestützten hydraulischen Zusammenhänge der Halbkugeldichten und der einer logarithmischen Verteilung folgenden, relativen Strömungsgeschwindigkeiten in verschiedenen bodennahen Höhenlagen, d. h. damit auch der Sohlschubspannungen entlang dem Benthossubstrat auf der Flusssohle.

Eine weitere Vertiefung der für die FST-Halbkugelmethode neuartigen wissenschaftlichen Erkenntnisse ist dem 5. Kapitel zu entnehmen. Im Mittelpunkt stehen die Strömungsabläufe und die Strömungsbilder für der Hauptströmung ausgesetzte Störkörper unterschiedlicher Formgebung und Volumina, so auch Halbkugeln, zusammen mit Stau-, Ablösungs-, Turbulenz-, Wirbel- und Rückströmungszonen. Reynolds-, Froude- sowie Strouhalzahl und relativer Wasserüberdeckung der Halbkugeln, ferner Oberflächenrauheit, Auflagerbedingungen und bodennahe Druck- und Geschwindigkeitsverteilungen sind für die laminare und turbulente Strömungsausprägung mit Wirbelstraßen im Anschluss an den Halbkugelstandort entscheidend. Gewichts-, Reibungs-, Schlepp- bzw. Trägheits- und Auftriebskräfte kennzeichnen das Kräftebild.

Mit in der Fachliteratur verankerten physikalischen Beziehungen und dem Finite-Volumen-Programm FLUENT unter Einbeziehung greifbarer Laboruntersuchungen gelingt der Autorin der Nachweis, dass sich die dreidimensionalen instationären Strömungsabläufe um die Halbkugeln unterschiedlicher Dichte bei ebenso unterschiedlichen Rauheiten der Körperoberfläche und der Auflagerfläche auf dem Sohlensubstrat numerisch nachbilden lassen. Diese, nach umfangreichen, sehr ins Detail gehenden Untersuchungen der hydraulischen und mathematisch-physikalischen Zusammenhänge gewonnenen Erkenntnisse, die eine Vielzahl variierender Randbedingungen einschließen, erweisen sich mit vier Kernaussagen laut der in Abschnitt 5.6 erfolgten Zusammenfassung als sehr aufschlussreich für die Beurteilung der FST-Halbkugelmessungen.

Für die im vorausgegangenen Kapitel aussagekräftigen Untersuchungsergebnisse werden nun im 6. Kapitel insgesamt sechs Fallstudien aus der Labor- und Wasserbaupraxis zur Beweisführung herangezogen. Die vergleichbaren Labordaten stammen aus der Universität Karlsruhe, während die Felddaten an Fließgewässern in Belgien (Zwalm), Deutschland (Körsch), Frankreich (Rhône), Österreich (Schwechat) und schließlich Grenzgebiet

Deutschland/Schweiz mit dem Standort Rheinau ebenso aus vor Ort durchgeführten FST-Halbkugelmesskampagnen herrühren.

Hiermit sollen die beiden grundsätzlichen Fragen beantwortet werden, inwieweit die von Bezzola aufgestellte, einer logarithmischen Verteilung folgende Formel für die relative Geschwindigkeitsverteilung der Wasserströmung unmittelbar oberhalb des Sohlensubstrates zutrifft. Dasselbe ergibt sich in der Fragestellung für die durch Wassertiefe, Strömungsgeschwindigkeit , Halbkugelradius, Reibungsbeiwert und hydraulische dynamische Koeffizienten gekennzeichnete Gleichung ( 5.14) zur numerischen Bestimmung der das FST-Halbkugelverfahren ausweisenden Dichte. Dieser Halbkugeldichte entspricht eine der 24 Halbkugelnummern.

Der Gegenüberstellung von Rechnung und Laborversuch dienten insgesamt 11 Versuchsserien, die am Institut für Wasserwirtschaft und Kulturtechnik der Universität Karlsruhe 1999 im Theodor-Rehbock-Flussbaulaboratorium aufgenommen worden sind. Die Übereinstimmung konnte weitgehendst nachgewiesen werden.

Die zusätzlich genannten fünf Feldversuche lieferten gleichfalls in überwiegendstem Maße sehr gute Resultate. Für die gelegentlichen Abweichungen von Simulation und Feldmessung, die bis zu zwei Halbkugelnummern erreichen, werden überzeugende Begründungen gegeben. Von stärkerem Einfluss sind naturgemäß die einwandfreie Auflagerung der Grundplatte, die Reibung zwischen Halbkugel und Grundplatte sowie die tatsächliche Rauheit des Kornhaufwerkes des Sohlensubstrates. Bei den an der Körsch und an der Zwalm durch das Stuttgarter Institut für Wasserbau durchgeführten Messungen kamen zusätzlich für die Geschwindigkeitsmessung ein Mikroflügel und ein Akustik-Doppler-Geschwindigkeitsmesser zum Einsatz, die allerdings unterschiedliches Verhalten und größere Abweichungen zeigten und von der Verfasserin näher analysiert worden sind. Die eindrucksvollen Ergebnisse gaben Anlass, im Kapitel 7 die für das FST-Halbkugel-Messverfahren geschaffene rechnerische Grundlage zu verallgemeinern und als Ersatz demgegenüber das entwickelte numerische Verfahren in den Vordergrund zu stellen. Das von der Formel von Bezzola ausgehende Simulationsverfahren geht zunächst von der in 40 %-iger Höhe der vor Ort vorhandenen Wassertiefe zu messenden Fließgeschwindigkeit aus, dann von der Dicke der rauen Schicht entlang des Sohlensubstrates. Die Vorgehensweise ist in einer Bilderfolge gemäß einem üblichen Flussdiagramm veranschaulicht. Sie wird in den Textteilen ausführlich erläutert. Diese Erläuterungen schließen die weiteren Verbindungen zu den aufnehmenden Computerprogrammen CASIMIR und BHABIM (Casimir-Modul) unter Verwendung der Fuzzy-Logic-Methode sowie der zusätzlichen Unterprogramme ein. Wiederum dient als nachvollziehbares Beispiel der Fluss Körsch im Großraum Stuttgart. Offensichtlich ist der große Vorteil, dass für die Bewertung des aquatischen Lebensraumes für Fische und Benthos in Fließgewässern und für die Festlegung von Mindestwasserführungen zu deren Erhaltung die hier vorgestellte numerische Methode eine wesentliche Erleichterung im Vergleich zu den seitherigen FST-Halbkugelmessungen bedeutet. Jedoch bleibt das Prinzip der Übertragbarkeit der 24 sich in der Dichte unterscheidenden Halbkugel-Werte auf korrelierende Präferenzkurven für die in Gewässern vorherrschende Tierwelt davon unberührt. Die Simulationsmethode erlaubt darüber hinaus die Einbindung von Kennwerten wie die Wassertiefe und die individuelle Beschaffenheit des Sohlensubstrates und das örtliche Nahrungsangebot.

Ein weiterer Vorteil ist die Anwendung des rechnerischen Simulationsverfahrens bei Aufgaben der Gewässerrevitalisierung in Abhängigkeit variierender Fluss- und Habitatsparameter. Schließlich kann es für weiträumige Untersuchungen in das Arc View GIS 3.3-System eingebunden und mit den zweidimensional gewonnenen Datenaufnahmen direkt in das vielfach bewährte modellartig aufgebaute CASIMIR-Computerprogramm implementiert werden.

Im 8. Kapitel erfolgt abschließend eine Zusammenfassung der bewältigten, komplexen Untersuchungsschritte, der getroffenen Voraussetzungen und der erleichterten Handhabung des entwickelten Instrumentariums in der Wasserbaupraxis.

Der Ausblick auf den zukünftigen Forschungsbedarf erstreckt sich auf die Ausdehnung der Bezzola-Gleichung auf instationäre Strömungen, auf die verbesserte Formulierung der Schichtstärke für die raue Substratschicht (anstelle des bisher verwendeten mittleren Korndurchmessers) und schließlich auf die eindeutige Habitatmodellierung über den einen, durch die FST-Halbkugelmethode vorgegebenen Kennwert hinaus.

Von ähnlichem Interesse sind die Auswirkungen einer neuen Habitatbildung, die bei großen Störkörpern unterwasserseitig ausgelöst wird und zu Besiedlungen andersartiger Organismen führt. Schließlich sollte der Einfluss der Wassergüte auf das Benthos nicht außer Acht bleiben.

## Zusammenfassende Betrachtung

Frau Ianina Kopecki legte eine bemerkenswerte Dissertation vor. Gemäß dem Leitthema sollte eine numerische Basis für das empirische FST-Halbkugelverfahren geschaffen werden. Diesem seit fast zwei Jahrzehnten im Flussbau gängigen Messverfahren liegen 24 standardisierte Halbkugeln mit Einzeldichten von 1,015 $g/cm^3$ bis 10,009 $g/cm^3$ zugrunde, die der Reihe nach auf einer in das Sohlensubstrat eingebetteten Grundplatte von 13 x 18 cm Größe aufgesetzt werden, bis die bodennahe Wasserströmung sie verdriftet. Jene Halbkugel, die dem Abdriften eine genügend große Reibungskraft entgegensetzt, liefert einen Kennwert für die vorherrschende Sohlschubspannung, die über Präferenzfunktionen Aufschluss über das Benthos, die Lebensgemeinschaft wirbelloser Tiere, als Richtmaß für den ökologischen Zustand des Fließgewässers gibt. Die Doktorandin befasste sich eingehend mit den physikalischen Randbedingungen für laminare und turbulente Strömungsverhältnisse im Umfeld der der Wasserströmung ausgesetzten Halbkugeln. Die Analysen der hoch komplexen Strömungsabläufe führten zu neuartigen Erkenntnissen, dank derer tatsächlich die sehr aufwändige und kostenträchtige FST-Messmethode durch ein numerisches Simulationsmodell auf der Basis hydrodynamischer und morphologischer Parameter ersetzt werden konnte. Diese Ergebnisse werden anschaulich anhand von fünf Feldmessungen an verschiedenen Flussläufen im In- und Ausland und weiterer Modellversuche im Wasserbaulabor eindrucksvoll unterstrichen.

Für die unmittelbare Handhabung in der Wasserbaupraxis wurden in Anlehnung an ein Flussdiagramm durch näher beschriebene Bildfolgen die Vorgehensweisen und die zu erzielenden Ergebnisse erläutert. Der hohe Wert der vorgelegten Promotionsschrift zeigt sich hierin besonders deutlich, zumal sich die gute Aussagekraft für Hydraulik und Ökologie in hervorragender Weise mit beträchtlicher Kostenersparnis ergänzt.

Stuttgart, im Januar 2008 Jürgen Giesecke

# Danksagung

Ich möchte allen, die zum Gelingen dieser Arbeit beigetragen haben, ein herzliches Dankeschön sagen.

An erster Stelle möchte ich Herrn Professor Giesecke für die Anleitung und Unterstützung bei dieser Arbeit und nicht zuletzt für die Motivierung selbst in schwierigen Zeiten danken. Auch möchte ich ihm für die Regelung aller Formalitäten und die Bereitstellung der Rahmenbedingungen danken.

Frau Professor Wieprecht und Herrn Professor Zanke danke ich für die Übernahme des Koreferats, dem Einbringen interessanter Vorschläge zu Inhalt und Form der Arbeit und für die interresanten Fragen während der Prüfung.

Dem Ministerium für Wissenschaft, Forschung und Kunst Baden-Württemberg danke ich für die Bewilligung eines Stipendiums im Rahmen des Irene Rosenberg-Promotionsprogramms für Frauen in den Ingenieurwissenschaften, durch das dieses Promotionsvorhaben erst möglich geworden war.

Allen meinen Arbeitskollegen danke ich für die freundliche Arbeitsatmosphäre und die Hilfsbereitschaft, ganz besonderes Klaus Jorde, Andreas Eisner, Frank Zöllner, Franz Kerle, Stephan Heimerl, Beate Kohler, Walter Marx und Brigitte Muschong.

Für die Bereitstellung der Daten für die Validierung der Ergebnisse möchte ich mich bei den Kollegen Helmut Mader, Sylvie Mérigoux, Ans Mouton und Morten Lauge Pedersen aus COST 626 bedanken. Ohne diese breitgefächerte Auswahl an Beispielen wäre es nicht möglich gewesen, den Ansatz in dieser Tiefe zu validieren.

Eva Fenrich danke ich herzlich für Ihre Unterstützung und Ihrer Bereitschaft, selbst im kältesten Winter mit mir die Messkampagne an der Körsch durchzuführen.

Ganz besonders danke ich meinem Kollegen und Geschäftsführer der Firma sje, Matthias Schneider, für die ständige Unterstützung, Motivation, wissenschaftliche Begleitung und inhaltlichen Korrekturen der Erstfassungen.

Mein größter Dank gilt meiner Familie in Russland und meinen Lieben Lisa, Sonja und Andreas für die unbezahlbare Hilfe und den heroischen Verzicht auf viele gemeinsame Stunden, die der Dissertation zugeflossen sind.

Stuttgart, im Februar 2008 Ianina Kopecki

# Contents

# List of Figures

# List of Tables

# Symbols and Abbreviations

## Abbreviations

| | |
|---|---|
| 1D, 2D, 3D | one-, two-, three-dimensional |
| ADV | Acoustic Doppler Velocimeter |
| BHABIM | Benthos HABItat Model |
| CASiMiR | Computer Aided Simulation Model for Instream Flow Requirements |
| COST | European Co-operation in the field of Scientific and Technological Research |
| c.g. | center of gravity |
| c.p. | center of pressure |
| DOF | degree of fulfilment |
| DGPS | differential Global Positioning System |
| EFA | environmental flow assessment |
| FESWMS | Finite Element Surface Water Modeling System |
| FST | Fließwasserstammtisch |
| GB | gigabyte |
| GIS | geographic information system |
| GPS | Global Positioning System |
| HLRS | Höchstleistungsrechenzentrum Stuttgart |
| ID | identification number |
| IFIM | Instream Flow Incremental Methodology |
| KO | $k - \omega$ turbulent model |
| LES | Large Eddy Simulation |
| P-EMS | programmable electromagnetic velocity meter |
| PHABSIM | Physical HABitat SImulation Model |
| RAM | random access memory |
| RANS | Reynolds-averaged Navier-Stokes equations |
| rms | root mean square |
| RNG | Re-Normalization Group |
| SA | Spalart-Allmaras turbulent model |
| SI | Suitability Index |
| SORAS | Structure Orientated River Analysing System |
| SMS | Surface-Water Modeling System |
| SST | Shear Stress Transport turbulent model |

# Symbols

| | | |
|---|---|---|
| $\mathbf{A}$ | | fuzzy set |
| $A(x)$ | | membership function |
| $A_\perp$ | [m$^2$] | cross-section area of a hemisphere (or grain) perpendicular to the main flow direction |
| $A_1$ | [-] | constant in the log law distribution for hydraulically smooth flow |
| $A_{FST_i}$ | [m$^2$] | area of the cell with FST $= i$ |
| $A_i$ | [m$^2$] | surface area of inundated spatial unit $i$ |
| $A_q$ | [m$^2$] | area of a river cross-section |
| $A_{tot}$ | [m$^2$] | total wetted area of a river reach |
| $B_m$ | [m] | mean width of a river reach |
| $B_q$ | [m] | width of a river cross-section |
| $C_1$ | [-] | constant in the log law distribution for hydraulically rough flow |
| $C_\mu$ | [-] | empirical model constant in $k - \epsilon$ turbulence model) |
| $c_d$ | [-] | drag coefficient, total drag coefficient |
| $\widetilde{c}_d$ | [-] | drag coefficient deviation from the mean value |
| $c_{d,b}$ | [-] | base drag coefficient |
| $c_{d_{CL}}$ | [-] | centerline pressure drag coefficient |
| $c_{d_p}$ | [-] | pressure drag coefficient |
| $c_l$ | [-] | lift coefficient, total lift coefficient |
| $\widetilde{c}_l$ | [-] | lift coefficient deviation from the mean value |
| $c_{l,b}$ | [-] | base lift coefficient |
| $c_{l_p}$ | [-] | pressure lift coefficient |
| $c_p$ | [-] | pressure coefficient |
| $c_r$ | [-] | damping factor in Bezzola's log law |
| $D$ | [m] | characteristic size (diameter or spanwise width) of an object (obstacle) |
| $D_h$ | [m] | hydraulic diameter of a channel |
| $d$ | [m] | diameter of substrate material, mean grain diameter |
| $d_i$ ($d_{16}$, $d_{50}$, $d_{84}$) | [m] | characteristic diameter of substrate material, i per cent (of total weight) are finer |
| $d_h$ | [m] | diameter of a hemisphere |
| $d_s$ | [m] | diameter of a grain |
| $E$ | [-] | relation of impounded to freely flowing reach lengths in HABITAT |
| $F_d$ | [N] | drag force |
| $F_f$ | [N] | friction force |
| $F_h$ | [N] | hydrodynamic force |
| $F_g$ | [N] | immersed weight |
| $F_l$ | [N] | lift force |
| $F_n$ | [N] | component of $F_g$ normal to the surface of an inclined plane |
| $F_s$ | [N] | sliding force |
| $Fr$ | [-] | Froude number |

| | | |
|---|---|---|
| | | $Fr = u_{0.4}/\sqrt{g\,h}$ |
| | | open channel flow: $Fr = U_m/\sqrt{gA_q\,/B_q}$ |
| | | in FSTRESS: $Fr_m^2 = Q^2/(g\,H_m^3 B_m^2)$ |
| $FST_c$ | [-] | calculated FST-hemisphere number |
| $FST_m$ | [-] | measured FST-hemisphere number |
| $FST_{new}$ | [-] | FST-hemisphere number (on new, structured plate) |
| $FST_{old}$ | [-] | FST-hemisphere number (on old, smooth plexiglass plate) |
| $f$ | [$s^{-1}$] | frequency of vortex shedding |
| $f(n_i)$ | [-] | frequency of the i-th FST number in FSTRESS |
| $H$ | [m] | height of an object (obstacle) |
| $HHS$ | [-] | Hydraulic Habitat Suitability index of a river reach |
| $H_m$ | [m] | mean depth of a river reach |
| $HSI$ | [-] | Habitat Suitability Index |
| $HSI_i$ | [-] | Habitat Suitability Index of a spatial unit $i$ |
| $h$ | [m] | water depth |
| $h_p$ | [m] | thickness of the FST ground plate |
| $h_t$ | [m] | total water depth in the log law, $h_t = h + \Delta\, y_0$ |
| $I$ | [%] | normalized with $U_{avg}$ turbulent intensity, $I = u'/U_{avg}$ |
| $I_x$ | [-] | normalized with $u_*$ turbulent intensity in $x$-direction |
| $I_y$ | [-] | normalized with $u_*$ turbulent intensity in $y$-direction |
| $I_z$ | [-] | normalized with $u_*$ turbulent intensity in $z$-direction |
| $i_0$ | [-] | mean slope of a reach (channel) |
| $g$ | [$m/s^2$] | acceleration due to gravity |
| $k$ | [$m^2/s^2$] | turbulent kinetic energy |
| $k$ | [m] | geometrical roughness height |
| $k_m$ | [-] | mixing parameter in FSTRESS |
| $k_s$ | [m] | hydraulic (equivalent) roughness height |
| $l$ | [m] | Prandtl's mixing length |
| $n$ | [-] | Manning roughness coefficient |
| $n_i$ | [-] | i-th FST number in FSTRESS |
| $n_m$ | [-] | FST number – mean of the normal distribution in FSTRESS |
| $P_u$ | [-] | velocity profile form parameter |
| $p$ | [Pa] | instantaneous pressure |
| $\overline{p}$ | [Pa] | mean (time-averaged) component of pressure |
| $\overline{p}$ | [Pa] | local mean (time-averaged) static pressure |
| $p_0$ | [Pa] | reference static pressure of a free stream |
| $p_m$ | [-] | meandering degree in HABITAT |
| $Q$ | [$m^3/s$] | discharge |
| $R^2$ | [-] | coefficient of determination |
| $Re$ | [-] | Reynolds number |
| $Re_*$ | [-] | Reynolds number |
| | | $Re_* = h\,u_*/\nu$ |

| | | |
|---|---|---|
| | | $Re_* = D\, u_*/\nu$ |
| $Re_*$ | [-] | grain Reynolds number<br>$Re_* = k_s\, u_*/\nu$<br>$Re_* = k\, u_*/\nu$<br>$Re_* = d_s\, u_*/\nu$ |
| $Re_{0.4}$ | [-] | Reynolds number $Re_{0.4} = 2\, r_h\, u_{0.4}/\nu$ |
| $Re_{D_h}$ | [-] | Reynolds number $Re_{D_h} = D_h\, U_{avg}/\nu$ |
| $Re_{ht}$ | [-] | Reynolds number $Re_{ht} = 2\, r_h\, u_{ht}/\nu$ |
| $Re_t$ | [-] | transition Reynolds number $Re_t = x_t\, U_0/\nu$ |
| $Re_{U_0}$ | [-] | Reynolds number $Re_{U_0} = D\, U_0/\nu$ |
| $r_h$ | [m] | radius of a hemisphere |
| $SI$ | [-] | partial Suitability Index |
| $SI_m$ | [-] | Suitability Index in respect to parameter $m$ |
| $SI_d$, $SI_v$, $SI_s$ | [-] | Suitability Indexes in respect to water depth, velocity and substrate |
| $SI_{v,d}$ | [-] | joint Suitability Index for depth and mean column velocity |
| $St$ | [-] | Strouhal number $St = f\, D/U_0$ |
| $T$ | [s] | period of one shedding circle |
| $U_0$ | [m/s] | free stream velocity |
| $U_{avg}$ | [m/s] | average flow velocity |
| $U_m$ | [m/s] | velocity averaged over cross-section |
| $u$ | [m/s] | instantaneous velocity along $x$-axis, $u = \overline{u} + u'$ |
| $\overline{u}$ | [m/s] | mean (time-averaged) velocity component along $x$-axis |
| $u'$ | [m/s] | pulsation velocity component along $x$-axis |
| $u_*$ | [m/s] | shear velocity |
| $u^+$ | [-] | dimensionless mean velocity component along $x$-axis,<br>$u^+ = \overline{u}/u_*$ |
| $u_{0.4}$ | [m/s] | mean column velocity |
| $u_{hc}$ | [m/s] | velocity at the level of a hemisphere's center of mass |
| $u_{ht}$ | [m/s] | velocity at the top level of a hemisphere |
| $\overline{u}_{max}$ | [m/s] | maximum mean velocity (in the vertical) along $x$-axis |
| $V_h$ | [$m^3$] | volume of a hemisphere |
| $v$ | [m/s] | instantaneous velocity along $y$-axis, $v = \overline{v} + v'$ |
| $\overline{v}$ | [m/s] | mean (time-averaged) velocity component along $y$-axis |
| $v'$ | [m/s] | pulsation velocity component along $y$-axis |
| $WUA$ | [$m^2$] | Weighted Usable Area of a river reach |
| $w$ | [m/s] | instantaneous velocity along $z$-axis, $w = \overline{w} + w'$ |
| $\overline{w}$ | [m/s] | mean (time-averaged) velocity component along $z$-axis |
| $w'$ | [m/s] | pulsation component of velocity in $z$-direction |
| $x$, $y$, $z$ | [m] | system of rectangular cartesian coordinates |
| $x_t$ | [m] | distance along the surface from the stagnation to transition point |
| $y^+$ | [-] | dimensionless distance from the wall<br>$y^+ = y\, u_*/\nu$ |

| | | |
|---|---|---|
| $y_0$ | [m] | distance from the wall at which $\overline{u} = 0$ |
| $y_r$ | [m] | thickness of the roughness sublayer |
| $y_w$ | [m] | thickness of the inner region |
| $\alpha$ | [°] | angle of channel bottom |
| $\alpha$ | [°] | sliding angle for a hemisphere on the FST ground plate |
| | | $\alpha_{min}$ - minimum angle, $\alpha_{max}$ - maximum angle |
| $\Delta$ | | Laplace operator |
| $\Delta\, y_0$ | [m] | offset of the log law profile origin below roughness tops |
| $\overline{\Delta}_{FST}$ | [-] | average difference between calculated and measured FST numbers |
| $\delta$ | [m] | boundary layer thickness |
| $\delta_{FST_i}$ | [%] | contribution of i-th FST number in the sample |
| $\epsilon$ | [$m^2/s^3$] | turbulence dissipation rate |
| $\eta_i$ | [-] | degree of fulfilment of a rule $i$ |
| $\theta$ | [-] | Shields' entrainment function |
| $\theta$ | [°] | elevation angle |
| $\kappa$ | [-] | von Kármán constant, $\kappa = 0.4$ |
| $\mu$ | [-] | friction coefficient |
| | | $\mu_{max}$ - maximum coefficient, $\mu_{min}$ - minimum coefficient |
| $\mu_{\mathbf{A}}(x_1)$ | [-] | degree of membership of parameter $x_1$ relating to fuzzy set **A** |
| $\mu_{\mathbf{B}}(x_2)$ | [-] | degree of membership of parameter $x_2$ relating to fuzzy set **B** |
| $\mu_{K_i}(x)$ | | membership function of the consequence $K_i$ |
| $\mu_{tot}(x)$ | | total consequence output |
| $\nu$ | [$m^2/s$] | kinematic viscosity of fluid |
| $\nu_t$ | [$m^2/s$] | kinematic eddy viscosity of fluid |
| $\widetilde{\nu}_t$ | [$m^2/s$] | modified kinematic eddy viscosity of fluid |
| $\pi$ | [-] | Pi number |
| $\rho$ | [$kg/m^3$] | density of fluid |
| $\rho_h$ | [$kg/m^3$] | density of a hemisphere |
| $\rho_s$ | [$kg/m^3$] | density of a substrate grain |
| $\rho_w$ | [$kg/m^3$] | density of water |
| $\tau$ | [$N/m^2$] | total shear stress |
| $\tau_0$ | [$N/m^2$] | bottom shear stress |
| $\tau_c$ | [$N/m^2$] | critical bottom shear stress |
| $\tau_l$ | [$N/m^2$] | viscous (laminar) shear stress |
| $\tau_m$ | [$N/m^2$] | bottom shear stress corresponding to the mean of the normal distribution $n_m$ in FSTRESS |
| $\tau_t$ | [$N/m^2$] | turbulent shear stress |
| $\omega$ | [1/s] | specific dissipation rate |

# Zusammenfassung

Ziel dieser Arbeit ist die Erweiterung der Modellierung benthischer Lebensräume in Fließgewässern. Derzeitige Modelle übertragen entweder die Ansätze der Fischhabitatmodellierung direkt auf Benthos, wie beispielsweise das in Nordamerika verbreitete PHABSIM, oder erlauben nur eine einparametrische Modellierung des Lebensraums, wie der in Europa verbreitete Ansatz auf Basis der FST-Halbkugelmethode. Bei letzterer Methode kann über eine große Anzahl existierender "Präferenzkurven" das Habitat bewertet werden. Dies setzt jedoch sehr arbeitsintensive Feldmessungen voraus, die den Einsatz dieser Modellierung sehr kostenintensiv und zeitaufwendig werden lassen. Auch werden dort weitere wichtige Parameter, die das Vorkommen und die Verteilung benthischer Arten beeinflussen, wie Substrat, Nahrungsangebot und andere bei der Modellierung nicht betrachtet. Hier soll eine Methode gefunden werden, wie einerseits die notwendigen Messungen auf ein Minimum reduziert werden und andererseits auch andere Parameter in die Modellierung einfließen können. Die vorliegende Arbeit hat einen multidisziplinären Charakter und richtet sich insbesondere an Wasserbauingenieure, Habitatmodellierer und Biologen.

Eine zeitgemäßen Benthoshabitatmodellierung, die die gleiche Mächtigkeit wie die schon existierende für Fische aufweist, lag im Fokus dieser Arbeit. Die physikalischen Grundlagen der FST-Halbkugelmethode werden geklärt und damit die Wichtigkeit bereits erhobener biologischer Daten unterstrichen. Ein rechnergestützter Ansatz macht früher benötigte Feldmessungen der FST-Halbkugelverteilung überflüssig und verwendet dabei die gleiche Datengrundlage wie die für Fischhabitatmodellierungen. Die räumliche Zuordnung der Halbkugelnummern erlaubt zusätzlich das einfache Miteinbeziehen neuer Parameter in die Benthoshabitatmodellierung. Damit eröffnen sich neue Möglichkeiten, beispielsweise im Bereich der Mindestwasser- und Renaturierungsstudien.

## Motivation

Fließgewässer – Flüsse und Bäche – sind wichtige ökologische Systeme, die sich sowohl durch eine große Variabilität und Dynamik als auch durch eine enorme Artenvielfalt auszeichnen. Gesunde Fließgewässer sind wesentlich für die Wasserqualität sowie den Erhalt der Artenvielfalt im Wasser und auf dem Land. Dieses wertvolle Ökosystem hat sich durch menschliche Eingriffe drastisch über die Jahrhunderte hinweg verändert. Die Beeinflussung des natürlichen Abflusses und des Sedimenttransports durch Ausleitungen für Wasserversorgung und Stromerzeugung, Hochwasserschutz und Schifffahrt führte zur Verarmung einzigartiger Ökosysteme. Schmutzwasser aus Landwirtschaft und Industrie führten zu weiterer Vernichtung von Lebensraum. In den 70er Jahren des letzten Jahrhunderts erreichte die Wasserqualität europäischer Flüsse ein Höchstmaß an Verschmutzung. Die Konsequenz daraus war eine fortlaufende Verringerung der Artenvielfalt.

Obwohl sich in den letzten Jahrzehnten die Wasserqualität von west- und mitteleuropäischen Flüssen aufgrund steigender Zahl an Kläranlagen ständig verbesserte, sind viele strukturelle und hydraulische Defizite geblieben oder sogar gewachsen, welche die ökologische Funktion von Fließgewässern beeinflussen. Hauptprobleme sind hier begradigte und kanalisierte Flussläufe, Migrationsbarrieren wie Wehre und Dämme sowie fehlende Verbindungen zwischen Hauptkanal und Auen. Diese strukturellen Defizite zeigen sich insbesondere in Flüssen mit Ausleitungsstrecken.

Als eines der wichtigsten Hilfsmittel für die Analyse der Gewässerfunktionen werden Habitatmodelle angesehen. Diese ermöglichen es, Aussagen über die Qualität der Lebensräume für die im betrachteten System angesiedelten Lebewesen zu treffen. Mit Habitatmodellen kann der Einfluss von Abfluss- und Strukturänderungen auf Fische, Invertebraten und Makrophyten vorausgesagt werden. Abflussänderungen in Fließgewässern wirken sich primär auf Wassertiefen, Fließgeschwindigkeiten und Substratzusammensetzung aus, die alle Hauptfaktoren der Habitatqualität und damit -modellierung sind. Durch den Bezug des Habitatangebots auf den Abfluss wird eine quantitative Basis geschaffen, die es erlaubt, ökologische Bewertungen den Nutzungsansprüchen gegenüberzustellen.

Ursprünglich aus Nordamerika sind physikalische Habitatmodelle seit den späten 1970ern zu Standardmethoden in der Wasserwirtschaft geworden. Es handelt sich dabei in der Regel um physikalisch basierte Modelle, welche Beziehungen zwischen den hydraulischen bzw. strukturellen Umgebungsparametern (Strömung, Sohlaufbau u.ä.) und den Ansprüchen der Gewässerorganismen nutzen, um Aussagen über Habitateignungen zu treffen. Bisher wurden hauptsächlich Fische, vor allem die wirtschaftlich interessanten Salmoniden (Lachsartige), betrachtet. Der Anwendungsbereich für derartige Modelle hat sich erweitert, und Habitatmodellierungen werden für die Behandlung folgender Fragestellungen eingesetzt: Abflussregelungen, Strukturgüteuntersuchungen, Gewässerrenaturierung, Auswirkungen von Gewässerausbaumaßnahmen und Einzugsgebietsmanagement.

Die vorliegende Arbeit beschäftigt sich mit *Benthos*-Habitatmodellierung für Fließgewässer. Als Benthos wird die am oder im Gewässergrund – dem Benthal – lebende Gemeinschaft von Organismen bezeichnet. Dies sind meist Wirbellose, jedoch können nach dieser Definition auch am Grund lebende Fischarten dazu gezählt werden. Benthosarten erfüllen eine Vielzahl wichtiger Funktionen in Fließgewässerökosystemen. So beschleunigen sie beispielsweise den Abbau toter organischer Masse, da diese zu ihren Hauptenergiequellen zählt. Viele wirbellose Benthosarten sind Räuber, die die Dichte, das Vorkommen und die Größe ihrer Beute beeinflussen. Insbesondere sind diese Arten eine wichtige Nahrungsquelle für viele andere Arten wie Fische, Schildkröten oder Vögel.

Die Entwicklung eines neuen Habitatmodellierungsansatzes für Benthosarten ist aus zweierlei Gründen als wichtig einzustufen. (1) Ein zeitgemäßes Verständnis der Flussökosysteme umfasst die Betrachtung aller seiner Komponenten und somit auch der Benthosarten, schon deswegen, weil diese teilweise spezifischere Ansprüche an ihre Umweltbedingungen stellen als beispielsweise Fische. (2) In einigen Fällen sind benthische Organismen die einzigen Zielarten von Habitatuntersuchungen, entweder weil in den Untersuchungsstrecken keine Fische vorhanden sind oder dort einzigartige Benthosarten vorkommen, die es auf jeden Fall zu erhalten gilt. Wegen der Besonderheiten des Benthoshabitats können Fischhabitatmodelle mit ihren typischen Parametern wie Wassertiefe, Substrat und tiefengemittelte Geschwindigkeit nicht direkt benutzt werden. Deren Parameter können jedoch in einem konzeptionell angepassten Modell Verwendung finden.

Diese Arbeit soll einen Beitrag zur Weiterentwicklung der Software CASiMiR – Computer Aided Simulation Model for Instream Flow Requirements – liefern, die an der Universität Stuttgart am Institut für Wasserbau entwickelt wurde. Insbesondere soll die Komponente BHABIM (Benthos HABItat Model) in seinem Anwendungsbereich und seiner Realitätsnähe, ferner zur Verringerung der Modellierungskosten verbessert werden. Neben BHABIM, dem ersten Modell, das auf Grundlage der FST-Halbkugelmethode entwickelt wurde, entstand in CASiMiR das Fischhabitatmodul SORAS (Structure Orientated River Analysing System). Mittels Fuzzy-Logik erlaubt SORAS die Bewertung der Einflüsse von Abflussregimeänderungen auf Fischhabitate über ein- oder zweidimensionalen hydraulischen Modelldaten. Das Ziel ist, die Benthoshabitatmodellierung auf den gleichen hohen Standard zu bringen, den das Fischhabitatmodul schon besitzt. In Zukunft sollte es diesem Modell möglich sein, Antworten auf die Frage nach den ökologischen Auswirkungen von Abfluss- und Morphologieänderungen auf Benthosarten zu geben, insbesondere als ein Werkzeug für Renaturierungsmaßnahmen.

## Aufgaben der Arbeit

Jede Veränderung setzt eine kritsche Aufarbeitung existierender Ansätze voraus. Dies wiederum setzt jedoch voraus, dass die wichtigen physikalischen und biologischen Parameter bestimmt wurden, die für eine Beschreibung eines Benthoshabitats und damit der Verteilung und Häufigkeit von Benthos ausschlaggebend sind. Hiermit ist eine Grundlage geschaffen, auf der ein Vergleich existierender Modelle im Zusammenhang ihrer Anwendbarkeit aufgebaut werden kann.

Zusätzlich ist es wichtig, die allgemeinen Habitatmodelle zu vergleichen, ohne sich auf eine spezielle Zielart festzulegen. Insbesondere die Integration weiterer Parameter in diese existierenden Modelle muss untersucht werden. Hier muss die Flexibilität des Modells in Bezug auf das Einbringen neuer Faktoren und dessen Konzept für das Sammeln und Verarbeiten biologischer Daten betrachtet werden, beispielsweise das Erstellen neuer Präferenzkurven.

Zwei Ansätze in der Benthoshabitatmodellierung sind von besonderer Bedeutung für diese Forschungsarbeit: Das PHABSIM-Modell und die FST-Halbkugelmethode. Jedoch zeigt das PHABSIM-Modell einige Defizite, weswegen in dieser Arbeit die FST-Halbkugelmethode als Basis für eine erweiterte Benthoshabitatmodellierung gewählt wurde. Die subjektiven Gründe für diese Entscheidung sind: (1) historisch, da das erste Habitatmodell in CASiMiR auf der FST-Halbkugelmethode basiert, (2) eine starke Verbreitung in Europa und (3) eine große Datenbank an Benthospräferenzkurven basierend auf FST-Halbkugeln.

Zwei grundlegende Fragen die FST-Halbkugeln betreffend müssen geklärt werden. Zum einen die physikalischen Hintergründe der Methode, da bis heute unklar ist, was genau mit dieser Methode gemessen wird und wieso es mit einer Ausrüstung, die ein oder zwei Größenordnung über der der meisten benthischen Arten liegt, überhaupt möglich ist, deren Lebensräume zu beschreiben. Zum anderen ist offen, ob FST-Halbkugelnummern über eine rechnerische Methode ermittelt werden können. Eine solche Methode sollte vorzugsweise auf den gleichen Eigenschaften basieren, die auch üblicherweise in Fischhabitatmodellen verwendet werden, idealerweise auf der Substratzusammensetzung und den Resultaten hydrodynamischer Modellierung – Wassertiefe und tiefengemittelter Geschwindigkeit. Ein solches Modell würde die sehr arbeitsintensiven Feldmessungen mit FST-Halbkugeln überflüssig machen.

Um zur Analyse in Renaturierungsmaßnahmen eingesetzt werden zu können, müssen die Eigenschaften eines Flusslaufs von einer statistischen in eine räumlich verteilte Form umgewandelt werden. Weiterhin sollte das Einbringen zusätzlicher Parameter, die für eine bestimmte Benthosart wichtig sind, in das neue Modell möglich sein. Die Einsatzmöglichkeiten von Fuzzy-Logik sollten auch betrachtet werden, da diese eine einfache Repräsentation und Kombination von Expertenwissen über die Ansprüche der Arten erlaubt und über die letzten fünf Jahre hinweg eine gute Verwendbarkeit in mit CASiMiR durchgeführten Fischhabitatstudien aufzeigte.

## Bestimmende Faktoren für benthische Makroinvertebraten

Der wichtigste bestimmende Faktor für den Großteil der benthischen Arten, der deren Verteilung und Häufigkeit auf Mikrohabitatebene festlegt, ist die Strömung. Dass diese Arten sich stark an den Strömungsverhältnissen orientieren, kann einmal über die direkte Krafteinwirkung erklärt werden. Jedoch zeigt sich, dass eher die indirekten Einwirkungen der Strömung ausschlaggebend sind, beispielsweise durch Atmungsmechanismen und Futterverhalten. So besitzen einige Arten keine aktive Atmungsmechanismen (*Rhyacophila nubila*, *Rhithrogena* cf. *semicolorata*), weshalb bei Strömungen mit einem geringeren Sauerstoffgehalt größere Geschwindigkeiten erforderlich sind, damit diese Tiere überleben können.

Es ist schwierig, für solch kleine, millimetergroße Lebewesen eine passende Messmethode für die Strömungsverhältnisse zu finden, die in deren Größenordnung liegt. Jedoch zeigen viele Labor- und Feldmessungen, dass auch über Strömungsmessungen, die auf groberen Skalen durchgeführt werden, die Mikroverteilung dieser Tiere festgestellt werden kann. Dies wurde mittels Studien überprüft, bei denen die Strömung nahe am Flussbett in einem Abstand von einigen Zentimetern mit Messflügeln oder FST-Halbkugeln ermittelt wurden.

Auch andere Parameter wirken sich oft bestimmend aus, insbesondere das Substrat, welches die physiologischen Prozesse eines Lebewesens in gleichem Maße beeinflussen kann wie die Strömung. So ist das Substrat als Schutz- und Rückzugsraum hier ein wichtiger Faktor. Andere Parameter, beispielsweise Wassertiefe oder Schatten, können eine gewisse Rolle spielen und sollten damit in den Modellierungsprozess wo sinnvoll integriert werden.

## Theoretische Grundlagen für einen Ansatz zur FST-Halbkugelberechnung

Ein Ansatz des Kräftegleichgewichts ergibt, dass die Dichte der schwersten Halbkugel, die gerade noch von einer Platte bei einer bestimmten Strömung abdriftet, proportional zum Quadrat der sohlnahen Strömung und einer Kombination der zugehörigen Auftriebs- und Widerstandskoeffizienten ist. Weiterhin ist dies vom Reibungskoeffizienten $\mu$ zwischen Halbkugel und FST-Grundplatte abhängig, der sich aus der jeweiligen Ausrüstung ergibt.

$$\rho_h = \rho_w \left[1 + \frac{3}{8}\frac{u^2}{r_h\, g}\left(c_l + \frac{c_d}{\mu}\right)\right]$$

Für die neue, strukturierte Standardgrundplatte zusammen mit einem neuen Satz FST-Halbkugeln konnte ein Reibungskoeffizient von 0.24 gefunden werden. Für die alte, glatte Grundplatte hängt der Reibungskoeffizient zusätzlich von der Platzierungsmethode der Halbkugel ab und variiert stark zwischen Werten von 0.6–0.7 bei der “Drück”- bis zu 0.05–0.1 bei der “Kipp”-Methode.

Während des Messvorgangs befindet sich die FST-Halbkugel im sohlnahen Strömungsfeld. Die Kenntnis dessen ist notwendig zur Anwendung der auf dem Kräftegleichgewicht basierenden Formel zur Ermittlung der Halbkugeldichte. Ein brauchbarer Weg, die sohlnahen Geschwindigkeiten zu bestimmen, bietet die modifizierte logarithmische Geschwindigkeitsverteilung von Bezzola. Basierend auf der Prandtl'schen Mischungsweg-Theorie sagt sie aus, dass hauptsächlich die turbulente Schubspannung die mittleren Strömungsbedingungen festlegt. Bezzolas modifiziertes logarithmisches Wandgesetz berücksichtigt die spezielle Verteilung turbulenter Schubspannungen, welche sich in der sogenannten Rauheitsschicht ausbilden, in Strömungen über rauhen Sohlen mit kleinen relativen Überdeckungen. Innerhalb dieser Schicht ist die turbulente Schubspannung konstant oder verringert sich sogar zu den Spitzen der Rauheitselemente hin. Unter Zuhilfenahme Bezollas Wandgesetzes kann die Geschwindigkeitsverteilung komplett über nur drei Parameter beschrieben werden – tiefengemittelte Geschwindigkeit $u_{0.4}$, Wassertiefe $h_t$ und die Dicke der Rauheitsschicht $y_r$.

Die Parameter $u_{0.4}$ und $h_t$ werden gewöhnlich in Fischhabitatstudien verwendet und können durch den Einsatz hydrodynamischer Modelle ermittelt werden. Der große Vorteil dabei ist, dass die Dicke der Rauheitsschicht $y_r$ im Gegensatz zum äquivalenten Rauhigkeitsmaß $k_s$, das in Nikuradses Formel verwendet wird, nur von der Substratkorngröße und -anordnung abhängt und nicht von der relativen Überdeckung.

Gleichzeitige Anwendung von Bezollas logarithmischem Wandgesetz und der kräftegleichgewichtsbasierten Formel erlaubt es zu beweisen, dass keine generelle Beziehung zwischen den FST-Halbkugelnummern und der Sohlschubspannung $\tau_0$ existiert. Bei unterschiedlichen Substratzusammensetzungen hat dieser, der Theorie nach lineare Verlauf unterschiedliche Steigungen.

## Numerische Simulation einer Strömung um eine Halbkugel

Eine Literaturrecherche zu sogenannten "Junction Flows" – Strömungsphänomenen um Hindernisse an einer Wand – bestätigt im Grunde die richtige Wahl einer Halbkugel als FST-Ausrüstung. Gegenüber hohen Hindernissen, die eine von-Kármán-Wirbelablösung in ihrem Nachlauf aufweisen, zeichnet sich die Strömung um eine Halbkugel durch die Ablösung schwächerer, bogenartiger Wirbel aus, die keine erheblichen Druckschwankungen erzeugen. Daher kann angenommen werden, dass die hydrodynamischen Auftriebs- und Widerstandskoeffizienten konstant über die Zeit bleiben.

Die numerischen Simulationen haben zum Ziel, die Beiwerte für den Auftrieb der Halbkugel nahe der Sohle unter Einfluss verschiedener, möglicherweise wichtiger Faktoren auf die hydrodynamischen Koeffizienten abzuschätzen, wie Froude- und Reynoldszahl, Turbulenzintensität der Strömung, Form des sohlnahen Geschwindigkeitsprofils und die Rauhigkeit der FST-Bodenplatte.

FST-Halbkugelmessungen decken einen großen Teil der Reynoldszahlen ab, in denen ein Übergang von einem unter- in ein überkritisches Strömungsregime stattfindet. Dieser Übergang führt bei einer Halbkugel zu einem verringerten Widerstands- und einem erhöhten Auftriebskoeffizienten. Numerische Untersuchungen zeigen, dass für eine auf der Sohle befestigte Halbkugel die Widerstands- und Auftriebskoeffizienten $c_{d,b}$ und $c_{l,b}$ in einem gleichmäßigen Strömungsfeld 0.44 bzw. 0.53 für ein unterkritisches Regime betragen. Für das überkritische Regime betragen diese 0.31 bzw. 0.76. Die kritische Übergangsreynoldszahl hängt von der Turbulenzintensität der Strömung und Rauheit der Halbkugeloberfläche ab. Da diese schwer, wenn überhaupt, abgeschätzt werden können, bildet diese kritische Übergangsreynoldszahl einen Unsicherheitsfaktor für die Berechnung der Halbkugeldichte. Für die glatte Halbkugel kann diese bei einer Geschwindigkeit am Halbkugelzenit $u_{ht}$ =0.9 m/s als $7\times10^4$ angenommen werden. Sind die Geschwindigkeiten am Halbkugelzenit $u_{ht}$ und deren Schwerpunkt $u_{hc}$ bekannt, kann für die Bestimmung des Kräftegleichgewichts folgende Formel herangezogen werden:

$$\rho_h = \rho_w \left[1 + \frac{3}{8}\frac{u_{ht}\,u_{hc}}{r_h\,g}\left(c_{l,b} + \frac{c_{d,b}}{\mu}\right)\right]$$

Numerische Simulationen zeigen auch, dass die FST-Bodenplatte keinerlei Auswirkungen auf die hydrodynamischen Koeffizienten hat. So gesehen ist es unwichtig, ob Messungen mit der alten, glatten oder der neuen, strukturierten Bodenplatte vorgenommen werden. Der Einfluss der Bodenplatte beschränkt sich damit auf den unterschiedlichen Reibungskoeffizienten.

Untersuchungen über den Einfluss des Geschwindigkeitsprofils auf die Kräfte an der Halbkugel zeigen, dass diese mit dem Geschwindigkeitsprofilparameter korreliert, der wiederum als eine Relation der Geschwindigkeit am Halbkugelzenit und am Halbkugelschwerpunkt ausgedrückt werden kann. Über obige Formel wird die Abhängigkeit der Halbkugelnummer von der Geschwindigkeit deutlich. Es kann daher angenommen werden, dass FST-Halbkugeln die zeitgemittelte, sohlnahe Geschwindigkeit in 4 cm Höhe über der Grundplatte messen.

## Validierung des rechnerischen Ansatzes zur Bestimmung der Halbkugeldichte

Die Validierung des neuen Ansatzes zur Bestimmung der Halbkugeldichte besteht aus zwei Hauptkomponenten: (1) Überprüfung von Bezzolas logarithmischem Wandgesetz zur Bestimmung der sohlnahen Geschwindigkeiten bei Feldbedingungen und (2) Untersuchung der Anwendbarkeit der kräftegleichgewichtsbasierten Formel zur Berechnung der FST-Halbkugeldichten. Eine durchgängige Methodik wird in sechs Fallstudien angewandt, die sowohl Laborexperimente als auch Feldmessungen beinhalten. Die Feldmessungen stammen aus Untersuchungen der Flüsse Schwechat, Rhein, Rhône, Zwalm und Körsch. Dabei konnten sehr gute Ergebnisse für Schwechat und Rhein erzielt werden. Hier wurde die neue, strukturierte Bodenplatte verwendet. Auch Laborexperimente zeigten zufriedenstellende Übereinstimmungen. Am schlechtesten waren die Vorhersagen bei der Rhône, bei der die alte, glatte Bodenplatte zur Anwendung kam und es unklar ist, welche Platzierungsmethode eingesetzt wurde. Die Verifikation der Methode für die Flüsse Zwalm und Körsch wird durch eine möglicherweise falsche Messung mit dem 3D Acoustic Doppler Velocimeter erschwert. Es bleibt unsicher, ob die neue Methode aufgrund der Bedingungen, insbesondere des sehr groben Substrats, in diesen Flüssen ungeeignet ist, oder ob die Abweichungen zwischen gemessenen und berechneten FST-Halbkugelnummern durch fehlerhafte Geschwindigkeitsmessungen erklärt werden können. In den meisten Studien lagen die Abweichungen selten höher als ±2 Halbkugelnummern.

## Der neue Ansatz in der Benthoshabitatmodellierung

Der rechnerische Ansatz zur Ermittlung der FST-Halbkugelverteilung erfordert üblicherweise drei Schritte. Diese werden in der Arbeit anhand der Körsch demonstriert und bestehen aus

1. der Berechnung der tiefengemittelten Fließgeschwindigkeit und der Wassertiefenverteilung mittels eines hydrodynamischen Modells bei festgelegten Abflusssituationen,
2. der Schätzung der sohlnahen Strömungsverhältnisse über Bezzolas logarithmisches Wandgesetz,
3. der Berechnung der FST-Halbkugeldichte über die Kräftegleichgewichtsformel.

Nachdem die FST-Halbkugelverteilungen für eine Abflusssituation ermittelt wurden, kann diese entweder in einem einparametrigen FST-Halbkugel basierten oder in einem multiparametrigen Benthoshabitatmodell verwendet werden. Die erste Variante ist ähnlich der “statistischen”, die im CASiMiR-Modul BHABIM implementiert ist. Die zweite entspricht der räumlich ausgerichteten Methode, die derzeit in CASiMiR für Fische verwendet wird. Hier empfielt sich der Einsatz der Fuzzy-Logik, da man dadurch die sehr subjektiv eingefärbte Erzeugung von Präferenzkurven über Feldmessungen vermeiden kann. Außerdem kann über diesen Ansatz sehr komfortabel multiparametrisch modelliert werden. Daher wurde dieser als Erweiterung zu ArcView GIS 3.3 implementiert und profitiert dadurch auch von den mächtigen Analyse- und Visualisierungswerkzeugen, die diese Anwendung bietet.

## Grenzen des FST-Halbkugel basierten Habitatmodellierungsansatzes

Zum Ersten ist es wichtig zu beachten, dass die derzeit exisitierende Datenbank an FST-basierten biologischen Daten keinerlei zusätzliche Informationen darüber enthält, welche Bedingungen an den Stellen der Probennahme herrschten. Insbesondere das vorherrschende Substrat, das genauso wichtig wie die Strömung sein kann, ist derzeit in der Datenbank nicht katalogisiert. Andere Parameter wie Wassertiefen, Algenbewuchs oder Schatten können ebenso relevant sein. Deshalb sollten die Autoren dieser Datensätze konsultiert werden, um diese Informationen bereitzustellen. Mit Hilfe derer könnten die Datensätze der FST-Halbkugelpräferenzen der Tiere ausgewählt werden, bevor sie im Habitatmodell benutzt werden.

Zum Zweiten gibt es konzeptionelle Probleme, wenn versucht wird, den neuen Ansatz in Flussläufen mit sehr grobem Substrat zu verwenden, beispielsweise in Gebirgsflüssen, in denen häufig große, einzelne Steine und/oder morphologische Strukturen wie Wasserfälle oder Kaskaden auftreten. Hier ist es nicht mehr möglich, eine zweidimensionale Strömungsannäherung anzunehmen. Weiterhin ist es fragwürdig, ob die existierenden biologischen Daten hierauf übertragen werden können. Die korrekte Platzierung der FST-Grundplatte der Größe $13 \times 18$ cm auf Substraten mit Korngrößen über 30 cm und auch die Schwierigkeiten bei der biologischen Probennahme, deren Methoden meist auf feinere Substrate ausgelegt sind, sind ein großes Problem.

Zum Dritten erlaubt die Methode eine Abschätzung der FST-Halbkugelverteilung in einem Flusslauf basierend auf der mittleren Höhe des Grundes. Örtliche Besonderheiten wie große Steine oder Totholz können nicht berücksichtigt werden. In der Realität würde ein Hindernis vor oder hinter einer FST-Messstelle eine vollständige Veränderung der hydrodynamischen Auftriebs- und Widerstandskoeffizienten der FST-Halbkugel bedeuten. Auch das logarithmische Wandgesetz ist für die Schätzung der sohlnahen Strömung unter solchen Voraussetzungen nicht anwendbar.

# 1 Introduction

Flowing waters – rivers and creeks – are extremely important ecological systems characterized by high temporal and spatial variability of physical conditions as well as by enormous species richness. Healthy freshwater ecosystems are vital for the maintenance of aquatic and terrestrial biodiversity, water quality, and industries such as aquaculture and fishing. These valuable systems changed drastically under anthropogenic impact, continually growing over the last centuries. The alteration of the natural flow regime and modification of sediment transport due to flow diversion for water supply and electricity generation, flood protection and navigation improvement measures resulted in suppression of unique ecological structures. Polluted wastewater from agriculture and industry caused an additional habitat reduction for the organisms. In the seventies of the last century, the quality of European rivers reached a peak of deterioration. As a consequence, a progressing reduction of species biodiversity has taken place.

Although in the last decades the water quality of West and Central-European rivers was continually improving as a result of wastewater treatment, structural and hydraulic deficits affecting ecological functionality of flowing waters remain or even grow. Major problems are straightened and canalized river reaches, presence of migration barriers such as weirs and dams, and missing connections of the main channel to riparian zones. These structural deficits are more pronounced in river reaches affected by water diversion [19].

More and more researchers concentrate on the development of tools for the assessment of anthropogenic impacts on riverine ecosystems. These tools are indispensable for environmentally conscious water management and are of great value for the implementation of the European Union Water Framework Directive. Reflecting the importance of the preservation of aquatic ecosystems, it stresses, that "Water is not a commercial product like any other but, rather, a heritage which must be protected, defended and treated as such" [92].

Among those tools, physical habitat models are considered as the most important for the analysis of ecological functionality of flowing waters. They allow an assessment of the living space quality for site-specific flora and fauna, usually fish, invertebrates and macrophytes. Such models can predict the available habitat quantity and quality for a target species in dependency from flow rate and structural properties of a river reach. Discharge variation results primarily in a change in water depths and flow velocities, which are the basic parameters in aquatic habitat modelling. Discharge as a parameter allows habitat models to serve as quantitative tools, confronting water management endeavors with ecological preservations. Originating from North America, physical habitat models are water management practice since the late 1970's. First approaches were developed for the impact assessment on commercial fish species (mainly salmonids), but today their applicability has expanded to a wider range of questions, for example, like river catchment management and renaturation.

The present study concerns with *benthos* habitat modelling for flowing waters. Benthos is the community of organisms living in/on the bottom under a water body – *benthal*. That are mostly invertebrates, but according to definition, bottom dwelling fish species also belong to benthos. Benthic species perform a variety of very important functions in freshwater ecosystems. For example, they accelerate detrital decomposition, as dead organic matter is one of their main sources of energy. Many benthic invertebrates are predators that control the numbers, locations, and sizes of their prey. Last but not least, benthic invertebrates supply food for both, aquatic and terrestrial vertebrate consumers (e.g. fishes, turtles, and birds). Due to the specifics of the benthos habitat, the typical parameters of fish habitat models for streams, which are water depth, substrate and mean column velocity, should not be used directly here and the models have to be conceptually adjusted.

This work is targeted to contribute to CASiMiR – Computer Aided Simulation Model for Instream Flow Requirements – developed at the Institut für Wasserbau of the Universität Stuttgart [27], [26]. In particular, the sub-model BHABIM (Benthos HABItat Model) of CASiMiR should be improved in respect to its applicability range, robustness, and study costs. BHABIM, the debut model within CASiMiR, based on the FST-hemisphere approach, is now supplemented by the fish habitat sub-module SORAS (Structure Orientated River Analysing System). The latter is presently the program used most in habitat studies by the Universität Stuttgart as well as by the engineering consulting company sje - Schneider & Jorde Ecological Engineering GmbH. It continuously gains popularity in Europe and all over the world. Comprising a fuzzy logic approach, SORAS allows evaluation of flow regime altering on fish habitats on basis of 1D or 2D hydraulic modelling data. The aim is to bring the benthos habitat model to the same high standards the fish habitat module shows. In future, this model should be able to answer questions concerning the ecological impact of flow and morphological changes on benthos species, and also to serve as a tool in river restoration studies.

## 1.1 Objectives of the study

Any intended improvement requires a critical review of existing approaches. The first step is however to review, which physical and/or biological parameters are important for the description of benthos habitat, thus defining distribution and abundance of benthos species.

This review has to supply initial information for the comparison of existing models in context of their applicability range.

Further, it is important to compare the general habitat modelling approaches, without concentrating on any target species. Especially their potential to integrate new parameters has to be evaluated. Here, such aspects like the flexibility of the model concept for introduction of new factors, their conceptual processing and acquisition of biological information concerning those (for example, production of new preference curves) have to be considered.

Especially two approaches for benthos habitat modelling are interesting for this research: The PHABSIM model and the FST-hemispheres method. Due to certain shortcomings in the PHABSIM model, the FST-hemispheres method is chosen as a basis for the extended benthos habitat model. The subjective facts which play a role for the selection are: (1) historical, as the first habitat model within CASiMiR is based on FST-hemispheres; (2) large prevalence of the method in Europe; and (3) existence of a large data base for benthos preference curves based on FST-hemispheres.

Two basic questions concerning the application of FST-hemispheres have to be clarified: the physical rationale of the method, as until now it is not clear, what exactly is measured by it and why it is possible with this equipment, which is one or two orders of magnitude larger than the size of benthic macroinvertebrates, to describe their physical habitat. The second question is, whether it is possible to estimate FST-hemisphere numbers using a computational method. This method should preferably be based upon some characteristics also used in conventional fish habitat research, ideally upon substrate characteristics and the results of hydrodynamic modelling: water depth and mean column velocity. The computational method would result in the elimination of the very laborious FST field measurements.

To be suitable for the analysis of restoration measures, the characterization of a river reach in the new model has to be transformed from a statistical one, like in BHABIM, into a spatially referenced one. Additionally, a flexible incorporation of various additional parameters relevant for particular benthos species should be possible in the new model. The possibilities and usefulness of fuzzy logic in the new model has to be considered. Fuzzy logic allows an easy incorporation of expert knowledge for species habitat requirements and has proven its use in fish habitat studies over the last seven years.

## 1.2 Outline of the work

The present work has a multidisciplinary character and will probably be interesting for water management engineers and habitat modelers, as well as for biologists. So, the work includes a description of the very basics in fluid dynamics, as well as habitat and hydrodynamical modelling, what constitutes an important and also quite extensive part of the work. These basics, indeed not pretending to be complete, aim to give starting points for the deepening into the respective subjects, necessary for the comprehension of the newly developed approach.

This study has the following layout:

**Chapter 2** will first give an introduction to the habitat modelling concepts and techniques. Major parameters defining distribution and abundance of benthic species will be described and analyzed. Finally, input parameters, spectrum of application and limitations of existing benthic habitat models are summarized, upon which the goals of the study are asserted.

**Chapter 3** is the most basics-laden, and aims for the presentation of turbulent flow description in fluid dynamics. Special attention is given to the flow over a rough bottom with small relative submergence. The new model of Bezzola for the vertical velocity distribution in such flows is described, as it will be further used for the computational approach to FST-hemispheres.

**Chapter 4** is completely devoted to the FST-hemisphere method for the assessment of near-bed flow conditions. The force balance based formula for the estimation of the hemisphere density is given, and potential and difficulties in its application are summarized.

**Chapter 5** can be seen as a stand-alone study of a hemisphere's hydrodynamics in a turbulent velocity gradient flow. Numerical flow investigations are conducted in the range of Reynolds numbers relevant for the FST-hemisphere measurements. Provided drag and lift coefficients for a hemispherical obstacle on a bed facilitate the calculation of FST-hemisphere densities by the force balance formula of Chapter 4.

**Chapter 6** shows first the applicability of Bezzola's velocity distribution law for the estimation of near-bed flow velocities in case studies. Upon these velocity data, the FST-hemisphere numbers are calculated with the theoretical formula using coefficients of Chapter 5 and compared to the measured FST numbers. The case studies are based on laboratory as well as field measurements from various rivers, ranging from small creeks to large streams, located in Germany, France, Belgium and Austria.

**Chapter 7** demonstrates the potential of the new computational method to FST-hemispheres for the benthos habitat modelling. Its application in the conventional, one-parametrical approach using preference curves and in a multi-parametrical fuzzy logic based approach is shown.

# 2 Benthos habitat modelling: capabilities and limitations

*Aquatic habitat modelling* represents a well established branch of *environmental flow assessment (EFA)* science. This relatively young area of knowledge arises around the middle of the last century in the western United States through the recognition of the urgent need to protect riverine fish and wildlife resources from further depletion as a consequence of the accelerated water development. Tharme [91] identifies the **modern goal** of EFA with an estimation to which extent the natural flow regime of a river can be altered for the purposes of water resource management in order to maintain specified, valued features of the ecosystem. Also, determination of measures aiming at the *restoration* or *rehabilitation* of rivers is a subject of EFA. The term "flow regime" should be stressed out here, as not the quantity of water itself, but much more the temporal variability of a natural flow, including extremes such as droughts and floods, is thought to be responsible for ecosystem maintenance.

Although in literature the terms *minimum flow*, *instream flow* and *environmental flow* are often used interchangeably, they are not synonyms, in fact, but reflect a scientific paradigm change as summarized in [39]:

**Minimum flow** is usually subjectively determined water depths or flows for the purpose of survival of selected fish species (mainly salmonids). Minimum flow assessment methods were developed in the 1960's and 1970's based on hydrologic analysis of the water supply and hydraulic geometry relations, coupled with observations of habitat quality and fish ecology.

**Instream flow** is an objective balance of the flow regime needs of in-channel (e.g. fish and water sports) and off-channel (e.g. irrigation, hydropower generation) users. The new management goals, associated mainly with the development of small hydropower plants in USA in the late 1970's and early 1980's, have led to the development of the Instream Flow Incremental Methodology (IFIM) under the guidance of the U.S. Fish and Wildlife Service [82]. Its central component, the Physical HABitat SImulation Model (PHABSIM), allows an evaluation of how the available habitat quantity and quality for a particular target species is changing with flow conditions, thus forming a quantitative basis for multiobjective decision making.

**Environmental flow** addresses ecosystem needs through maintenance of flow dependent structures and processes at various scales. Not only the river corridor, but also floodplains, ground water systems and receiving waters (e.g. lake, coastal zone) are considered. The so called *holistic methodologies* [5], undergoing rush development in Australia and South Africa, are trying to correct some shortcomings of instream flow, especially the concept of target species. These methodologies are based on a "natural flow paradigm" [61]. Flow requirements of each of the ecosystem components are evaluated using data derived from field studies, modelling and desktop techniques, and/or expert opinion, and are then incorporated into EFA recommendations [4].

Aquatic habitat models, appearing initially within the context of instream flow, do not become less important for environmental flow assessment, as they can be used as quantitative tools for the evaluation of flow requirements of particular ecosystem components, such as fish, macroinvertebrates and aquatic vegetation [43]. Within almost over 200 EFA methodologies, recorded in 44 countries within six world regions, they occupy a solid second place (28 %), slightly overtaken by hydrological methods (29.5 %) [91]. This statistics should be considered with caution, as methods and methodologies are pooled together in this review.

This chapter gives a short introduction into basic concepts, techniques, as well as capabilities and limitations of aquatic habitat modelling. Further, as could be expected, a special emphasis is placed on the description of physical (and biological) factors controlling distribution and abundance of benthos species. The choice of these descriptive parameters determines the area of application of the particular habitat model. Finally, a review of existing benthos habitat models will be done with the aim to assess their reliability, adequateness and robustness, as well as defining further research needs and possibilities to improve these models.

## 2.1 Organism and its habitat

The term *habitat* is defined as a physical part of the community structure in which an organism finds its home. It is a common approach in ecology to assign organisms a specific range of tolerance and an optimal range for parameters which characterize its environment [46]. Usually, a unimodal curve (with a single maximum) is assumed to exist which correlates the response of an organism to the gradient of an environmental factor. The highest point of the curve defines the optimum condition, the distance between the points, where the curve line crosses the zero level, forms the tolerance range for that particular factor. Organisms with a wide range of tolerance are referred to as *euryokous*, and those with a narrow range as *stenokous* species.

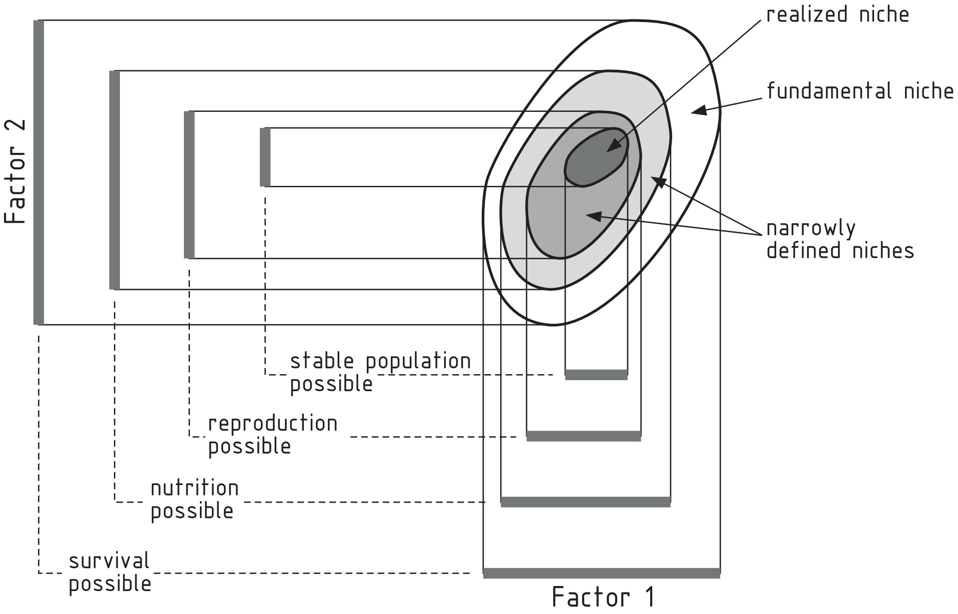

**Figure 2.1:** Two-dimensional niche and tolerance ranges for two environmental factors, from Lampert and Sommer (1997) [46].

A distinction should be made between *physiological* and *ecological* optima and tolerance ranges. The former relates to the physiological functions that can be determined through controlled experiments with individual organisms. The latter is usually assessed by measuring distributions of organisms in natural conditions and thus includes effects of biotic interactions such as predation and competition. Indeed, organisms have special ranges of tolerance not only for one parameter but for many. To deal with this fact, the concept of an *ecological niche* can be introduced. Aligning every important environmental factor to an axis in a hypothetical, multidimensional coordinate system, the niche can be defined as an n-dimensional volume within this coordinate system (Figure 2.1). In analogy to the one-dimensional case, *fundamental* and *realized* niches are distinguished. The former is related to the physiological tolerance range and the latter to the ecological one.

As can be seen from Figure 2.1, the realized niche always comprises a smaller volume than a fundamental niche. Predators, parasites or competitors can prevent species from establishing a stable population in a particular habitat, even though the conditions lie within the physiological tolerance range for reproduction. It should be noted, that this example is a rather strong idealization. In reality, almost always more than two parameters play an important role, and also multiple niches can be defined for one and the same species. Also, ranges of tolerance change for the particular organism during its life cycle. This is a natural adaptation of organisms to the environmental variability, in particular expressed for riverine species.

## 2.2 Scales and parameters

Prior to consideration of modelling parameters, questions of spatial and time scales should be addressed. Using the hierarchical organization of a river system proposed in [23] (see Figure 2.2), most habitat models operate upon microhabitats – patches or transects – spatial units of the same order of magnitude as the target animals. These models are thus commonly named *micro-scale* models. Models operating at higher scales (reach or segment) also start to appear, and are referenced to as *meso-* and *macro-* scale models.

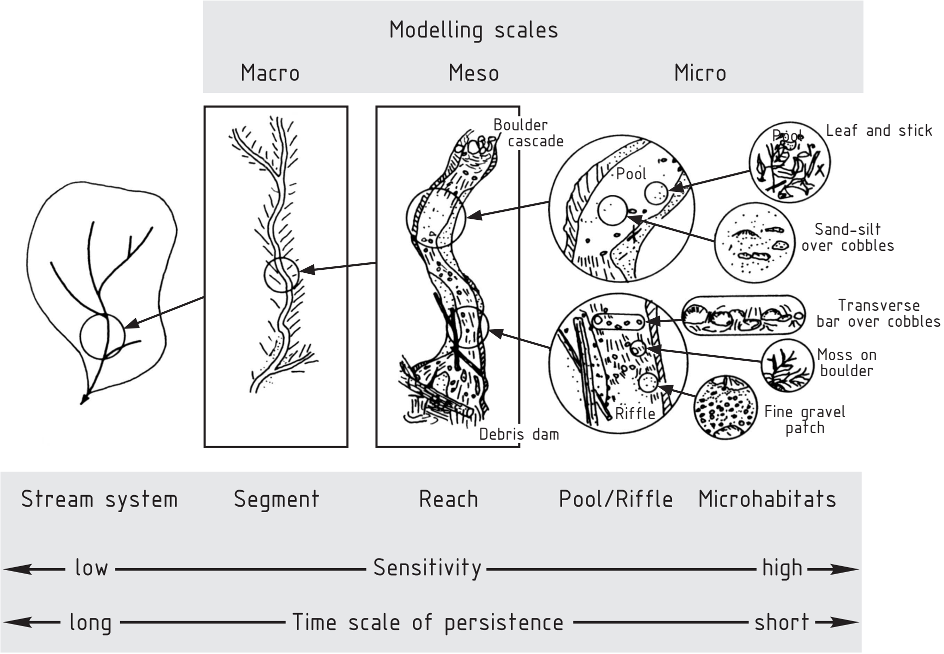

**Figure 2.2:** Hierarchical organization of a stream system and corresponding habitat model scales, modified after Frissell et al. (1986) [23]

The building blocks for a river system organization are characterized by a different sensitivity to disturbances, which decreases with increasing spatial size. Consequentially, the time scales of continuous potential persistence are growing with an increasing spatial scale. The temporal aspect can be accounted for in habitat models through the incorporation of hydrological time series, thus allowing the time-dependent evaluation of quality and quantity of the available living space.

Every spatial scale can be associated with a number of factors, which can, but not need to, be relevant for the particular species at another scale. For example, among the key parameters characterizing the distribution and abundance of macroinvertebrates at a reach scale are mainly velocity and substrate type. At river system scale, however, the macroinvertebrates' community structure is governed by general physical-chemical parameters, such as salinity and temperature [40]. Micro-scale models, such as PHABSIM, are mostly sufficient for the impact assessment of local water intakes or small diversion type hydropower stations. However, large scale projects often require management tools acting at higher spatial and temporal scales, such as stream networks and even the whole river catchment. The choice of a modelling scale should be based upon the objectives of a study and be appropriate for the life-cycle and home range of the species.

Factors that characterize an organism's habitat can be categorized as *biotic* and *abiotic*. Stream abiotic factors, which form a basis of the traditional (physical) habitat modelling, can be further split into *morphologic*, *hydraulic* and *hydrologic* ones. Other physical characteristics, like water temperature, light availability, or water quality, may play an important role for the distribution and abundance of riverine organisms. Under certain conditions, these factors may override the importance of stream abiotic factors, therefore they are usually referenced to as *limiting* parameters. Many modern habitat modelling approaches incorporate these limiting factors [12].

## 2.3 Basic concepts of aquatic habitat modelling

The underlying idea of physical habitat modelling is, that an impact on riverine organisms can be assessed through the evaluation of the influence on their living space, i.e. their habitat. The word "impact" here should be understood in a broader sense, not only as negative effects of water diversion or discharge control, for example, but also as positive effects, for example rehabilitation measures. Further, it is assumed that organism preferences for any particular environmental parameter or a combination thereof can be expressed by some sort of function (see the concept of tolerance and optimum ranges introduced in Section 2.1). Combining this biological information with distributions of measured and/or calculated environmental parameters – commonly flow velocity, water depth, and substrate characteristics – for different flow situations, the change in habitat quality and quantity for this species can be evaluated. The measure for habitat quality of a spatial unit is called *Habitat Suitability Index* ($HSI$). It is represented by a value ranging from 0 to 1, with 0 for an unsuitable and 1 for the best suitable habitat. The overall characteristics of a river reach usually used in the decision making process are the Weighted Usable Area ($WUA$) and Hydraulic Habitat Suitability index ($HHS$), which are obtained as:

$$WUA = \sum_{i=1}^{N} A_i \cdot HSI_i \qquad [m^2] \tag{2.1}$$

$$HHS = WUA \Big/ \sum_{i=1}^{N} A_i \qquad [-] \tag{2.2}$$

| | | | | |
|---|---|---|---|---|
| with | $WUA$ | = | Weighted Usable Area of a river reach, | [m$^2$] |
| | $HHS$ | = | Hydraulic Habitat Suitability index of a river reach, | [-] |
| | $N$ | = | total number of inundated spatial units within a river reach, | [-] |
| | $A_i$ | = | surface area of inundated spatial unit $i$, | [m$^2$] |
| | $HSI_i$ | = | habitat suitability index of a spatial unit $i$, | [-] |

$WUA$ or $HHS$ curves – for example, versus discharge – should be used carefully in the analysis: large areas of a low-quality habitat can produce the same weighted usable area as a few small sized, high-quality habitats. Other characteristics of a river reach, such as minimum depths and maps of $HSI$ and their advancement with changing flow conditions, are recommended to be used additionally. In general, interpretation of habitat modelling results is no trivial task, and cannot be reviewed in detail here. Guidelines for using modelling results for instream flow regulations can be found in [29], [20].

It should be stressed here, that "conventional" habitat modelling cannot supply information about the total biomass of animals which can be found in a river reach at given conditions. These methods, in a quantitative manner, allow an assessment of the available habitat which can be **potentially** used by a particular target species. Within the context of environmental flow assessment, habitat modelling for a target species represents the most critical point, as there is no guaranty that the more or less subjective choice of animals would ensure the entire river ecosystem functioning. To address this question, much more additional information and modelling is needed; among the crucial factors are:

- interspecies competition, maintenance of food chains;
- connectivity of instream and also adjacent semi-terrestrial and terrestrial habitats;
- temporal aspects of flows and their influence on species' life history patterns.

Data on organism preferences/requirements comes in various forms, depending on the modelling method. The most common way, also used in PHABSIM [9], is to apply so called *preference curves*. Nowadays, advanced techniques (for example *fuzzy logic*) allow to incorporate expert knowledge of biologists into habitat modelling.

### 2.3.1 Classical approach using preference curves

In a classical approach, biological information is defined using so called preference curves. For every computational cell of a river reach model, partial suitability indexes (SI) related to water depth, mean column velocity and substrate type are obtained through univariate preference curves of a hypothetical fish species (see the modelling example in Figure 2.3). Distributions of the depth and mean column velocity are obtained by hydrodynamic modelling and the substrate type through mapping in the field.

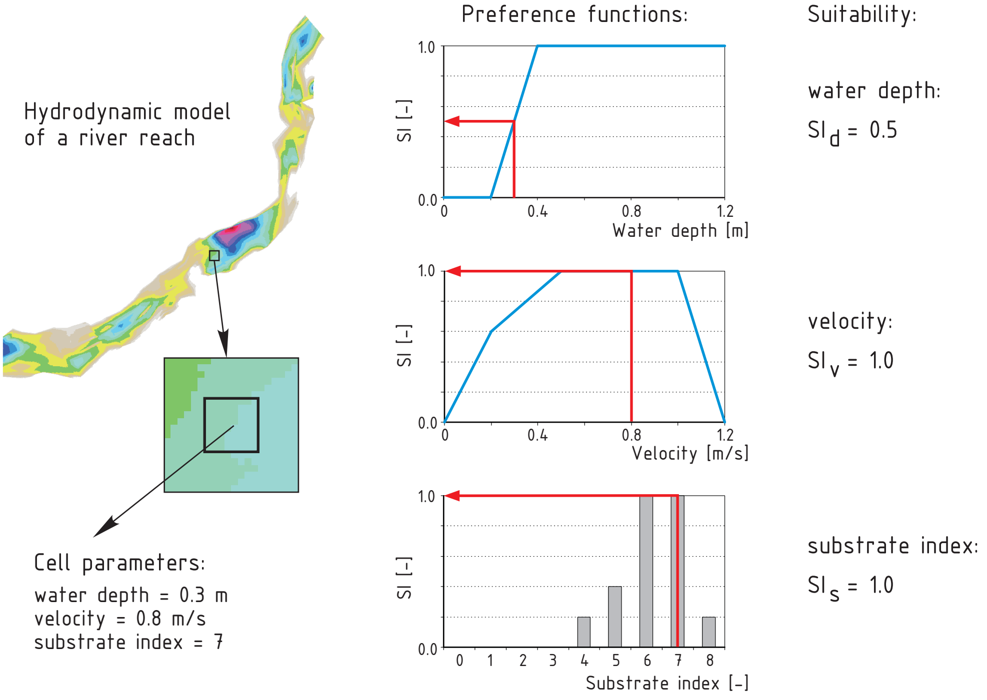

**Figure 2.3:** Principle of a habitat modelling based on univariate preference functions, after Schneider (2001) [72]

To obtain an overall habitat suitability index $HSI_i$ for a cell, various averaging operations can be applied; for example in PHABSIM, product combination is used:

$$HSI_i = SI_d \cdot SI_v \cdot SI_s \qquad \text{or in general:} \qquad HSI_i = \prod_{m=1}^{K} SI_m \qquad [-] \qquad (2.3)$$

or arithmetic mean:

$$HSI_i = \frac{1}{K} \sum_{m=1}^{K} SI_m \qquad [-] \qquad (2.4)$$

or geometric mean:

$$HSI_i = \left( \prod_{m=1}^{K} SI_m \right)^{\frac{1}{K}} \qquad [-] \qquad (2.5)$$

with $HSI_i$ = habitat suitability index of a spatial unit $i$
$SI_d, SI_v, SI_s$ = suitability indexes in respect to water depth, velocity and substrate, [-]
$SI_m$ = suitability index in respect to parameter $m$, [-]
$K$ = total number of parameters, [-]

The overall $WUA$ of a reach for a given flow situation is calculated with Formula 2.1.

Three different categories of base data for the generation of preference curves, listed here in order of increasing objectivity, are distinguished [9]:

**Category I** Data derived from personal experience, literature review or expert opinion. Preference curves are produced at low cost but lack any real data observations.

**Category II** Data based on frequency distributions of microhabitat parameters measured at locations used by the target species. This type of information is more reliable than the previous, but errors can be introduced due to a bias of environmental availability. That is, a highly favored resource will be hardly used by animals if difficult to find and, on contrary, a less favored resource will be used in a larger extent if it is the only available.

**Category III** The same as Category II, but a special sampling strategy is applied to correct for the availability bias. This category of data is characterized by the best transferability to other rivers.

Methods for the calculation of composite $HSI$ (see Formulas 2.3, 2.4, 2.5) deserve critical consideration. Depending on the formula used, very different estimates of $HSI$, and consequentially $WUA$, can be obtained.

The use of univariate preference curves also fails to catch effects of parameter interaction, that cannot be neglected sometimes. For example, for some species of fish, deep water can serve as an equivalent for missing overhead cover. As such, it will occupy shallow water areas if overhead cover is present, but will dwell in deeper areas if cover is absent.

To account for the interdependency of parameters, different augmentations to the classical approach were tried. One technique is to perform *conditional modelling* [9]: taking the previous example, two preference curves for water depths (with and without cover) are generated and accounted for in the calculation of composite $HSI$.

Gore and Judy [32] describe a method using multiple regression with an exponential polynomial curve to account for the interdependency of flow velocity and water depth in habitat studies of macroinvertebrates. The joint SI for depth and mean column velocity is expressed as:

$$SI_{v,d} = \frac{1}{N_t} \exp\{-(a_1 u_{0.4} + a_2 h + a_3 u_{0.4}^2 + a_4 h^2 + a_5 u_{0.4} h)\} \qquad [-] \qquad (2.6)$$

with $SI_{v,d}$ = joint SI for depth and mean column velocity, [-]
$a_1, a_2, a_3, a_4, a_5$ = regression coefficients, [s/m], [1/m], [s$^2$/m$^2$], [1/m$^2$], [s/m$^2$]
$u_{0.4}$ = mean column velocity, [m/s]
$h$ = water depth, [m]
$N_t$ = normalizing term, [-]

Bovee et al. [9] point out, however, that the multivariate exponential function is symmetrical having one maximum and this form does not really correlate to the species' requirements.

Considerable disadvantages of all preference curve based methods are the enormous requirements for obtaining the input biological data and a questionable transferability to different river bodies.

### 2.3.2 Fuzzy logic approach

It was shown previously, that classical habitat modelling based on the use of preference curves has a number of disadvantages. A relatively new method, based on a fuzzy logic approach, can help to overcome some of these difficulties. Fuzzy logic appears to be promising in the area of environmental science, as the modelled processes possess many parameters of influence that are not well understood or lack a certain discreteness. The fuzzy logic approach is integrated in the habitat model CASiMiR [72], [75] for fish and receives a continuously growing acceptance in Europe and worldwide.

*Fuzzy logic* can be considered as a problem solving control system methodology which provides a simple way to arrive to a definite conclusion based on imprecise, incomplete, noisy input information. This approach mimics the way a human would solve a problem, but – implemented as a computer program – allows a much faster solution.

A fuzzy logic based model is driven by so called *fuzzy rules* which can be constructed upon expert knowledge, defined in a form of linguistic expressions. For example, an expert's statement "these fish seem to avoid deep water" is not of much use in a conventional mathematical approach, but can be perfectly translated into the fuzzy rule:

**IF** water depth is 'high' **THEN** probability of occurrence is 'low'

Indeed, the system of fuzzy rules (rulebase) can contain more than one input and one output parameter. Unfortunately, defining the rulebase becomes complex quickly for a growing number of parameters, therefore, it is important to keep the latter at a minimum.

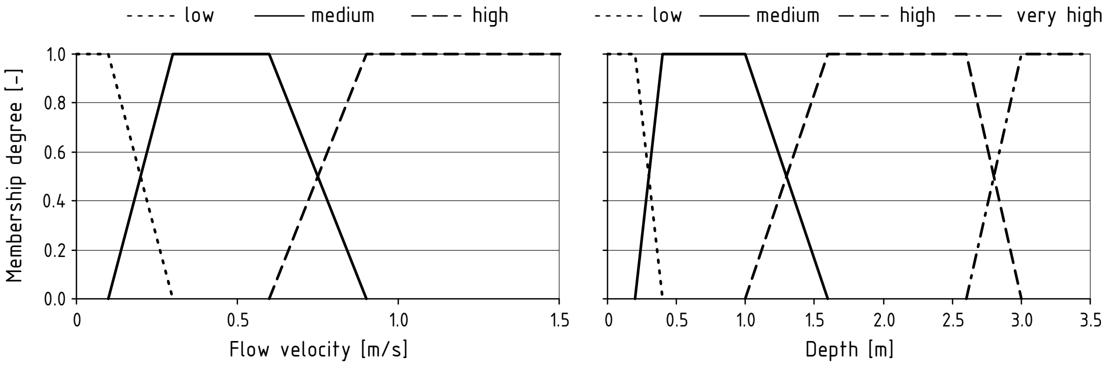

**Figure 2.4:** Example of fuzzy sets for water depth and mean column velocity for spawning grayling (*Thymallus thymallus*), from Schneider and Jorde (2005) [76]

A central element of fuzzy logic are fuzzy sets which are identified by so-called membership functions. A fuzzy set **A** is defined by a membership function $A(x)$, which gives the degree of membership (between 0 and 1) of a parameter $x$ (e.g. flow velocity) to the fuzzy set **A** (e.g. "high" flow velocity). Although the functions can have any shape, the ones most often used are triangular or trapezoidal. Other than two-valued Boolean logic, that only distinguishes between the two alternatives "true" and "untrue/false", fuzzy sets allow the definition of partial memberships. That means that some element can belong up to a certain degree of membership to one fuzzy set, at the same time it can also belong with a certain degree of membership to another fuzzy set. Degree of membership ranges from 0 (no membership) to 1 (full membership).

Fuzzy sets are defined for all input parameters in the so called *fuzzification* process (see an example in Figure 2.4)). In the model CASiMiR, the output parameter – Habitat Suitability Index – is defined in correspondence with other habitat simulation models on a scale between 0 (unsuitable) and 1 (maximum suitability) and has also the corresponding fuzzy sets.

In the modelling process, the *inference processor* runs through the rulebase and determines the degree of fulfilment (DOF) of each rule depending on the combination of input variables. For the calculation of DOF, either the min-max inference or product inference methods can be applied, which, in case of two input parameters, are defined by:

$$\text{Min-Max:} \qquad \eta_i = \min(\mu_{\mathbf{A}}(x_1),\ \mu_{\mathbf{B}}(x_2)) \qquad [-] \qquad (2.7)$$

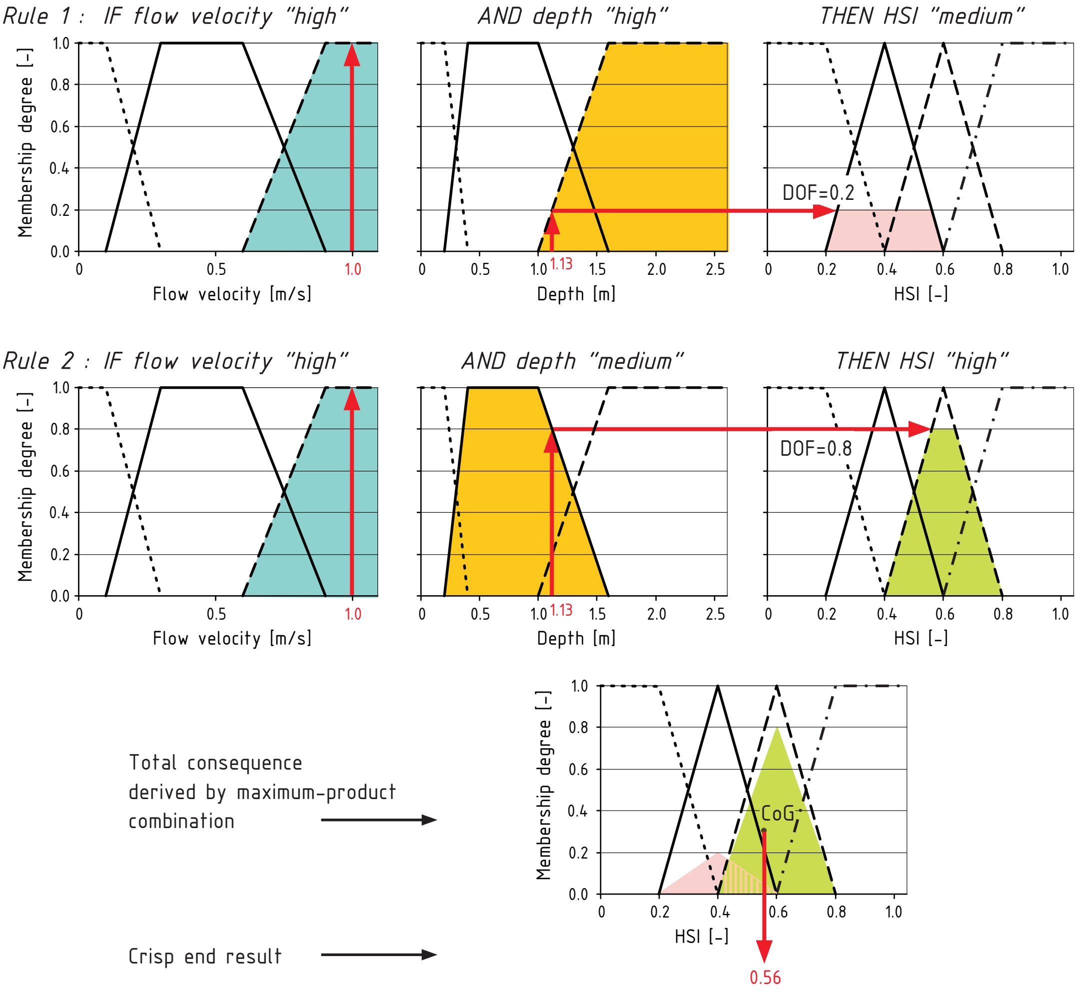

**Figure 2.5:** Example of a simplified inference process (only two rules and two input parameters, flow velocity 1.0 m/s and water depth 1.13 m) with DOF computed by the min-max method; aggregation into a total consequence using the maximum-product combination, and defuzzification by the center of gravity method, from Schneider and Jorde (2005) [76]

$$\text{Product:} \qquad \eta_i = \mu_{\mathbf{A}}(x_1) \cdot \mu_{\mathbf{B}}(x_2) \qquad [-] \tag{2.8}$$

with $\eta_i$ = degree of fulfilment of a rule $i$, [-]
$\mu_{\mathbf{A}}(x_1)$ = degree of membership of parameter $x_1$ relating to fuzzy set **A**, [-]
$\mu_{\mathbf{B}}(x_2)$ = degree of membership of parameter $x_2$ relating to fuzzy set **B**, [-]

After DOFs for every rule are calculated, they are combined to obtain the total consequence output. Generally, not all of the rules will fire and they also will have different DOFs. A number of methods can be applied for obtaining the total consequence, the simplest method is the maximum-product combination:

$$\mu_{tot}(x) = \max_{i=1..N}(\eta_i \cdot \mu_{K_i}(x)) \tag{2.9}$$

with $\mu_{tot}(x)$ = total consequence output,
$\mu_{K_i}(x)$ = membership function of the consequence $K_i$,
$\eta_i$ = degree of fulfilment of a rule $i$, [-]
$N$ = total number of rules fired, [-]

In Figure 2.5, an example of DOF calculation for just two parameters is shown. Here, the maximum-product method is used for the evaluation of total consequence output and the result is defuzzificated afterwards to obtain a crisp output value of the Habitat Suitability Index. For *defuzzification*, the center of gravity method is used in this example.

A detailed explanation of fuzzy logic concepts and their application to fish habitat modelling can be found in [72].

In general, fuzzy logic based approach offers the following advantages in comparison to the classical one based on preference curves [76]:

- interdependency of habitat variables can easily be accounted for;
- simple enrollment of expert knowledge, formulated in a qualitative or semi-qualitative way; application of crisp information for input as well as for the calibration of the model is possible in the same time;
- in theory, no restrictions imposed to the number of input variables;
- the simplicity of the approach is an advantage when negotiating with stakeholders in a decision making process. It is not a black box, rather it allows to analyze how a result was obtained.

So far, the method implemented within the model CASiMiR is applied only to fish, but listed above advantages make it very promising for other areas of habitat modelling.

## 2.4 Benthic macroinvertebrates and their controlling factors

In this work the terms *benthos*, *macrozoobenthos* and *macroinvertebrates* are used interchangeably, but this is not completely correct. In freshwater and marine ecosystems, *benthos* is the community of organisms, dwelling in or on the bottom sediments. Depending on the size of the organisms, benthos is classified as *macrobenthos* ($>$ 1 mm), *meiobenthos* (between 0.042 mm and 1 mm) and nanobenthos or *microbenthos* ($<$ 0.042 mm). There are some variations in the size of groups defined in literature, for example Cummins [13] refers to macrobenthos as those full grown animals with a length of at least 3-5 mm. Another widely used definition of macrobenthos or (macrozoobenthos) based on size is the animal's visibility to the naked eye. The taxa of primary importance that are generally included as macrobenthos are: *Insecta*; *Mollusca*; *Oligochaeta* (earthworms); *Crustacea - Amphipoda* (lawn shrimps), *Isopoda* (pill- and sowbugs), *Decapoda* (crabs and relatives); and sometimes *Nematoda* (roundworms) [13]. Historically, study emphasis is placed on the *macroinvertebrate* bottom fauna, particulary aquatic insects, probably due to their role as fish food.

Many factors control occurrence, distribution and abundance of benthic macroinvertebrates. According to Cummins [13], their macrodistribution patterns can be well predicted from general physical-chemical conditions. Thus, it is possible to describe differences in benthos faunas adapted to, for example, small or large, cool or warm, fast or slow flowing, oxygen at or below saturation, high or low light intensity, hard or soft alkalinity running water systems.

At a micro-scale, general physical-chemical parameters such as temperature, chemical composition of water and oxygen saturation can be assumed to be constant. Thus, in the absence of human perturbations, *flow velocity*, *substratum* and availability of *food*, are named as primary parameters determining macrozoobenthos distribution patterns within a river reach. Additional factors which play a role at a micro-scale are *shadow* and *competition between species*. Unfortunately, the particular contribution of every parameter is difficult to assess due to a high reciprocity of these factors [40]. For example, current controls largely the substratum. The latter in its own turn represents not only the living space for animals but also serves as a source of food for many. Hereafter, the factors affecting benthos microdistribution and interplay between them are considered in more detail.

### 2.4.1 Flow velocity

Flow velocity in rivers is characterized by a very high variability in time and space and its proper description in general depends on the scale of the interest. Current ranks first for many researchers when defining benthos microdistribution, but there is no consensus concerning different aspects of its influence. This is not surprising, taking into account the vast amount of benthic species with all the possible adaptations to an environment of moving fluid. Two kinds of flow action – direct and indirect – are generally distinguished.

Direct effect of flow is associated with *friction* and *pressure* forces which act on an object, or an animal, submerged in moving fluid. The contribution of friction is large in comparison to the pressure part for streamlined objects, or flattened animals grazing on upper rock surfaces, and small for non-streamline animals whose body form results in a strong distortion of the flow field with a large dead water zone appearing behind it. The total flow force (friction and pressure put together), acting along the main flow direction, is called *drag* and that perpendicular to the main flow direction – *lift*. Flow forces have to be withstood by an animal, otherwise it would be dislodged. Also, corrosion due to transport of fine particles which can damage important organs of an animal, is related to the direct action of flow.

From the laboratory experiments with dead macroinvertebrates, Statzner and Holm [84], [85] conclude, that a benthic organism cannot be well adapted to all effects of flow, such as lift, drag, corrosion, and also diffusive exchange processes, at the same time. These effects are also changing with the life stage of an animal as its form and size change. Giving a rough picture of the flow field, such experiments cannot be used, however, for an estimation of critical forces acting on animals, because, as the organisms are dead, they: (1) cannot hold their positions using special adaptations (for example suction discs by *Simulium*), and (2) are not able to change their position or body form as well as to search for shelter under unpleasant flow conditions.

Indirect effects of flow, such as oxygen transport, seston load, and influence on bottom substrate, are considered by many researches to be more important than direct ones [96]. Experimental studies show that current can largely affect respiration rates of some species with no active breathing mechanisms (*Rhyacophila nubila*, *Rhithrogena* cf. *semicolorata*), and that faster flows decrease the minimum level of oxygen concentration at which those insects can survive [3]. This fact restricts these animals exclusively to running waters. Also, some net-spinning insects (Hydropsychidae) can use their filtering devices only in running water [40]. Substrate type, which is largely defined by flow history, can affect respiration rates of some species at the same extent as current. For example, oxygen consumption of *Ephemera danica* nymphs drops by 65 per cent when they are allowed to dig in sand, their normal habitat, and that of *Ecdyonurus venosus* falls by 30–40 per cent when they are allowed to sit on stones rather than on smooth glass [40].

Direct and/or indirect effects of current play indeed a role at a scale relevant for benthic macroinvertebrates, i.e. within some millimeters above the stone or sand surface, and not at a scale of a bulk river flow. A high variability of flow at this scale and the millimeter range of sample volumes, where flow parameters have to be measured, make studies very complicated, both methodologically and technically. An alternative way, here, is to measure flow properties at a larger scale (for example, velocity with conventional measuring device, such as a propeller flow meter, at a distance of some centimeters above bed) and to relate them to the animal density of a particular species obtained through benthic collection device such as, for example, a *Surber sample* [38].

A study of Hart et al. [35] suggests, that fine scale measurements can be very important for understanding patchy animal distributions. The authors could observe in field conditions, that the distribution of the black fly larvae *Simulium vittatum* in areas within surfaces of single stones was strongly correlated to flow velocity measured at 2 mm above the surface (at animal height) but uncorrelated to a velocity at 10 mm. They also point out, that temporal aspects of flow variation at this scale are much more complex than was thought before.

On the other hand, there are numerous field and laboratory studies, in which flow velocities or other near-bed parameters are measured at a much larger scale than those relevant for macroinvertebrates, and still, definite preferences of some animals to specific parameter ranges can be found. Lancaster [47] shows, that flow velocity measured at 3 cm and 1 cm above the substrate in field and a laboratory flume, respectively, defines the microdistribution of the adult beetle *Oreodytes sanmarki* quite well. In field conditions its species were found in areas of low velocity (0 to 20 cm/s). This correlates well to the laboratory experiments, in which the beetle moved from initial positions into areas of reduced flow velocities (refugia) with increasing discharge simulating spate and, then, some individuums were found crawling or swimming upstream into their original habitats as the flow rate was reduced. Ulfstrand [96] shows, that species of Lapland streams have definite flow preferences. For example, *Baetis rhodani* shows a strong preference to a velocity class over 75 cm/s (velocity measured at 5 cm above the substrate). Also, distinct preferences of benthic animals to the so called *FST-hemisphere* numbers are found. FST-hemispheres, invented by Statzner and Müller (1989) [88], is an unconventional device measuring “near bottom flow conditions”. This equipment, consisting of a ground plate, comparable in size with common Surber samples, and hemispheres with a diameter of 7.8 cm (see Chapter 4 for details) measures also at a larger scale than that of benthic organisms.

Last should be noted, that permanent high velocities often make life intolerable for almost all species. For example, very few invertebrates can be found in the middle-stream area of the Danube near Vienna, although many occur in the gravel beds of lateral river parts [40]. The same effect on river benthos fauna have very low velocities. The resulting accumulation of silt restricts the occurrence of typical limno-fauna, but periodical spates do not allow lacustrine species to develop, also.

### 2.4.2 Substrate

Substrate is the medium of existence for benthos. It can either restrict or enhance the animals' ability to adhere, cling, burrow, escape from predators, be protected from current, construct cases, or deposit eggs. The substratum consists of various types of organic and inorganic materials, and can be virtually anything sufficiently stable to support insects – leaves, branches, algae, moss, mineral particles ranging in size from microscopic silts to large boulders or even man-made objects such as bottles, concrete and cars [54].

Many benthos species show unique requirements for the supporting medium. A number of insects, for example *Simulium*, *Rhithrogena*, has developed special devices – suction discs – which function only on relatively smooth surfaces, enabling them to withstand large flow velocities. Some species prefer rough stones which offer better protection from predators, and some live only on wood. There are species (for example, *Ephemera*) which burrow into substrate and are thus restricted to sediments they can penetrate. Some insects, such as stonefly *Leuctra*, require looser particles to slither between and others (mayfly *Ephemerella grandis*, caddisfly *Rhyacophila vaccua*) are more susceptible for predation on bare sand than when pebbles and cobbles are present [54]. Another example of complex requirements on substrate composition is given by the case building incest larvae of *Rhyacophila* and *Hydropsyche*, which, although dwelling on cobbles in swiftly flowing waters of riffles, need a special kind of fine sediment material for constructing their shelters [89].

In general, the larger the stones, hence the more complex the substrate composition, the more diverse is the invertebrate fauna. Sand is a relatively poor habitat, but silty sand is richer, and muddy substrata can be very rich in biomass, although not in variety of species [40].

### 2.4.3 Food availability

Food availability is favored as a primary parameter defining the distribution of animals by some researchers. In his study, Ulfstrand [96] concludes, that, when viewing microdistribution of species from an angle of food preferences, the evident conclusion is that their distribution is more closely related to this factor than to any other.

The following classification is used for defining the trophic groups of macroinvertebrates [13]:

**Grazers and scrapers** – herbivores feeding on attached algae;

**Shredders** – large particle feeding detritivores;

**Collectors** – both suspension and deposit fine particle feeding detritivores;

**Predators** – carnivores.

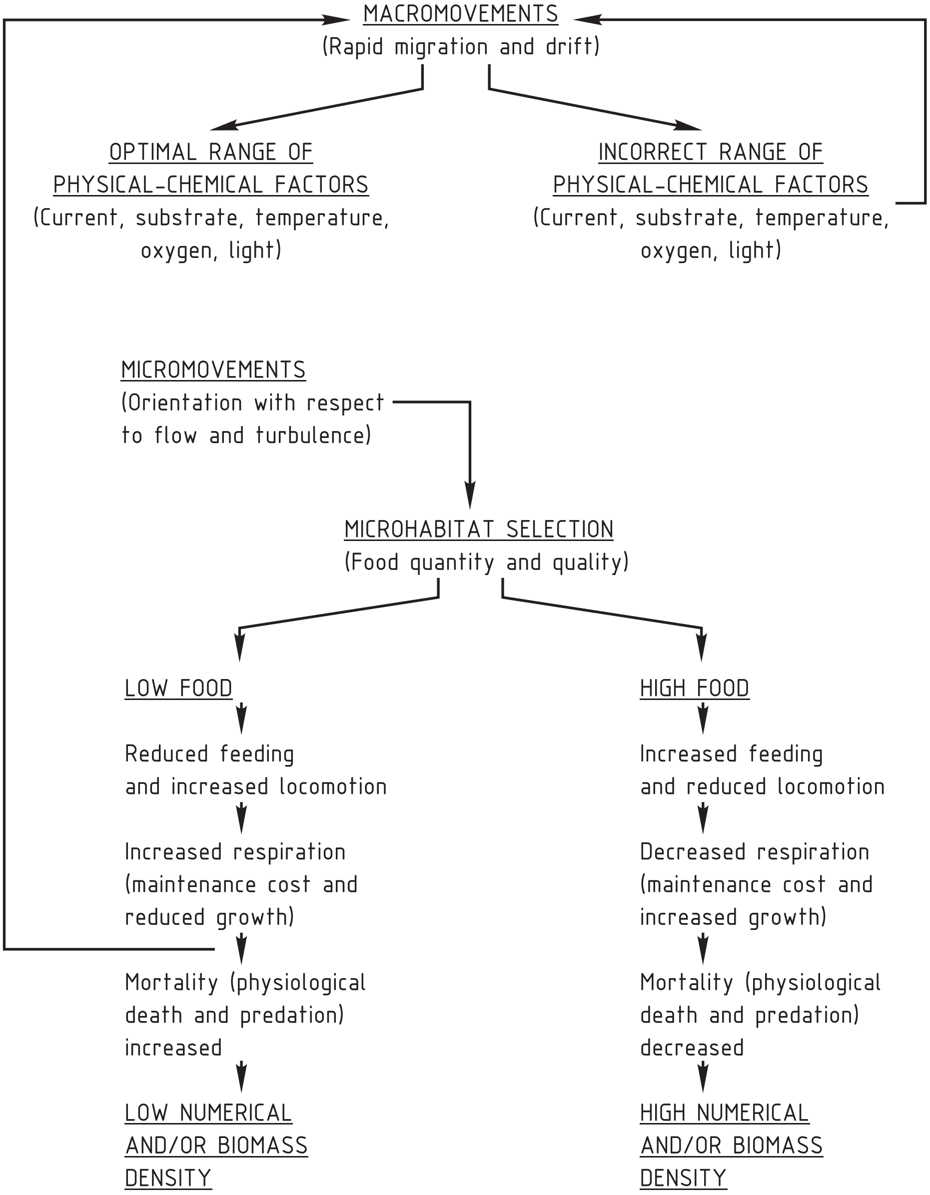

**Figure 2.6:** Relationship between locomotion, feeding, growth, respiration and selection of physical-chemical ranges in determining macroinvertebrate distribution and abundance, from Cummins (1975) [13]

Depending on the trophic group, some general substrate/flow conditions can be summarized. For example, the grazers *Baetis spp.* and *Glossosoma intermedium* are found on naked stones with unshaded surfaces, as it is the most suitable place for algae growth. Favorable surface and flow conditions are required for fine particle feeders like *Simuliidae*. Deposit collectors are not expected to be found on top of stones but behind them in shelter. And shredders are also not expected to dwell in an erosional habitat but more in a depositional one like a pool [13].

Predators' distributions are affected largely by the presence of prey: thus, young *Baetis* nymphs are known to be a preferred food for some stoneflies, and the density of the former can influence that of the latter, as well as other predators like caddis fly *Rhyacophila* [96].

Unfortunately, the majority of macroinvertebrates are non-selective feeders and their distribution patterns in a stream with a suitable food supply may often be controlled by other parameters like sediment, flow, competition for place, and predation. In Figure 2.6, the relationship proposed by Cummins [13] between major processes like locomotion, feeding, growth, respiration and selection of physical-chemical ranges in determining macroinvertebrate distribution and abundance is shown. In this diagram, under macro-movements is more likely meant migration between habitats within a river reach (see parameters defining macrodistribution of benthos in Section 2.4), and under micromovements – searching for favorite conditions within areas of stone surfaces.

### 2.4.4 Other factors

**Shade** or **light availability** is not a very well investigated parameter, but a few studies indicated, that it can be important. For example, *Baetis rhodani* showed a consistent pattern of high abundance in unshaded areas, and a sparse one under trees in a spring stream in Denmark [40]. This may be not surprising, as this species feeds upon attached algae. The indirect influence of light vs. shadow is possible through intensified algal growth, temperature or oviposition habits of adults.

**Interaction with other organisms** can be very important for bottom dwelling species. Even though other conditions are the same, abundance and distribution of macroinvertebrates can vary from one substratum patch to another, due to effects of competition for food, space, or of predation.

Also some other factors like **water depth**, **oviposition habits**, **diseases** and **proximity of suitable habitats** can determine the distribution of benthic species [40].

## 2.5 Review of existing benthos habitat models

The number of studies and habitat models allowing impact assessment for benthos species is sparse in comparison to fish models. The main reasons for this are difficulties in collecting (large sample size) and taxonomic identification of benthic species, as well as methodological problems in identifying the main controlling parameters. Additionally, the "unpopularity" of benthos in ecological studies can be explained with the inability to assign a direct "benefit" to the maintenance of benthic communities in contrast to fish. Usually, it has been assumed that macroinvertebrate responses to flow regime altering would closely match those of fish. Gore et al. [33] points out, however, that, due to a restricted mobility, benthos species possess much more narrow preferences for some parameters than fish and it is not justified to make conclusions on benthic fauna from fish studies.

The majority of past benthos habitat studies are "instream" cases, concerning with water abstraction from the main river channel. Therefore, the main attention in the past was given to the flow component (velocity or bottom shear stress).

### 2.5.1 PHABSIM for benthos habitat modelling

Applications of PHABSIM, a central operational tool of IFIM, show no special adjustments to benthos habitat studies. Like for fish, the preference curves for the main parameters water depth, mean column velocity and substrate class, are usually produced using various field sampling techniques and, then, in a standard way (see Section 2.3.1) combined with distributions of these parameters within a river reach at different discharges [32], [42]. Maps of joint habitat suitability and diagrams of $WUA$ and $HHS$ vs. discharge are used for the assessment of flow requirements of benthic species.

It can be argued whether these standard parameters, especially the mean column velocity, represent the optimal choice for benthic habitat modelling. Such a direct transferability of the "fish approach" onto benthos is not supported theoretically and shows merely the problems ecologists have describing the benthic habitat and selecting the relevant parameters.

Like in fish habitat studies, application of PHABSIM's three-parametrical approach is criticized for its inability to account for the interdependency of parameters, for example of depth and mean column velocity. The use of exponential polynomial analysis, suggested by Gore and Judy [32], can theoretically account for such interactions, but results only in a slight improvement for habitat suitability predictions.

It is difficult to justify the predictability of the PHABSIM approach in benthos studies. For some species, a very low percentage of the explained microdistribution variability is reported [42], [83], but whether this is related to a poor choice of parameters or to not accounting for other important factors is difficult to say. As macroinvertebrates are not as mobile as fish, it is possible that not only the present hydraulic situation within a reach, but also the recent flow history can be a reason for the discrepancies between predicted and measured habitat quality [42].

### 2.5.2 FST-hemispheres based models

In the end of the eighties, Statzner et al. [83] postulated, that stress resulting from flow and temporal exposure to it may define the distribution of lotic macrozoobenthos. They point out, that the shape of many benthic animals is not well adapted to minimize flow forces, therefore, these forces should be very stressful for these animals. The authors suggest, that complex hydraulic parameters, such as Froude and Reynolds numbers, and, especially the grain Reynolds number $Re_*$ defined as:

$$Re_* = \frac{k\,u_*}{\nu} = \frac{k\,(\tau_0/\rho_w)^{0.5}}{\nu} \qquad [-] \qquad (2.10)$$

| | | | | |
|---|---|---|---|---|
| with | $Re_*$ | = | grain Reynolds number, | [-] |
| | $\tau_0$ | = | bottom shear stress, | $[N/m^2]$ |
| | $\rho_w$ | = | density of water, | $[kg/m^3]$ |
| | $u_*$ | = | shear velocity, | [m/s] |
| | $k$ | = | geometrical roughness height, | [m] |
| | $\nu$ | = | kinematic viscosity of water, | $[m^2/s]$ |

would be more appropriate to define animal distributions than single parameters like velocity, depth or substrate characteristics (or their combinations). To estimate the grain Reynolds number, the bottom shear stress should be known. For the estimation of $\tau_0$, they suggest a new method – the so called *FST-hemispheres* [88] (see Chapter 4 for a detailed description of this method). It should be pointed out, that in the pioneer article the method was declared as to be "an integrated indicator of key hydraulic characteristics (turbulence or force of flow prevailing at the stream bottom)". Preliminary and later conducted calibrations of FST-hemispheres showed the best correlation to bottom shear stress and thus, in all forthcoming articles, FST hemispheres stand for a synonym for a bottom shear stress measuring device.

Unfortunately, further studies revealed that there is no unique correlation of FST-hemispheres to bottom shear stress, and that these correlations change with the substrate conditions [16]. Nevertheless, even if it was not clear, what exactly is measured by FST-hemispheres, Statzner's idea was greatly supported by biologists and habitat modelers and encouraged many studies, in which FST-hemispheres were used [71], [25]. Biological samplings show, that many benthic species possess a clear preference for a specific range of "near-bed" forces expressed in terms of FST-hemisphere numbers. For 53 taxa the so called *standard* preference functions (transferable within rivers in Germany) are found [20]. The majority of species (24) therein are rheophil (liking flow), 12 species are rheobiont (exclusively strong flow preferential), 10 are limnophilic species (liking low flow) and 3 limnobiont (exclusively standing water inhabitants). 4 species are identified as limno-rheophil. Using this preferential functions, the description of habitat suitability for benthic species can be based upon the only one parameter – the FST hemisphere number.

So far, those curves were used in a practical, empirical way. Never validated, they offered a simple method for the estimation of minimum flow. Sometimes even biologists wondered, why there is a dependency between "macro-scale" flow forces registered by FST-hemispheres and "micro-scale" environment of animals [71]. But for the correct assessment of the studies based on this method, it is important to understand the rationale behind the workings of FST based preference curves. Presumably, not only flow forces but also the indirect effects of flow are expressed by FST-hemispheres. Some hints can be found in the physiology of the considered species. For example, the adult bug *Oreodytes sanmarki* requires brief emergences from bottom to the water surface for respiration [47], so its preferences for low flow forces (small FST numbers) can be explained (see preference curve in Figure 2.7a). Another species, the mayfly *Rhithrogena semicolorata*, which lives exposed on stones, is most susceptible to flow velocity due to its respirational system [3]. According to the preference curve shown in Figure 2.7b, it can sustain very large flow forces, but cannot live in stagnant water. This can be explained by the flattened form of the animal and its specialized mechanism to attach itself to a substrate (friction pads) [40]. Thus, living close to the stone surface or in small crevices, it does not experience large flow forces. Rather, it profits from flow due to intensified exchange processes.

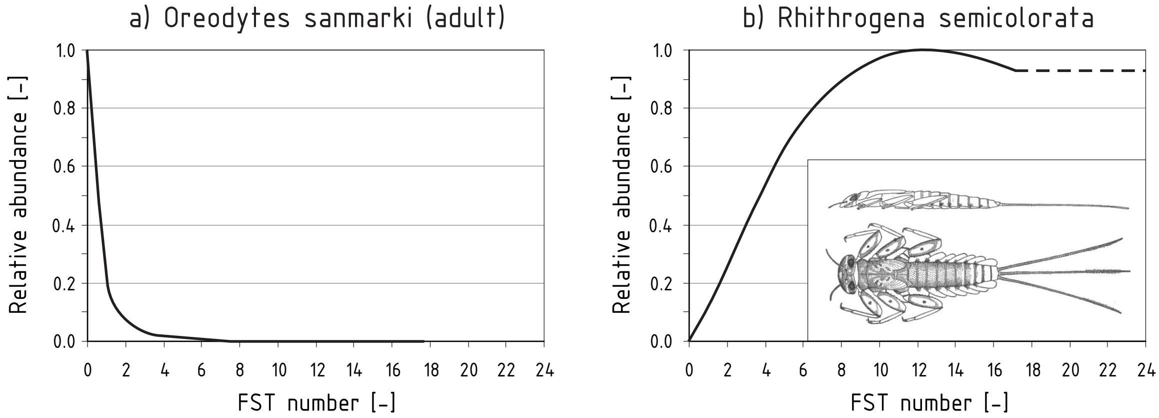

**Figure 2.7:** Standard FST-hemisphere preference curves for: a) *Oreodytes sanmarki* (adult) and b) *Rhithrogena semicolorata*, from [20]

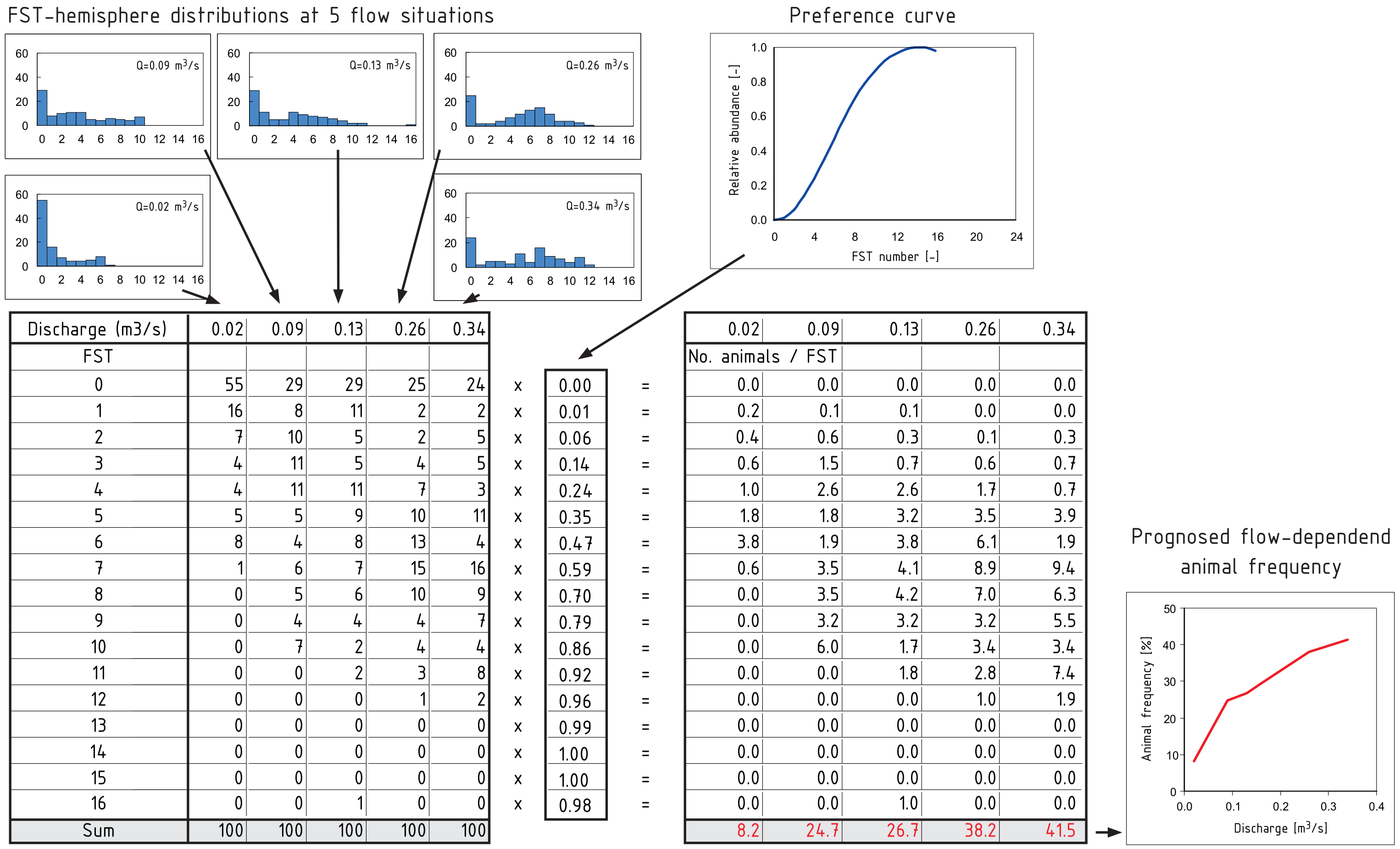

| Discharge (m3/s) | 0.02 | 0.09 | 0.13 | 0.26 | 0.34 |  |  |  | 0.02 | 0.09 | 0.13 | 0.26 | 0.34 |
|---|---|---|---|---|---|---|---|---|---|---|---|---|---|
| FST |  |  |  |  |  |  |  |  | No. animals / FST |  |  |  |  |
| 0 | 55 | 29 | 29 | 25 | 24 | x | 0.00 | = | 0.0 | 0.0 | 0.0 | 0.0 | 0.0 |
| 1 | 16 | 8 | 11 | 2 | 2 | x | 0.01 | = | 0.2 | 0.1 | 0.1 | 0.0 | 0.0 |
| 2 | 7 | 10 | 5 | 2 | 5 | x | 0.06 | = | 0.4 | 0.6 | 0.3 | 0.1 | 0.3 |
| 3 | 4 | 11 | 5 | 4 | 5 | x | 0.14 | = | 0.6 | 1.5 | 0.7 | 0.6 | 0.7 |
| 4 | 4 | 11 | 11 | 7 | 3 | x | 0.24 | = | 1.0 | 2.6 | 2.6 | 1.7 | 0.7 |
| 5 | 5 | 5 | 9 | 10 | 11 | x | 0.35 | = | 1.8 | 1.8 | 3.2 | 3.5 | 3.9 |
| 6 | 8 | 4 | 8 | 13 | 4 | x | 0.47 | = | 3.8 | 1.9 | 3.8 | 6.1 | 1.9 |
| 7 | 1 | 6 | 7 | 15 | 16 | x | 0.59 | = | 0.6 | 3.5 | 4.1 | 8.9 | 9.4 |
| 8 | 0 | 5 | 6 | 10 | 9 | x | 0.70 | = | 0.0 | 3.5 | 4.2 | 7.0 | 6.3 |
| 9 | 0 | 4 | 4 | 4 | 7 | x | 0.79 | = | 0.0 | 3.2 | 3.2 | 3.2 | 5.5 |
| 10 | 0 | 7 | 2 | 4 | 4 | x | 0.86 | = | 0.0 | 6.0 | 1.7 | 3.4 | 3.4 |
| 11 | 0 | 0 | 2 | 3 | 8 | x | 0.92 | = | 0.0 | 0.0 | 1.8 | 2.8 | 7.4 |
| 12 | 0 | 0 | 0 | 1 | 2 | x | 0.96 | = | 0.0 | 0.0 | 0.0 | 1.0 | 1.9 |
| 13 | 0 | 0 | 0 | 0 | 0 | x | 0.99 | = | 0.0 | 0.0 | 0.0 | 0.0 | 0.0 |
| 14 | 0 | 0 | 0 | 0 | 0 | x | 1.00 | = | 0.0 | 0.0 | 0.0 | 0.0 | 0.0 |
| 15 | 0 | 0 | 0 | 0 | 0 | x | 1.00 | = | 0.0 | 0.0 | 0.0 | 0.0 | 0.0 |
| 16 | 0 | 0 | 1 | 0 | 0 | x | 0.98 | = | 0.0 | 0.0 | 1.0 | 0.0 | 0.0 |
| Sum | 100 | 100 | 100 | 100 | 100 |  |  |  | 8.2 | 24.7 | 26.7 | 38.2 | 41.5 |

**Figure 2.8:** Principle of FST-hemisphere based habitat modelling, from Scherer (1999) [69]

In Figure 2.8, the principle of habitat modelling with FST-hemispheres is shown. It is implemented in such models as HABITAT [20] and BHABIM [41]. At a given flow situation, 100 randomly distributed FST-hemisphere measurements are recommended for the statistical characterization of a river reach [87]. To evaluate the effect of changing flow conditions on benthos habitat, FST-hemispheres measurements should be done at a number of different discharges. The measurements should start at the lowest (technically set or naturally occurring) possible flow and each higher, consecutive flow should be approximately twice of the preceding one. The flows measured should cover the range of discharges that is of interest. Locations for measurements have to be chosen randomly in longitudinal and transverse direction. Either method generating random locations is appropriate. The locations for measurements are usually not the same for all flows (this would actually introduce a bias into the measurements unless the channel has a rectangular cross section). For practical purposes it is suggested that 100 measurements are taken within 10 or 20 cross sections of the river, depending on the width and length of the investigated reach. Distances between cross-sections are 1 or 2 mean river widths to prevent possibly following a regular riffle-pool system and thus introducing a bias again. The number of measurements on each cross section depends on the number of cross sections chosen to represent an investigation reach [41].

100 FST-hemisphere measurements at, from experience, 5 to 8 flow situations means a high effort for field investigations and, respectively, high costs for the habitat studies. To reduce the time-consuming measurement procedure, attempts to develop approaches for the estimation of FST-hemisphere numbers distributions upon some main river reach characteristics have been undertaken (see Sections 2.5.2.1, 2.5.2.2).

#### 2.5.2.1 FSTRESS

FSTRESS is a statistical tool for estimation of FST-hemisphere numbers distributions designed to replace time consuming field FST measurements. The model uses the calibration curve “FST number vs. bottom shear stress” obtained for a coarse pebble bed in a laboratory flume [86] (see calibration curves 5.1, 5.2 in Table 4.4).

Measured FST-hemisphere distributions from 14 river reaches of the River Ruhr catchment and 9 reaches of various Bavarian streams form the model basis. At every reach, FST measurements were conducted at a number of discharges, resulting in a pool of 102 distributions. For all river reaches, independently from their morphological characteristics, a similar pattern of change in frequency distributions with the flow rate (see arrows in Figure 2.9a) is assumed: the percentage of small FST numbers decreases and that of large FST numbers increases with a rising flow rate. The frequency of the i-th FST number in the sample is defined by an analytical model, which is basically a mixture of exponential and normal statistical distributions:

$$f(n_i) = k_m \exp(-n_i) + (1 - k_m) \left[ \frac{1}{2.5(2\pi)^{1/2}} \exp \left( -0.5 \left( \frac{n_i - n_m}{2.5} \right)^2 \right) \right] \qquad [-] \quad (2.11)$$

with $f(n_i)$ = frequency of the i-th FST number, [-]
$n_i$ = i-th FST number, [-]
$n_m$ = FST number – mean of the normal distribution, [-]
$k_m$ = mixing parameter, [-]

Bottom shear stress $\tau_m$ corresponding to the mean of the normal distribution $n_m$ and mixing parameter $k_m$ are found via the functional dependencies derived from the measured distributions at above mentioned reference river reaches (see Figure 2.9b). Here, a Froude number for a river reach $Fr$ is defined by:

$$Fr^2 = \frac{Q^2}{g \, H_m^3 B_m^2} \qquad [-] \qquad (2.12)$$

with $Fr$ = Froude number for a river reach, [-]
$Q$ = discharge, [$m^3/s$]
$H_m$ = mean depth of a river reach, [m]
$B_m$ = mean width of a river reach, [m]
$g$ = acceleration due to gravity, [$m/s^2$]

The value of $n_m$, limited to the range [2, 18], is further obtained by an iterative procedure, until the value of $\tau_m$ corresponds to the one estimated previously from Figure 2.9b.

Although authors imply, that the FSTRESS model is capable to predict “general” trends in cumulative frequency distributions of FST-hemispheres well, considerable deviations can be seen between computed and observed curves in many cases. Catching those discrepancies requires a close look at the diagrams. Moreover, on contrary to the authors’ statement, it appears to be unimportant which river reaches (Bavarian rivers, Ruhr rivers or a mixed pool of rivers) are taken as a basis for the determination of the functional dependency in Figure 2.9b: for some of them, cumulative frequency distributions are very different in form from those obtained with the analytical model.

Generally, it is questionable whether the specific river reach morphology is unimportant in determining the FST frequency distribution. It is obvious, that in case of a channelized river, these will have quite a different form than those for a natural river. The former will be characterized by the presence of a large number of the same FST-hemisphere numbers, the latter by the presence of FST numbers in every class likely.

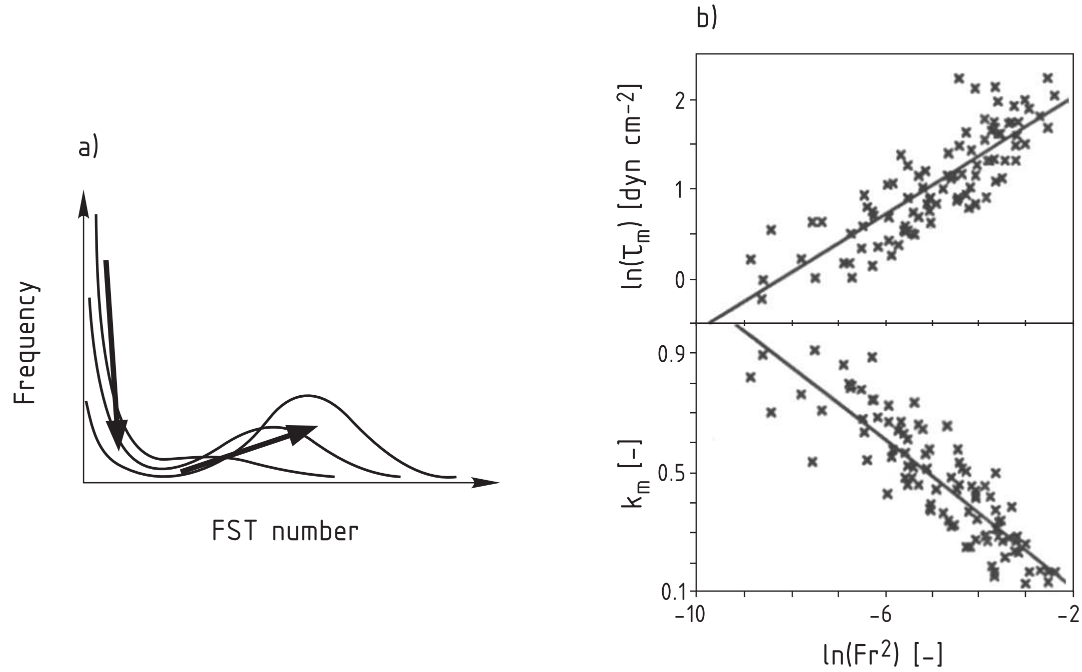

**Figure 2.9:** a) Assumed pattern of change in FST-hemisphere frequency distributions with flow rate in model FSTRESS; b) Diagrams for the determination of parameters in Equation 2.12

#### 2.5.2.2 HABITAT model

The model HABITAT [69] can be considered conceptually as an improvement of FSTRESS. It also aims to predict frequency distributions of FST hemispheres upon some main characteristics of a river reach, but, in contrast to FSTRESS, accounts for the special morphological characteristics of a river channel.

The model is built upon analysis of hemisphere distributions from 35 river reaches in total, 24 of which are those used for the development of the FSTRESS model. All river reaches are subdivided into four classes. For these classes, special analytical models of FST distributions are assigned. The classification of the river reaches is conducted upon the parameters listed in Table 2.1. In this table, also the ranges of these parameters for which the model HABITAT is applicable, are specified.

This relatively new model did not find wide application in habitat studies, probably due to a tendency to switch from benthos to fish as an indicator species in recent times. Also, validation data for the model is missing and some researchers (K. Jorde – personal communication) suggest, that the number of input parameters is still not enough for a proper description of the river morphology. Like FSTRESS, the HABITAT model only allows inte-

| Parameter | Description | Range |
|---|---|---|
| $E$ | relation of impounded to freely flowing reach lengths | 0.1–11 |
| $d_{50}$ | characteristic diameter of substrate material | 0.1–150 mm |
| $d_{84}/d_{16}$ | homogeneity of substrate material | 0.5–20 |
| $i_0$ | mean slope of a river reach | 0.001–0.05 |
| $B_m$ | mean width of a river reach | 2–30 m |
| $p_m$ | meandering degree | 1.0–1.9 |

**Table 2.1:** Parameters and application range of the model HABITAT

gral evaluation of near-bed flows, without spatial reference. This renders it impossible to integrate additional parameters into the modelling, as the effect of their spatial interplay cannot be accounted for. For the same reason, this model is difficult to use in restoration studies, where within a part or a whole river reach, a change of near bottom flows and/or other parameters (for example, substrate) takes place.

## 2.6 Summary

Development of benthos habitat modelling approaches appears to be important for two main reasons. (1) Modern understanding of river ecosystem functioning requires consideration of all its components, including benthic species, as these can have narrower habitat requirements than, for example, fish. (2) In some cases, benthic species are the exclusive target for habitat assessment studies, either due to the absence of fish or presence of unique benthic species which have to be preserved at any cost.

For most benthic species, flow is the most important parameter defining their distribution and abundance at a micro-habitat scale. It is difficult to select the spatial scale for the appropriate flow characterization for millimeter-sized animals living on/in the substrate. However, many laboratory and field studies show, that flow measurements conducted at a larger scale than those of small bottom dwelling animals can describe their micro-distribution. This is proven by studies, where near-bed flow conditions are assessed by velocity meters at a distance of some centimeters above the bed or by FST-hemispheres. The physiology of species can explain much about their flow preferences. In this respect, the physical stress from flow appears to be not as important as respiration and feeding specialities of a particular species. Another important parameter, which is necessary to include in modelling, is the substrate. It can influence the physiological processes of some species at the same degree as flow. Some other parameters, such as depth or shade, can also play a role and, if relevant, should be integrated into a modelling process.

Two major habitat modelling techniques were applied in the past for benthos: the three-parametrical approach of PHABSIM and the one-parametrical approach based on FST-hemispheres. The main disadvantage of the PHABSIM approach is the use of mean column velocity, which requires a special adjustment to integrate the interdependency of flow velocity and water depth. The FST-hemisphere based approach appears to be more capable to describe the requirements of benthic species, as the equipment is designed to measure near-bed flow characteristics. Rich data on flow preferences of animals expressed in FST-hemisphere numbers vs. animal density represents a very valuable and expensively acquired information, thus, it should be used in future studies. At the same time, the original FST-hemisphere based approach has considerable disadvantages. Among them: (1) It is not clear which physical parameter is measured by FST-hemispheres; (2) high costs of field survey; (3) integration of additional parameters is not possible due to the statistical way of a river reach characterization (100 randomly distributed FST measurements at one flow situation).

Further in this study, an attempt to clarify the physical rationale of the FST-hemispheres will be undertaken. Also, the approach to compute their spatially referenced distributions will be elaborated. The goal hereby is to reduce field survey costs and to allow for the integration of additional parameters in benthos habitat modelling.

# 3 Turbulent flow field over rough bed

Flow is one of the major parameters defining microdistribution of many bottom-dwelling animals. Therefore, the success of benthos habitat modelling is directly dependent on the proper characterization of the near-bed flow field. This knowledge can serve also for clarifying the physical rationale of the FST-hemispheres method: a hemisphere, as an object submerged in a fluid, resists a hydrodynamic force resulting from flow movement around it. Besides of the object's size and shape, the characteristics of a flow field define the direction and magnitude of this force. Thus, assuming an approach to characterize the near-bed flow exists, it should be possible to estimate the magnitude and direction of the hydrodynamic force and subsequently, through the force balance, to calculate the density of a hemisphere which will be moved away at specific flow conditions.

Flow in rivers is generally turbulent. It develops over a highly irregular and mobile river bed which makes its description a very difficult task. Considerable advancements have been achieved in simulation of river flows by application of large scale numerical tools (one-, two-dimensional hydrodynamic models). These tools are also often used for fish habitat modelling. Two-dimensional models allow calculation of water depths and mean column flow velocities with a good accuracy, but the step to the estimation of near-bed flow conditions is still large. Detailed three-dimensional simulations are still not justified economically for most practical cases due to the enormous surveying and modelling costs.

Main attention in this chapter is given to the so called *logarithmical velocity distribution law*. Theoretically, it could allow estimation of near-bed conditions from the mean flow characteristics obtained with a two-dimensional hydrodynamic model. Practically, due to the assumptions in the derivation of the Nikuradse's log law for flows over rough bed, it is applicable only at large relative submergences, that is the relation of water depth to the substrate roughness height. In benthos habitat studies, however, modelling is usually required for river channels with relatively small water depths and coarse substrates. Specific features of flows over rough beds with small relative submergences and the modified logarithmical velocity distribution law after Bezzola developed especially for such flows, are the essence of this chapter.

## 3.1 Characteristics of flows in gravel bed rivers

In the present work, mainly fast-flowing streams with coarse substrates and relatively small water depths are considered. These streams belong to the *rhithron* – the region of the river course extending from the source (*krenon*) to the point where mean monthly water temperatures rise up to 20°C. In rhithron, oxygen concentrations are always high, flow is fast and turbulent, and the bed is composed of rocks, stones or gravel with occasional sandy or silty patches. Rhithron is further subdivided into the steeper epi-rhithron, meta-rhithron and hypo-rhithron, which eventually merges into the *potamon* – the part characterized by monthly mean temperatures over 20°C, possible oxygen deficits, slow flow and a bed composed mainly of sand or mud [98].

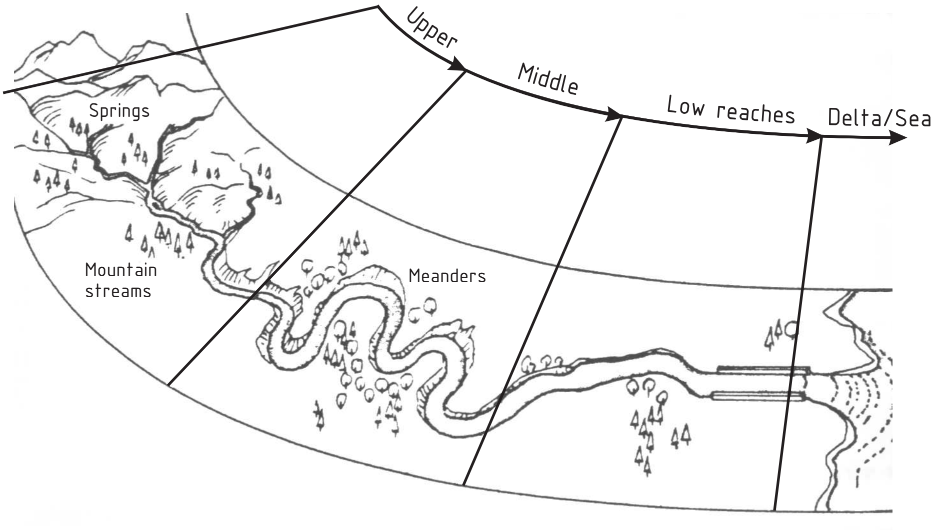

**Figure 3.1:** Zonal subdivision of a river course, after Gunkel (1996) [34]

According to the definition, to rhithron belongs a wide range of water courses, from small streams to large rivers, in which mountain streams as well as midland rivers can be included (see Figure 3.1). In following, the main characteristics of rhithron rivers and their flow regimes are summarized.

### 3.1.1 Longitudinal slope and morphological features

Following types of streams are commonly distinguished upon the mean longitudinal bed slope [8]:

| | |
|---|---|
| Mid- and lowland rivers | $i_0 \leq 1$ % |
| Mountain streams | $i_0 \leq 6$ % |
| Wild water streams | $i_0 > 6$ % |

Bathurst [7] references longitudinal slopes in the range of 0.4 % to 5 % as typical for mountain streams.

The main morphological characteristic of rhithron rivers is the alternation of *pools* and *riffles* which arise from changes in a gradient (see Figure 3.2).

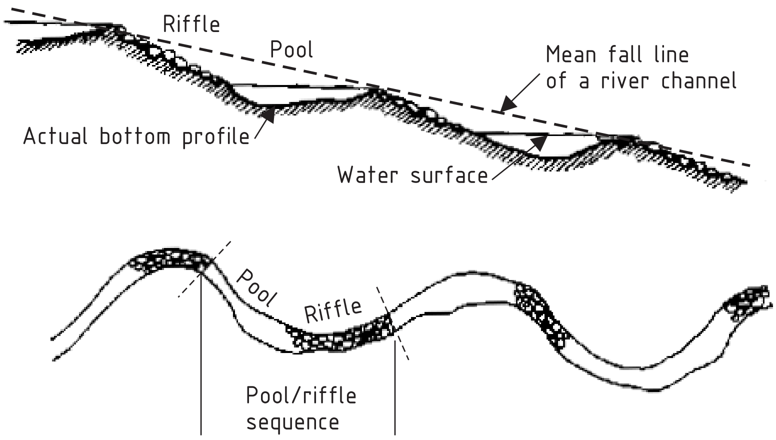

**Figure 3.2:** The division of a river channel into a sequence of pools and riffles, from Welcomme (1985) [98]

The steeper epi-rhithron is dominated by rapids, waterfalls and cascades, but as the river proceeds downstream, the proportion of pool-like reaches increases relative to the riffles. Riffles are steep, shallow zones having coarse bottoms of boulders, rocks or pebbles. Pools are flatter and deeper, with bottoms of finer material. One pool-riffle sequence usually occupies a channel length of an equivalent of five to seven channel widths, irrespective of the form or geographic location of the river [98]. The third category of morphological features typical for rhithron is *glide*. It is represented by moderately shallow reaches with an even flow, that lack obstructions or pronounced turbulence. Bottoms are usually gravel and small cobbles. Glides are particularly common in large rivers passing through mountainous terrain where channels may run relatively straight for many kilometers.

### 3.1.2 Influence of roughness on a flow field

Every single roughness element of a river bottom resists flow through friction and pressure forces. At roughness elements, flow separates and complex vortical structures are produced as a result. During transport of vortices downstream and away from the river bed, they break down and dissipate energy. Energy losses, in general, depend on height, shape, spatial density and arrangement of roughness elements.

In respect of the distance between bottom roughness elements (spatial density in a three-dimensional case) Morris [55] distinguishes following flow regimes (see Figure 3.3). In case of an *isolated-roughness* flow, the distance between neighboring elements in flow direction is that large, that recirculation zones – wakes, arising due to flow separation on the objects – are not affected by any downstream elements. Reducing the distance that much, that the vortex generation and dissipation phenomena associated with each wake starts to interfere with those at the adjacent obstacles, results in a *wake-interference* flow regime characterized by an abnormally intense turbulence and mixing. Reducing the distance further, leading to the appearance of dead-water pockets between elements, causes a *skimming* flow, as the interaction between those pockets and bulk flow acts like a pseudo-wall.

Flow over a smooth bottom is characterized by solely friction losses. Introducing occasional isolated roughness elements increases the energy losses due to additional form drag forces on the obstacles. Entering a wake-interference flow regime, energy losses increase even more and then, further reducing the distance between the elements, start to decrease, until they are reduced to pseudo-friction losses again in a skimming flow.

Another important characteristic of flow over rough surface which defines energy losses in a channel, is the roughness scale. It is defined by the *relative submergence* (Figure 3.4), that is the relation of the water depth $\mathtt{h}$ to the diameter of substrate material $\mathtt{d}$. In this perspective Bathurst [7] distinguishes upon the value of relative submergence $\mathtt{h}/\mathtt{d}_{84}$:

**Large scale roughness** at $\mathtt{h}/\mathtt{d}_{84} < 1$;

**Transition region** at $1 < \mathtt{h}/\mathtt{d}_{84} < 4$;

**Small scale roughness** at $\mathtt{h}/\mathtt{d}_{84} > 4$.

Small scale roughness (or flow with large relative submergence) defines the so called shear flow, whether large scale roughness is associated with the so called jet-wake dissipation process (German: Strahl-/Nachlaufdissipation). When elements are closely spaced to each other, energy dissipation occurs generally through interaction of wakes of preceding elements with downstream ones. With decreasing density of elements, the process transforms to a jet-like dissipation [8].

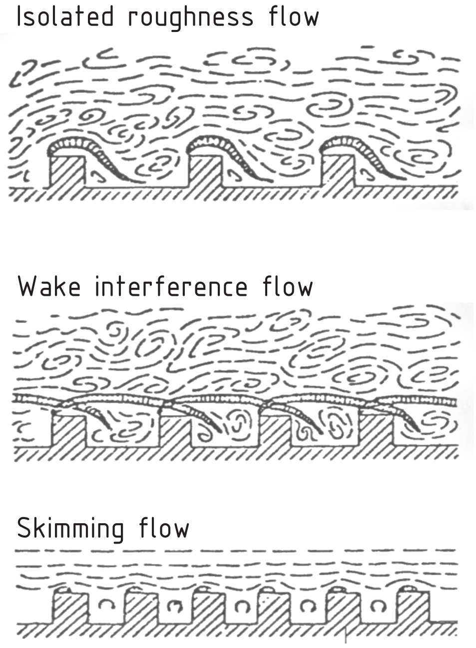

**Figure 3.3:** Flow regimes over rough beds, after Morris (1959) [55]

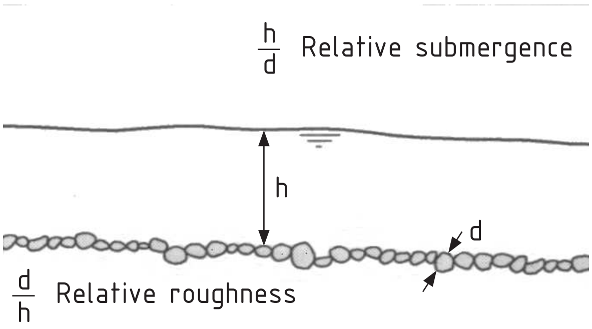

**Figure 3.4:** Definition of relative submergence and relative roughness height

At large relative submergences, bed material and river bottom structures do not influence the free surface. Such flow is called *channel flow* and a certain analogy exists to a *boundary layer flow* or shear flow. In boundary layer flow (for example, flat plate boundary layer in a wind tunnel), in the vicinity of the solid boundary the so called *wall region* exists in which the logarithmical velocity distribution law is valid (see also Section 3.3.1, Figure 3.7). It occupies approximately 20 % of the total boundary layer thickness $\delta$. The wall region is followed by the *outer region* with the upper border at a level where velocity reaches 99 % of the free stream velocity. The *free flow* area, where the velocity is constant and almost free from turbulence, encloses the outer region.

The presence of a free surface and absence of a free flow region is typical for the channel flow. Taking the boundary layer thickness $\delta$ equal to the water depth, under condition that roughness elements do not jut out the wall region, the flow can be considered as being of the channel type if the relative submergence is larger than 5 [8]. At smaller relative submergences, the flow is not anymore of channel type and the analogy to the boundary layer approximation is in general questionable.

### 3.1.3 Flow regimes

For open channel flows, the Froude number $Fr = U_m/\sqrt{gA_q\,/B_q}$, the ratio of inertial forces to gravity forces, is an important parameter. In gravel-bed rivers, especially at steep longitudinal slopes, Froude numbers can attain large subcritical values or even supercritical ones [7].

Additionally to continuous sub- or supercritical regimes, the so called *tumbling* flow regime can take place. It is characterized by the periodical acceleration and deceleration of flow in which supercritical and subcritical flow regimes alternate. The length of the cycle is of the order of the magnitude of the distance between the roughness elements. This kind of flow can only occur at extremely small relative submergences [8].

## 3.2 Basic equations of turbulent motion

Flow in a turbulent regime is characterized by random fluctuations of the velocity field. These fluctuations result in a mixing of the transported quantities, such as momentum, energy and species concentration, and cause these quantities to fluctuate as well. Although the Navier-Stokes equations, the equations of impulse balance and mass conservation for fluid flow, theoretically describe nearly all flows of practical interest, their direct solution is too computationally expensive for most engineering problems. Instead, a special form of these equations, the so called Reynolds-averaged Navier-Stokes equations (RANS) is commonly used. The RANS form of the equations introduces new terms, for the definition of which additional assumptions about small scale turbulent motions are needed.

### 3.2.1 Reynolds-averaged Navier-Stokes equations (RANS)

The basic idea lying behind the RANS approach is the decomposition of instantaneous flow field variables into mean and fluctuation components. Thus, the instantaneous value of the variable $f$ is defined as:

$$f = \overline{f} + f' \tag{3.1}$$

with $\overline{f}$ = mean component,
$f'$ = fluctuation component

Assuming the averaging over a time period $T$ that is sufficiently long to insure the independence of the mean component from time:

$$\overline{f} = \frac{1}{T} \int_{t_0}^{t_0+T} f dt \tag{3.2}$$

The average of the fluctuation component is by definition zero:

$$\overline{f'} = 0 \tag{3.3}$$

Following averaging rules formulated by Reynolds apply:

$$\overline{f + g} = \overline{f} + \overline{g}, \tag{3.4a}$$

$$\overline{a\, f} = a\, \overline{f}, \tag{3.4b}$$

$$\overline{\overline{f}\, g} = \overline{f}\, \overline{g}, \tag{3.4c}$$

$$\overline{\frac{\partial f}{\partial x_i}} = \frac{\partial}{\partial x_i} \overline{f}, \qquad \overline{\frac{\partial f}{\partial t}} = \frac{\partial}{\partial t} \overline{f}. \tag{3.4d}$$

with $f, g$ = independent functions,
$a$ = constant,
$x_i$ = coordinate system directions,
$t$ = time

The time-averaged Navier-Stokes equations are obtained by substituting Expression 3.1 for the velocity and pressure variables into the instantaneous continuity and momentum equations. The RANS equations for incompressible flow ($\rho = const$), also accounting for the gravity force, are:

$$\frac{\partial \overline{u}}{\partial x} + \frac{\partial \overline{v}}{\partial y} + \frac{\partial \overline{w}}{\partial z} = 0 \qquad \text{and} \qquad \frac{\partial u'}{\partial x} + \frac{\partial v'}{\partial y} + \frac{\partial w'}{\partial z} = 0 \tag{3.5a}$$

$$\begin{aligned}
\frac{\partial \overline{u}}{\partial t} + \overline{u}\frac{\partial \overline{u}}{\partial x} + \overline{v}\frac{\partial \overline{u}}{\partial y} + \overline{w}\frac{\partial \overline{u}}{\partial z} &= -\frac{1}{\rho}\frac{\partial \overline{p}}{\partial x} + \nu\Delta\overline{u} - \frac{\partial \overline{u'u'}}{\partial x} - \frac{\partial \overline{u'v'}}{\partial y} - \frac{\partial \overline{u'w'}}{\partial z} \\
\frac{\partial \overline{v}}{\partial t} + \overline{u}\frac{\partial \overline{v}}{\partial x} + \overline{v}\frac{\partial \overline{v}}{\partial y} + \overline{w}\frac{\partial \overline{v}}{\partial z} &= -\frac{1}{\rho}\frac{\partial \overline{p}}{\partial y} + \nu\Delta\overline{v} - \frac{\partial \overline{v'u'}}{\partial x} - \frac{\partial \overline{v'v'}}{\partial y} - \frac{\partial \overline{v'w'}}{\partial z} - g \\
\frac{\partial \overline{w}}{\partial t} + \overline{u}\frac{\partial \overline{w}}{\partial x} + \overline{v}\frac{\partial \overline{w}}{\partial y} + \overline{w}\frac{\partial \overline{w}}{\partial z} &= -\frac{1}{\rho}\frac{\partial \overline{p}}{\partial z} + \nu\Delta\overline{w} \underbrace{- \frac{\partial \overline{w'u'}}{\partial x} - \frac{\partial \overline{w'v'}}{\partial y} - \frac{\partial \overline{w'w'}}{\partial z}}_{\text{Reynolds stresses}}
\end{aligned} \tag{3.5b}$$

with $\overline{u}, \overline{v}, \overline{w}, u', v', w'$ = mean and pulsation components of velocity along $x$, $y$ and $z$ axes, respectively, [m/s]

$g$ = acceleration due to gravity, [m/s$^2$]

$\overline{p}$ = mean (time-averaged) component of pressure, [Pa]

$\rho$ = density of fluid, [kg/m$^3$]

$\nu$ = kinematic viscosity of fluid, [m$^2$/s]

$\Delta$ = Laplace operator

The RANS equations 3.5a, 3.5b have the same general form as the instantaneous Navier-Stokes equations, but include additional terms, so called Reynolds stresses, accounting for the effect of turbulent motion. These equations are not closed and additional hypotheses concerning the Reynolds stresses are needed to solve them.

### 3.2.2 RANS equations for uniform open channel flow

For a better understanding of the role which Reynolds stresses play in the mechanism of turbulent flows, consider here the case of a steady uniform free surface flow in a very wide channel. Defining the main flow direction along the x- axis (see Figure 3.5), the mean velocity components are:

$$\overline{u} = \overline{u}(y); \qquad \overline{v} = 0; \qquad \overline{w} = 0;$$

The RANS equations for this case will be:

$$0 = g\ \sin\alpha + \nu\frac{\partial^2\overline{u}}{\partial y^2} - \frac{\partial\overline{u'v'}}{\partial y} \tag{3.6a}$$

$$0 = -g\ \cos\alpha - \frac{1}{\rho}\frac{\partial\overline{p}}{\partial y} - \frac{\partial\overline{v'^2}}{\partial y} \tag{3.6b}$$

with $\alpha$ = angle of channel bottom [°]

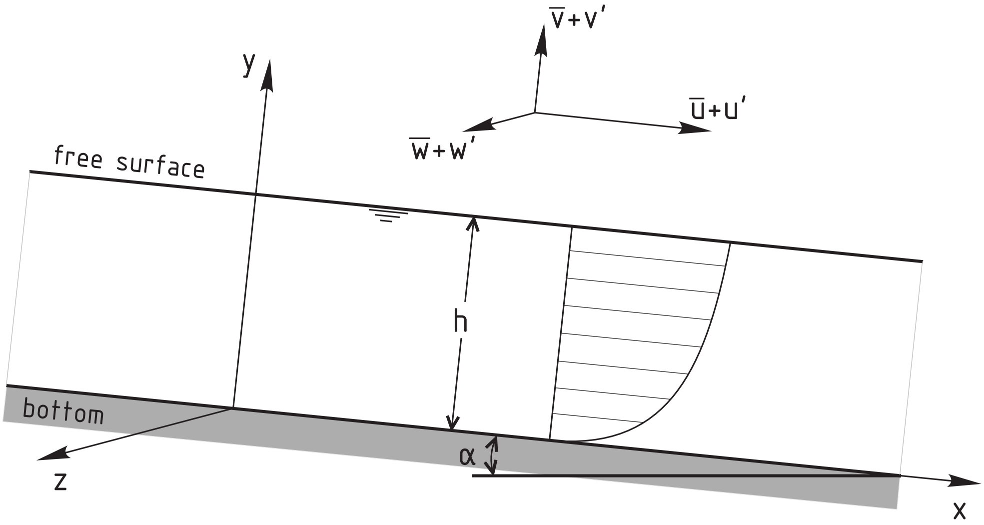

**Figure 3.5:** Definition of the coordinate system and velocity components for an example of uniform open channel flow

After integration of Equations 3.6a,b along the $y$- axis with the boundary conditions $\partial\overline{u}/\partial y = 0$, $\overline{p} = 0$ and $v' = 0$ at the free surface ($y = h$), we get:

$$g\ \sin\alpha(h - y) = \nu\frac{\partial\overline{u}}{\partial y} - \overline{u'v'} \tag{3.7a}$$

$$\frac{\overline{p}}{\rho} = g\ \cos\alpha(h - y) - \overline{v'^2} \tag{3.7b}$$

The left part term of Equation 3.7a corresponds to the total shear stress $\tau$ divided by the fluid density $\rho$. The total shear stress increases linearly with water depth and is the sum of the viscous (or laminar) $\tau_l$ and turbulent $\tau_t$ stresses:

$$\tau = \tau_l + \tau_t = \rho\nu\frac{\partial\overline{u}}{\partial y} - \rho\overline{u'v'} \tag{3.8}$$

The value of $\tau$ at the bottom ($y = 0$) is called *wall* or *bottom shear stress*:

$$\tau_0 = \rho\, g\, h\, \sin\alpha \tag{3.9}$$

with $\tau_0$ = bottom shear stress [N/m$^2$]
$\rho$ = density of fluid [kg/m$^3$]
$g$ = acceleration due to gravity [m/s$^2$]
$h$ = water depth [m]
$\alpha$ = angle of channel bottom [°]

The viscous stresses have only a considerable value directly near the bottom, where the gradient of the velocity $\partial\overline{u}/\partial y$ is relatively large. As it follows from Equation 3.7b, the mean pressure distribution in a channel in a turbulent regime deviates from the hydrostatic one due to the turbulent mixing motion expressed by the term $-\overline{v'^2}$.

### 3.2.3 Estimation of Reynolds stresses - Boussinesq hypothesis

The common way to close the RANS equations employs the Boussinesq hypothesis, which establishes a relation between Reynolds stresses and mean velocity gradients [37]. By analogy to a laminar flow, where viscosity dominates energy dissipation and transport of mass and momentum normal to the streamlines, it is assumed that the effect of turbulence can be represented as increased viscosity, so the Reynolds stresses can be defined as:

$$\tau_t = \rho \nu_t \frac{\partial\overline{u}}{\partial y} \tag{3.10}$$

with $\tau_t$ = turbulent shear stress [N/m$^2$]
$\rho$ = density of fluid [kg/m$^3$]
$\nu_t$ = kinematic eddy viscosity of fluid, [m$^2$/s]
$\overline{u}$ = mean velocity component along x-axis, [m/s]
$y$ = vertical coordinate, [m]

The Boussinesq hypothesis is commonly used in turbulence closure models employed in various fluid dynamics packages [22]. The advantage of this approach is the relative low computational cost of determining the turbulent viscosity. For example, for the standard $k - \epsilon$ turbulence model, only two additional transport equations – for the turbulent kinetic energy $k$ and the turbulence dissipation rate $\epsilon$ – have to be solved. Then, turbulent viscosity is computed as a function of $k$ and $\epsilon$ as:

$$\nu_t = C_\mu \frac{k^2}{\epsilon} \tag{3.11}$$

| | | | | |
|---|---|---|---|---|
| with | $\nu_t$ | = | kinematic eddy viscosity of fluid, | $[m^2/s]$ |
| | $k$ | = | turbulent kinetic energy, | $[m^2/s^2]$ |
| | $\epsilon$ | = | turbulence dissipation rate, | $[m^2/s^3]$ |
| | $C_\mu$ | = | empirical model constant, | [-] |

The disadvantage of the Boussinesq hypothesis is, that it assumes the turbulent viscosity is an anisotropic scalar quantity, which is not strictly true. For situations in which the anisotropy of turbulence has a dominant effect on the mean flow (for example swirling flows and stress-driven secondary flows) the turbulence models based on the Boussinesq hypothesis perform not so well and Reynolds Stress Transport models should be employed.

### 3.2.4 Prandtl's mixing length theory

A very important advancement of Boussinesq ideas represents the mixing length theory of Prandtl (1925) [62].

Consider the case of a two dimensional shear flow. The main flow direction coincides with the $x$- direction and the mean velocity components are defined as:

$$\overline{u} = \overline{u}(y); \qquad \overline{v} = 0; \qquad \overline{w} = 0;$$

According to Prandtl, a simplified mechanism of turbulent flow mixing can be described as a motion of fluid clusters, which on a certain part of a way move as a whole in longitudinal and transverse directions, preserving their initial impulse in longitudinal direction.

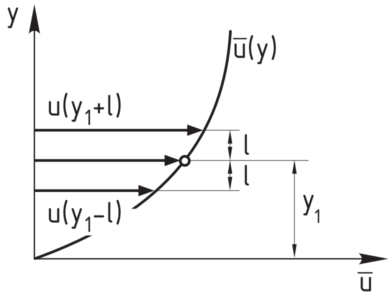

**Figure 3.6:** To the explanation of a mixing length theory

Assuming the fluid element with the mean velocity $\overline{u}(y_1 - l)$, originating from the layer $(y_1 - l)$, drifts to a layer $y_1$ (see Figure 3.6); if its impulse in $x$-direction is preserved, the difference in mean velocity for the element and its new surrounding is:

$$\triangle u_1 = \overline{u}(y_1) - \overline{u}(y_1 - l) = l\left(\frac{d\overline{u}}{dy}\right)_1$$

In this case of transverse motion, $v' > 0$. The same can be written for the element which moves from layer the $(y_1 + l)$:

$$\triangle u_2 = \overline{u}(y_1 + l) - \overline{u}(y_1) = l \left( \frac{d\overline{u}}{dy} \right)_1$$

In this case, $v' < 0$. The last two expressions represent first-order Taylor series approximations for $\overline{u}(y_1 - l)$ and $\overline{u}(y_1 + l)$. The velocity differences $\triangle u_1$ and $\triangle u_2$ due to the transverse motion of fluid elements can be interpreted as a longitudinal velocity fluctuation $\overline{|u'|}$ in the layer $(y_1)$:

$$\overline{|u'|} = \frac{1}{2}(|\triangle\overline{u}_1| + |\triangle\overline{u}_2|) = l \left| \frac{d\overline{u}}{dy} \right| \tag{3.12}$$

From Equation 3.12, the following physical meaning of the quantity $l$ can be derived. The *mixing length* $l$ is the distance which the fluid element has to cover for the difference between its initial mean layer velocity and the mean velocity of the new layer to be equal to the mean longitudinal pulsation component of the turbulent flow in that new layer. Additionally, the mixing length $l$ accounts for the unknown relation between the values of velocity fluctuations $\overline{u'}$ and $\overline{v'}$ and obtaining the value $\overline{u'v'}$ from them (see Schlichting [70] for more detailed explanation):

Finally, the turbulent shear stress is defined as:

$$\tau_t = \rho \, l^2 \left| \frac{\partial \overline{u}}{\partial y} \right| \left( \frac{\partial \overline{u}}{\partial y} \right) \tag{3.13}$$

| | | | | |
|---|---|---|---|---|
| with | $\tau_t$ | = | turbulent shear stress | $[N/m^2]$ |
| | $\rho$ | = | density of fluid | $[kg/m^3]$ |
| | $l$ | = | mixing length, | [m] |
| | $\overline{u}$ | = | mean velocity component along $x$-axis, | [m/s] |
| | $y$ | = | vertical coordinate, | [m] |

This formulation has a big advantage to the Boussinesq approach. It is known from experiments, that in turbulent flows the resistance is proportional to the second power of the velocity. This quadratic resistance law can be obtained from Prandtl's theory assuming that the mixing length is independent from the velocity magnitude. The mixing length is not a property of the fluid as is the molecular viscosity $\nu$, rather it is only a function of location within the turbulent flow field. For simple flows, the value of $l$ can be derived by considering the characteristic flow dimensions. So, for example, at a smooth wall $l$ should be zero, as movement in the direction perpendicular to the wall is not possible. However, at a rough wall, the mixing length can be reasonably assumed to be proportional to the height of roughness elements.

### 3.2.5 Universal velocity distribution

Prandtl's formulation for the turbulent shear stress $\tau_t$ allows further derivation of the velocity distribution law for the simple two-dimensional channel flow. Following Prandtl, the mixing length $l$ is assumed to be proportional to the distance from the wall $y$:

$$l = \kappa\, y, \tag{3.14}$$

with $l$ = mixing length, [m]
$\kappa$ = proportionality factor (von Kármán constant), [-]
$y$ = vertical coordinate, [m]

Here $\kappa$ is the proportionality factor which has to be determined from experiments. This is a reasonable assumption, as the turbulent shear stress at the wall should be zero. The next important simplification is the constant total shear stress $\tau$ in the proximity to the wall. For flows at high Reynolds numbers, the laminar shear stress is only important within the immediate vicinity of the wall and thus can be neglected, resulting in $\tau = \tau_t = \tau_0$. Introducing the *shear velocity*:

$$u_* = \sqrt{\frac{\tau_0}{\rho}} \qquad [\mathrm{m/s}] \tag{3.15}$$

with $u_*$ = shear velocity, [m/s]
$\tau_0$ = bottom shear stress, [N/m$^2$]
$\rho$ = density of fluid, [kg/m$^3$]

we get from Expressions 3.13 and 3.14:

$$\rho\, u_*^2 = \rho(\kappa\, y)^2 \left|\frac{\partial \overline{u}}{\partial y}\right| \left(\frac{\partial \overline{u}}{\partial y}\right) \qquad \Rightarrow \qquad \frac{\partial \overline{u}}{\partial y} = \frac{u_*}{\kappa y} \tag{3.16}$$

Integrating 3.16 along the $y$-axis, we get for the mean velocity distribution over the channel depth:

$$\frac{\overline{u}(y)}{u_*} = \frac{1}{\kappa} \ln y + C \tag{3.17}$$

The integration constant C is determined by the conditions at the wall. With the assumption of a constant shear stress, the Prandtl's velocity distribution is valid only in the proximity to the wall. Neglecting this, and applying the boundary condition $\overline{u} = \overline{u}_{max}$ at a free surface at $y = h$, yields:

$$\frac{\overline{u}_{\max} - \overline{u}(y)}{u_*} = \frac{1}{\kappa} \ln\left(\frac{h}{y}\right) \tag{3.18}$$

with $\overline{u}_{max}$ = maximum mean velocity (in the vertical) along $x$-axis, [m/s]
$\overline{u}(y)$ = mean velocity along $x$-axis, [m/s]
$u_*$ = shear velocity, [m/s]
$\kappa$ = proportionality factor (von Kármán constant), [-]
$h$ = water depth, [m]
$y$ = vertical coordinate, [m]

The universality of this formulation appears therein, that the normalized with $u_*$ velocity distribution plotted against the relative depth is the same for different Reynolds numbers and independent from conditions at a channel bed (smooth/rough).

As it was mentioned, the integration constant C in Equation 3.17 has to be estimated from the conditions at the wall. For example, in the case of a flow over a smooth wall, the turbulent velocity profile given by the log law has to merge with the velocity profile in the near-wall viscous sublayer. Requiring, that at some small distance $y_0$ from the wall velocity equals zero, we get for Prandtl's formulation:

$$\frac{\overline{u}(y)}{u_*} = \frac{1}{\kappa} \ln \frac{y}{y_0} \tag{3.19}$$

with $y_0$ = distance from the wall at which $\overline{u} = 0$, [m]

Above formula implies, that the mean velocity below the distance $y_0$ is equal zero, which is generally not the case and the distribution there should depend on the kind of the wall. As experiments reveal, the term $\kappa$, in contrast, represents a universal number of the turbulent flow and equals 0.4 for flows over smooth and rough beds, in closed and open conduits.

## 3.3 Turbulent velocity profiles

Unfortunately, the universal velocity distribution law has its applicability only within the so called *logarithmical* or *inertial* sublayer in which the assumptions on the distribution of the mixing length $l$ and negligibility of the viscous stresses are fulfilled. The upper border of the inertial sublayer for open-surface, two-dimensional, as well as axis-symmetric pipe flows is located approximately at a distance of $0.2h$ from the wall. The location of the lower border is determined by the conditions at the wall. Hereafter, the complete velocity distributions over the smooth and rough bottoms will be considered.

### 3.3.1 Smooth bottom

For smooth walls, $y_0$ in Expression 3.19 is supposed to be proportional to the thickness of a viscous sublayer. For dimensional reasons, the characteristic length for the latter can be constructed from the molecular viscosity of the fluid $\nu$ and a shear velocity $u_*$. Setting the proportionality as:

$$y_0 = \beta \, \frac{\nu}{u_*} \tag{3.20}$$

| | | | | |
|---|---|---|---|---|
| with | $y_0$ | = | distance from the wall at which $\overline{u}$ =0, | [m] |
| | $\beta$ | = | proportionality factor, | [-] |
| | $\nu$ | = | kinematic viscosity of fluid, | [$m^2/s$] |
| | $u_*$ | = | shear velocity, | [m/s] |

we get from Formula 3.19 for the logarithmical velocity distribution over the smooth bed:

$$\frac{\overline{u}(y)}{u_*} = \frac{1}{\kappa} \, \ln \frac{y \, u_*}{\nu} - \frac{1}{\kappa} \, \ln \beta \tag{3.21}$$

Introducing the following notations:

$$u^+ = \frac{\overline{u}}{u_*}; \qquad y^+ = \frac{y \, u_*}{\nu}; \qquad A_1 = -\frac{1}{\kappa} \, \ln \beta$$

Equation 3.21 can be rewritten in the form:

$$u^+ = \frac{1}{\kappa} \ln y^+ + A_1 \tag{3.22}$$

| | | | | |
|---|---|---|---|---|
| with | $u^+$ | = | dimensionless mean velocity along x-axis, | [-] |
| | $\kappa$ | = | von Kármán constant, | [-] |
| | $y^+$ | = | dimensionless distance from the wall, | [-] |
| | $A_1$ | = | constant, | [-] |

The value of $A_1$ found in the literature scatters between 5.0 and 5.5 (see [8] for a summary). A value of 5.3 can be taken for open surface flows in a wide channel.

In general, the following layers of a velocity profile over a smooth bed can be distinguished (see Figure 3.7):

- Within the *viscous sublayer*, which upper border is approximately at $y^+ = 5$, velocity is growing linearly with distance from the wall:

  $$u^+ = y^+ (1 - \frac{y}{2h}) \approx y^+ \tag{3.23}$$

  In this region viscous forces dominate the flow.

- *Buffer sublayer* with the lower and upper borders at $y^+ = 5$ and $y^+ = 50$–$70$, respectively, represents the transition zone between viscous and logarithmic regions. In this layer both viscous and inertial forces are important.

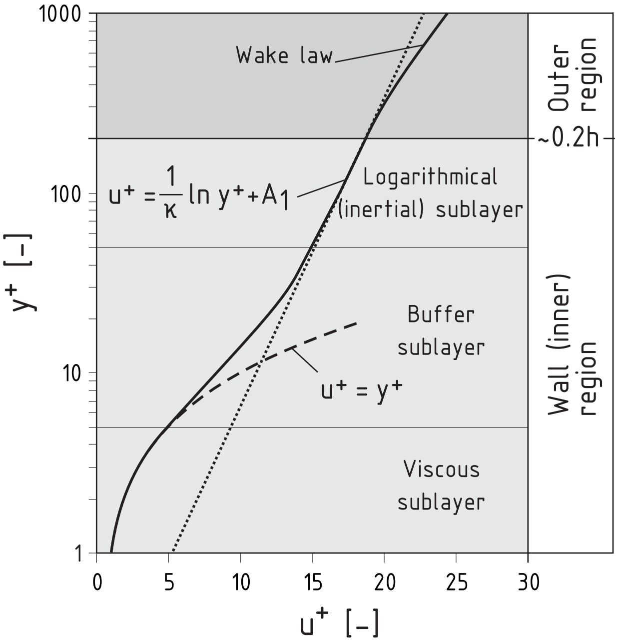

**Figure 3.7:** Layers of a turbulent velocity profile over smooth bed (note a logarithmic scale of the ordinate axis), from Bezzola [8]

- The *logarithmical sublayer* stretching from the $y^+ = 50\text{–}70$ to $y \approx 0.2h$ is described by Equation 3.22. Inertial forces override the viscosity ones here.
- Velocity distribution in the *outer region* also follows the logarithmical distribution, but needs a correction. This is commonly done with the help of the so called *wake function* after Coles [10].

### 3.3.2 Rough bottom

For rough walls, $y_0$ should be proportional to the size of roughness elements $k_s$. With $y_0 = \beta\, k_s$, Equation 3.19 yields:

$$\frac{\overline{u}(y)}{u_*} = \frac{1}{\kappa}\, \ln \frac{y}{k_s} - \frac{1}{\kappa}\, \ln \beta \tag{3.24}$$

Experiments of Nikuradse [58] with rough pipes reveal the general applicability of the logarithmical velocity distribution law also for flows over rough beds. Depending on the grain Reynolds number:

$$Re_* = \frac{k_s\, u_*}{\nu} \tag{3.25}$$

and notifying:

$$C_1 = -\frac{1}{\kappa}\ \ln\beta$$

the following flow regimes can be distinguished:

**Hydraulically smooth:** $Re_* \leq 5$

In this regime, roughness elements are much smaller than the thickness of a viscous sublayer and do not affect the velocity distribution in the log-sublayer. Function $C_1$ takes a linear form:

$$C_1 = \frac{1}{\kappa}\ \ln(Re_*) + 5.5,$$

which basically gives us the formula for the velocity distribution over smooth bed, obtained already in Section 3.3.1. Thus, the value of constant $A_1$ in Equation 3.22, as determined by Nikuradse, equals 5.5.

**Transitional:** $5 \leq Re_* \leq 70$

Roughness tops protrude the laminar sublayer and the velocity distribution in the log layer is affected by viscosity as well as bottom roughness. The near bottom region is characterized by a spatial and temporal alternation of turbulent and laminar flow and according to Zanke [100] can be described using a stochastic approach. The function $C_1$, adjusted to give the best fit to Nikuradse's measurement data, is given then by:

$$C_1 = C_{1s} * P_s + C_{1r} * P_r,$$

with $C_{1s} = \frac{1}{\kappa}\ \ln(Re_*) + 5.25$ = function $C_1$ for a hydraulically smooth regime, [-]
$C_{1r} = 8.5$ = function $C_1$ for a hydraulically rough regime, [-]
$P_s = 1 - P_r = e^{-0.08Re_*}$ = probability that the flow is in a hydraulically smooth regime, [-]
$P_r$ = probability that the flow is in a hydraulically rough regime, [-]

**Hydraulically rough:** $Re_* > 70$

Roughness elements protrude even higher and the velocity distribution in the log layer is not affected by fluid viscosity. At this regime, the function $C_1$ is a constant equal to 8.5.

Thus, in the hydraulically rough regime relevant for flows in natural channels, the logarithmical velocity distribution takes the form:

$$\boxed{\frac{\overline{u}(y)}{u_*} = \frac{1}{\kappa} \ln \frac{y}{k_s} + 8.5 \qquad (3.26)}$$

| | | | | |
|---|---|---|---|---|
| with | $\overline{u}(y)$ | = | mean velocity along $x$-axis, | [m/s] |
| | $u_*$ | = | shear velocity, | [m/s] |
| | $\kappa$ | = | von Kármán constant, | [-] |
| | $y$ | = | vertical coordinate, | [m] |
| | $k_s$ | = | hydraulic roughness height, | [m] |

Special attention in the application of Formula 3.26 should be given to the values of roughness height $k_s$ and the constant $C_1$. In experiments of Nikuradse, roughness is constructed by gluing grains to the wall at a density as high as possible and the value of $k_s$ is set equal to the mean diameter of the grain material $k$. As the influence of $k_s$ and $C_1$ in the log law is interchangeable, the value of a constant $C_1 = 8.5$ corresponds to Nikuradse's "maximum density" roughness. The value of a roughness height satisfying Equation 3.26 along with $C_1 = 8.5$ is called hydraulic or *equivalent* roughness height and in general differs from the *geometrical* roughness height $k$. Thus, also the following expression is valid:

$$\frac{\overline{u}(y)}{u_*} = \frac{1}{\kappa} \ln \frac{y}{k} + C_1 \qquad (3.27)$$

Determination of the equivalent roughness height $k_s$ stays in connection with the determination of the origin of the logarithmical profile and the shear velocity and will be described in the next section.

## 3.4 Methods for determination of bottom shear stress

In practice, the determination of the bottom shear stress $\tau_0$ related to a shear velocity $u_*$ via Expression 3.15 is hampered by the fact, that neither the equivalent roughness $k_s$ nor the origin of the logarithmical velocity profile are known in advance.

The following approach can be applied for the determination of the quantities in Equation 3.26 and also of the bottom shear stress $\tau_0$ if the velocity profile data is available:

1. At first, the origin of the logarithmical velocity profile is assumed to be at the level of the roughness tops.

2. By adding successive offsets $\Delta y_0$ to the water depth $h$ above the roughness tops, the best log-linear fit to the velocity profile is found (see Formula 3.27). The best regression coefficient and corresponding $\Delta y_0$ define the origin of the logarithmical velocity profile.

3. Using Equation 3.27 and measured velocity values at two elevations with adjusted ordinates, the shear velocity $u_*$ and consequentially the bottom shear stress $\tau_0$ can be found from:
$$\frac{u_1 - u_2}{u_*} = \frac{1}{\kappa}\left(\ln\frac{y_1}{k} - \ln\frac{y_2}{k}\right) \implies u_* = \kappa\,\frac{u_1 - u_2}{\ln(y_1/y_2)} \implies \tau_0 = u_*^2\,\rho \quad (3.28)$$
Here, only points lying inside the inertial sublayer should be taken (with ordinates $y < 0.2\ h$), as only there the log law is applicable.

4. Assuming appropriate value of the geometrical roughness height $k$ (for example, the mean grain diameter) and knowing the shear velocity $u_*$, the constant $C_1$ can be found from Formula 3.27 by:
$$C_1 = \frac{u_1}{u_*} - \frac{1}{\kappa}\ln\left(\frac{y_1}{k}\right) \quad (3.29)$$

5. Using the difference between Equations 3.26 and 3.27, the equivalent roughness height $k_s$ can be found through:
$$\frac{1}{\kappa}\ \ln(k/k_s) = C_1 - 8.5 \implies k_s = \frac{k}{\exp(\kappa\,(C_1 - 8.5))} \quad (3.30)$$

This method is applicable for flows with large relative submergences and small roughness heights. However, according to Bezzola [8], for flows over rough beds with small relative submergence the value of the equivalent roughness height $k_s$ in Nikuradse's formula is not a constant but changes with $h/k_s$. Thus, if $k_s$ is found for a particular substrate configuration at one flow situation, no estimate for the bottom shear stress can be done for the same substrate at another flow situation without measuring the velocity profile again.

Often not the vertical velocity distribution in a channel but the bottom shear stress is of interest. Then, under assumption of a steady uniform flow, Expression 3.7a can be used for the estimation of $\tau_0$ [14]. The right part of the equation expresses the total shear stress divided by a fluid density. Thus, if the channel slope is small:

$$g\ \sin\alpha(h - y) = \nu\frac{\partial \overline{u}}{\partial y} - \overline{u'v'} = \tau_0/\rho \implies \tau_0 = \rho\,g\,i_0\,h \qquad [\mathrm{N/m^2}] \quad (3.31)$$

with $\tau_0$ = bottom shear stress, $[\mathrm{N/m^2}]$
$\rho$ = density of fluid, $[\mathrm{kg/m^3}]$
$g$ = acceleration due to gravity, $[\mathrm{m/s^2}]$
$i_0 = tg\alpha \approx sin\alpha$ = slope of a channel, [-]
$h$ = water depth, [m]

This formula gives the same result as the described above method via velocity profile if the water depth $h$ in it corresponds to those measured from the origin of the log profile[1]. For

---

[1] if its position would be known

flows with large relative submergence it gives good estimate of $\tau_0$, as the relation $h/(h+\Delta y_0)$ is close to one.

Flows over rough substrates are generally characterized by the presence of the so called *roughness sublayer* in which turbulent shear stress distribution deviates from those over smooth bed (see Sections 3.5, 3.6). Within this layer $\tau_t$ stays constant or even reduces towards substrate tops. The thickness of the roughness sublayer is of the order of magnitude of geometrical roughness height. Thus, for flows with small relative submergence, $\tau_0$ estimated with Formula 3.31 would not reflect properly the force experienced by the substrate material, even with the known position of the log profile origin.

## 3.5 Distributions of turbulent intensity and turbulent shear stress

Turbulent intensity, the root-mean-squared (rms) value of a velocity fluctuation, represents a measure for the turbulence level of a flow. As, in general, the turbulence is not isotropic, turbulent intensities $\sqrt{\overline{u'^2}}$, $\sqrt{\overline{v'^2}}$ and $\sqrt{\overline{w'^2}}$ are defined for every component of a velocity vector.

Figure 3.8a shows distributions of longitudinal and transverse turbulent intensities for a flow in a wind channel with a smooth bottom. The longitudinal intensity is larger and has a more expressed maximum than the transverse one. In Figure 3.8b, distributions of $\overline{u'v'}$ and total shear stress $\tau/\rho$ for the same channel are shown. Apparent is, that the turbulent shear stress distribution, measured by a hot-wire anemometer, coincides with the total shear distribution, obtained through the pressure distribution, almost over the whole channel depth. Only near the wall it reduces to zero. Also, the correlation coefficient $\psi$ between the longitudinal and transverse pulsation components is shown. It is defined as:

$$\psi = \frac{\overline{u'v'}}{\sqrt{\overline{u'^2}}\,\sqrt{\overline{v'^2}}} \qquad [-] \qquad (3.32)$$

and reaches a maximum value of 0.45 near the solid boundary.

For two dimensional flows over hydraulically smooth beds, Nezu and Nakagawa [57] give following empirical dependencies for normalized turbulence intensity distributions:

$$I_x = \frac{\sqrt{\overline{u'^2}}}{u_*} = 2.30\, e^{(-\frac{y}{h})} \qquad [-] \qquad (3.33a)$$

$$I_y = \frac{\sqrt{\overline{v'^2}}}{u_*} = 1.27\, e^{(-\frac{y}{h})} \qquad [-] \qquad (3.33b)$$

$$I_z = \frac{\sqrt{\overline{w'^2}}}{u_*} = 1.63\, e^{(-\frac{y}{h})} \qquad [-] \qquad (3.33c)$$

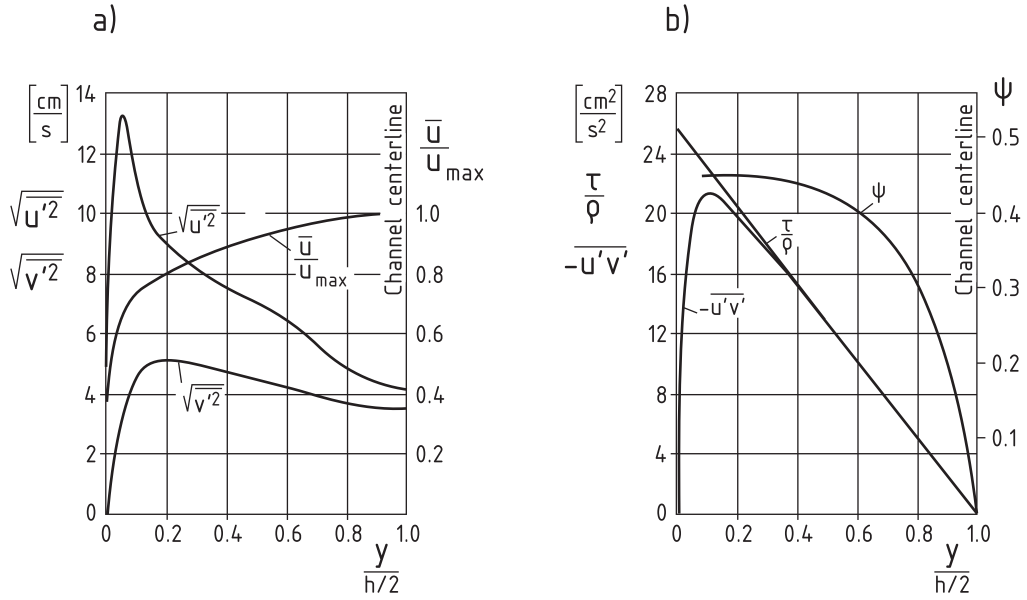

**Figure 3.8:** Distributions of: a) longitudinal $\sqrt{\overline{u'^2}}$ and transverse $\sqrt{\overline{v'^2}}$ turbulent intensities; b) product $\overline{u'v'}$, total shear stress $\tau/\rho$ and correlation coefficient $\psi$ in a wind channel, from experiments of Reichardt referenced in [70]

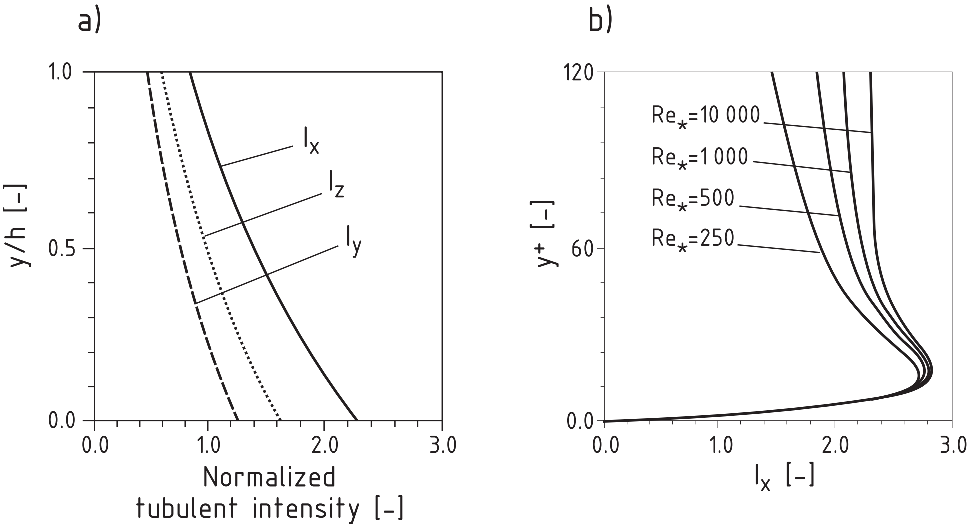

**Figure 3.9:** a) Empirical functions of normalized turbulent intensity distributions, Equations 3.33a-c; b) Distribution of a normalized longitudinal turbulent intensity in the proximity to a wall

According to these expressions, the normalized turbulent intensity in the longitudinal direction is the largest, followed by transverse and vertical components (see Figure 3.9a). The ratios $I_x/I_y$ and $I_x/I_z$ stay constant almost over the whole water depth.

Near the bottom (below $y^+ = 70$), distributions of turbulent intensities deviate from the dependencies 3.33a–c. There, the turbulent intensity slightly increases, showing a maximum approximately at $y^+ = 17$, and then decreases to zero at the boundary (see distributions of normalized longitudinal intensity $I_x$ for different $\mathrm{Re}_* = h\,u_*/\nu$ in Figure 3.9b).

While for a rough bed distributions of turbulent intensities at a distance from the bottom coincide with those for a smooth bed, they show quite a different behavior near a wall. Flow separation from roughness elements results in intensive mixing and therefore less pronounced inhomogeneity of turbulence. Thus, components of velocity fluctuations differ less than in case of a smooth bed [8]. Under influence of flow separation from roughness elements, the so called *roughness sublayer* is formed. Its thickness is comparable with the geometrical size of roughness elements. Therefore, at small relative submergences and a very rough bottom, it is of the order of magnitude of the water depth. Laboratory and field measurements show, that the thickness of the roughness sublayer is independent from the relative submergence and is just a function of the size and arrangement of roughness elements. Within the roughness sublayer, turbulence intensities remain the same or get smaller gradually towards roughness tops (see Figure 3.10). In this figure $k$ is the grain diameter, $y$ is the distance from and $h$ is the water depth above the mean elevation of the roughness tops.

## 3.6 Modified velocity distribution law of Bezzola

Flows over rough beds are characterized by the presence of a roughness sublayer which thickness is comparable to the size of roughness elements. The distribution of turbulent shear stress in this layer deviates from those for flows over smooth beds. Within this layer $\tau_t$ stays constant or even reduces towards roughness tops. The suppression of turbulent stresses in a roughness sublayer can be explained as a consequence of small secondary flows caused by flow separation from the individual grains [8]. With decreasing relative submergence, the proportion of stresses due to these small-scale flows in total shear increases. The damping of turbulent shear stresses at low relative submergence results in a disproportionate reduction of flow velocity in the near-bed area.

The new model of Bezzola [8] for the velocity distribution over rough beds tries to integrate the above illustrated features of flows with small relative submergence. It is based on Prandtl's mixing length concept (Section 3.2.4) and assumes, that not the total shear stress, but only its portion related to the turbulent stress controls the mean motion. The thickness

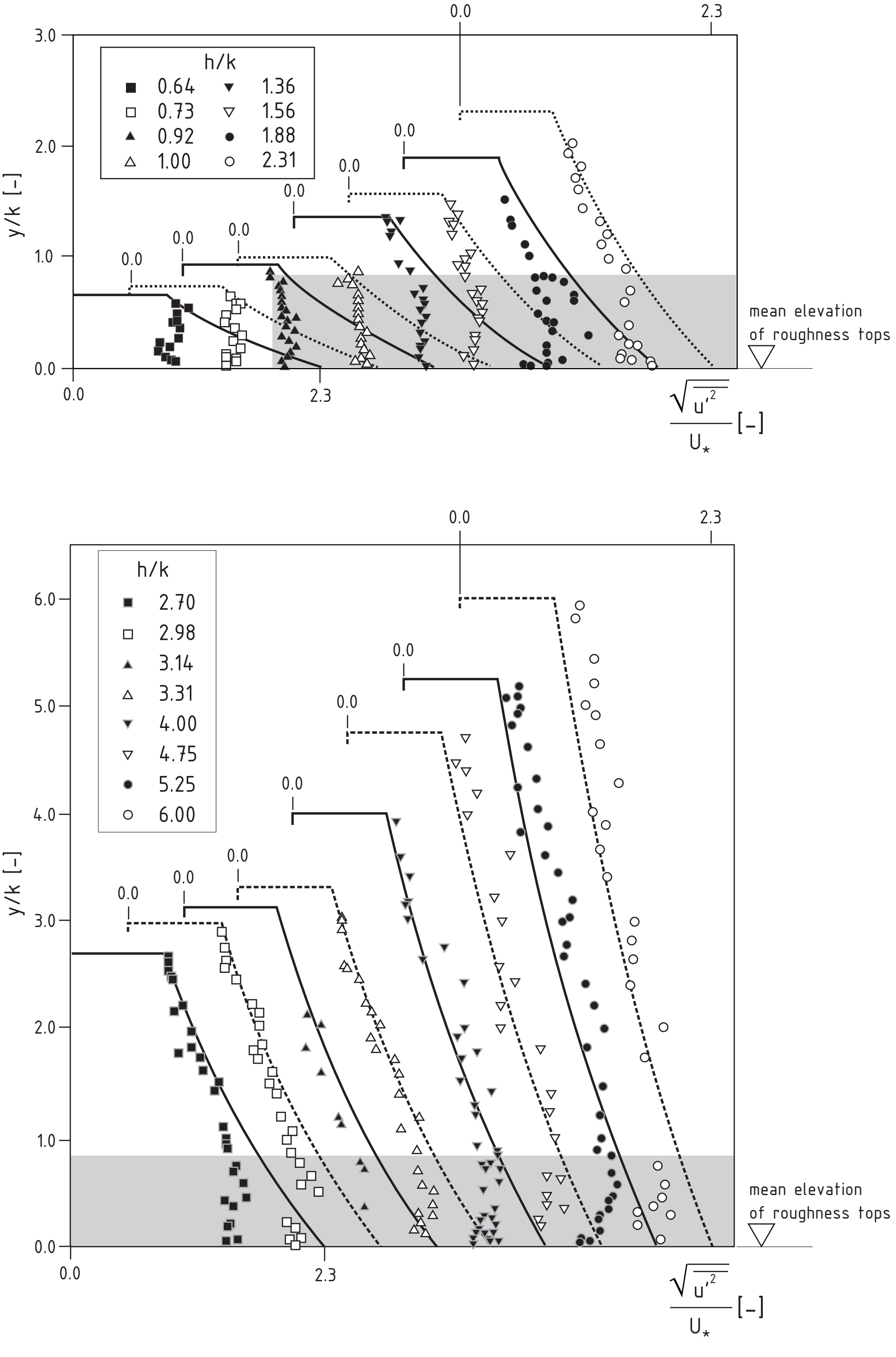

**Figure 3.10:** Turbulent intensity distributions over bottom covered with one layer of uniform grain material with a grain diameter k in comparison to the empirical function 3.33a, from Dong et al. [17]. The zero of the abscissa is shifted for every profile to show all of them on one figure

of the roughness sublayer $y_r$ as a roughness parameter is introduced. As an additional parameter, the thickness of an inner region $y_w$ is adopted. It allows to adjust the distribution of the mixing length $l$ according to experimental data and to avoid the modification of the logarithmical velocity distribution in the outer region with the wake-function approach after Coles [10]. The geometrical definitions are depicted in Figure 3.11. The model is applicable for rivers and creeks with maximum mean longitudinal slopes of 6 % and cannot account for such bed features as steps and cascades, common for streams with larger gradients.

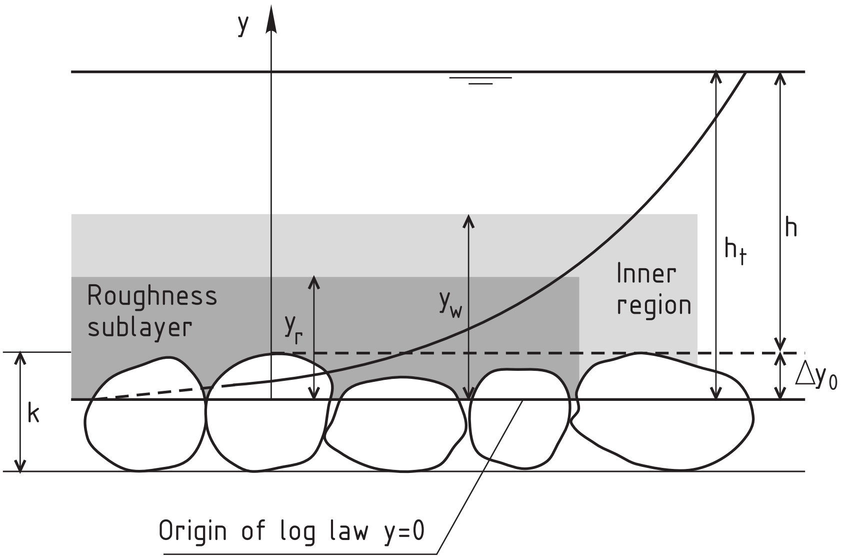

**Figure 3.11:** To the definition of roughness sublayer and inner region thickness

In the derivation of the new model, the author assumes a constant value of the turbulent shear stress $\tau_t$ within the roughness sublayer. Outside of this region, the turbulent shear stress $\tau_t$ is equal the total shear stress $\tau$. At the wall, the value of $\tau_t$ is related to the bottom shear stress $\tau_0$ through the introduction of a damping factor $c_r$ (see Figure 3.12):

$$c_r^2 = \frac{\tau_t}{\tau_0} = \frac{\rho\,\overline{u'v'}}{\rho\,u_*^2} \tag{3.34}$$

Two cases are differentiated in the concept of this model: large and small relative submergence (Figure 3.13). For the former it is assumed, that the thickness of the roughness sublayer and consequentially the size of the eddies within is small in comparison to the total water depth $h_t$ and eddies in the outer region. Here, the thickness of the inner region is larger than that of the roughness sublayer. For the latter, the thickness of the inner region $y_w$ is equal to the thickness of the roughness sublayer $y_r$.

Velocity distribution in Bezzola's model is given by following formulas:

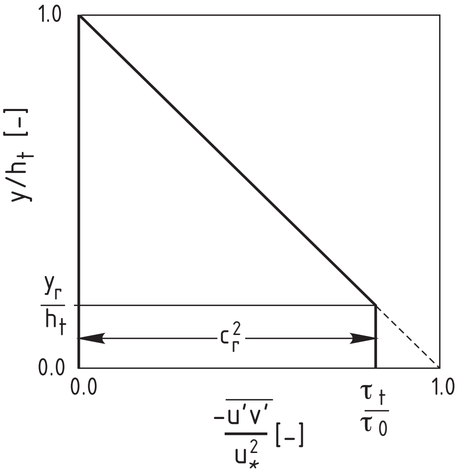

**Figure 3.12:** Approximation of the dimensionless turbulent shear stress distribution, from Bezzola (2002) [8]

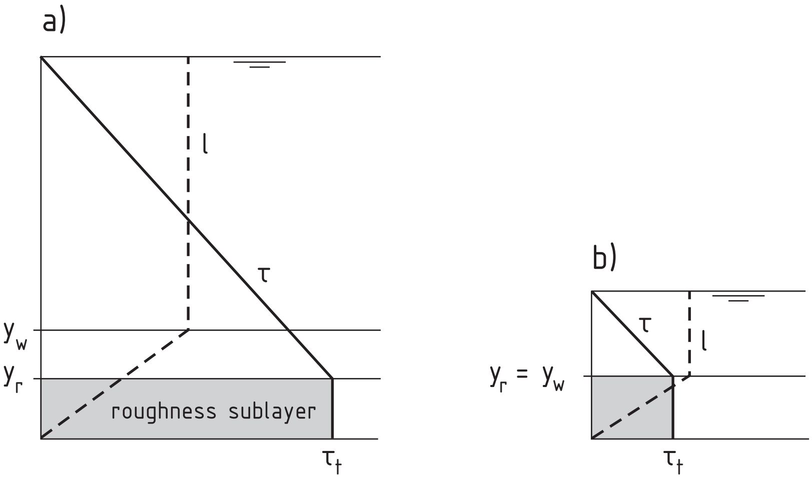

**Figure 3.13:** Distribution of the turbulent shear stress and mixing length in the case of large (a) and small (b) relative submergence, from Bezzola (2002) [8]

$$\boxed{\begin{aligned}
&\frac{\overline{u}(y)}{u_*} = c_r\left(\frac{1}{\kappa}\ln\frac{y}{y_r} + 8.48\right) \qquad \text{for} \quad y \leq y_w &&\text{(3.35a)}\\
&\frac{\overline{u}(y)}{u_*} = c_r\left(\frac{1}{\kappa}\ln\frac{y_w}{y_r} + 8.48\right) + \frac{2}{3}\frac{h_t}{\kappa y_w}\left[\left(1-\frac{y_w}{h_h}\right)^{\frac{3}{2}} - \left(1-\frac{y}{h_t}\right)^{\frac{3}{2}}\right] \qquad \text{for} \quad y > y_w &&\text{(3.35b)}
\end{aligned}}$$

with $\overline{u}$ = mean velocity along x-axis, [m/s]
$u_*$ = shear velocity, [m/s]
$c_r$ = damping factor, [-]
$\kappa$ = von Kármán constant, [-]
$y$ = vertical coordinate, [m]
$y_r$ = thickness of roughness sublayer, [m]
$y_w$ = thickness of inner region, [m]
$h_t$ = total water depth, [m]

In Equations 3.35a,b, the damping factor $c_r$ is defined as follows:

$$c_r^2 = 1 - \frac{y_r}{h_t} \qquad \text{for} \quad \frac{h_t}{y_r} > 2 \tag{3.36a}$$

$$c_r^2 = 0.25\,\frac{h_t}{y_r} \qquad \text{for} \quad 0 \leq \frac{h_t}{y_r} \leq 2 \tag{3.36b}$$

It should be noted, that at large relative submergences the part of Equations 3.35 responsible for the velocity distribution in the log-region is identical to those of Nikuradse.

The thickness of the inner region is differentiated for cases of large and small relative submergence:

$$y_w = h_t \qquad \text{for} \qquad \frac{h_t}{y_r} \leq 1 \tag{3.37a}$$

$$y_w = y_r \qquad \text{for} \qquad 1 < \frac{h_t}{y_r} \leq 3.2 \tag{3.37b}$$

$$y_w = 0.31\ h_t \qquad \text{for} \qquad \frac{h_t}{y_r} > 3.2 \tag{3.37c}$$

Comparison with existing data from laboratory and field measurements confirm the application of the Bezzola's model. In particular, the thickness of the roughness sublayer proves to be independent from relative submergence. This allows determination of the explicit roughness values for a particular substrate type. Following recommendations for the thickness of the roughness sublayer are given in the work. For relatively even beds of grains with uniform mean diameter (one-layer of elements on a plane) $y_r/k \approx 1$. For multi-layer beds of grains with similar mean diameter or natural substrates, the exposition of elements is not so uniform anymore, and $y_r/k \approx 1.5$–$2$.

One problem also typical for the application of the Nikuradse's log law – identification of the velocity profile origin – is not completely solved. In comparisons with existing data, the value of the zero level displacement $\Delta y_0$ is in the range of 0.1–0.4$y_r$, with a mean value of 0.25$y_r$.

Surely, this model is not the only one among the new approaches especially developed for cases of flow over rough bed and integrating the concept of a roughness sublayer (see for example developments in [44]). The considerable advantages of this new approach are however:

- Solely founded on Prandtl's mixing length concept;
- integration of experimental evidence on distributions of turbulent intensities and shear stress over rough beds;
- keeping constant the universal number of the turbulent flow $\kappa$ and the constant $C_1$ at values 0.4 and 8.48, respectively;
- no need for additional theories (wake-function after Coles) to adjust the velocity profile in the outer region.

The model of Bezzola has an important implication for the assessment of sediment stability, or of the incipient motion of the body placed on the river bed such as an FST-hemisphere. The damping factor $c_r$ in the velocity distribution equations 3.35 accounts for the reduction of the relative near-bed velocity with decreasing relative submergence. As the flow force acting on a sediment grain is proportional to the square of the near-bed velocity, not accounting for the flow velocity reduction for small relative submergences would lead to the overestimation of the stress on the sediment. Thus, a more realistic value of shear stress acting on the bottom is provided by $\tau = \tau_t = c_r^2\, \rho\, u_*^2$, corresponding in its dimensionless form to the Shield's parameter $\theta$ (see also Section 4.3.2). The factual influence of relative submergence is supported by different experimental data [8]. The theoretical support can be found also in the analytical formulation of Zanke [101], [102] for the initiation of sediment motion.

The concept of Zanke presupposes that the critical shear stress responsible for inducing a sediment motion in a hypothetical "non-turbulent" flow is solely defined by the angle of internal friction or the angle of repose of single grains. In reality, sediment transport is only possible when the flow is turbulent. In turbulent flows the shear stress is not constant but fluctuates, and owing to this, the actual (effective) shear stress on a grain is larger than the time averaged stress. Additionally, turbulence-induced lift forces, which are mainly attributable to the coherent structures of the flow in the proximity to the bed, result in the reduction of the effective weight of grains. Accounting for these effects of turbulent flow the dimensionless time-averaged critical shear stress for natural sediments (approx. 30% porosity) is given by:

$$\theta_c = \frac{\tau_0}{(\rho_s - \rho_w)\ g\ d_s} = \frac{\rho_w\, u_*^2}{(\rho_s - \rho_w)\ g\ d_s} = \frac{0.7\ \tan\phi}{(1+\frac{u'_{c,b}}{u_b})^2\ (1+\frac{\sigma_L}{\tau_0}\ \tan\phi)} \qquad [-] \qquad (3.38)$$

with $\theta_c$ = dimensionless critical shear stress, [-]

$\tau_0$ = bottom shear stress, [N/m$^2$]

$\rho_s, \rho_w$ = density of a grain and water, respectively, [kg/m$^3$]

$u_*$ = shear velocity, [m/s]

$d_s$ = diameter of a grain, [m]

$g$ = acceleration due to gravity, [m/s$^2$]

$\phi$ = angle of internal friction, [°]

$u'_{c,b}$ = instantaneous magnitude of fluctuating velocity at the bed, responsible for the initiation of motion, [m/s]

$u_b$ = velocity at the bed, [m/s]

$\sigma_L$ = lift stress acting on the grain, [N/m$^2$]

Analysis for the relation $\frac{u'_{c,b}}{u_b}$ in the above formula shows the dependency from relative submergence, which disappears for $h/d > 100$. Therefore, application of Zanke's formulation for the assessment of the critical shear stress in conjunction with influence of the relative submergence shows, similar to the Bezzola's model: with decreasing relative submergence the critical shear stress for initiation of sediment movement increases (i.e. the load on the bed reduces for otherwise constant conditions).

## 3.7 Summary

Turbulent flows over rough beds with small relative submergences are characterized by the presence of a roughness sublayer. The vertical distribution of the turbulent shear stress for such flows deviates from the linear one typical for flows with large relative submergence. Within the roughness sublayer, the turbulent stress is either constant or even reduces towards the bed. Damping of turbulent shear stress in this area has an influence on the mean flow expressed through the disproportionate reduction of the near-bed velocity.

The new model of Bezzola for mean flow velocity distribution accounts for the presence of a roughness sublayer in flows over rough beds. The particular value of the new approach is, that the thickness of the roughness sublayer $y_r$ proves to be a unique property of a particular substrate size and configuration, and is independent from the relative submergence. This feature makes it very attractive for determination of near-bed velocities from the mean flow quantities obtained from measurements or via two-dimensional hydrodynamic modelling.

One of the case studies tasks in the present work is to test for the applicability of the model in field conditions, i.e. to check, how well the predicted near-bed velocity corresponds to the measured one.

# 4 FST-hemispheres method: myth and reality

Since the introduction of FST-hemispheres by Statzner and Müller (1989) [88], many pros and cons of the method appeared in the literature. The authors of the method hypothesized, that for some benthic organisms, which can be used as target species in environmental flow assessment studies, hydraulic stress appears to be a major factor determining their distribution and abundance. FST-hemispheres had to replace more sophisticated and lengthy techniques used for the determination of bottom shear stress and grain Reynolds number in ecological studies. The method was widely advertised as capable to measure bottom shear stress. Before clarifying this question, a massive, Germany-wide biological measurement program was initiated and resulted in 53 standardized (river site independent), FST-based preference curves for macrozoobenthos species [20].

Unfortunately, later studies revealed, that an unique correlation ”FST-density vs. bottom shear stress” does not exist. Although most correlation curves show a theoretically expected linear dependency, the curve slope is highly dependent on substrate characteristics [16], [69]. Some researches have started to question the general eligibility of the FST method for the characterization of benthos habitat [24], pointing out, that the size of the FST-hemisphere is one or two orders of magnitude above that of most benthic organisms. Technical application problems of the original FST equipment together with restrictions on water depths (arm length) and special substrate kinds (plate placement problems on muddy, but also on monolith rock river bottom) caused additional criticism. The method, generally accepted by biologists for the establishment of preference curves, causes nowadays great distrust among habitat modelers, forced to flounder about in the water in winter and in summer with the aim to collect hundreds of FST-measurements for the characterization of a river reach at different discharges. An attempt to avoid extensive measurements by establishing a unique, river site independent correlation of FST-hemisphere numbers (densities) to any conventional physical variable did not succeed either.

In this chapter, the original FST method, together with its modifications, is thoroughly reevaluated as a tool for the assessment of near bottom hydrodynamics. A great deal of attention is devoted to the correlation curves of the hemispheres to flow velocity and bottom shear stress as they, in an empirical way, can give valuable hints for the understanding of the

FST measurement principle. The formula for the hemisphere's movement condition based on the force balance is given. Furthermore, the possibility of calculating FST-hemisphere number distributions by means of this formula is discussed.

## 4.1 FST-hemispheres: state-of-the-art

### 4.1.1 Original method

FST-hemispheres have been proposed by Statzner and Müller [88] as a method for rapid characterization of near bottom flow conditions and, consequentially, for the assessment of the forces acting on benthos organisms. The mysterious abbreviation "FST" stems from the name "Fließwasserstammtisch" (regulars' table) of colleagues from stream teams in Konstanz, Lunz, and Schlitz, where first discussions of the method took place.

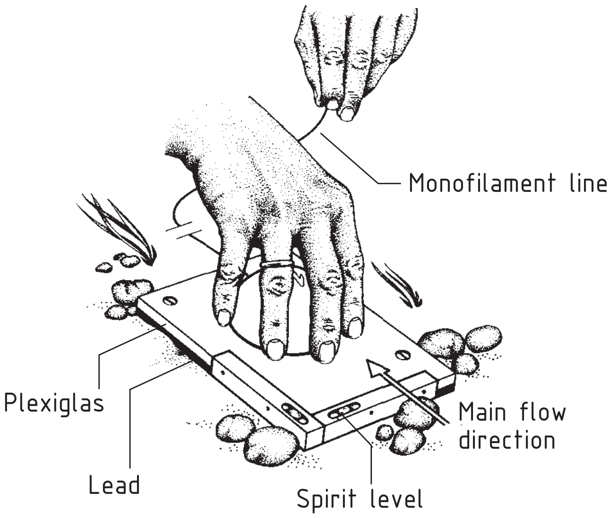

**Figure 4.1:** Original FST-hemisphere placement method, from Statzner and Müller (1989) [88]

The original measurement equipment consists of 24 hemispheres with identical radius $r_h$ = 3.9 cm but different densities (see Table 4.1) and a smooth plexiglas ground plate with dimensions of 13×18×0.8 cm. The uneven increase in density is needed to ensure a high resolution in the range of small flow forces. The standard field procedure is as follows. The plate is placed in a shallow horizontal pit dug with a foot or a shovel in the stream bottom and the hemispheres, one by one are exposed, to the current (see Figure 4.1). The number of the heaviest hemisphere just moved by the given flow is used as the result of the measurement. If the lightest hemisphere does not move, the measurement point is assigned the fictive FST number "0".

| FST N° | Density | FST N° | Density | FST N° | Density | FST N° | Density |
|---|---|---|---|---|---|---|---|
| - | g/cm$^3$ | - | g/cm$^3$ | - | g/cm$^3$ | - | g/cm$^3$ |
| 1 | 1.015 | 7 | 1.274 | 13 | 2.637 | 19 | 5.460 |
| 2 | 1.031 | 8 | 1.439 | 14 | 2.987 | 20 | 6.166 |
| 3 | 1.063 | 9 | 1.624 | 15 | 3.361 | 21 | 6.958 |
| 4 | 1.095 | 10 | 1.834 | 16 | 3.795 | 22 | 7.854 |
| 5 | 1.129 | 11 | 2.070 | 17 | 4.284 | 23 | 8.867 |
| 6 | 1.199 | 12 | 2.337 | 18 | 4.836 | 24 | 10.009 |

**Table 4.1:** FST-hemisphere numbers and corresponding densities

As difficulties existed in discrimination of the hemisphere moved in the range of small density increments, the following release procedure was recommended to ensure the reproducibility of the method. The hemisphere is held with one hand slightly above the plate, with a wire loop facing downstream and a monofilament line loosely connected to the other hand. Then, the upstream edge of the hemisphere is brought into contact with the plate, and the hemisphere is allowed to drop down between the fingers completely to the plane, i. e. it is not pressed down on the plate. The hand is then slowly removed from the water. Short hemisphere movements (less than about 2 cm) during this phase are considered as artifacts and neglected.

Positioning the ground plate on sandy-gravel substrates is straightforward. With growing substrate size, however, difficulties concerning the arrangement of the plate's surface levelled with the tops of roughness elements arise, as it is difficult to estimated the mean bottom level in this case.

The use of the FST-hemispheres method "should ideally be as simple as the use of a thermometer, so that complex hydraulics can be as easily evaluated as temperature" [88]. Although not going into detail of the method's underlying physics, the authors reckon that forces responsible for the hemisphere's movement in a flow field are drag and lift forces (see Section 4.2) and the hemisphere's movement condition should be related to the bottom shear stress.

### 4.1.2 Modification of the measurement equipment, "new" standard method

Two major weak points hamper the application of the original FST-hemispheres method. The first one concerns the hemispheres' placement method described in Section 4.1.1. With the original method as well as its modifications (Figure 4.2), the hand of the user is immersed in water when a hemisphere is released to the flow. This results in a modification of the flow field, which at some extent is also dependent on the hand's size. This effect is expected to be more pronounced at conditions of subcritical flow and low absolute velocities. The second weak point, referenced by some authors [36], [15], is the texture of the hemispheres and the ground plate. Originally, they both have smooth surfaces. Thus, if during release an FST-hemisphere is pressed too hard against the plate, it occasionally sticks to the plate due to a water film. If released too early, however, even heavy hemispheres easily slide away. Thus, the old equipment is characterized by a very strong effect of the placement method and, consequentially, poor reproducibility of the measurements.

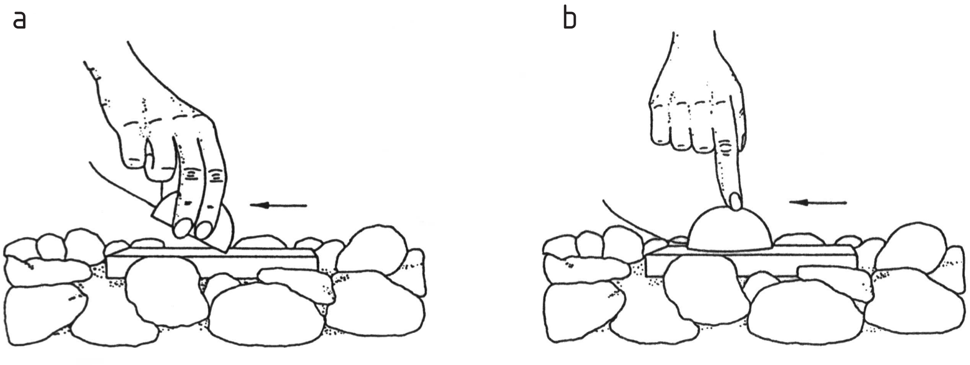

**Figure 4.2:** Variants of the original FST placement method: a. “drop” (“kippen” - German); b. “press” (“drücken” - German), from Heilmair and Strobl (1994) [36]

The work of Scherer (1999) [69] is partly devoted to the elimination of the above mentioned technical deficiencies. The first problem is fixed by the introduction of a pair of pins which are used for a preliminary fixation of hemispheres on the plate. The flow field disturbance due to the hand is therefore eliminated as the pins are put away by the distance controlled mechanism.

To reduce the adhesive/sliding effects, Scherer tests and compares the performance of the original smooth and four other plates with differently structured surfaces. He measures the friction coefficient between these and the hemispheres with an automatic tilting facility which registers the start of hemisphere movement using a light barrier. An expected improvement of structured plates in comparison to the smooth one would show in the reduction of the scatter in friction coefficient. Surprisingly, an analysis of his experimental data shows, that there is no significant difference in the absolute minimum and maximum and also the spread of friction coefficients for structured plates and the old, smooth plate (see Table 4.2).

Nevertheless, Scherer refers to the structured plate N°4 with pyramidal elements of 2 mm height as the best performing one. This plate, supplied with the distance controlled pins, is recommended for future use in [20].

| Plate N° <br> - | Description | $\alpha_{min}$ <br> ° | $\alpha_{max}$ <br> ° | $\mu_{min}$ <br> - | $\mu_{max}$ <br> - |
|---|---|---|---|---|---|
| **1** | **Original smooth** | 19.9 | 34.7 | **0.36** | **0.69** |
| 2 | Structured cuboid elements with height 1 mm | 18.4 | 27.9 | 0.33 | 0.53 |
| 3 | Structured pyramidal elements with height of 1 mm | 17.2 | 31.5 | 0.31 | 0.61 |
| **4** | **Structured pyramidal elements with height of 2 mm** | 18.0 | 34.0 | **0.32** | **0.67** |
| 5 | Structured pyramidal elements with height of 3 mm | 18.8 | 33.2 | 0.34 | 0.65 |

**Table 4.2:** Sliding angles and corresponding friction coefficients for the smooth and the structured plates, from Scherer (1999) [69]

### 4.1.3 Transferability of results between old and new method

Experiments in the laboratory and in the field are conducted to compare the performance of old and new plates [69]. This aspect is very important, because the standardized preference curves listed in [20] are obtained with the old method as described by Statzner and Müller [88]. However, for future use, the structured plate suggested by Scherer is recommended. The transferability formula is given in [20] as:

$$\mathsf{FST}_{new} = \mathsf{FST}_{old} - 1 \tag{4.1}$$

For habitat modelling purposes, either the standardized preference curves or the FST measurements – if conducted using the new equipment – have to be adjusted according to Expression 4.1. This adjustment will result consequentially in the appearance of an FST number "-1" in the preference curves or elimination of FST number "0" in field measurement results. This actually means, that the new method has a lower resolution in the range of small flow velocities than the old one, what can have some consequences for habitat modelling for limnobiotic stenokous species (exclusively standing water inhabitants).

In the majority of laboratory measurements, FST-numbers registered with the new method are smaller than those with the old method. This trend, but also the spread of values, remains for measurements at different water depths, mean column velocities, substrate sizes and vertical positions of the plate within a velocity profile (see Figures 4.3, a-d). It is apparent from these results, that the mean difference between measurements with the old and the new method is larger than 1 FST number and comprises about 2 to 4 FST numbers. For field measurements, the difference comprises in fact 1 FST number (see Figure 4.4 where also Scherer's laboratory measurements are shown). Thus, depending on the institution which conducted the comparison test, the mean difference between the old and the new methods ranges from 1 to 4 FST numbers, presumably reflecting the differences in the placement techniques used by the particular surveyors.

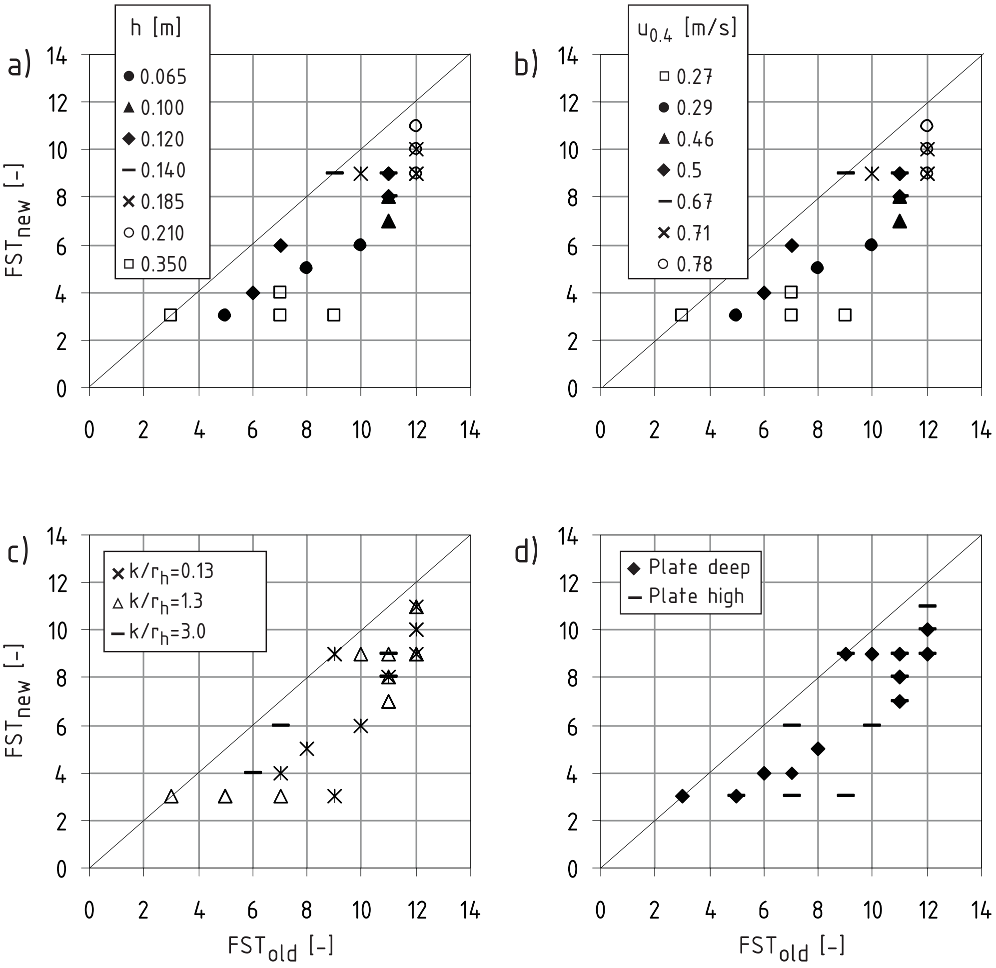

**Figure 4.3:** Comparison of measurements with the old and the new method at different: a) water depths; b) mean column velocities; c) substrate size to hemisphere radius relations; d) vertical positions in velocity profile, from Scherer (1999) [69]

## 4.2 Equilibrium of forces on a hemisphere in a velocity profile

Let us consider the system of forces acting on the FST-hemisphere placed on a river bottom (see Figure 4.5).

The forces here are: *hydrodynamic force* $F_h$ resulting from fluid motion around the hemisphere; *friction force* $F_f$ acting between the hemisphere and the plate; and *immersed weight* $F_g$ of a hemisphere in water. It is common to split the net hydrodynamic force into *drag* – the component along, and *lift* – the component perpendicular (or normal) to the direction of the undisturbed fluid flow. Two equilibrium equations for forces – in longitudinal and vertical flow direction – and one for moments can be written to obtain the FST-hemisphere's incipient movement conditions. The latter two conditions are weaker than those for the lon-

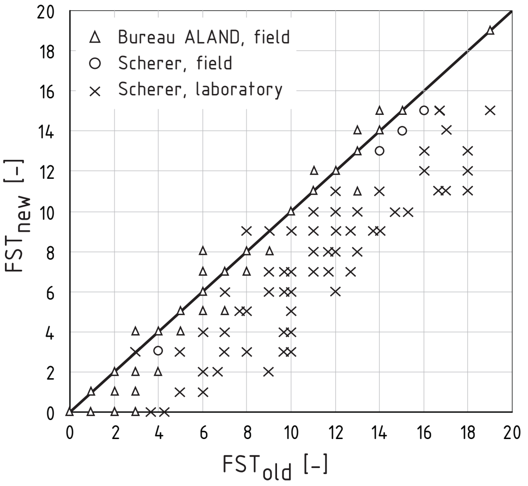

**Figure 4.4:** Comparison of measurements with the old and the new method in field and in laboratory conditions, from Scherer (1999) [69]

gitudinal movement and will be not considered further. Assuming the lift force being larger than the immersed weight, the hemisphere would lift up and move before the restraining pins are put away. The pins also would not hinder a rotation of the hemisphere around the pivot point (see Figure 4.5).

Projecting the forces on the horizontal axis, we get:

$$\overrightarrow{F}_d + \overrightarrow{F}_f = 0 \tag{4.2}$$

The friction force between a hemisphere and a plate is proportional to the normal force between their contact surfaces:

$$F_f = \mu \left(F_g - F_l\right) \qquad [N] \tag{4.3}$$

with $F_f$ = friction force, [N]
$F_g$ = immersed weight, [N]
$F_l$ = lift force, [N]
$\mu$ = friction coefficient, [-]

The weight force of a hemisphere in water is defined as:

$$F_g = V_h g (\rho_h - \rho_w) \qquad [N] \tag{4.4}$$

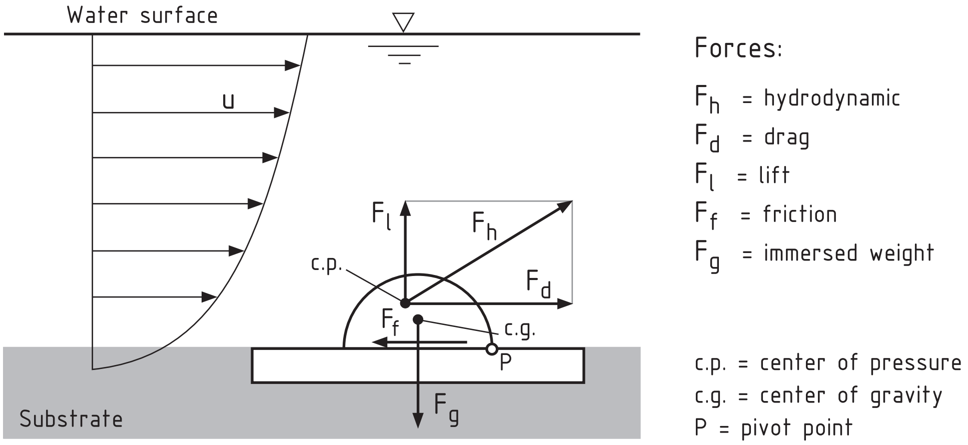

**Figure 4.5:** Forces acting on a hemisphere in a velocity profile

with $F_g$ = immersed weight, [N]
$V_h$ = volume of a hemisphere, [$m^3$]
$\rho_h$ = density of a hemisphere, [$kg/m^3$]
$\rho_w$ = density of water, [$kg/m^3$]
$g$ = acceleration due to gravity, [$m/s^2$]

Hydrodynamic force components are commonly defined as:

$$F_d = \frac{1}{2}\, c_d\, \rho_w\, u^2\, A_\perp \qquad [\mathrm{N}] \tag{4.5a}$$

$$F_l = \frac{1}{2}\, c_l\, \rho_w\, u^2\, A_\perp \qquad [\mathrm{N}] \tag{4.5b}$$

with $F_d$ = drag force, [N]
$F_l$ = lift force, [N]
$c_d, c_l$ = drag and lift coefficients, [-]
$u$ = representative velocity of an undisturbed flow, [m/s]
$A_\perp$ = cross-section area of a hemisphere perpendicular to the main flow direction, [$m^2$]

Substituting expressions for drag (4.5a), lift (4.5b) and weight (4.4) into the force balance equation 4.2 yields:

$$\frac{1}{2}\, c_d\, \rho_w\, u^2\, A_\perp - \mu \left[ V_h g (\rho_h - \rho_w) - \frac{1}{2}\, c_l\, \rho_w\, u^2\, A_\perp \right] = 0 \tag{4.6}$$

Recalling, that for a hemisphere the area $A_\perp$ and the volume $V_h$ are:

$$A_\perp = \frac{1}{2}\,\pi\, r_h^2 \qquad [m^2]$$

$$V_h = \frac{2}{3}\,\pi\, r_h^3 \qquad [m^3],$$

with $A_\perp$ = cross-section area of a hemisphere perpendicular to the main flow direction, $[m^2]$
$r_h$ = radius of a hemisphere, [m]
$V_h$ = volume of a hemisphere, $[m^3]$

and transforming Expression 4.6 for $\rho_h$, the formula for the hemisphere's density calculation is obtained:

$$\boxed{\rho_h = \rho_w \left[1 + \frac{3}{8}\frac{u^2}{r_h\, g}\left(c_l + \frac{c_d}{\mu}\right)\right] \qquad [kg/m^3] \qquad (4.8)}$$

with $\rho_h$ = density of a hemisphere, $[kg/m^3]$
$\rho_w$ = density of water, $[kg/m^3]$
$c_d$, $c_l$ = drag and lift coefficients, [-]
$\mu$ = friction coefficient, [-]
$r_h$ = radius of a hemisphere, [m]
$u$ = representative velocity of an undisturbed flow, [m/s]
$g$ = acceleration due to gravity, $[m/s^2]$

Thus, supposing the friction coefficient $\mu$, the representative undisturbed velocity $u$ and the corresponding drag $c_d$ and lift $c_l$ coefficients are known, the density of the hemisphere which will be just moved away by this flow can be estimated by Formula 4.8.

A number of difficulties arise when we want to apply this expression. Due to a velocity gradient in the vicinity to a bottom, the choice of a representative velocity for a hemisphere is not straightforward. Also, the influence of the river bottom complicates the flow pattern around a hemisphere, as not only the flow separation from the body itself but also separation of the bottom boundary layer takes place. In Section 4.2.1, the factors which influence the drag and lift coefficients for simple bodies in a uniform velocity profile with implications for the FST-hemisphere placed in a shear flow are discussed. Furthermore, updated information on friction coefficients for different plates is summarized in Section 4.2.2.

### 4.2.1 Hydrodynamic forces

To explain the nature of hydrodynamic forces, let us consider an axis-symmetrical object, moving in a fluid parallel to its axis of symmetry. The total time averaged hydrodynamic force acting on the body will be equal to the total drag. It does not matter whether the body is moving in the fluid or the fluid is moving around the resting body. The following force components in general contribute to the total drag [63]:

- deformation drag,
- friction drag, and
- pressure drag.

All three components originate from the viscosity of fluid. For practical cases, where the velocities are so great, that the deformation force contribution is negligible, the effect of viscosity on the drag is twofold. (1) The change in velocity from the value of the outer field to zero at the body's surface takes place within a thin boundary layer and, consequentially, causes shear stresses in that layer. These stresses integrated over the entire area of the body make up the *friction drag*. (2) The viscosity causes a change in the geometry of streamlines, resulting in the fluid breaking away from the body and the formation of vortices. This separation of the boundary layer flow adjacent to a body's surface over its backward facing part causes a change in the pressure field in turn and, consequentially, leads to a *pressure* or form drag.

The relation between the friction and the pressure drag depends to a great extent on the shape and orientation of the body in respect to the flow direction. In hydrodynamics, streamline and bluff (non-streamline) bodies are commonly distinguished. A bluff body is defined as an object for which the major contribution to the total flow force is due to pressure forces. Contribution of the force due to skin friction is negligible for such bodies in comparison to the pressure component. For example, a sphere is a bluff body and so is a thin plate placed perpendicular to the oncoming flow (Figure 4.6a). On the other hand, a thin plate placed parallel to a free stream flow direction is a streamline body. Here, the boundary layer flow remains attached to the surface and skin friction accounts for up to 90 % of the total flow force (Figure 4.6b). Flow past a hemispherical obstacle on a wall would separate from the object, causing a large pressure force. Thus, an FST-hemisphere belongs to the class of bluff bodies.

Considering a uniform flow field, only for a symmetrical body with its symmetry axis parallel to the flow direction is the pressure drag equal to the resulting total pressure force. If a symmetrical body is positioned pitched to the flow (Figure 4.6c), or generally for a unsymmetrical body, the total hydrodynamic force direction is not aligned with that of the flow.

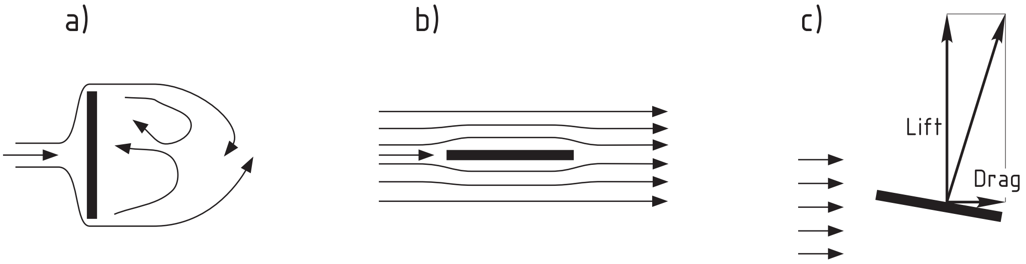

**Figure 4.6:** To the explanation of drag and lift on bluff and streamline bodies: a) bluff body; b) streamline body; c) lift and drag components of the total hydrodynamic force for a pitched symmetrical object in a uniform flow field

The component of the force perpendicular to the free stream flow direction, usually vertical, is called *lift*. The component normal to both, the free-stream and the vertical directions, is called *side* force.

For bodies of similar shape and same orientation to the flow, Expressions 4.5a,b are valid for determination of flow force components. Drag and lift coefficients in these formulas can be estimated in wind tunnel experiments. These coefficients are not constant but change with the Reynolds number. However, if a dynamic similarity is ensured, the flow forces acting at a particular combination of the body's characteristic size, free stream flow velocity and fluid viscosity can be estimated if the dependencies $c_d = f(Re)$ and $c_l = f(Re)$ are known.

A typical example of drag coefficient dependency from the Reynolds number for a sphere in a uniform velocity profile is shown in Figure 4.7. At large Reynolds numbers, relevant for practical cases (over $10^3$), two flow regimes are distinguished: subcritical and supercritical. For a sphere, these regimes correspond to zones with $c_d = 0.4$–$0.5$ and $c_d \approx 0.2$, respectively. The change of regimes associated with a sudden drop of the drag coefficient – the so called drag crisis – occurs at the *critical Reynolds number*, which is approximately $2{\times}10^5$ for the sphere. The presence of one or another flow regime depends on the state of a body's boundary layer at a separation point. Subcritical regime corresponds to a laminar boundary layer separation, supercritical to a turbulent one. The critical Reynolds number can be influenced by two other parameters – free-stream turbulence level and surface roughness [93]. These aspects in application to a hemisphere will be considered in the next chapter.

Besides free-stream turbulence and a surface roughness (wear of the object's surface), additional factors can theoretically influence the drag and lift coefficients of an FST-hemisphere as an obstacle on the bottom, such as: velocity gradient in the oncoming boundary layer flow developing over the bed, type of the ground plate, and flow interaction with the elements

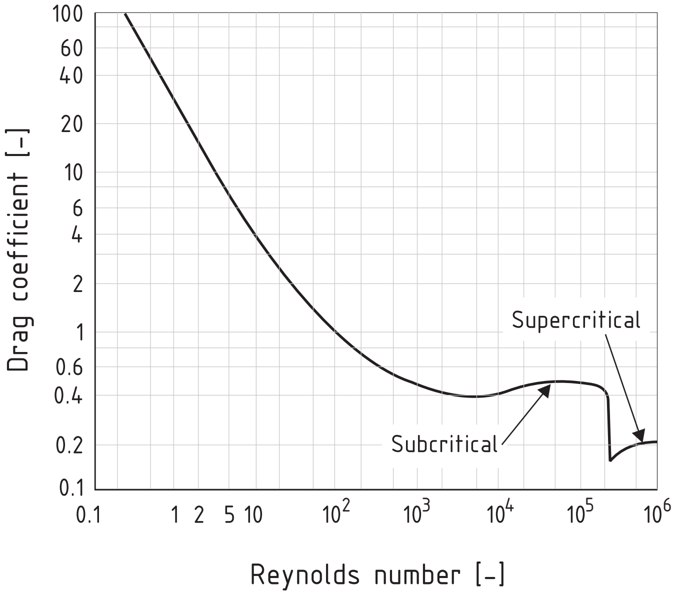

**Figure 4.7:** Drag coefficient for sphere in a uniform flow field, from Prandtl and Tietjens (1957) [63]

protruding the velocity profile in front of and behind the hemisphere. These aspects will be also investigated in the next chapter.

### 4.2.2 Friction force

The coefficient of static friction $\mu$ between an FST-hemisphere and a plate is dependent on material and configuration of the contact surfaces, and highly on the hemisphere placement method for the old plate.

There are two ways how the coefficient of static friction $\mu$ can be estimated. The first one, referenced in [36], [16] and [69], is based on the force balance for a hemisphere on an inclined plane. The moment a hemisphere starts to move, the friction force $F_f$ is equal to the sliding force $F_s$ (see Figure 4.8); thus, the friction coefficient can be estimated through:

$$F_f = \mu \cdot F_n = F_s \qquad \Longrightarrow \qquad \mu \cdot F_g \cdot \cos\alpha = F_g \cdot \sin\alpha$$

$$\mu = \tan\alpha \qquad\qquad [\text{-}] \tag{4.9}$$

with $F_f$ = friction force, [N]
$F_s$ = sliding force, [N]
$F_g$ = immersed weight, [N]
$F_n$ = component of $F_g$ normal to the surface of a plane, [N]
$\alpha$ = angle of the inclined plate, [°]

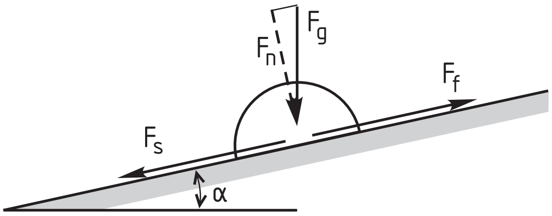

**Figure 4.8:** Force balance for a hemisphere on an inclined plane

The second way, used by Statzner and Müller [88], is to apply a known force to a hemisphere placed on a horizontally levelled plate. Knowing the density of a hemisphere and the applied force, the friction coefficient is:

$$\mu = \frac{F_f}{F_g} = \frac{F_f}{V_h\, g\, (\rho_h - \rho_w)} \qquad [-] \qquad (4.10)$$

This method requires very precise force measuring devices for hemispheres with low densities. For example, to insure a 50 % relative error of friction coefficient measurements[1] for the hemisphere with a density of 1.031 g/cm$^3$ (FST N°2), the device has to resolve 0.005 N (or 0.5 gram). Statzner and Müller obtained following relationship for a smooth plexiglass plate placed horizontally in an aquarium at 20°C:

$$F_f = 1.22\, \rho_h - 1.36 \qquad [N] \qquad (4.11)$$

with $F_f$ = horizontal force on a hemisphere, [N]
$\rho_h$ = density of a hemisphere, [g/cm$^3$]

The friction coefficient estimated from this relationship, ranges from -6.66 (!) for hemisphere 1 over 0.58 for hemisphere 7 to 0.98 for hemispheres 21–24.

Friction coefficients for the different plates and hemisphere placement methods are summarized in Table 4.3. As the only value for the new plate comes from [69], own experiments were performed with the use of an inclined plane.

Experiments in [69], [16] were conducted starting initially with a horizontal position of the plate. Gradually inclining the plate, authors noticed an angle at which a hemisphere

---

[1] Assuming a friction coefficient of $\mu = 0.24$ (see Table 4.3)

| Reference | Plate type | Placement method | $\mu$ | $\mu_{\text{min}}$ | $\mu_{\text{max}}$ |
|---|---|---|---|---|---|
| | | | - | - | - |
| Heilmair and Strobl [36] | smooth plexiglass | press | 0.601 | 0.488 | 0.726 |
| Heilmair and Strobl [36] | smooth plexiglass | drop | 0.052 | 0.017 | 0.087 |
| Scherer [69] | smooth (PVC or plexiglass?) | press[a] | 0.506 | 0.362 | 0.690 |
| Scherer [69] | new standard (PVC) | - | 0.476 | 0.325 | 0.675 |
| Dittrich and Schmedtje [16] | smooth plexiglas | press[a] | 0.594 | 0.487 | 0.701 |
| own | smooth steel | press | 0.605 | 0.510 | 0.700 |
| own | smooth steel | drop | - | - | 0.087 |
| own | new standard (steel) | - | 0.240 | 0.213 | 0.268 |

a – presumably, as not explicitly stated in the reference

**Table 4.3:** Coefficient of static friction $\mu$ for various plates and FST placement methods

started to slide, so presumably they used a “press” method as we can assume that during positioning of hemisphere it could adhere to the plate. In own experiments and presumably in the experiments of [36], first, the angle of the plate was installed and then hemispheres were placed on the inclined plate.

Own experiments for hemispheres N° 1, 2, 5, 8, 11, 14, 17 and 20 were conducted in an aquarium at 20 °C. In the above table, for the structured and the smooth plate using “press” method, the minimum friction coefficient $\mu_{\text{min}}$ corresponds to the smallest angle at which one or some FST-hemispheres begin to slide away. The maximum $\mu_{\text{max}}$, respectively, to the angle at which all tested hemispheres slide away. For the structured plate, hemispheres N° 5 and 8 are the first to move at low angles. In opposite, using the “press” method these are the heaviest hemispheres. Abnormal behavior is observed for the hemispheres N° 1 and 2: during the test of the structured plate they could not be placed on the inclined plate as they floated on their horizontal, flat surface. Using the “press” method they do not slide even at an angle of 60°. As the usability of an inclined plane for testing of the “drop” method is questionable, only the angle at which all hemispheres slide away is noted.

Generally, friction coefficient estimates for the smooth plate and the “press” method do not vary much among the authors. Own result for the “drop” method with $\mu = 0.605$ correlate well with the values of Heilmair and Strobl (0.601) and Dittrich and Schmedtje (0.594). Apparent is the considerable difference between friction coefficients for the structured plate: 0.476 from [69] vs. 0.24 estimated from own experiments.

## 4.3 Calibration curves

Since the introduction of FST-hemispheres, quite a number of calibration curves, that is the dependency between FST number/density and a common measurable physical variable, were established for specific field/laboratory conditions. The majority of those curves use a near bottom or mean column velocity, or bottom shear stress as a calibration parameter. The other category of calibration curves, which did not find actual applications due to the questionable physical rationale, is represented by correlations with water depth, substrate or combined parameters such as Froude and Reynolds numbers [83], [88].

Analyzing and comparing calibration curves obtained by different authors, the following should be kept in mind:

- Practical evidence shows, that in field conditions it is difficult to obtain evenly distributed FST-hemispheres' sample. Usually, FST-hemispheres with small densities are over-represented and those with large densities are under-represented in a sample. A calibration curve built upon such data has a very poor reliability in the range of heavier hemispheres due to the scarcity of measurement points there.
- FST-hemispheres are not a single value measuring device. Every hemisphere is responsible for a certain range of forces which increases with growing FST number (density). This fact results in a widening of the calibration curves in the range of heavier hemispheres.
- The range of the FST-method practicability results in calibration curves being valid only at water depths up to 70–80 cm.

It is expected, that FST-hemispheres' calibration in general should depend on: the type of measurement equipment (ground plate type, velocity measurement device), FST-hemisphere's placement method, vertical position of the ground plate in the velocity profile (levelled with roughness tops, put over substrate), substrate characteristics and water depth.

### 4.3.1 FST-hemispheres vs. velocity

Considering the force balance for a hemisphere placed in a velocity profile, Heilmair and Strobl [36] show, that FST-hemisphere numbers should theoretically correlate to the velocity acting at the level of a hemisphere, as given by Formula 4.8. They compare in detail the performance of both, FST-hemispheres and micro-flow-meter, for the assessment of near bottom hydraulic conditions. Results of laboratory measurements for two bottom types – smooth and rough (covered with stones of diameters 64 to 180 mm) and two hemisphere placement methods – "drop" and "press" – are shown in Figures 4.9a,b. In experiments, the smooth FST plate is levelled with the substrate roughness tops and velocity is measured with the micro-flow-meter at a distance of 2 cm from the plate's surface.

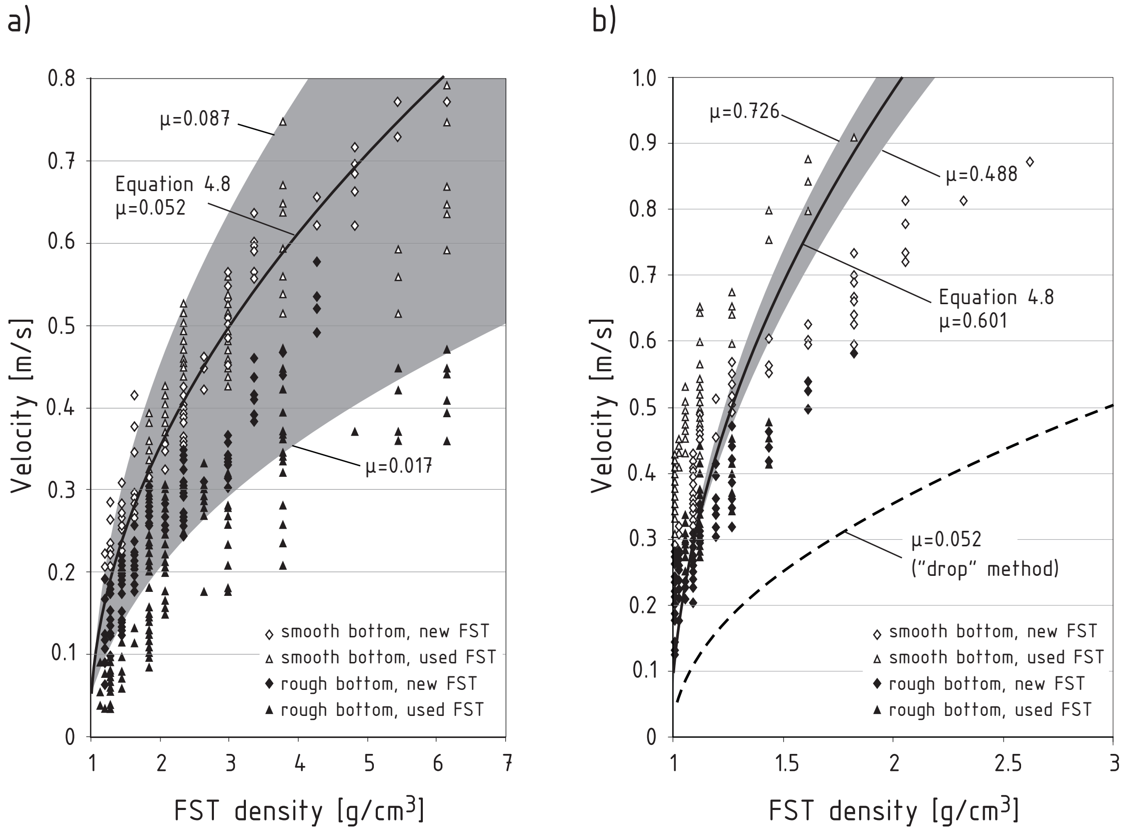

**Figure 4.9:** FST-hemisphere densities vs. velocity at 2 cm away from a plate: a) "drop" method, b) "press" method; after Heilmair and Strobl (1994) [36]

Also, in Figures 4.9a,b, the correlation curves calculated with Formula 4.8 are shown. The reference value 0.4 for the drag coefficient is assumed upon recommendations of Morris [55] and the lift coefficient is $c_l = c_d = 0.4$. The friction coefficient for every FST placement method is taken from Table 4.3. Grey regions depict the areas between the curves calculated with the minimum and maximum values of friction coefficient for every particular placement method.

A very strong influence of the placement method on the calibration curves is clearly seen: approximately three times a larger velocity is required to move the same hemisphere when the "press" method (Figure 4.9b) instead of the "drop" method (Figure 4.9a) is used. Effects of bottom type as well as wearout of the equipment (new vs. extensively used hemispheres) are also noticeable but of secondary importance in comparison to the placement method effect. It can be seen, that in the case of the "drop" method most of the experimental points are inside of the "theoretical area". Only points acquired with extensively used

FST-hemispheres on rough bottom lie outside. For the "press" method, the theoretical area is very narrow and many points lie outside of it.

An extensive study of Mader and Meixner [49] also concentrates on the correlation of FST numbers and near bottom velocity. Measurements were done in nine reaches of small streams with mean widths up to 15 m and mean slopes ranging from 2 to 15 ‰. Substrate composition in all streams was similar, dominated by a pebble-cobble group according to the Wentworth scale (see for example [31] for a reference to the Wentworth scale). Flow velocity was measured with 2D and 3D electromagnetic inductive flow-meters 1 cm above the substrate, and, in some cases, was compared to measurements with a laboratory propeller current meter. The smooth plate, with the upper surface levelled with the roughness tops during measurements, was used together with the standard hemisphere placement technique.

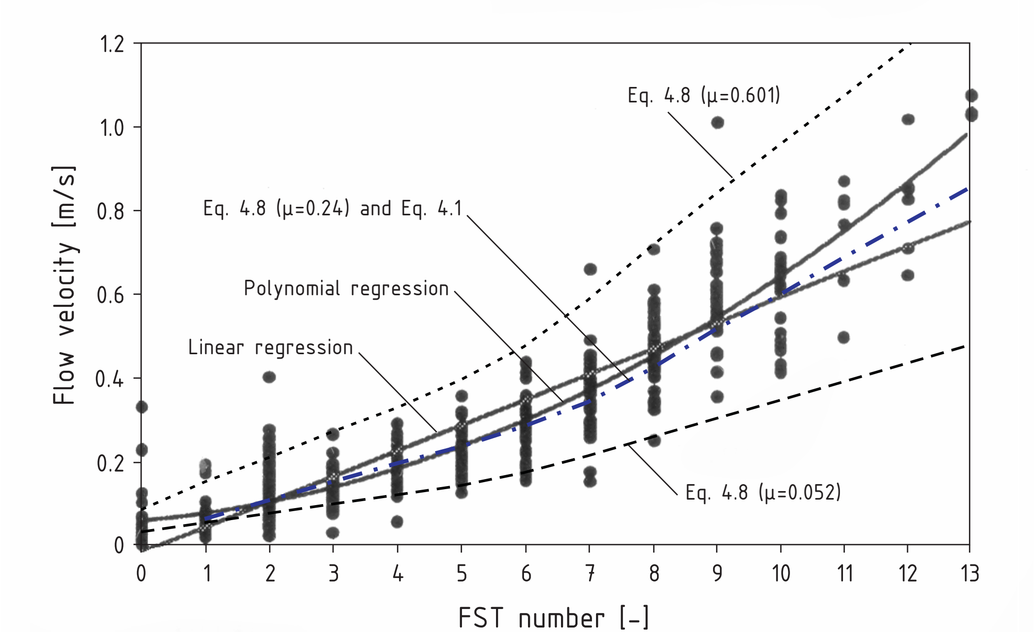

**Figure 4.10:** FST numbers vs. 2D time averaged velocity at 1 cm away from roughness tops, from Mader and Meixner [49]

In Figure 4.10, two correlation curves of the FST hemispheres and the time averaged near-bed velocities, based on data from all rivers, are shown. In the range of low FST densities, data points can be approximated with a linear as well as a polynomial expression. With growing density (FST numbers larger than 10), correlation curves diverge, and the authors suggest that for reaches with high velocities the polynomial dependency should be used. Correlation of FST against time averaged and maximum velocities have principally the same regression coefficients, what probably indicates, that turbulent fluctuations of velocity do not – at least primarily – define the hemisphere movement condition. Opposite to investigation [36], no effects resulting from wear and tear of equipment are noticed.

Also in Figure 4.10, the three theoretical curves obtained with the use of Formula 4.8 are shown. For two curves, the friction coefficients are equal to those of Heilmair and Strobl [36] estimated for the "drop" and "press" methods. The other uses a friction coefficient $\mu = 0.24$ for the new standard method and is corrected applying Formula 4.1 for the transferability between the old and new method. The latter reflects better the field data, and, it can be hypothesized, that "drop" and "press" methods represent two extremes of Statzner's original placement method.

In some studies, velocity at different distances from the bottom is measured together with the FST-hemispheres measurements. Surprisingly, correlations of FST-hemisphere numbers with the mean column velocity, measured at 40 % of the water depth, have higher coefficients of determination, than those with near-bed velocity. For example, in the study [77], with velocities measured over the FST ground plate, the coefficients of determination ($R^2$) for the FST-hemisphere vs. velocity correlation are 0.921 and 0.952 for the near-bed velocity at a distance of 2 cm above the plate and mean column velocity, respectively. In the study [18], where the velocity is measured after the ground plate removed from the substrate, the difference is larger. For the near-bed velocities at distances of 0.5 cm, 1 cm and 2 cm, the coefficients of determination are about 0.75 and for the mean column velocity 0.91. A possible explanation for such behavior could be the different measurement volume of the much larger FST-hemisphere, which representative linear size is 7.8 cm, compared to the sampling volume of the particular velocity-meters in the range of maybe some millimeters. As the near-bed flow field is much more variable in horizontal as well as in vertical direction than the flow at a distance from bottom, a higher fluctuation in the correlation follows.

### 4.3.2 FST-hemispheres vs. bottom shear stress

There is a number of laboratory and field studies in which the FST-hemispheres are calibrated against bottom shear stress $\tau_0$ [16], [41], [86], [88]. In doing so, the hemisphere's movement condition is assumed to be similar to that of the substrate grain lying on the bottom. Let us consider the latter in more detail. Like for a hemisphere, two forces control a particle's movement: the holding – immersed weight $F_g$ – and the driving – hydrodynamic – force $F_h$ (see Figure 4.11). The latter can be split into the drag $F_d$ and the lift $F_l$ components.

Moreover, there are three ways the particle can start to move:

- lift off from the grains beneath it (requires a large lift force);
- slide along the particle downstream from it;

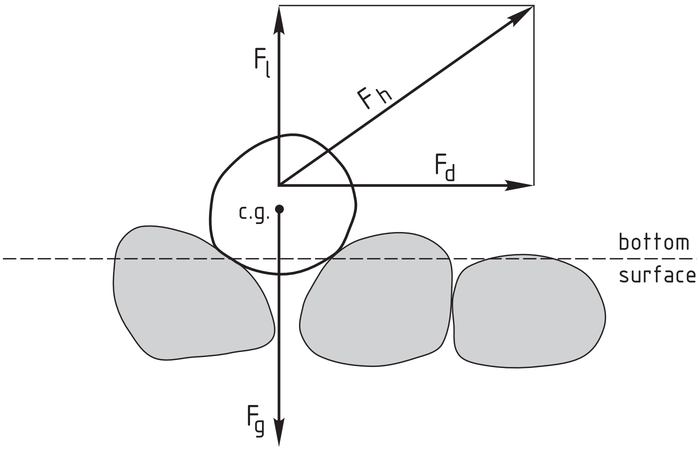

**Figure 4.11:** Forces acting on a substrate grain

- rotate along the pivot of the downstream grain.

Experiments show, that in case of substrate grains, on contrary to FST-hemispheres, the third option is the most likely to occur.

Application of dimensional analysis allows Shields (1936) [79] to express the incipient motion condition of an elevated grain as a function of the dimensionless bottom shear stress $\theta$ (Shields' parameter) and the grain Reynolds number $Re_*$:

$$\theta = \frac{\tau_0}{(\rho_s - \rho_w)\ g\ d_s} = \frac{\rho_w\, u_*^2}{(\rho_s - \rho_w)\ g\ d_s} \qquad [\text{-}] \qquad (4.12)$$

$$Re_* = \frac{d_s\, u_*}{\nu} \qquad [\text{-}] \qquad (4.13)$$

with $\theta$ = entrainment function after Shields, [-]
$\tau_0$ = bottom shear stress, [N/m$^2$]
$\rho_s, \rho_w$ = density of a grain and water, respectively, [kg/m$^3$]
$Re_*$ = grain Reynolds number, [-]
$u_*$ = shear velocity, [m/s]
$d_s$ = diameter of a grain, [m]
$g$ = acceleration due to gravity, [m/s$^2$]
$\nu$ = kinematic viscosity of water, [m$^2$/s]

In case of rough flow conditions ($Re_* > 70$), which are expected in gravel bed rivers, the Shields' parameter comes to a constant value of 0.04–0.05 (see Figure 4.12), thus implicating a linear dependency between bottom shear stress and grain density. Despite the principally different movement mechanism of hemispheres in comparison to substrate grains, most of the calibration curves show the linear correlation type. Unfortunately, there is no single correlation curve but many, and their slopes are dependent on substrate grain size. To investigate the reason for this, we consider in detail the work of Shields for the derivation of the incipient motion condition.

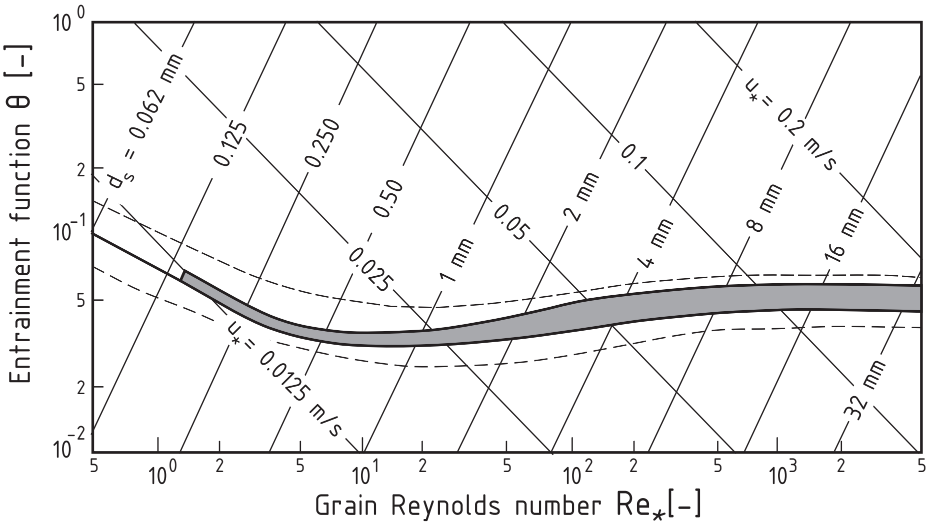

**Figure 4.12:** Shields Diagram – condition of incipient sediment motion, from Raudkivi (1990) [64]

Assuming a uniform particle size and a levelled bed, Shields implies proportionality between the grain's resistance to flow and its immersed weight $F_g$ written as:

$$F_g = a_1 \, a_2 \, (\rho_s - \rho_w) \, g \, d_s^3 \qquad [N] \tag{4.14}$$

with $a_1$ = factor accounting for substrate pore volume, [-]
$a_2$ = factor accounting for friction characteristics of substrate particles, [-]

The hydrodynamic flow force $F_h$ acting at level $y_s$ of an elevated grain, without detailed partition into drag and lift components, is expressed as:

$$F_h = c_h \, A_\perp \frac{\rho_w \, u_s^2}{2} \qquad [N] \tag{4.15}$$

with $F_h$ = hydrodynamic force, [N]
$c_h$ = flow resistance coefficient of a grain, [-]
$A_\perp$ = cross-section area of a grain perpendicular to the main flow direction, [m$^2$]
$u_s$ = flow velocity at level of center of pressure $y_s$, [m/s]

The flow resistance coefficient $c_h$ generally depends on the grain shape and Reynolds number, thus can be written as:

$$c_h = f_1(a_3, Re_s) \qquad [-] \tag{4.16}$$

with $c_h$ = flow resistance coefficient of a grain, [-]
$a_3$ = grain shape factor, [-]
$Re_s = u_s\ d_s/\nu$ = grain Reynolds number, [-]

With 4.16, Expression 4.15 takes the form:

$$F_h = f_1(a_3, Re_s)\ \rho_w\ d_s^2\ u_s^2 \tag{4.17}$$

To define $u_s$, the logarithmical velocity distribution is applied:

$$\frac{u(y)}{u_*} = \frac{1}{\kappa}\ \ln\left(\frac{y}{k_s}\right) + f(Re_*) \tag{4.18}$$

with $\overline{u}(y)$ = mean velocity along x-axis, [m/s]
$u_*$ = shear velocity, [m/s]
$\kappa$ = von Kármán constant, [-]
$y$ = vertical coordinate, [m]
$k_s$ = hydraulic roughness height, [m]
$Re_* = d_s\ u_*/\nu$ = grain Reynolds number, [-]

Setting the grain diameter $d_s$ equal the Nikuradse's roughness $k_s$ and assuming that the distance $y_s$ to the center of pressure of an elevated grain is proportional to the grain diameter $d_s$, the velocity $u_s$ can then be expressed as:

$$u_s = u_*\left(\frac{1}{\kappa}\ \ln\left(\frac{y_s}{d_s}\right) + f(Re_*)\right) = u_*\left(\frac{1}{\kappa}\ \ln(a_4) + f(Re_*)\right) = u_*\ f_2(a_4, Re_*) \tag{4.19}$$

with $a_4$ = proportionality factor between grain size $d_s$ and distance $y_s$, [-]

Substituting 4.19 into 4.17 and recalling that $\tau_0 = \rho_w\ u_*^2$, we get:

$$F_h = f_1(a_3, Re_s)\ \rho_w\ d_s^2\ u_*^2\ f_2^2(a_4, Re_*) = \tau_0\ d_s^2\ f_3(a_3, a_4, Re_*) \tag{4.20}$$

Equating the expressions for the forces, 4.14 and 4.20, and replacing bottom shear stress $\tau_0$ with critical bottom shear $\tau_c$ at which the grain starts to move, we get the Shields' condition:

$$\theta_c = \frac{\tau_c}{(\rho_s - \rho_w)\ g\ d_s} = f(\frac{u_*\ d_s}{\nu}) \tag{4.21}$$

For the correlation of the FST-hemispheres to bottom shear stress, the assumption of a uniform grain size is not applicable. Depending on the substrate type, the FST-hemisphere's diameter is smaller, equal or larger than that of a mean substrate grain (see Figure 4.13) and, therefore, variable factor $a_4$ in Equation 4.19, which in Shields' considerations is of the order of 1 for all substrate types. This fact has the consequence that no unique calibration curve for FST-hemispheres against bottom shear stress exists, which will be demonstrated on a simple example below.

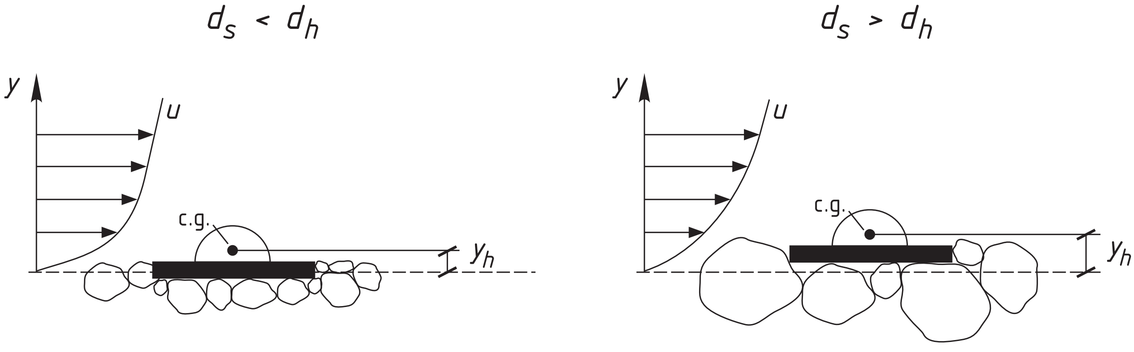

**Figure 4.13:** Influence of substrate size on a distance from the log-profile origin to the velocity reference point for a hemisphere

Let us consider two substrate types upon which the FST measurements should be done. The first substrate has a mean grain diameter $d_{s_1} = 8$ mm and the second $d_{s_2} = 80$ mm. The flows in both cases have a large relative submergence, so Nikuradse's log law is applicable. Setting $d_s = k_s$ and assuming, that the flow velocity is large enough, so that the flow is in a rough regime, the logarithmical velocity distribution can be written as:

$$\frac{u(y)}{u_*} = \frac{1}{\kappa}\ \ln(\frac{y}{k_s}) + 8.48 \tag{4.22}$$

We assume the level $y_h$ at which the representative velocity $u_h$ acts at the hemisphere's center of mass:

$$y_h = 0.25\ k_s + \frac{3}{8} r_h \tag{4.23}$$

with $r_h$ = hemisphere radius, [m]
$0.25\ k_s$ = the distance between the origin of the log-profile and the level of roughness tops (cf. Chapter 3.6, Page 58) [m]

For substrates 1 and 2 we get:

$$y_{h_1} = 0.25 \cdot 0.008 + \frac{3}{8} \cdot 0.039 = 0.017\ \mathrm{m} \qquad \Longrightarrow \qquad \frac{y_{h_1}}{k_{s_1}} = \frac{0.017}{0.008} = 2.1 \tag{4.24}$$

$$y_{h_2} = 0.25 \cdot 0.08 + \frac{3}{8} \cdot 0.039 = 0.035\ \mathrm{m} \qquad \Longrightarrow \qquad \frac{y_{h_2}}{k_{s_2}} = \frac{0.035}{0.08} = 0.4 \tag{4.25}$$

If the same would be written for an elevated substrate grain, but not a hemisphere, we would obtain:

$$\frac{y_{s_1}}{k_{s_1}} = \frac{y_{s_2}}{k_{s_2}} \simeq 1$$

Substituting 4.24 and 4.25 into Equation 4.22, we get for the representative velocities $u_{h_1}$ and $u_{h_2}$:

$$\boxed{\begin{aligned} u_{h_1} &= u_* \cdot \left(\frac{1}{\kappa}\ \ln\left(\frac{y_{h_1}}{k_{s_1}}\right) + 8.48\right) = 10.36\ u_* \\ u_{h_2} &= u_* \cdot \left(\frac{1}{\kappa}\ \ln\left(\frac{y_{h_2}}{k_{s_2}}\right) + 8.48\right) = 6.41\ u_* \end{aligned}}$$

As velocity $u_h$ is in second power in the formula for the hydrodynamic force, the bottom shear stress corresponding to the FST-hemispheres' incipient motion condition has to be **2.65** times larger for the coarse substrate than for the fine one in this example.

Above mentioned has a decisive influence on calibration results. Failure to obtain a unique, from river to river transferable calibration curve "FST vs. bottom shear stress" has been proven to be a theoretically impossible task. Additionally, other important issues such as FST-hemisphere's placement method and method used for bottom shear stress calculation are expected to have a comparable or even larger influence on correlation curves.

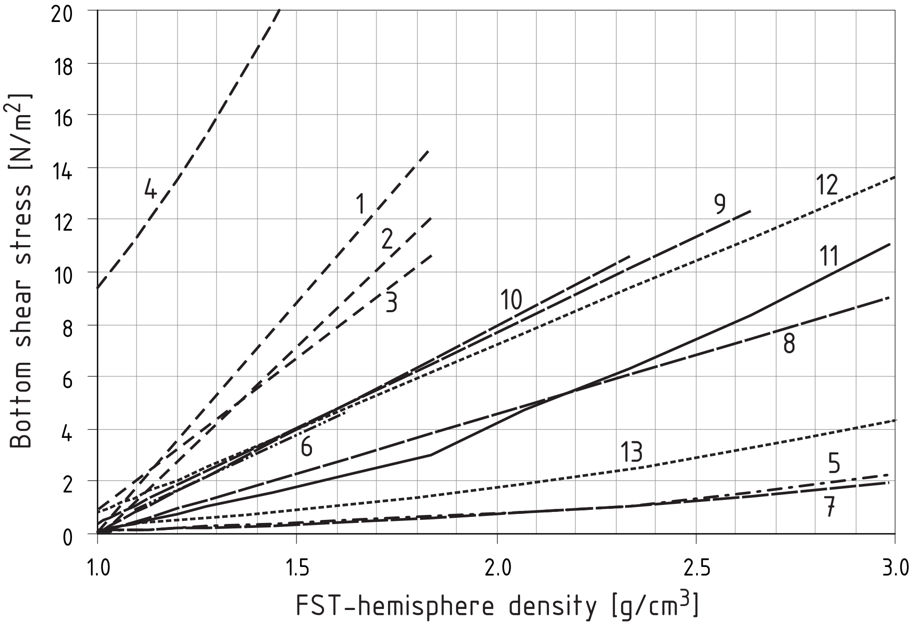

**Figure 4.14:** Calibration curves "FST-hemispheres vs. bottom shear stress", from Table 4.4

In Table 4.4, selected characteristic calibration curves are listed (see also Figure 4.14). Analyzing the curves, it is seen:

1. For the curves obtained by one and the same author in laboratory conditions (see curves 7, 8, 10 by Dittrich and Schmedtje [16]), the effect of substrate size can be clearly seen and it shows the same tendency as it was foreseen in the theoretical considerations. Moreover, assuming the mean grain diameters for the curves 8 and 10 to be 3 and 7 cm respectively, we get a factor of 1.45 in flow force magnitudes, which is close to the measured factor of approximately 1.7.

2. Comparison of curves 8 and 9 [16] shows the problem of calculating the bottom shear stress over the rough bottom via the integral method at small water depths (see Section 3.4). Due to the presence of the roughness sublayer, a distribution of the turbulent shear stress cannot be approximated by the triangular one and the shear stress determined by the integral method is higher than those that would be obtained through the application of the corrected velocity distribution law after Bezzola: the shear stress corresponding to the one and the same FST-hemisphere number is higher at a lower depth than that at a larger depth. The failure of the integral method is also supported by the fact, that the authors could not find a correspondence between bottom shear stress determined via velocity profile and via the integral method at such low depths, which was no problem at larger water depths.

3. The curve 4 from [88] shows again, that the integral method, especially in field condi-

tions, is inappropriate for the determination of local ("skin") shear stress which was believed to be measured by FST-hemispheres. Even if the flow can be assumed to be quasi-uniform, the estimate of shear stress from the mean water surface slope reflects not only the skin shear, but also shear due to micro and macro channel structures.

4. Curves 1,2,3 from the field study [88], with the bottom shear stress obtained through the application of the log velocity distribution, show the opposite to the theoretical behavior. Possible reasons for this can be the already mentioned effects of relative submergence or, simply, derivation of curves based on two less measurement points. Also, very low coefficients of determination for these curves can be noticed.

5. Curves 12 and 13 from [69] prove, that the hemisphere's placement method together with the type of equipment – smooth vs. structured plate – plays an important role. The structured plate is characterized by a higher friction coefficient in comparison to the smooth plate combined with original or "drop" placement methods. Therefore, FST-hemisphere numbers obtained using the new method are lower than those using the old method at the same bottom shear stress. The mean difference between the two methods is about 3 to 4 hemisphere numbers in Scherer's experiments.

| N° | Reference | Experiment conditions | Substrate size | FST range | n | Method | Depth range | $\tau_0 = f(\rho_h)$ | $R^2$ |
|---|---|---|---|---|---|---|---|---|---|
| - | - | - | cm | - | - | - | cm | $N/m^2$ | - |
| 1 | Statzner and Müller [88] | field$^{a}$ | <4 | 1–10 | 30 | VP | no data | $17.7\rho_h - 17.7$ | 0.561 |
| 2 | Statzner and Müller [88] | field$^{a}$ | ~8 | 1–10 | 23 | VP | no data | $14.7\rho_h - 14.9$ | 0.514 |
| 3 | Statzner and Müller [88] | field$^{a}$ | >16 | 1–10 | 19 | VP | no data | $11.6\rho_h - 10.7$ | 0.584 |
| 4 | Statzner and Müller [88] | field$^{a}$ | - | 1–17 | 90 | IR | no data | $9.369\rho_h^{2.02}$ | 0.860 |
| 5.1 | Statzner et al. [86] | lab.$^{a}$ | 1.6–3.0 | 1–24 | 69 | VP | 24–51 | $0.1\rho_h^{2.85}$ | 0.993 |
| 5.2 | Statzner et al. [86] | lab.$^{a}$ | 1.6–3.0 | 1–12 | 35 | VP | 24–51 | $0.732\rho_h - 0.66$ | 0.983 |
| 6 | Restle [65] | lab.$^{a}$ | 0.8–1.6 | 4–9 | 25 | IR | 7–19 | $7.1\rho_h - 6.85$ | 0.800 |
| 7 | Dittrich and Schmedtje [16] | lab.$^{a}$ | 0.3–0.5 | 1–19 | ~20 | IR | 19–25 | $0.139\rho_h^2.4$ | 0.980 |
| 8 | Dittrich and Schmedtje [16] | lab.$^{a}$ | 0.3–6.5 | 1–16 | ~20 | IR | 19–25 | $4.50\rho_h - 4.45$ | 0.990 |
| 9 | Dittrich and Schmedtje [16] | lab.$^{a}$ | 0.3–6.5 | 1–13 | - | IR | 6–8 | $7.30\rho_h - 6.91^{d}$ | - |
| 10 | Dittrich and Schmedtje [16] | lab.$^{a}$ | 0.3–14.0 | 1–12 | 15 | IR | 19–25 | $7.86\rho_h - 7.80$ | 0.99 |
| 11.1 | Jorde [41] | lab.$^{b}$ | 1.6–3.2 | 1–9 | 30 | VP | no data | $3.483\rho_h - 3.412$ | 0.99 |
| 11.2 | Jorde [41] | lab.$^{b}$ | 1.6–3.2 | 9–22 | 30 | VP | no data | $\rho_h^2.22 - 0.276$ | 0.96 |
| 12 | Scherer [69] | lab.$^{c}$ | 2.0–6.5 | 1–15 | 13 | IR | 18–25 | $6.42\rho_h - 5.63$ | - |
| 13 | Scherer [69] | lab.$^{a}$ | 2.0–6.5 | 4–19 | 13 | IR | 18–25 | $0.57\rho_h^2 - 0.28\rho_h + 0.047$ | - |

| | |
|---|---|
| a | old smooth plate levelled with roughness tops, original FST placement method of Statzner and Müller [88] |
| b | old smooth plate positioned over the substrate, modified FST placement method of Jorde [41] |
| c | new structured plate levelled with roughness tops |
| n | number of FST measurements |
| VP | velocity profile method for the determination of $\tau_0$, see Section 3.4 |
| IR | integral method for the determination of $\tau_0$, see Section 3.4, Eq. 3.31 |

**Table 4.4:** "FST-hemispheres vs. bottom shear stress" calibration curves

## 4.4 Summary

It is shown in this chapter, that, based on the force balance analysis, the FST-hemisphere density can be theoretically estimated by the following equation:

$$\boxed{\rho_h = \rho_w \left[ 1 + \frac{3}{8} \frac{u^2}{r_h\, g} \left( c_l + \frac{c_d}{\mu} \right) \right]}$$

with $\rho_h$ = density of a hemisphere, [kg/m$^3$]
$\rho_w$ = density of water, [kg/m$^3$]
$c_d, c_l$ = drag and lift coefficients, [-]
$\mu$ = friction coefficient, [-]
$r_h$ = radius of a hemisphere, [m]
$u$ = representative velocity of an undisturbed flow, [m/s]
$g$ = acceleration due to gravity, [m/s$^2$]

To make use of this expression, the friction coefficient $\mu$ between the plate and the hemisphere, and the hydrodynamic coefficients $c_d$ and $c_l$, which stand in connection with the determination of the reference flow velocity $u$, have to be known.

As experiments show, the friction coefficient is strongly dependent on the FST equipment, more precisely on the type of the FST ground plate (old smooth or new structured) and the associated hemisphere's placement method. The reference values for $\mu$ are 0.24 for the new structured plate, and approximately 0.05 and 0.6 for the "drop" and "press" methods, respectively, when using an old smooth plate.

More study require hydrodynamic coefficients, as in the literature only rough estimates for the drag coefficient (0.4) can be found. The next chapter is devoted to this subject.

Analysis of empirical correlations of FST-hemispheres to such physical parameters like flow velocity and bottom shear stress reveals that:

- In spite of the considerable scatter in the correlation curves, the near-bed flow velocity appears to be the best descriptive parameter for the FST-hemispheres. These correlations follow in general the theoretical formula for the estimation of hemisphere's density based on force balance.

- Surprisingly higher regression coefficients of the curves "FST vs. mean column velocity" in comparison to the one of "FST vs. near-bed velocity" propose a possible success of the new method for FST-hemisphere density estimation via mean column velocity using log law for near-bed velocity calculation. The possible explanation of this phenomena lies in different sampling volumes of FST-hemispheres ($d_h = 7.8$ cm) and velocity measuring equipment (few millimeters to few centimeters, depending on the type) which can have a pronounced effect in the near-bed area.

- Detailed analysis of the Schields' condition for initiation of sediment transport allows to prove, that no single but multiple, dependent mainly on diameter of substrate material, correlations of FST-hemispheres to the bottom shear stress are theoretically possible. Thus, the past calibration curves "FST vs. bottom shear stress" are applicable at most only at substrate conditions similar to those in calibration experiments.

# 5 Numerical modelling of velocity-gradient flow past a hemisphere

It is shown in Chapter 4, that the density of an FST-hemisphere which will be moved at particular flow conditions can be estimated with Formula 4.8, assuming the friction coefficient between the plate and hemisphere and the velocity with the corresponding drag and lift coefficients are known. This chapter aims to comprehend, how the lift and drag forces on a hemisphere depend on flow conditions near river bed and on FST equipment.

Flows around surface mounted obstacles are studied intensively due to their large relevance for many practical problems, among which are effective cooling of components in electronics, wind load on buildings, and operation safety for aircraft in hill areas. These so called *junction* flows are characterized by a number of various interacting processes, including separation of the oncoming boundary layer, separation of the flow from the body itself and formation of the recirculation zone. Flows around square and circular cylinders, pyramids, cones and hemispheres submerged in a wall boundary layer show some common, as well as some very distinct flow features, specific only for those particular body forms and proportions. Due to the complexity of junction flows, it is not possible to study them theoretically, and most studies are performed experimentally or, in recent times, using numerical models.

Although studies for hemispherical objects are not as multiple as, for example, for a circular cylinder, some experimental and numerical studies exist. These form a basis for the study of the factors influencing drag and lift coefficients, which further can be used in a computational approach to FST-hemispheres. In particular, the influence of the Reynolds and Froude numbers, relative submergence of a hemisphere, near-bed velocity profile form, surface roughness of a plate and a hemisphere, and of the free stream turbulence level are of interest.

## 5.1 Flow pattern around an obstacle on a surface

### 5.1.1 Classification of flow separations

A hemispherical obstacle in a flow field is a bluff body, characterized by a major contribution of pressure drag (and lift) to the total hydrodynamical force (see Section 4.2.1). Magnitude and temporal variation of pressure forces, associated with a separation of a boundary layer developing along a body, depend on the flow pattern within and the size of the *wake* – a region of strongly retarded flow immediately to the rear of an obstacle. Leder [48] in his topological classification of flows with separations distinguishes three main classes. Depending on the geometrical arrangement of free shear layers, these classes are (see Figure 5.1):

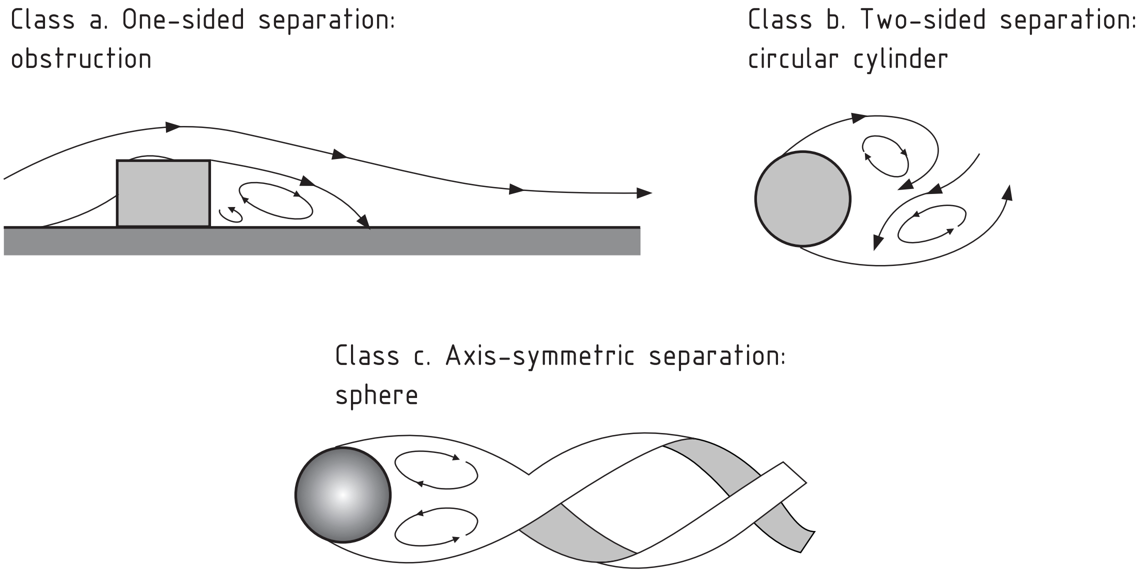

**Figure 5.1:** Classes of flows with separation, from Leder (1992) [48]

**Class a:** One-sided shear layer separation with further reattachment;

**Class b:** Two-sided shear layer separation with mutual interactions;

**Class c:** Axis-symmetric shear layer separation with mutual interactions.

Flow characteristics in the wake differ considerably between those classes. Flows of class **b**, with a typical example of an infinite circular cylinder, are characterized by a more distinct frequency of velocity and pressure pulsations and a higher level of turbulent stresses in the wake than those of classes **a** and **c**. Periodic pulsations of flow quantities in the wake are associated with the formation of large scale *coherent structures* – vortices. The shear layers that separate from the sides of a body tend to roll up, producing vortices with dimensions approaching the size of the body generating them. After formation, these are transported downstream, leaving unique signatures in the power spectra of pulsations.

Formation and transport of vortices is associated with a pulsation of the pressure field, which results in a temporal variation of integral lift and drag forces acting on a body. For example, for an infinite circular cylinder in a uniform flow field, the time-averaged lift is around zero, but the magnitude of the periodical lift component is considerable and the deviation of the periodical lift coefficient from the mean reaches values of $\widetilde{c}_l = \pm 0.2$–$0.6$ at Reynolds number[1] $Re_{U_0} = 5\times 10^4$ [94]. For a sphere at $Re_{U_0} = 10^4$, the magnitude of the periodical span-wise force components (lift and side forces) is less than for a cylinder and $\widetilde{c}_l$ is only about ±0.05, according to numerical simulations [11]. The flow around a cylinder belongs to class **b** of the topological classification, identified by a well known *von Kármán vortex* shedding phenomena. Flow around a sphere belongs to class **c** and is characterized by formation and transport of special helical vortex structures.

### 5.1.2 Vortex systems for the flow around a surface mounted hemisphere

The large relevance of body–wall junction flows for many practical problems resulted in numerous experimental, as well as numerical studies. Flows around pyramids, cubes, cones, hemispheres and other objects mounted on a wall show some common, as well as some very distinct flow features. The so called *horseshoe vortex* structure, resulting from the separation of the oncoming wall boundary layer, is typical for all flows around bluff obstacles. In contrast, flow separation patterns on a body itself vary considerably, depending mainly on the object's form and proportions.

#### 5.1.2.1 Horseshoe vortex

The combined effects of streamwise and vertical pressure gradients upstream of a body-wall junction, respectively due to a blockage effect of the obstacle and momentum deficit in the boundary layer, force the latter to separate, forming this complex vortical structure [52]. It is represented by one or more vortices trailing around and downstream of the obstacle in form of a horseshoe (see Figures 5.2a,b): a horseshoe vortex.

The structure of a horseshoe vortex system greatly depends on the state – laminar or turbulent – of a bottom boundary layer: starting with a no-recirculation pattern at very low Reynolds numbers, the number of primary and secondary vortices in the symmetry plane grows, and up to six vortices can be observed for laminar boundary layers; at higher Reynolds numbers, the vortex system becomes unsteady and finally turbulent. For the turbulent horseshoe vortex, which is of interest for the present study, an extensive review of Ballio et al. [6] concludes the following:

- the main parameter affecting the vortex structure is the width of an obstacle in the transverse direction; extreme ratios of an object's height to width can also affect the longitudinal and vertical size of a vortical structure;

---

[1] Reynolds number $Re_{U_0} = D\,U_0/\nu$ based on a body's diameter $D$ and a free steam flow velocity $U_0$.

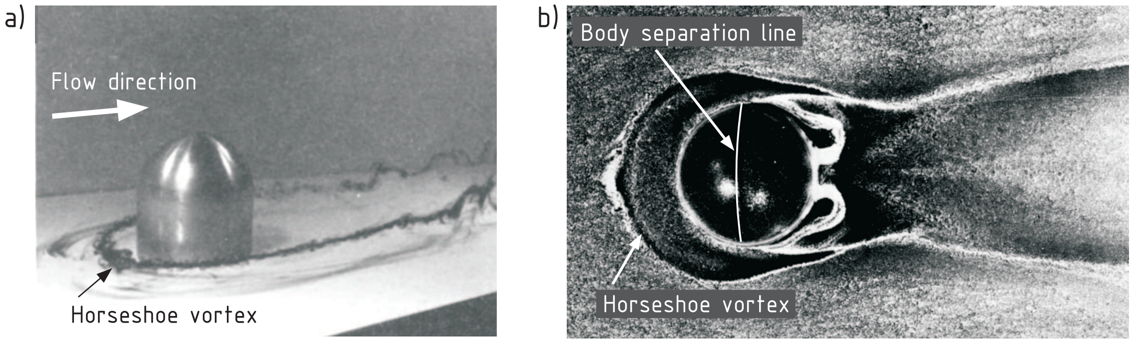

**Figure 5.2:** Horseshoe vortices for flows around: a) hemisphere-cylinder at $Re_{U_0} = D\,U_0/\nu = 1\times10^3$ (side view), from Okamoto (1982) [60]; b) hemisphere at $Re_* = D\,u_*/\nu = 1.1\times10^3$ (top view), from Taniguchi and Sakamoto (1982) [90]

- blunt obstacles distort the flow more than slender ones, therefore generating larger vortex systems; prisms generate generally larger structures than cylinders and round-nosed wings;
- the bottom shear stress generated by a horseshoe vortex is several times larger than that of the undisturbed flow;
- numerical simulations of the turbulent horseshoe vortex generally reproduce well the experimental data. This fact is particulary surprising, as most calculations were performed with eddy viscosity turbulent models (for example, $k-\epsilon$ model), which, theoretically, cannot resolve such flows. Despite the complex unsteady nature of a vortex system, a steady solution of RANS equations can properly resolve the mean flow quantities, and, if the computation runs in an unsteady mode, solutions turns out to be time independent.

#### 5.1.2.2 Von Kármán and arch vortices

The flow pattern behind an obstacle, in contrast to a formally “steady” horseshoe vortex structure, shows a distinct dynamical behavior. Depending mainly on form and proportions of a body, the vortices dominating the flow in a wake are either asymmetric spanwise vortices, known as *von Kármán* vortices, or symmetric *arch* (hairpin) vortices. The former regime corresponds to class **b** of Leder’s topological flow classification and shows a much higher degree of flow parameters’ fluctuations than the regime with symmetrical vortex shedding. As these pulsations are not as much pronounced for the latter, often a "suppression" of vortex shedding is reported [66], [97].

The criteria for the existence of one or another regime vary for different object forms and proportions. Generally, the more the flow approximates the two-dimensional case, the higher the possibility of asymmetrical vortex shedding. For example, for square prisms and circular cylinders placed vertically in a turbulent boundary layer, Sakamoto and Arie [66] have found, that the switch between two regimes of vortex shedding occurs at object's height to spanwise width (diameter) ratios $H/D$ of 2 and 2.5, respectively. At smaller aspect ratios, arch vortices dominate the wake (Figure 5.3a), at larger ones, those of the von Kármán type (Figure 5.3b). It is hypothesized, that for bodies with small aspect ratios, the flow over the top edge is responsible for the suppression of the von Kármán vortex shedding process. Values for the critical aspect ratio variate slightly among references, even for bodies of the same form, pointing out the influence of other factors, for example, the velocity gradient in the boundary layer.

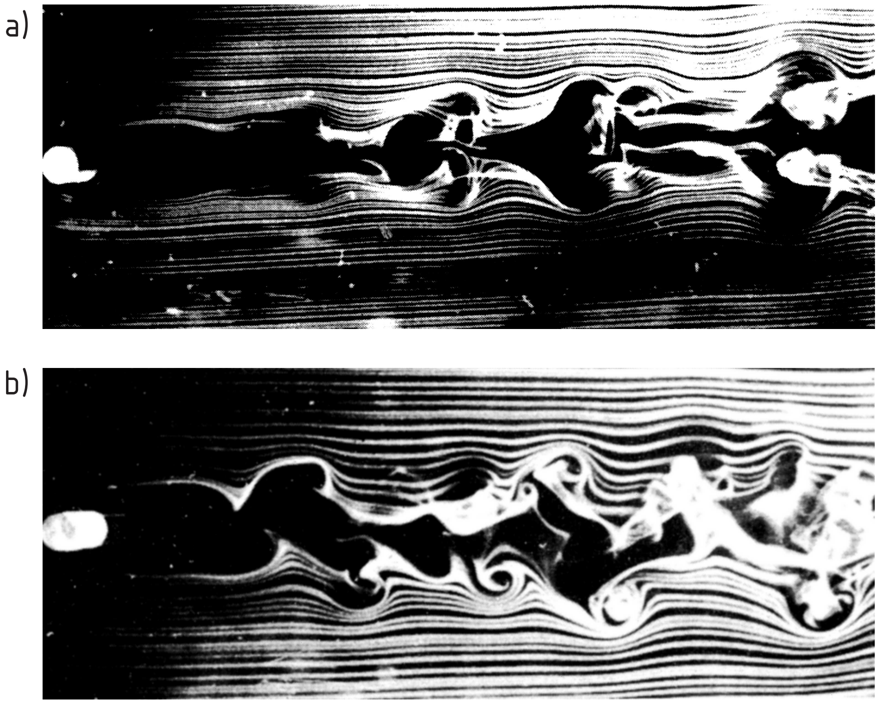

**Figure 5.3:** Top view of vortices in a wake of a circular cylinder: a) arch type ($H/D = 2.5$); b) von Kármán type ($H/D = 4$), from Sakamoto and Arie (1983) [66]

Most references for flow around a surface attached hemisphere allow to suggest the dominance of symmetrical vortex shedding in a wake of this body. For a hemisphere in a laminar boundary layer, this thesis is supported experimentally by flow visualizations in

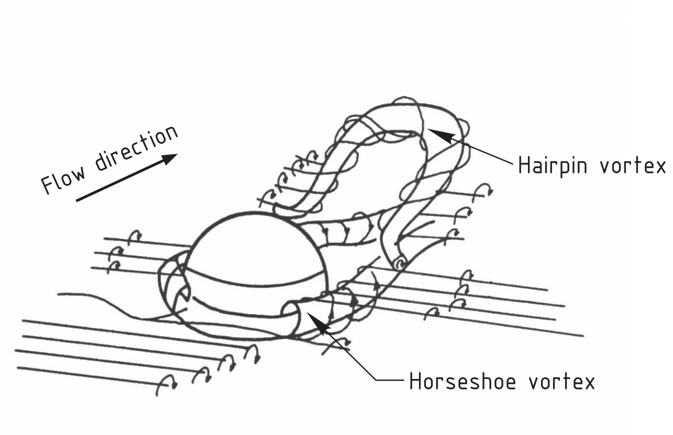

**Figure 5.4:** Sketch of vortical structures for a hemisphere submerged in a laminar boundary layer, from Acalar and Smith (1987) [2]

water flumes [2], [67]. In Figure 5.4, a schematic view of a horseshoe and arch vortex[2] for a hemisphere is shown. According to Acalar and Smith [2], periodical vortex shedding in form of distinct hairpins is initiated at Reynolds number $\mathrm{Re}_{ht} = 2\, r_h\, u_{ht}/\nu = 240$, with $r_h$ the hemisphere radius and $u_{ht}$ a velocity of an undisturbed boundary layer at the level of a hemisphere's top. With $\mathrm{Re}_{ht} = 2\,800$ the "wake becomes irregular" with multiple peaks in the power spectra, suggesting that the dominant frequency of vortex shedding does not exist at higher Reynolds numbers. Savory and Toy [67] presume, that for a hemisphere in a turbulent boundary layer, if any periodic vortex shedding exists, the associated vortical structures do not persist very far downstream. Shamloo et al. [78] investigated, among other aspects, the effect of relative submergence on a flow pattern around a hemisphere in a laboratory flume. For flows at Reynolds numbers[3] $\mathrm{Re}_{0.4}$ ranging from 3000 to 44 000, they distinguish two major regimes. When the relative submergence $h/r_h$ is greater than one, separation from the top and the sides of the obstacle produces arch vortices. However, when flow depth $h$ is less than the height of an obstacle, the typical von Kármán vortex street develops in a wake.

The evidence of symmetrical vortex shedding for a hemisphere in a laminar boundary layer is supported by numerical simulations of Tufo et al. [95]. Vortex structures obtained through flow visualization techniques are very similar to those documented by Acalar and Smith [2]. Manhart [51] studied turbulent separation flow from a hemisphere at $\mathrm{Re}_{u_0} = 1.4\times10^5$ using Large Eddy Simulation (LES) and the Proper Orthogonal Decomposition method for identification of coherent structures. He resumes, that von Kármán vortices

---

[2] Arch vortices are sometimes referenced as *hairpin* vortices

[3] $\mathrm{Re}_{0.4} = 2\, r_h\, u_{0.4}/\nu$, with $r_h$ the radius of a hemisphere and $u_{0.4}$ the mean column flow velocity

are also shed from a hemisphere in a quasi-periodic regime and contribute about 24 % of total turbulent energy dissipation in a wake. The remaining energy dissipation is associated with a symmetrical vortex shedding process in form of arch vortices. This numerical study, however, is the only one in which asymmetrical vortex shedding for a hemisphere is found.

Summarizing, a hemisphere as a three-dimensional obstacle with a small aspect ratio of $H/D = 0.5$, should probably represent a mixed case of classes **a** and **c** according to the classification of Leder. Thus, a relatively small magnitude of periodical lift and drag force components, associated with shedding of symmetrical arch vortices, can be hypothesized for a FST-hemisphere.

### 5.1.3 Parameters governing flow around a hemispherical obstacle

Following, the main parameters influencing the flow pattern around a hemisphere mounted on a wall and consequentially the integral forces on it, are described.

#### 5.1.3.1 Reynolds number

The Reynolds number is a very important parameter for flows past bluff bodies, and its influence is connected to the phenomenon of boundary layer flow.

Even for a fluid of negligible viscosity like water, the no–slip condition (fluid has zero velocity at a solid boundary) is valid. This means, that along the body's surface a layer exists, in which velocity should grow from zero to the value of a free stream flow. This layer, with a large velocity gradient normal to the surface, is called *boundary layer* and the flow in it is referred to as *shear flow*. The thickness of a boundary layer, negligible at the stagnation point (see Figure 5.5a), increases in general with distance along the body. Initially in a laminar regime, a boundary layer flow progresses downstream and somewhere, if the velocity of the free stream is sufficiently high, it encounters a transition to a turbulent state.

The switch from laminar to turbulent regime in a boundary layer takes place at the so called *transition Reynolds number* defined as:

$$Re_t = \frac{x_t\, U_0}{\nu} \qquad [\text{-}] \tag{5.1}$$

with $Re_t$ = transition Reynolds number [-]
$x_t$ = distance along the surface from the stagnation to transition point, [m]
$U_0$ = free stream velocity, [m/s]
$\nu$ = kinematic viscosity of fluid [$m^2/s$]

$Re_t$ itself is affected by many parameters, the most important ones being the pressure

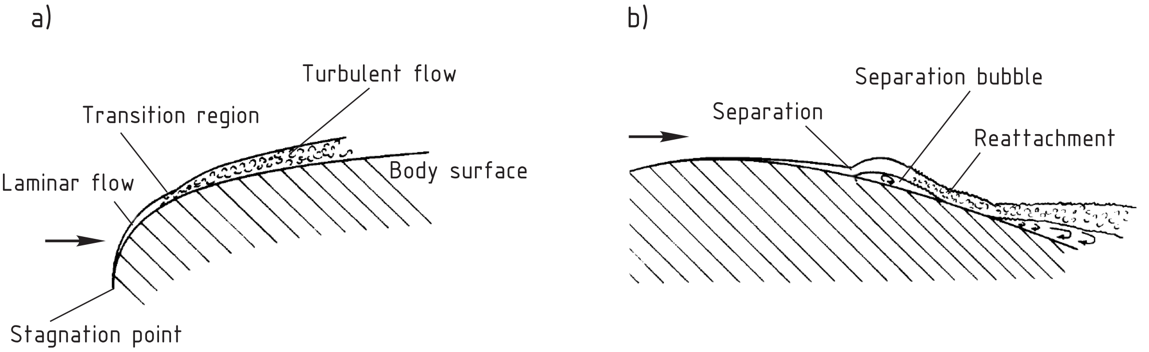

**Figure 5.5:** Boundary layer flow around a bluff body: a) transition from laminar to turbulent state; b) separation bubble in case of laminar separation, from Thompson (2003) [93]

distribution in the external flow, the roughness of the body surface, and the intensity of turbulence in the external flow.

As the boundary layer of bluff bodies would separate in most practical cases, Reynolds number plays an important role for determination of pressure drag, as it defines the state of the boundary layer prior to its separation. If the boundary layer, developing along the body's surface, is laminar and separation occurs, then, for a given free-stream velocity, the drag force is usually greater than when the boundary layer is turbulent, even if the latter also separates. The reason for this is, that for bodies without sharp edges, a turbulent boundary layer can remain longer attached to the surface than a laminar one, causing the separation point to move downstream. This postponement of separation results in a considerable size reduction of a wake and, as a consequence, a remarkable drop in the drag coefficient. It is also possible, that a laminar boundary layer undergoes transition after separation with a possible reattachment of the turbulent boundary layer and formation of a separation bubble (see Figure 5.5b). The Reynolds number based on the characteristic size of a body at which this sudden drop in the drag coefficient occurs is called *critical Reynolds number*. The flow regimes with laminar and turbulent boundary layer separation are referred to as subcritical and supercritical regimes, respectively. Fortunately, for flows around bluff bodies, if either the laminar flow predominates or the turbulent flow is well established in the boundary layer, the exact value of Reynolds number tends to become unimportant. Thus, within the ranges of $Re$ corresponding to the subcritical and supercritical regimes, the drag (and lift) coefficients vary only slowly with change in Reynolds number.

The influence of Reynolds number on the total drag coefficient $c_d$ for a hemisphere mounted on a wall is investigated in a water flume by Flammer et al. [21]. The total drag

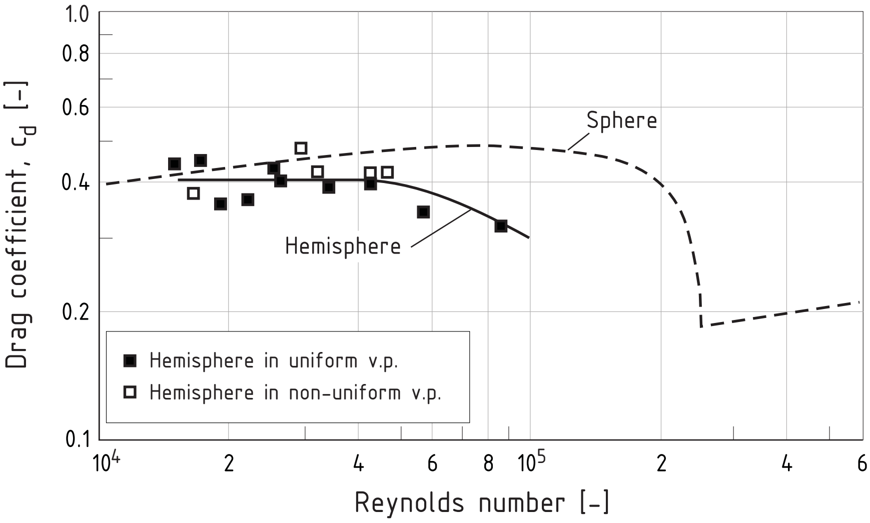

**Figure 5.6:** Drag coefficient for a hemisphere mounted on a bottom of a laboratory flume in dependency from $\mathrm{Re}_{0.4} = 2\, r_h\, u_{0.4}/\nu$, from Flammer et al. (1970) [21].

force – the sum of the viscose and pressured drag – is measured with a strain-gage dynamometer. Reynolds number is defined upon the mean column velocity $u_{0.4}$ of a channel flow and the radius of a hemisphere $r_h$. From Figure 5.6 can be seen, that in the range of $\mathrm{Re}_{0.4}$ from 1.5 to $4.5\times10^4$, the drag coefficient has an approximately constant value of 0.4 and then slowly starts to decrease, reaching a value of 0.3 at $\mathrm{Re}_{0.4} = 10^5$. Transition from a subcritical to a supercritical regime for a hemisphere attached to a wall is more gradual and starts at a lower Reynolds number than for a free floating sphere in a uniform velocity profile. Flows with Reynolds numbers corresponding to a supercritical regime are not examined in that study. These findings correspond to the experimental results of Savory and Toy [67] (see also Sections 5.1.3.4 and 5.3.1), in which, upon the pressure distribution over a hemisphere in a wind tunnel, the authors conclude, that for a smooth hemisphere even at $\mathrm{Re}_{ht} = 2r_h u_{ht}/\nu = 1.4\times10^5$ the supercritical regime is still not reached. In contrast, for a hemisphere with a roughened surface, transition is completed already at $\mathrm{Re}_{ht} = 5\times10^4$. Unfortunately, the integral drag and lift coefficients are not evaluated in this study.

The data in Table 5.1 serves to define the range of Reynolds numbers $\mathrm{Re}_{ht}$ relevant for the FST-hemispheres method. Here, the minimum and maximum flow velocities corresponding to the condition of incipient motion for the lightest and heaviest hemispheres with densities of 1.015 and 10.009 g/cm$^3$, respectively, are calculated using Formula 4.8. Equal drag and lift coefficients of 0.4 are assumed and the friction coefficient from Table 4.3 for the corresponding FST-hemisphere placement methods is taken.

It follows, that FST measurements correspond mostly to subcritical and transitional flow

| Plate type | FST placement method | $\mu$ | $u_{ht}^{min}$ | $u_{ht}^{max}$ | $Re_{ht}^{min}$ | $Re_{ht}^{max}$ |
|---|---|---|---|---|---|---|
| | | – | m/s | m/s | – | – |
| smooth | drop | 0.05 | 0.043 | 1.046 | $3.3\times10^3$ | $8.1\times10^4$ |
| smooth | press | 0.60 | 0.120 | 2.935 | $9.3\times10^3$ | $2.3\times10^5$ |
| structured | - | 0.24 | 0.086 | 2.109 | $6.7\times10^3$ | $1.6\times10^5$ |

**Table 5.1:** Minimum and maximum near-bed velocities and corresponding Reynolds numbers for various FST ground plates and hemisphere's placement methods

regimes, assuming the other parameters which can influence the transition are the same as in the experiments of Flammer et al. [21]. The FST-hemisphere numbers, until which the drag coefficient can be assumed to be a constant of 0.4 (this corresponds to the Reynolds number $4.5\times10^4$ – see Figure 5.6) are 16 and 7–8 for the "drop" and "press" placement methods with the smooth plate, and 9 with the structured plate, respectively.

#### 5.1.3.2 Velocity profile form

The studies of Flammer et al. [21] and Savory and Toy [67] suggest, that velocity profile form is practically irrelevant for determination of drag on a hemisphere.

In [21], the drag coefficient evaluated from measurements in a uniform velocity profile (just behind the inflow to a flume) and fully developed velocity profile (in the middle of a flume) is $0.4 \pm 0.1$ in the range of $Re_{0.4}$ of $2\times10^4$ to $10^5$. It is independent from the velocity profile form parameter defined as:

$$P_u = \frac{u_{0.8r_h} - u_{0.2r_h}}{0.6\, r_h} \cdot \frac{h}{u_{0.4}} \qquad [-] \qquad (5.2)$$

with $P_u$ = velocity profile form parameter, [-]
$u_{0.8r_h}, u_{0.2r_h}$ = velocities at distances of $0.8\, r_h$ and $0.2\, r_h$ above bottom, [m/s]
$u_{0.4}$ = mean column velocity, [m/s]
$r_h$ = hemisphere radius, [m]
$h$ = water depth, [m]

However, these results show a relative large scatter of ±0.05 even for measurements at the same Reynolds number.

In [67], the normalized with $u_{ht}$ pressure coefficient distributions around hemispheres submerged in three boundary layers with different velocity gradients are almost identical. This fact suggests, that the integral drag and lift coefficients, obtained through the integration of pressure over the body's surface, would also be the same for these boundary layers.

Still, a large scatter in the drag coefficient in [21], absence of values for an integral drag coefficient in [67], and the general absence of reference values for the lift coefficients make the numerical investigation of the velocity profile form influence necessary.

#### 5.1.3.3 Froude number and relative submergence

Froude number $\mathrm{Fr}$, the dimensionless quantity representing the ratio of the inertia to gravity forces in the flow, is defined as:

$$\mathrm{Fr} = \frac{u_{0.4}}{\sqrt{g\,h}} \qquad [\text{-}] \tag{5.3}$$

with $\mathrm{Fr}$ = Froude number, [-]
$u_{0.4}$ = mean column velocity, [m/s]
$g$ = acceleration due to gravity, [m/s$^2$]
$h$ = water depth, [m]

Influence of Froude number and relative submergence $h/r_h$ on the integral drag on a hemisphere is well documented in [21]. As it follows from Figure 5.7, the influence of the Froude number is negligible at relative submergences higher than 4. The remaining scatter in the total drag coefficient in the zone of the “negligible free surface effects” is related to the effect of a drag drop at transition Reynolds numbers. By definition, if the Froude number increases, so does the Reynolds number. As most measurements are done in the range of transitional Reynolds numbers, an increase in the Reynolds number is the reason for the decrease in the drag coefficient (see Section 5.1.3.1) and, consequently, a scatter in coefficient values. In contrast, the drag coefficient at smaller relative submergences increases considerably, reaching values of 2–2.5 at $h/r_h = 1$ in the range of Froude numbers 0.3–0.9.

An interesting parallel to the study of Shamloo et al. [78] can be noticed. Their results show, that for relative submergences less than 1, the symmetrical vortex shedding from a hemisphere is replaced by shedding of von Kármán vortices. Here, the flow around a hemisphere already does not resemble a three-dimensional, but a two-dimensional flow around a circular cylinder. The drag coefficient for a circular cylinder in the infinite uniform flow is at least two times larger than for a hemisphere and has a value of $\approx$1 in a subcritical regime.

This imposes a restriction on water depth during FST-hemisphere measurements: measured from the plate, it should exceed at least 16 cm to eliminate the influence of Froude number and relative submergence on hydrodynamic coefficients. This restriction should be accounted for in numerical modelling.

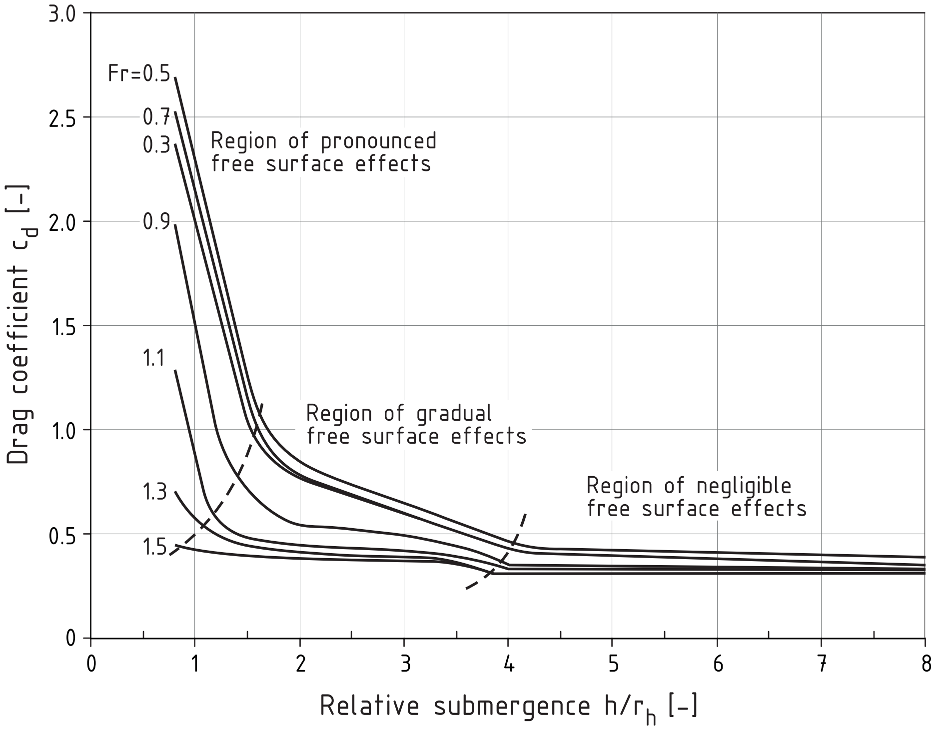

**Figure 5.7:** Total drag coefficient for a hemisphere in dependency from Froude number $Fr = u_{0.4}/\sqrt{g\,h}$ and relative submergence $h/r_h$, from Flammer et al. (1970) [21]

#### 5.1.3.4 Surface roughness and free stream turbulence

Surface roughness and increased free stream turbulence can influence the critical Reynolds number at which the drop in the drag coefficient occurs. For example, if in experiments a body without sharp edges is supported by means of a strut attached to it in the dead water region, and the turbulent intensity of the oncoming stream is low, the boundary layer is not disturbed, and the diminished drag on a body can be obtained without influencing the critical Reynolds number. On the other hand, if the flow is very turbulent or the body is supported by means of thin wires attached in the streamline region, the critical Reynolds number is found to be much smaller [63].

Savory and Toy [67] investigated the influence of roughness on transition for a hemisphere. In Figure 5.8, a change of the centerline pressure drag coefficient with Reynolds number for smooth and rough, wall mounted hemispheres is shown. Centerline pressure drag coefficient is defined as:

$$c_{d_{CL}} = \int_0^{\pi} \frac{\overline{p} - p_0}{1/2\,\rho\,U_0^2} \cos\theta \; d\theta \qquad [-] \tag{5.4}$$

with $c_{d_{CL}}$ = centerline pressure drag coefficient [-]
$\overline{p}$ = local mean (time-averaged) static pressure [Pa]
$p_0$ = reference static pressure of a free stream , [Pa]
$U_0$ = free-stream velocity, [m/s]
$\rho$ = density of fluid, [kg/m$^3$]
$\theta$ = elevation angle (see Figure 5.11b) [°]

The rough hemisphere in the experiment has a roughness ratio $k/d_h = 0.01$, what would result for our FST-hemisphere in a geometrical roughness height $k$ of 0.8 mm. It follows from Figure 5.8, that for the rough hemisphere, the transition occurs much earlier (and faster) than for a smooth one – at $Re_{U_0} = 2\text{–}5 \times 10^4$. For the smooth hemisphere, even at $Re_{U_0} = 1.4 \times 10^5$, the centerline drag coefficient still decreases.

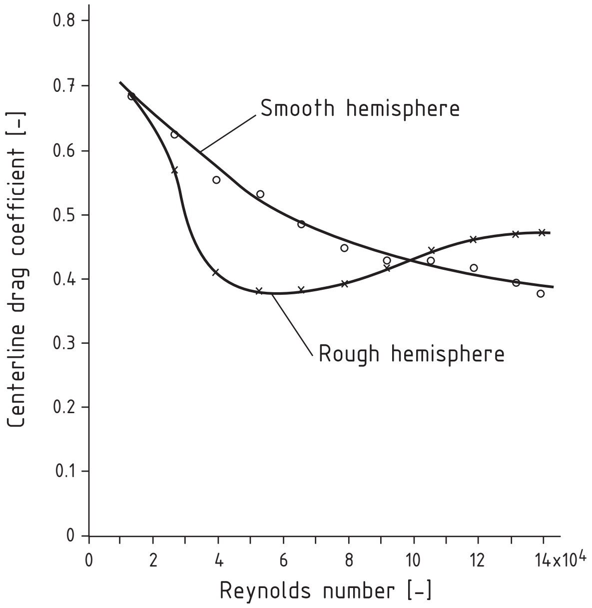

**Figure 5.8:** Centerline pressure drag coefficient $c_{d_{CL}}$ in dependency from Reynolds number $Re_{U_0}$ for smooth and rough hemispheres on a wall, from Savory and Toy (1986) [67]

In wind tunnels, free stream turbulence levels can be as low as 0.05 % [22], allowing to separate the effects of roughness and turbulence on the critical Reynolds number. This is true for bodies in infinite flow fields, but questionable for those attached to a wall, as the turbulence intensity near the wall always exhibits very high levels. In numerical studies, the possibility to evaluate the effect of free-stream turbulence would depend on the capabilities of the turbulent model used.

Generally, it seems to be impossible to assess the effect of surface roughness on the drag coefficient for FST-hemispheres. Some scratches always appear on their surfaces during field measurements, but they are not equally distributed, and also amount and depth of scratches varies from hemisphere to hemisphere within the set. Theoretically, it is possible, that a new FST-hemisphere would have a higher drag coefficient than a worn-out at the same Reynolds number, as for the latter an earlier transition can be facilitated by scratches.

It is also possible, that the kind of the FST ground plate (smooth, rough) can affect transition for a hemisphere and thus drag and lift coefficients. It would be of advantage to investigate this in numerical experiments.

## 5.2 Numerical model

FLUENT [22], a state-of-the-art computer program for modelling fluid flow and heat transfer in complex geometries, is used for numerical simulation of the velocity gradient flow past a hemisphere. The two main applications within the FLUENT software package used in the present study are:

- FLUENT, the solver and
- GAMBIT, the preprocessor for geometry modelling and mesh generation.

Once a mesh generated with GAMBIT has been read into FLUENT, all remaining operations are performed within the solver. These include setting boundary conditions, defining fluid properties, executing the solution, refining the mesh, and viewing and post-processing the results.

Among important FLUENT solver's modelling capabilities are:

- two- and three- dimensional flows;
- mesh flexibility allowing quadrilateral, triangular, hexahedral (brick), tetrahedral, prism (wedge), pyramid, and mixed element meshes;
- steady-state or transient flows;
- inviscid, laminar, and turbulent flows;
- free surface and multiphase models for gas-liquid, gas-solid, and liquid-solid flows.

Thus, this software package includes all important prerequisites for modelling the flow around a hemisphere, offering additionally a flexible setup of experiment conditions and various capabilities for the analysis of results.

### 5.2.1 Physical equations

The velocity gradient flow past an FST-hemisphere placed on a river bottom is in general non-stationary, three-dimensional, turbulent, and with the presence of a free surface. It is clear, that a complete modelling of above mentioned features is an impossible task, thus a simplified physical model has to be found.

First, the presence of a free surface can be excluded from consideration, as at relative submergences $h/r_h > 4$ the drag coefficient is independent from the Froude number and remains a constant, assuming all other parameters are kept the same (see Section 5.1.3.3). Thus, the open channel flow can be modelled as a closed conduit with a symmetry condition at the top boundary.

Second, as it is not possible to model every stone at the bottom, the influence of substrate and, therefore, near-bed velocity profile form, can be accounted for only in a simplified way. It is supposed, that a predefined velocity profile at the inflow boundary and a moving wall condition at the level of the substrate tops can reproduce a flow field over a rough bed. In doing so, a hemisphere should be placed not too far away from the inflow boundary to ensure, that the prescribed velocity profile does not change considerably from entrance to obstacle. At the same time, this distance should not be too short so that the distortion the obstacle produces in the flow does not collide with the inflow profile.

For all kinds of flows, laminar and turbulent, FLUENT solves conservation equations for mass and momentum. To account for small-scale turbulent fluctuations, it employs two alternative methods to transform Navier-Stokes equations: Reynolds averaging and filtering.

The Reynolds-averaged Navier-Stokes (RANS) equations are transport equations for mean flow quantities only, with all the scales of the turbulence being modelled (see also Section 3.2.1). This approach greatly reduces the computational effort and is generally adopted for practical engineering calculations.

Large Eddy Simulation (LES) provides an alternative approach, in which the large eddies are computed in a time-dependent simulation that uses a set of “filtered” equations. Filtering is essentially a manipulation of the exact Navier-Stokes equations to remove only those eddies that are smaller than the size of the filter, which is usually the mesh size. Until recent time, typical applications of LES have been flows in simple geometries. This is mainly because of the large computing resources required to resolve the energy-containing turbulent eddies.

In general, the choice of the specific turbulence model should be based on the physics encompassed in the flow, the established practice for a specific problem class, the level of accuracy required, the available computational resources, and the amount of time available for the simulation. For practical applications, the use of conventional turbulence models employing the Reynolds-averaged approach is recommended [22]. To predict correctly a laminar boundary layer separation for a hemisphere in subcritical regime, the so called low Reynolds number turbulence model, capable to resolve a flow in a laminar sublayer, should be applied. Within the current FLUENT solver, following low Reynolds number models are available: Spalart-Allmaras, RNG $k-\epsilon$ model and SST $k-\omega$ turbulence model. Unfortunately, as later calculations showed, the RNG $k-\epsilon$ model could be employed only in the high Reynolds number mode, so it was disregarded for further simulations.

#### 5.2.1.1 Spalart-Allmaras turbulence model

The Spalart-Allmaras model [81] is designed specifically for aerospace applications involving wall-bounded flows and has shown to give good results for boundary layers subjected to adverse pressure gradients. This one-equation model solves a transport equation for a modified kinematic eddy viscosity $\widetilde{\nu}_t$. The transported variable $\widetilde{\nu}_t$, in principle, is identical to the turbulent kinematic viscosity, except in the near-wall (viscous-affected) region. As only one transport equation for turbulent quantities has to be solved, the Spalart-Allmaras model is the least expensive turbulence model offered within FLUENT in terms of computational effort.

In this study, the model is used with default modelling constants, the values for which, together with the complete model description, can be found in the FLUENT 6.1 User's Guide [22]. The option "strain/vorticity-based production" is activated, what allows a more correct accounting for the effects of rotation on turbulence in the vortical flows.

#### 5.2.1.2 The SST $k-\omega$ turbulence model

The shear-stress transport (SST) $k-\omega$ model [53] is developed to effectively blend the robust and accurate formulation of the standard $k-\omega$ model in the near-wall region with a free-stream independence of the $k-\epsilon$ model in the far field. Like a standard $k-\omega$ model it is an empirical model based on transport equations for the turbulence kinetic energy $k$ and the specific dissipation rate $\omega$, which is basically a ratio of turbulence dissipation rate $\epsilon$ to $k$. The SST $k-\omega$ model is more accurate and reliable for a wider class of flows (e.g., adverse pressure gradient flows, airfoils, transonic shock waves) than the standard $k-\omega$ model.

In this study, this model is used with default modelling constants of FLUENT. The option "transitional flows" is enabled to ensure the low-Reynolds-number correction to the turbulent viscosity [22].

### 5.2.2 Computational domain

For practical reasons, it is decided to model a real size FST-hemisphere of radius $r_h = 3.9$ cm. Water density and kinematic viscosity are set to 998 $\mathrm{kg/m^3}$ and $1.003\times10^{-6}$ $\mathrm{m^2/s}$, respectively, in all simulations. The advantage of symmetrical vortex shedding (see Section 5.1.2.2) is used to reduce the size of the mesh and therefore computational effort. Only half of a channel – 0.25 m high and 0.5 m wide – is modelled (see Figure 5.9). The blockage in the numerical experiment, defined as a ratio of the body cross-sectional area to the channel cross-sectional area, is less than 1 %.

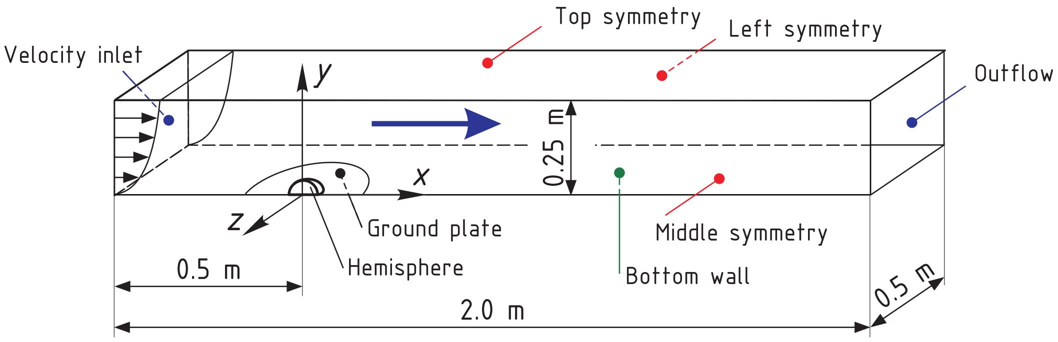

**Figure 5.9:** Computational domain: half of a rectangular channel with a hemisphere

The total length of the channel is 2 m and the hemisphere is placed 0.5 m downstream from the inflow boundary. To allow modelling the FST ground plate, the circle within the bottom wall around the hemisphere with a radius of 0.2 m is marked as a separate zone. The influence of the plate on the flow is investigated by specifying a roughness height in this area or leaving it smooth. The round shape is easier to implement during mesh generation. It is assumed, that the form of the plate does not play a critical role.

All simulations are subdivided into two classes: flows over "smooth" bottom and flows over "rough" bottom. The first class is used for the verification of numerical model performance by comparison of the results with laboratory data. Simulations over rough bottom serve to find out the influence of the velocity profile form on drag and lift coefficients. For the first class, the bottom wall coincides with the physical channel bottom. For the rough bottom, it coincides with the level of the imaginary roughness element tops.

Like shown in Figure 5.9, following boundary conditions are applied: at the center-plane, water surface and left channel side – the symmetry boundary condition; the channel bottom, FST ground plate and FST-hemisphere surface are walls. The inflow boundary is set to "velocity inlet" with a specified vertical velocity profile and mean turbulence quantities. The outlet is modelled with a standard FLUENT outflow boundary condition. Details of the inflow velocity profile specifications are given in Sections 5.3.1 and 5.4.1.

One necessary step in numerical modelling is to test for dependence of the solution on mesh resolution. Three mesh types are constructed: a very fine *Mesh 1*, a fine *Mesh 2* and a coarse *Mesh 3*, with a total number of cells of 920 610, 891 995 and 210 037, respectively. Mesh 1 and 2 have the same resolution over almost the whole domain and only near the hemisphere Mesh 1 is two times finer than Mesh 2. On contrary, Mesh 3 is coarser than the others in the whole domain. Near the hemisphere, it is five times coarser than Mesh 1.

### 5.2.3 Computational procedure

A single precision segregated solver is used for all simulations, as there are no differences between results obtained by single and double precision solvers. The convergence criteria for continuity, velocity components and turbulent quantities is set to $10^{-5}$.

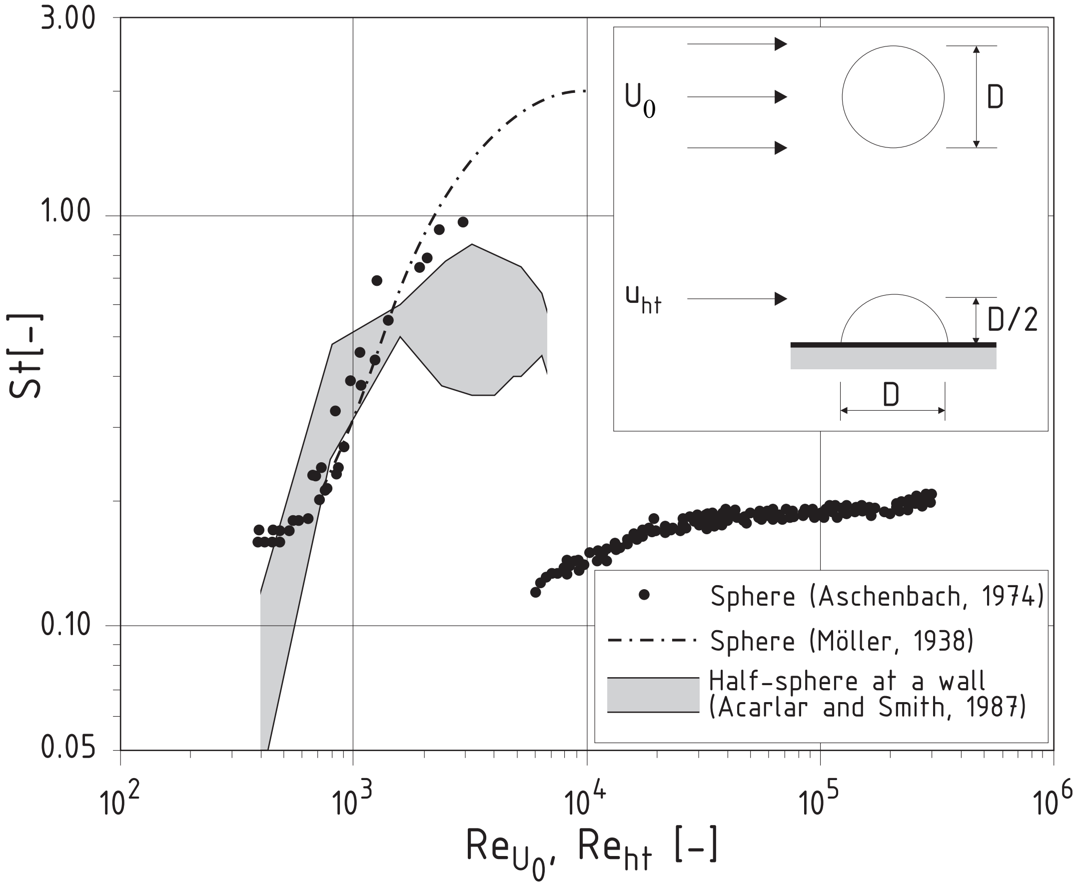

**Figure 5.10:** Dependency of Strouhal number St from Reynolds number $Re_{U_0}$, $Re_{ht}$ for a sphere in uniform flow and a hemisphere on a wall in a boundary layer

The calculation procedure is as follows: at first, the flow in the domain is initialized with constant quantities for the turbulent parameters and zero components of vertical ($v$) and span-wise ($w$) velocity. A logarithmical velocity profile ($u$ velocity component) is patched over the domain from the inflow boundary. Then, a simulation is started in a steady-state regime and continues while residuals reduce. Very often, especially in runs with a low free stream turbulence intensity, the solution starts to diverge after 10–20 iterations and has to be switched to an unsteady regime. In favorable situations, a maximum of 80 iterations can be performed in a steady regime with the residuals decreasing to $10^{-3}$.

Calculations are continued in an unsteady regime until the values of drag and lift coefficients stabilize. In almost all cases, the solution converges to a quasi steady-state and the coefficients change at max $\pm 0.005$ from the mean value. This fact could support the suggestion of Savory and Toy [67], that in high turbulent flow, arch vortices are very weak and do not persist long downstream of a hemisphere. However, it can also mean, that the numerical model is unable to reproduce symmetrical vortex shedding, for example, due to a coarse mesh resolution. After a quasi steady-state has been reached, residuals remain below $2\times10^{-5}$ in every iteration. In one run, however, performed at a transitional Reynolds number and characterized by a low level of inflow turbulent intensity, the solution reaches a point of seeming steady-state at first, but collapses after some iterations and, finally, diverges.

The time step for unsteady calculations is chosen according to Figure 5.10, where the dependency of the Strouhal number from Reynolds number for a sphere and a hemisphere is shown. Strouhal number, a dimensionless value correlating to the frequency of vortex shedding, is defined as:

$$St = \frac{f\,D}{U_0} \qquad [-] \tag{5.5}$$

with $St$ = Strouhal number, [-]
$f$ = frequency of vortex shedding, $[s^{-1}]$
$D$ = characteristic size of an object, [m]
$U_0$ = characteristic velocity of a flow, [m/s]

For a hemisphere, the characteristic size is its diameter and the characteristic velocity is at the top of it. As the Reynolds number based on these quantities is larger than $10^4$ in the calculations, Strouhal numbers for a sphere are taken as a reference. The period of one shedding circle was calculated as $T = 1/f$ and the time step is set up by dividing the period by 40. The maximum number of iterations per time step is limited to 20.

Calculations were performed at the High Performance Computing Center (HLRS) of Stuttgart University. A dual processor Opteron 246 with 4GB RAM was used for every run. To facilitate all of the computer performance, up to four simulations on two nodes were started at a time. The simulation time for one time step on Mesh 2 for example is about 4 and 6 minutes using Spalart-Allmaras and $k-\omega$ turbulent models, respectively.

## 5.3 Hemisphere on a smooth bed

### 5.3.1 Experiment conditions

To assess the performance of the turbulence models, a numerical experiment for a hemisphere placed over a smooth bed is performed in the range of Reynolds numbers $\mathrm{Re}_{ht}$ from $1.31\times10^4$ to $1.4\times10^5$. This corresponds to the same range of $\mathrm{Re}_{ht}$ that is tested in the laboratory experiments of Savory and Toy [67], [68] in a wind tunnel, and Flammer et al. [21] in a water flume. Thus, obtained detailed pressure distributions over a hemisphere and the integral drag coefficient can be compared with data from physical experiments.

In Table 5.2, the conditions of numerical experiments for a smooth bottom are given. Some of the experiments are repeated with other than specified in the table turbulent intensities I; using the different turbulence models on Meshes M1, M2, M3 and with two variants of roughness for the FST ground plate: smooth and rough.

In Runs C1–C3 the uniform inflow velocity profile, in Runs S1–S5 the logarithmical velocity distribution are specified. The flow velocities at a level of the hemisphere's top $u_{ht}$ and the center of mass $u_{hc}$, respectively, are obtained by substituting the corresponding distances from the bottom into Equation 5.6:

$$\frac{\overline{u}(y)}{u_*} = \frac{1}{\kappa}\,\ln\frac{y\,u_*}{\nu} - 5.2 \tag{5.6}$$

$$y_{ht} = r_h = 0.039\mathrm{m}$$

$$y_{hc} = \frac{3}{8}\,r_h = 0.0146\mathrm{m}$$

with $\overline{u}(y)$ = mean velocity along x-axis, [m/s]
$u_*$ = shear velocity, [m/s]
$\kappa$ = von Kármán constant, [-]
$y$ = vertical coordinate, [m]
$\nu$ = kinematic viscosity of fluid, [m$^2$/s]
$r_h$ = radius of a hemisphere, [m]
$y_{ht}, y_{hc}$ = distances from the bottom to the levels of hemisphere's top and center of mass, [m]

Mean column velocities $u_{0.4}$, at a distance of 10 cm from the bottom, are also specified in Table 5.2.

In Figure 5.11a, the normalized vertical velocity distributions in the experiments of Savory and Toy [67] are shown. Generally, they measured hemisphere pressure distributions in three kinds of boundary layer – "rough", "smooth" and "thin", but only for the latter

| Cases | $u_{ht}$ | $u_{hc}$ | $u_{hc}/u_{ht}$ | $Re_{ht}$ | $u_{0.4}$ | $u*$ | $\tau_0$ | $h_t$ | $I$ | $l$ |
|---|---|---|---|---|---|---|---|---|---|---|
| | m/s | m/s | - | - | m/s | m/s | $N/m^2$ | m | % | m |
| **S1** | 0.169 | 0.148 | 0.88 | $1.31\times10^4$ | 0.189 | 0.00855 | 0.07 | 0.249 | 4.17 | 0.023 |
| **S2** | 0.337 | 0.298 | 0.88 | $2.62\times10^4$ | 0.374 | 0.01586 | 0.25 | 0.249 | 3.83 | 0.023 |
| **S3** | 0.505 | 0.449 | 0.89 | $3.93\times10^4$ | 0.559 | 0.02279 | 0.52 | 0.249 | 3.64 | 0.023 |
| **S4** | 1.000 | 0.896 | 0.90 | $7.78\times10^4$ | 1.099 | 0.04218 | 1.78 | 0.249 | 3.35 | 0.023 |
| **S5** | 1.796 | 1.620 | 0.90 | $1.40\times10^5$ | 1.964 | 0.07175 | 5.14 | 0.249 | 3.11 | 0.023 |
| **C1** | 0.169 | 0.169 | 1.00 | $1.31\times10^4$ | 0.169 | | | 0.249 | 4.17 | 0.023 |
| **C2** | 0.200 | 0.200 | 1.00 | $1.56\times10^4$ | 0.200 | | | 0.249 | 4.00 | 0.023 |
| **C3** | 1.000 | 1.000 | 1.00 | $7.78\times10^4$ | 1.000 | | | 0.249 | 3.30 | 0.023 |

**Table 5.2:** Conditions of numerical simulations, smooth bottom cases

the range of Reynolds numbers corresponds to the region of interest of the present study. For the first two velocity profiles only measurements at $Re_{ht} = 1.4\times10^5$ are documented. The “thin” boundary layer was generated naturally, allowing the flow to develop from the channel entrance over the smooth bottom on a length of 4.5 m. The “smooth” and “rough” boundary layers were produced artificially by using a barrier fence and a set of vorticity generators placed near the entrance to the channel.

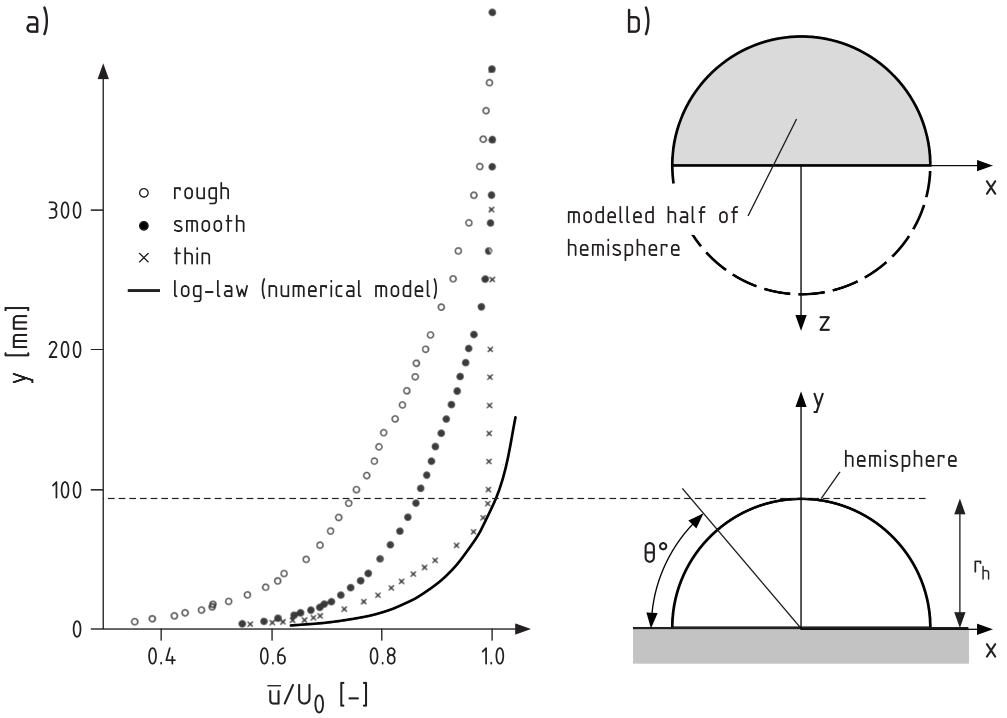

**Figure 5.11:** a. Normalized velocity distributions in "thin", "smooth" and "rough" boundary layers from [67] and in numerical experiments; b. Definition of angle $\theta$ and coordinate system in numerical experiments

Flow velocity distributions in the wind tunnel experiments were matched by the power law:

$$\frac{\overline{u}(y)}{U_0} = \left(\frac{y}{\delta}\right)^{1/n} \qquad [\text{-}] \qquad (5.8)$$

with $\overline{u}(y)$ = mean velocity along $x$-axis, [m/s]
$U_0$ = free stream velocity, [m/s]
$\delta$ = thickness of the boundary layer, [m]
$n$ = power law exponent, [-]

Boundary layer thickness $\delta$ is defined as the height at which velocity reaches a value of 99% of the free stream velocity. The power law exponent $n$ for a "thin" boundary layer is found to be equal 5.99.

In the laboratory experiments the Reynolds number is defined through the free stream velocity $U_0$. This is not important for the comparison, though, as the "thin" boundary layer thickness $\delta = 86$ mm is almost equal to the radius of a hemisphere $r_h = 95$ mm. It is seen from Figure 5.11a, that flow velocities at the top of a hemisphere coincide, but for the wind tunnel experiments the profile is not as full as in numerical simulations. Still, the maximum difference between the two is no larger than 15 %, and it is assumed, that the experiments are comparable.

In numerical experiments, the inflow boundary turbulent intensity $\mathrm{I}$ and turbulence length scale $\mathrm{l}$ are specified following recommendations of [22]:

$$\mathrm{I} \equiv \frac{u'}{U_{avg}} = 0.16\,(Re_{D_h})^{-1/8} \qquad [\%] \tag{5.9}$$

with $\mathrm{I}$ = turbulent intensity, [%]
$u'$ = root-mean-square of the velocity fluctuations, [m/s]
$U_{avg}$ = average flow velocity, [m/s]
$Re_{D_h} = D_h\,U_{avg}/\nu$ = Reynolds number based on the hydraulic diameter $D_h$ of a channel, [-]

The average flow velocity $U_{avg}$ is taken equal to the mean column velocity $u_{0.4}$ in calculations. Instead of the hydraulic diameter the channel water depth $h$ is taken as a geometric characteristic, as we assume, that the hemisphere is placed in a very wide channel.

The turbulence length scale $l$ is also defined empirically upon the geometrical size of a channel. Following recommendations exist:

$$\text{FLUENT :} \qquad l = 0.07\,D_h \qquad [\text{m}] \tag{5.10a}$$

$$\text{Bezzola [8] :} \qquad \text{from} \quad l = 0.09\,h \quad \text{to} \quad l = 0.12\,h \qquad [\text{m}] \tag{5.10b}$$

Bezzola's recommendation with a factor 0.09 is taken for the calculation of the turbulence length scale $l$.

## 5.3.2 Results

### 5.3.2.1 Criteria for comparison of results

Distributions of the pressure coefficient $c_p$ along the longitudinal centerline of a hemisphere (see definition sketch in Figure 5.11b) and values of a total drag coefficient serve for the comparison of numerical and experimental results. The pressure coefficient is defined as:

$$c_p = \frac{\overline{p} - p_0}{0.5\,\rho u_{ht}} \qquad [-] \tag{5.11}$$

| with | | | | |
|---|---|---|---|---|
| | $c_p$ | = | pressure coefficient | [-] |
| | $\overline{p}$ | = | local mean (time-averaged) static pressure | [Pa] |
| | $p_0$ | = | reference static pressure of a free stream, | [Pa] |
| | $u_{ht}$ | = | reference velocity, here –<br>undisturbed velocity velocity at the top level of a hemisphere, | [m/s] |

Total drag $F_d$ and lift $F_l$ forces in the numerical model are computed by summing the dot product of the pressure and viscous forces on each cell face of a hemispherical model surface with the specified force vector. Then, the associated force coefficients are computed as:

$$c_d = \frac{F_d}{\frac{1}{2}\,\rho\,u_{ht}\,A_\perp} \qquad [-] \tag{5.12a}$$

$$c_l = \frac{F_l}{\frac{1}{2}\,\rho\,u_{ht}\,A_\perp} \qquad [-] \tag{5.12b}$$

| with | | | | |
|---|---|---|---|---|
| | $c_d, c_l$ | = | drag and lift coefficients, | [-] |
| | $F_d$ | = | drag force, | [N] |
| | $F_l$ | = | lift force, | [N] |
| | $u_{ht}$ | = | velocity at the top level of a hemisphere, | [m/s] |
| | $A_\perp$ | = | cross-section area of a hemisphere<br>perpendicular to the main flow direction, | [$m^2$] |
| | $\rho$ | | density of fluid, | [$kg/m^3$] |

#### 5.3.2.2 Influence of mesh resolution and discretization order

To model a laminar boundary layer separation, the mesh near a solid surface has to be fine enough to resolve flow in a viscous sublayer. Thus, at least some mesh nodes within this sublayer, which upper border lies at $y^+ \approx 5$ (see Section 3.3.1), are required. The near-wall spacing in the order of $y^+ = 1$ is recommended for both Spalart-Allmaras (SA) and $k-\omega$ (KO) turbulent models in a low Reynolds number regime[4] [22]. The value of $y^+$ can be checked after the simulation and, if out of the recommended range, the mesh can be refined in the required area [5] and the simulation repeated.

---

[4] but a value the order of $y^+ = 4$–$5$ is still acceptable

[5] For the present study the refinement function of the FLUENT solver could not be used as it produces a mesh which is generally not aligned with a geometry

FLUENT supplies various first- and second-order discretization schemes for the transformation of the governing equations into the algebraic form for a numerical solution. While the first-order discretization yields better convergence than the second-order one, it will generally provide less accurate results, especially on tri/tet grids and when flow is not aligned with a mesh, being the case for flow separation from a hemisphere. Indeed, very large convergence difficulties are encountered in the study, particulary for runs with low levels of inflow turbulent intensity. The initial test simulations were run using first order discretization. However, that had a considerable effect on the results.

Effect of discretization for the $k-\omega$ turbulence model is seen in Figure 5.12, where longitudinal centerline pressure coefficient distributions computed at $Re_{ht} = 1.38\times10^4$ on the very fine Mesh 1 and the coarse Mesh 3 are shown. Suction magnitudes at the top of a hemisphere ($\theta \approx 80°$), obtained using the second-order discretization scheme on the quite different mesh resolutions, are comparable, while the value obtained on the very fine mesh using first-order discretization is very far away from these two.

In general, there is a large difference between the numerical results, obtained with a high turbulent intensity level of 4.17 %, and the experiment points in Figure 5.12. At $Re_{ht} = 1.38\times10^4$, computation on Mesh 1 yields a maximum value of $y^+ = 1.1$ on the front face of a hemisphere, thus the mesh resolution is theoretically sufficient to resolve a laminar boundary layer. The pressure distribution differences on the front face of a hemisphere ($\theta \approx 20°$) can be related to the velocity profile form influence (see Section 5.3.2.3). In contrast, the differences at the top of a hemisphere can be manipulated by adjusting an inflow turbulent intensity level (see the curve obtained with $I = 0.5$ % for comparison, explanation in Section 5.3.2.4).

Pressure coefficient distributions obtained using the Spalart-Allmaras model are a bit different to those using the $k-\omega$ model in respect to mesh resolution (Figure 5.13). In particular, large differences can be seen between distributions obtained on the fine Mesh 1 and the coarse Mesh 3 using the same second-order discretization schemes. The magnitudes of peak suction at the top of a hemisphere are -0.57 and -0.77 with values of a maximum $y^+$ of 1.2 and 6, respectively[6]. Pressure distributions obtained on Mesh 1 and Mesh 2 (with $y^+$ of 1.2 and 2.2, respectively) almost coincide, yielding the same drag and lift coefficients in these runs. This allows to suggest, that further mesh refinement would not lead to a considerable change in results.

---

[6] Compare with the values of $c_p$ -0.53 and -0.6 using the $k-\omega$ model with values of a maximum $y^+$ of 1.1 and 7, respectively

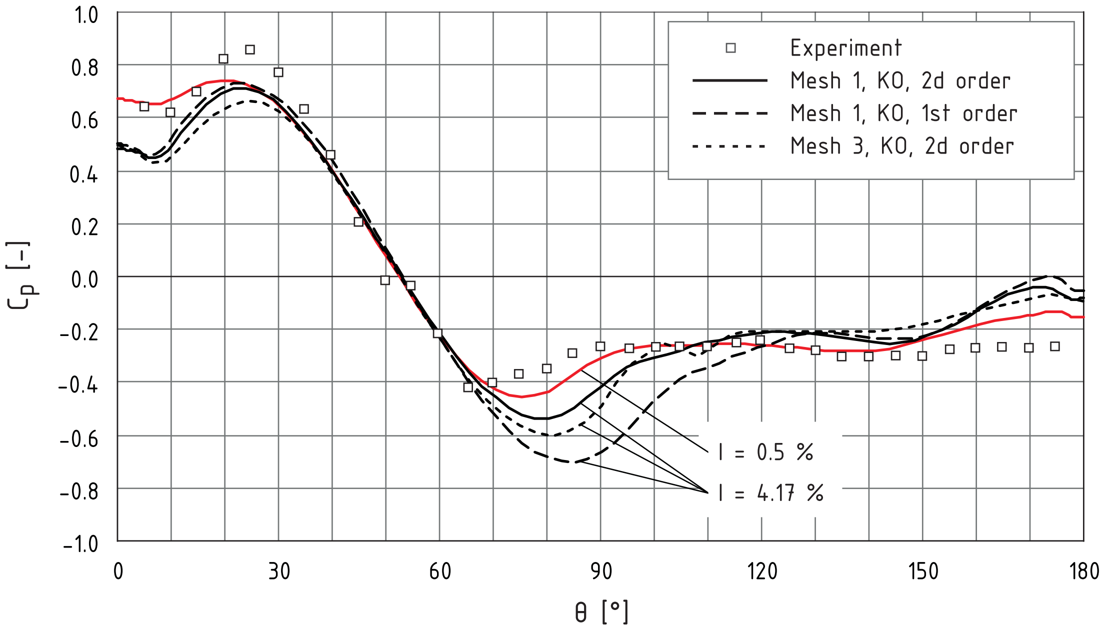

**Figure 5.12:** Pressure coefficient distributions over hemisphere's centerline, case S1, $Re_{ht} = 1.38 \times 10^4$, $k - \omega$ turbulence model

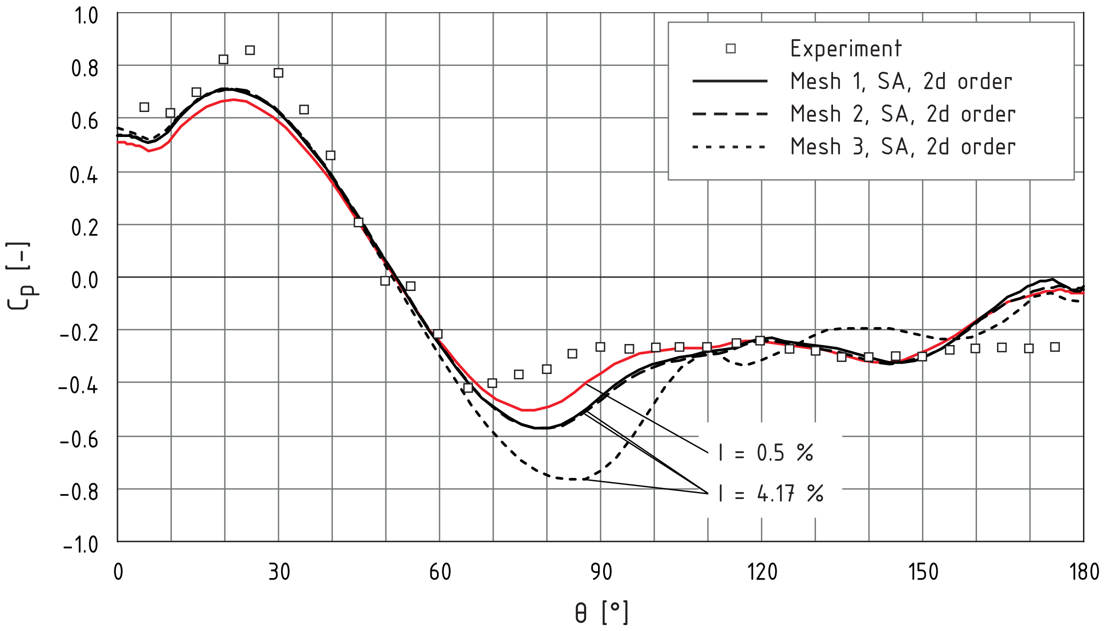

**Figure 5.13:** Pressure coefficient distributions over hemisphere's centerline, case S1, $Re_{ht} = 1.38 \times 10^4$, Spalart-Allmaras turbulence model

#### 5.3.2.3 Influence of velocity profile form

Discrepancies in pressure distributions in the front face of a hemisphere can be related to the influence of the velocity profile form. As seen in Figure 5.14, the $c_p$ distribution obtained for the uniform inflow velocity profile in Run C1 is characterized by a larger magnitude of the maximum pressure coefficient at $\theta \approx 22^\circ$ than that obtained for the log law profile in Run S1.

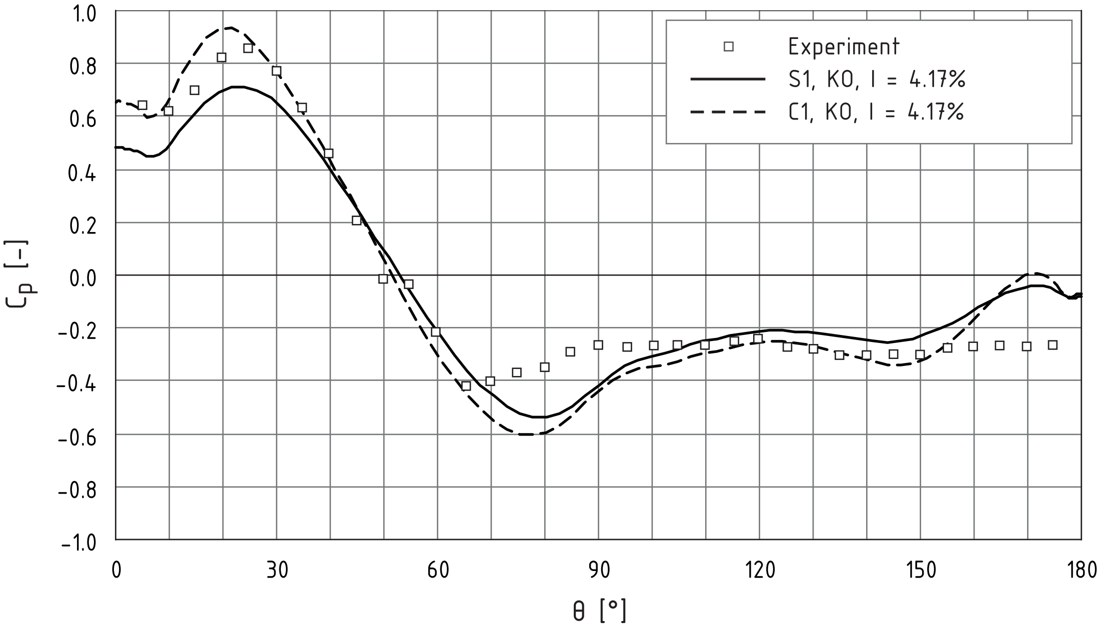

**Figure 5.14:** Pressure coefficient distributions over hemisphere's centerline, cases S1 and C1, $\mathrm{Re}_{ht} = 1.38\times10^4$, $k-\omega$ turbulence model

This finding is supported by the results of simulations for a rough bed (see Section 5.4.2).

#### 5.3.2.4 Influence of turbulence intensity and Reynolds number

$k-\omega$ and, to a lesser extent, the Spalart-Allmaras turbulent models show a sensitivity to the inflow turbulence intensity level. In modern wind tunnels, the free-stream turbulence intensity may be as low as 0.05 % [22], and it is possible, that high values of I, taken initially for the numerical experiments, do not correspond to those in the experiments of Savory and Toy [67].

It is seen from Figure 5.15, that reduced to 0.5 % turbulence intensity results in a closer match of the pressure coefficient distributions, computed using the $k-\omega$ model at $\mathrm{Re}_{ht} = 1.38\times10^4$ and $2.62\times10^4$, to the measured ones. Remarkably, for $\mathrm{Re}_{ht} = 3.93\times10^4$, no solution can be obtained with the model. The simulation comes very close to the distribution at $\mathrm{Re}_{ht} = 2.62\times10^4$ and then starts to diverge. At some point, the pressure distribution is similar to the one measured at this Reynolds number, but the residuals have very large values and further calculation leads to a complete divergence of the solution.

From distributions in Figure 5.16 follows, that the Spalart-Allmaras model is generally less sensitive to the turbulence intensity level. Subcritical pressure distributions with a reduced level of inflow turbulence intensity using this model match the measured ones worse than those obtained by the $k-\omega$ model.

Interesting results are obtained in the calculations at high Reynolds numbers of $7.8\times10^4$ and $14\times10^4$. As Figure 5.17 shows, the distributions obtained with the $k-\omega$ model are quite away from those measured at these Reynolds numbers. On the other hand, they are very close to the distribution obtained for a rough hemisphere at $\mathrm{Re}_{ht} = 14\times10^4$ in [67], corresponding to the supercritical flow regime. This fact can be explained as follows: unfortunately neither the $k-\omega$ nor Spalart-Allmaras models are suitable for modelling the transition regimes, as they tend to underestimate the transition Reynolds number at least by one order of magnitude [99]. For the fact that transition already took place speaks, that pressure distributions for simulation cases S4 and S5 are almost the same, while those corresponding to the measured cases are quite different.

Pressure coefficient distributions obtained with the Spalart-Allmaras model at these high Reynolds numbers unfortunately match neither the measured distributions for the smooth hemisphere nor the distribution corresponding to the supercritical regime for a rough hemisphere in the experiments of Savory and Toy [67]. The fact, that the distribution obtained at $\mathrm{Re}_{ht} = 7.8\times10^4$ is identical to that at $\mathrm{Re}_{ht} = 14\times10^4$ speaks again for the predicted supercritical regime. The later separation of the boundary layer in comparison to the experimental supercritical distribution can be related to the sensitivity of the Spalart-Allmaras model to the mesh resolution. At these Reynolds numbers, the maximum $y^+$ (4.7 and 7.3 for runs S4 and S5, respectively) is already out of the recommended range for the low Reynolds number models and by far not in the range of those recommended for the high Reynolds number models (it should be above 30).

Differences in pressure distributions over the hemisphere's surface are reflected by integral drag and lift coefficients. While the pressure difference between the front and the back faces of a hemisphere (at $\theta \approx 20^\circ$ and $160^\circ$) defines a drag force, the value of suction at the top of a hemisphere defines the lift force. In general, with increasing Reynolds number, the drag coefficient decreases due to a reduction of the wake size and the lift coefficient increases due to a displacement of the separation line along the hemisphere's centerline in the flow direction. The coefficients obtained for the smooth bottom are summarized in Table 5.3.

In conclusion, the $k-\omega$ is used further down for the calculations over rough bed. Although the Spalart-Allmaras model is approximately 1.3 times faster than the $k-\omega$ model, it fails to obtain close to measured distributions of pressure coefficients for the turbulence

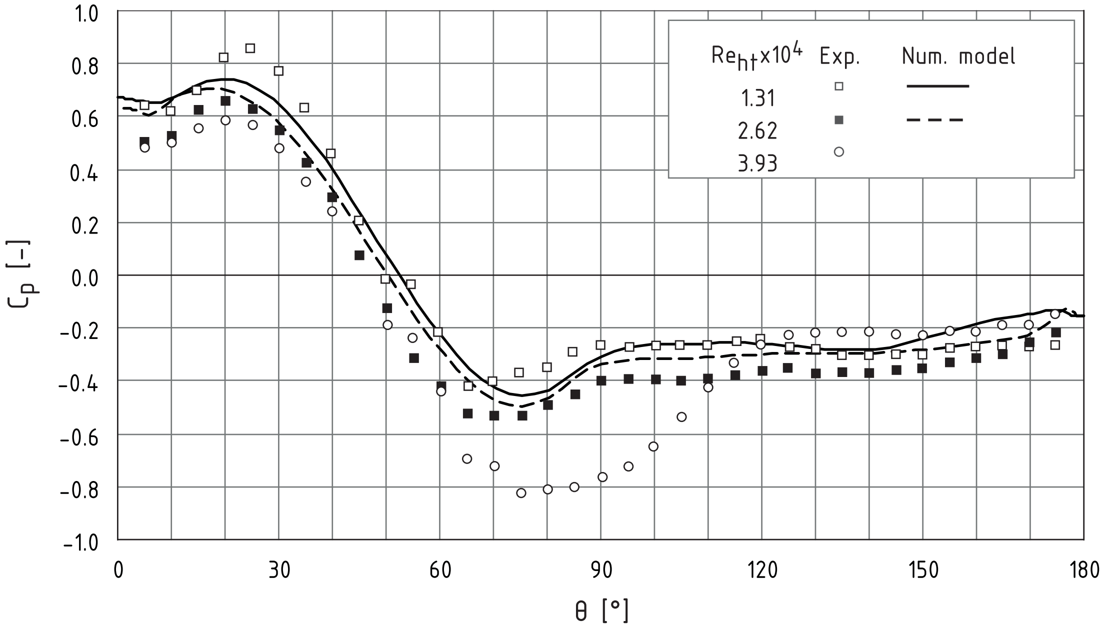

**Figure 5.15:** Pressure coefficient distributions over hemisphere's centerline, cases S1 and S2, I = 0.5%, $k-\omega$ turbulence model

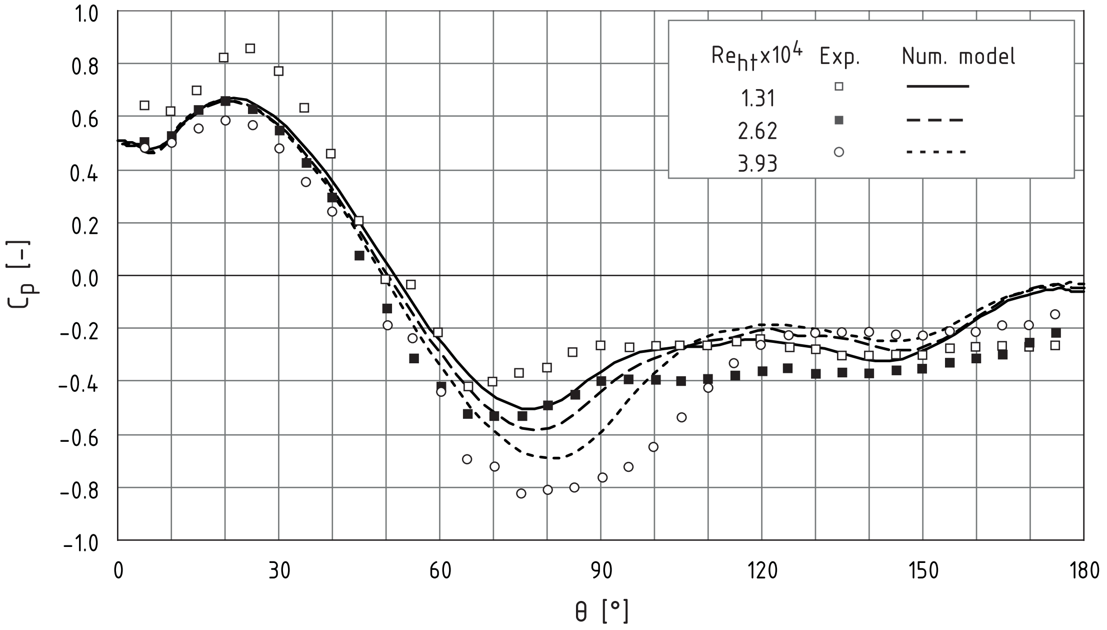

**Figure 5.16:** Pressure coefficient distributions over hemisphere's centerline, cases S1, S2 and S3, I = 0.5%, Spalart-Allmaras turbulence model

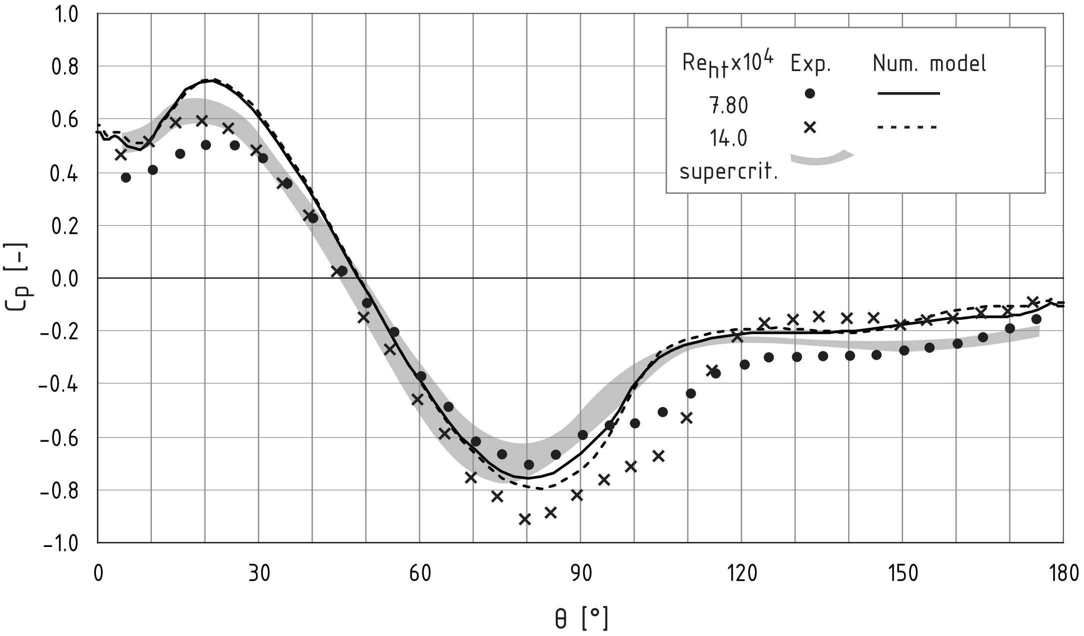

**Figure 5.17:** Pressure coefficient distributions over hemisphere's centerline, cases S4 and S5, $I = 0.5\%$, $k - \omega$ turbulence model

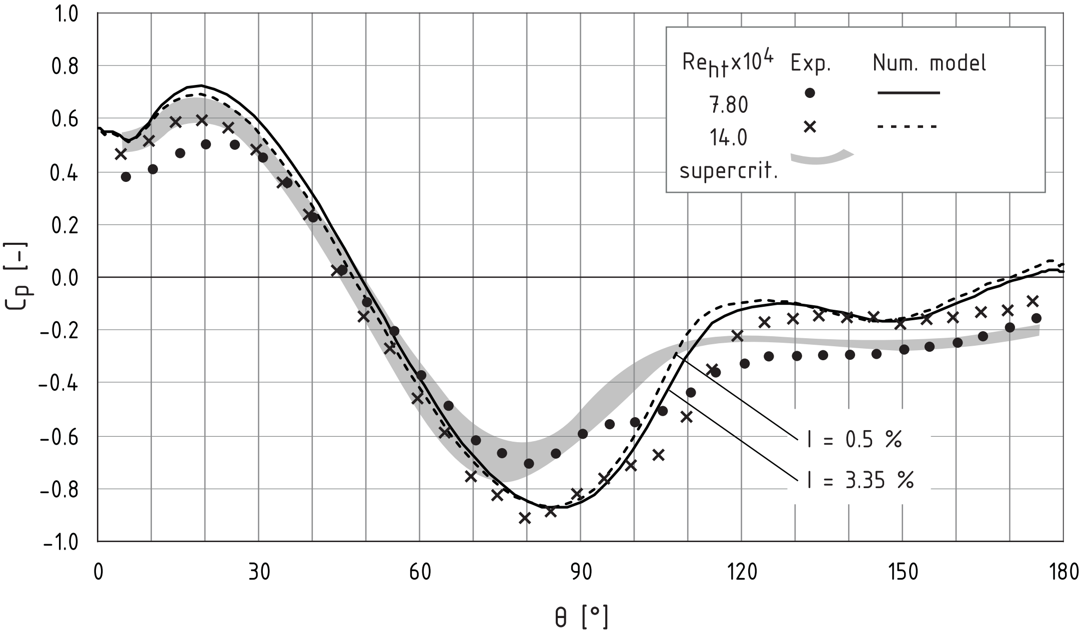

**Figure 5.18:** Pressure coefficient distributions over hemisphere's centerline, cases S4 and S5, Spalart-Allmaras turbulence model

| Cases | Mesh | I | Turb. model | $y^+_{\text{max}}$ | $c_{d_p}$ | $c_d$ | $c_{l_p}$ | $c_l$ | $c_d \cdot \frac{u_{ht}}{u_{hc}}$ | $c_l \cdot \frac{u_{ht}}{u_{hc}}$ |
|---|---|---|---|---|---|---|---|---|---|---|
| | | % | | - | - | - | - | - | - | - |
| **S1** | Mesh 1 | 4.17 | KO | 1.1 | 0.32 | 0.35 | 0.46 | 0.47 | **0.40** | **0.54** |
| | Mesh 1 | 4.17 | SA | 1.2 | 0.35 | 0.38 | 0.53 | 0.54 | 0.43 | 0.62 |
| | Mesh 1 | 0.50 | KO | 1.1 | 0.42 | 0.44 | 0.44 | 0.45 | 0.50 | 0.51 |
| | Mesh 1 | 0.50 | SA | 1.1 | 0.34 | 0.37 | 0.49 | 0.50 | 0.42 | 0.57 |
| **S2** | Mesh 1 | 3.83 | KO | 2.0 | 0.28 | 0.30 | 0.59 | 0.60 | 0.34 | 0.68 |
| | Mesh 1 | 3.83 | SA | 2.0 | 0.28 | 0.30 | 0.64 | 0.65 | 0.34 | 0.73 |
| | Mesh 1 | 0.50 | KO | 1.9 | 0.41 | 0.43 | 0.54 | 0.54 | 0.49 | 0.61 |
| | Mesh 1 | 0.50 | SA | 1.9 | 0.28 | 0.30 | 0.53 | 0.54 | 0.34 | 0.61 |
| **S3** | Mesh 1 | 3.64 | SA | 2.7 | 0.25 | 0.27 | 0.68 | 0.68 | 0.30 | 0.76 |
| | Mesh 1 | 0.50 | SA | 2.6 | 0.25 | 0.26 | 0.63 | 0.63 | 0.29 | 0.71 |
| **S4** | Mesh 1 | 3.35 | SA | 4.7 | 0.20 | 0.22 | 0.76 | 0.76 | 0.25 | 0.85 |
| | Mesh 1 | 0.50 | KO | 4.5 | 0.26 | 0.27 | 0.67 | 0.68 | **0.30** | **0.76** |
| **S5** | Mesh 1 | 0.50 | KO | 8.3 | 0.24 | 0.26 | 0.68 | 0.68 | **0.29** | **0.75** |
| | Mesh 1 | 0.50 | SA | 7.3 | 0.17 | 0.19 | 0.76 | 0.76 | 0.21 | 0.84 |
| **C1** | Mesh 1 | 4.17 | KO | 1.2 | 0.40 | 0.43 | 0.54 | 0.55 | **0.43** | **0.55** |
| **C2** | Mesh 2 | 4.00 | KO | 2.7 | 0.41 | 0.44 | 0.51 | 0.52 | 0.44 | 0.52 |
| | Mesh 2 | 0.50 | KO | 2.7 | 0.52 | 0.55 | 0.50 | 0.52 | **0.55** | **0.52** |
| **C3** | Mesh 2 | 3.30 | KO | 10.7 | 0.29 | 0.32 | 0.75 | 0.76 | **0.32** | **0.76** |

**Table 5.3:** Computed pressure and integral drag and lift coefficients for smooth bottom cases

intensity affected subcritical regime as well as for the supercritical regime appearing at high Reynolds numbers in the present study.

Further, it should be taken into account, that even with the $k - \omega$ model, either sub- or supercritical regime, but not a transition, can be modelled. This is not very pleasant, as for a hemisphere mounted on a bottom, transition takes place over a large range of Reynolds numbers.

#### 5.3.2.5 Influence of ground plate roughness

To test the influence of the FST ground plate type, experiments S1 (with $I = 0.5\%$) and S5 are computed twice using the $k - \omega$ model: with a smooth ground plate surface and with a roughness of 2 mm height. This change in roughness influences neither the hemisphere's centerline pressure distributions nor integral drag and lift coefficients. Thus, from a hydrodynamical point of view, it does not matter whether FST measurements are performed with an old, smooth or a new, structured ground plate.

## 5.4 Hemisphere on a rough bed

### 5.4.1 Numerical experiment conditions

In this part, the influence of the flow velocity profile form on drag and lift coefficients for a hemisphere is investigated. We want to find out, how these would change in a real river, where different substrate types influence the near bottom flow field. As already mentioned, although we speak about "rough bed" conditions, the sediment grains are not modelled here directly. Velocity gradient fields are "constructed" applying the inflow boundary condition given by the modified velocity distribution law after Bezzola (see Section 3.6). For simplification, the same formula is used for the inner as well as for the outer flow regions:

$$\frac{\overline{u}(y)}{u_*} = c_r \left( \frac{1}{\kappa} \ln \frac{y}{y_r} + 8.48 \right)$$

with $\overline{u}$ = mean velocity along x-axis, [m/s]
$u_*$ = shear velocity, [m/s]
$c_r$ = damping factor, [-]
$\kappa$ = von Kármán constant, [-]
$y$ = vertical coordinate, [m]
$y_r$ = thickness of roughness sublayer, [m]

In the computational domain, the bottom boundary now coincides with the level of imaginary roughness elements' tops. The origin of the log velocity profile is $0.25y_r$ below the numerical bottom boundary.

Parameters of numerical experiments are summarized in Table 5.4. All calculations are performed on Mesh 2 with second order discretization schemes (see Section 5.2.2). Accounting for the results obtained for the smooth bottom, only conditions corresponding to the sub- and supercritical flow regimes are simulated. For every flow regime four cases with different velocity profile forms are done. For all four cases, the velocity at the top of a hemisphere $u_{ht}$ – reference velocity – remains the same. For the subcritical regime this reference velocity is 0.2 m/s, for the supercritical regime 1 m/s. Moreover, calculations are made twice for the subcritical regime – with two different levels of inflow turbulence intensity.

### 5.4.2 Results

Simulations for the rough bottom, performed with the same second order discretization schemes and on the same Mesh 2, show different degrees of convergence. While in all runs of the supercritical regime but R-Super4 the residuals for all parameters fall below $10^{-5}$, this does not occur in the subcritical regime. For the latter, a better convergence is achieved for the runs with an inflow turbulence intensity of 4 % than of 0.5 %. Residuals for the continuity are always the highest among the parameters. In general, the larger the relation $u_{hc}/u_{ht}$, the worse is the convergence. For example, residuals for the continuity are below $10^{-5}$ for Run R-Sub1 and R-Sub2, equal to $2.4\times10^{-4}$ and $7.5\times10^{-4}$ for Run R-Sub3 and R-Sub4 (at $I = 4$ %), respectively. For comparison, Runs C1–C3 with uniform inflow velocity profiles show also poor convergence, with residuals of $9.8\times10^{-4}$ and $5\times10^{-5}$ for the continuity in Run C2 (at $I = 0.5$ %) and C3, respectively. Nevertheless, in all runs an unsteady simulation converges to the quasi steady-state, with force coefficients practically not changing with time.

Like in smooth bottom simulations, centerline pressure distributions for the subcritical regime are affected by the value of inflow turbulence intensity. At the same Reynolds number $Re_{ht} = 1.56\times10^4$, the point with a peak suction and the separation line lie further downstream at $I = 0.5$ % (Figure 5.19) than at $I = 4$ % (Figure 5.20). This postponing of separation has an influence on the lift coefficient – for the latter case it is higher. The drag coefficient is not affected by this postponing (see Table 5.5).

From Figures 5.19, 5.20 follows, that the velocity profile form defines the pressure distribution on the frontal part of a hemisphere to a large extent. The larger the relation $u_{hc}/u_{ht}$ is, the larger the value of the maximum pressure coefficient around $\theta \approx 20°$. At the same time, the angle $\theta$ corresponding to the maximum value of pressure coefficient tends to decrease, for example, from about 24 degrees in R-Sub1 to 15 degrees in R-Sub4 (see Figure 5.19). The same is true for the supercritical regime (Figure 5.21). Recalling smooth bottom simulations, pressure distributions obtained for the uniform velocity profiles in Runs C1–C3, but also for

| Cases | $u_{ht}$ | $u_{hc}$ | $u_{hc}/u_{ht}$ | $Re_{ht}$ | $u_{0.4}$ | $u*$ | $\tau_0$ | $h$ | $y_r$ | $\Delta y_0$ | $h_t$ | $h_t/y_r$ | $y_w$ | $c_r$ | $I$ | $l$ |
|---|---|---|---|---|---|---|---|---|---|---|---|---|---|---|---|---|
| | m/s | m/s | - | - | m/s | m/s | N/m$^2$ | m | m | m | m | - | m | - | % | m |
| **R-Sub1** | 0.2 | 0.161 | 0.80 | $1.56\times10^4$ | 0.24 | 0.0222 | 0.49 | 0.249 | 0.03 | 0.008 | 0.257 | 8.55 | 0.08 | 0.94 | 4.0 | 0.023 |
| **R-Sub2** | 0.2 | 0.165 | 0.83 | $1.56\times10^4$ | 0.24 | 0.0309 | 0.95 | 0.249 | 0.08 | 0.020 | 0.269 | 3.36 | 0.08 | 0.84 | 4.0 | 0.023 |
| **R-Sub3** | 0.2 | 0.173 | 0.86 | $1.56\times10^4$ | 0.23 | 0.0444 | 1.97 | 0.249 | 0.16 | 0.040 | 0.289 | 1.81 | 0.16 | 0.67 | 4.0 | 0.023 |
| **R-Sub4** | 0.2 | 0.176 | 0.88 | $1.56\times10^4$ | 0.22 | 0.0535 | 2.86 | 0.249 | 0.22 | 0.055 | 0.304 | 1.38 | 0.22 | 0.59 | 4.0 | 0.023 |
| | | | | | | | | | | | | | | | | |
| **R-Super1** | 1.0 | 0.806 | 0.81 | $7.78\times10^4$ | 1.21 | 0.1111 | 12.32 | 0.249 | 0.03 | 0.008 | 0.257 | 8.55 | 0.08 | 0.94 | 3.3 | 0.023 |
| **R-Super2** | 1.0 | 0.827 | 0.83 | $7.78\times10^4$ | 1.19 | 0.1545 | 23.82 | 0.249 | 0.08 | 0.020 | 0.269 | 3.36 | 0.08 | 0.84 | 3.3 | 0.023 |
| **R-Super3** | 1.0 | 0.863 | 0.86 | $7.78\times10^4$ | 1.14 | 0.2217 | 49.05 | 0.249 | 0.16 | 0.040 | 0.289 | 1.81 | 0.16 | 0.67 | 3.3 | 0.023 |
| **R-Super4** | 1.0 | 0.882 | 0.88 | $7.78\times10^4$ | 1.10 | 0.2678 | 71.57 | 0.249 | 0.22 | 0.055 | 0.304 | 1.38 | 0.22 | 0.59 | 3.3 | 0.023 |

**Table 5.4:** Conditions of numerical simulations, rough bottom cases

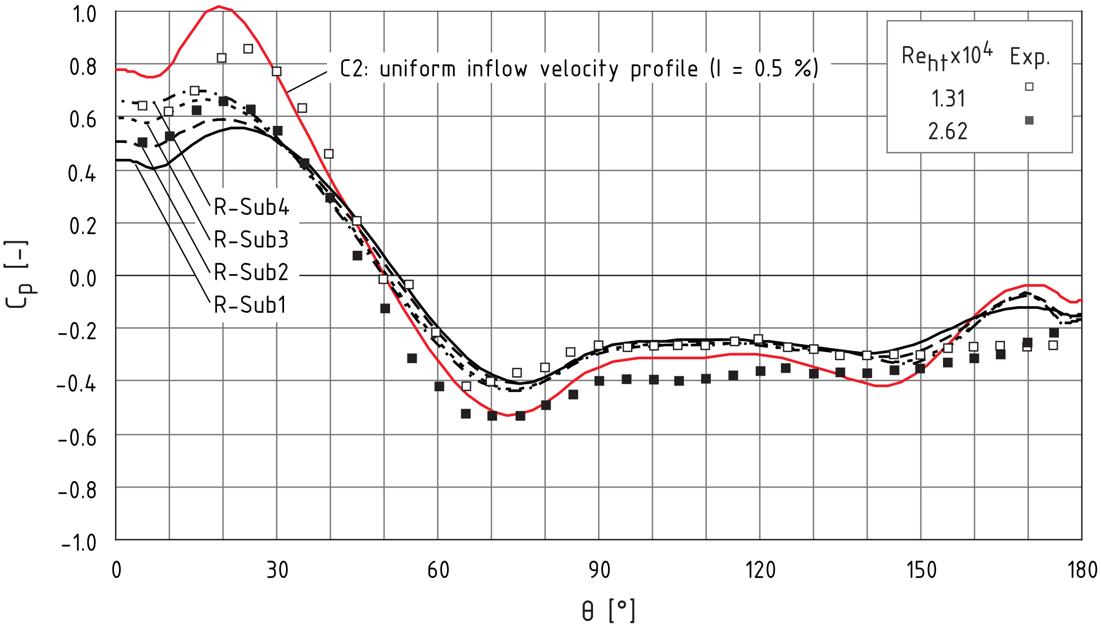

**Figure 5.19:** Pressure coefficient distributions over the hemisphere's plane of symmetry: subcritical regime over rough bottom, I = 0.5 %

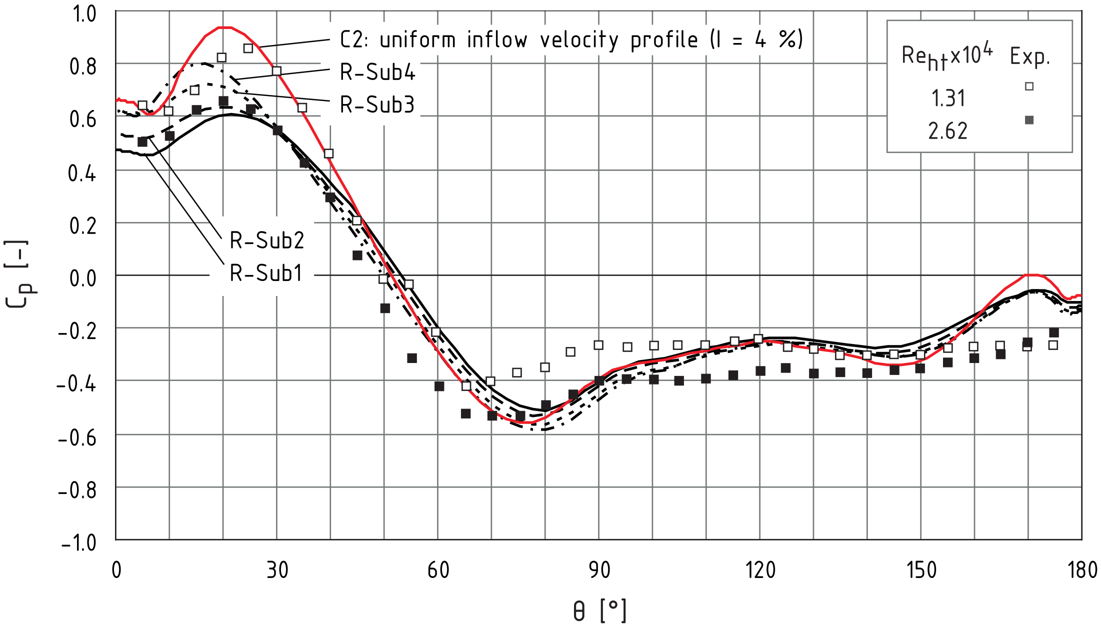

**Figure 5.20:** Pressure coefficient distributions over the hemisphere's plane of symmetry: subcritical regime over rough bottom, I = 4 %

| Cases | Turb. intensity | $c_{d_p}$ | $c_d$ | $c_{l_p}$ | $c_l$ | $c_d \cdot \frac{u_{ht}}{u_{hc}}$ | $c_l \cdot \frac{u_{ht}}{u_{hc}}$ |
|---|---|---|---|---|---|---|---|
| | % | - | - | - | - | | |
| **R-Sub1** | 4.0 | 0.32 | 0.35 | 0.48 | 0.49 | 0.43 | 0.61 |
| | 0.5 | 0.32 | 0.35 | 0.42 | 0.43 | 0.43 | 0.53 |
| **R-Sub2** | 4.0 | 0.34 | 0.36 | 0.51 | 0.52 | 0.44 | 0.63 |
| | 0.5 | 0.34 | 0.36 | 0.43 | 0.44 | 0.44 | 0.53 |
| **R-Sub3** | 4.0 | 0.36 | 0.39 | 0.55 | 0.56 | 0.45 | 0.65 |
| | 0.5 | 0.36 | 0.38 | 0.45 | 0.46 | 0.44 | 0.53 |
| **R-Sub4** | 4.0 | 0.36 | 0.39 | 0.56 | 0.58 | 0.44 | 0.66 |
| | 0.5 | 0.37 | 0.39 | 0.46 | 0.47 | 0.44 | 0.53 |
| **R-Super1** | 3.3 | 0.22 | 0.24 | 0.61 | 0.62 | 0.30 | 0.77 |
| **R-Super2** | 3.3 | 0.23 | 0.25 | 0.62 | 0.63 | 0.30 | 0.76 |
| **R-Super3** | 3.3 | 0.24 | 0.27 | 0.65 | 0.66 | 0.31 | 0.76 |
| **R-Super4** | 3.3 | 0.26 | 0.28 | 0.67 | 0.68 | 0.32 | 0.77 |

**Table 5.5:** Computed pressure and integral drag and lift coefficients for rough bottom cases

the log velocity profiles in S1–S5, do have a peak of the maximum pressure coefficient at approximately 20–22 degrees. In contrast, the position of minimum pressure coefficient coincide for cases of uniform and gradient velocity profile at the same Reynolds number and inflow turbulence intensity.

Pressure coefficient distributions for the supercritical regime match well the experimental data of Savory and Toy [67] (grey region in Figure 5.21) on the length of a centerline from 25 to 150 degrees. In the laboratory experiments, the relation $u_{hc}/u_{ht}$ is in the range of 0.83 to 0.88, similar to the conditions in Runs R-Super2 to R-Super4. However, the higher pressure coefficient in the range of $\theta > 155$ degrees, obtained in almost all numerical simulations, cannot be explained.

Pressure and total drag and lift coefficients obtained in the numerical experiments are summarized in Table 5.5. These show a similar trend as those obtained in smooth bottom simulations. In a subcritical regime, the drag coefficient is relatively independent from the turbulence intensity, but not so for the lift coefficient, which increases with growing turbulence intensity.

A very important result is, that force coefficients can be scaled with the velocity profile form parameter, more precisely with the relation $u_{ht}/u_{hc}$. As it follows from Table 5.5, if the obtained coefficient value is multiplied by the corresponding relation $u_{ht}/u_{hc}$, the value of coefficient related to the uniform velocity profile is obtained. This is completely true for simulations over rough bottom in supercritical regime. This is also true for the scaled coefficients obtained for the smooth bottom in supercritical regime (cases S4 and S5) given in

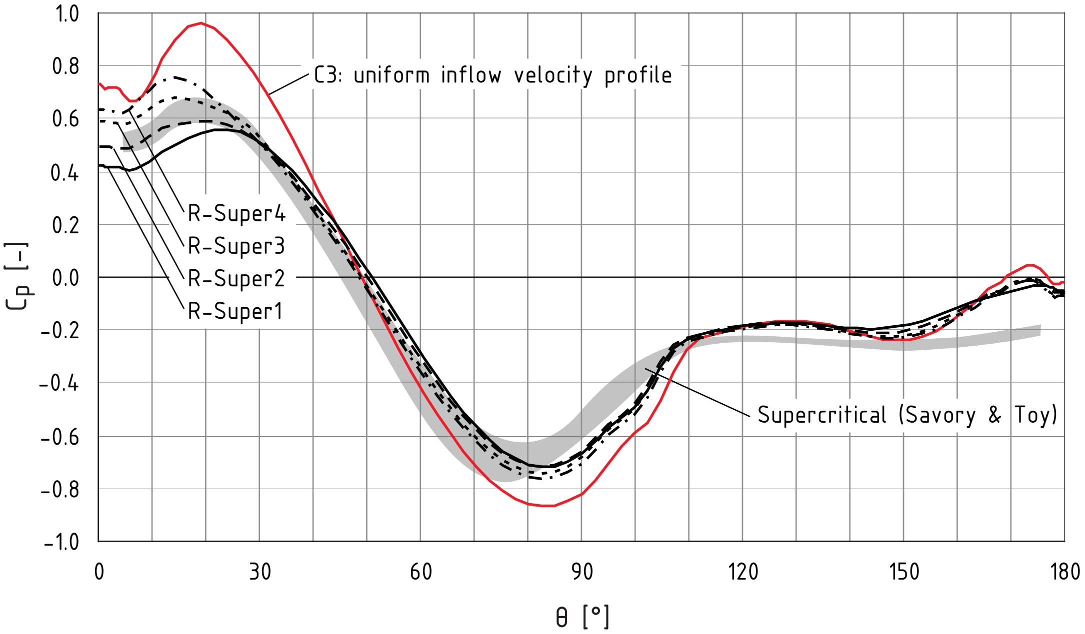

**Figure 5.21:** Pressure coefficient distributions over the hemisphere's plane of symmetry: supercritical regime over rough bottom

Table 5.3. However, although the scaled with the velocity profile form parameter coefficients for rough bottom conditions in the subcritical regime show consistently the same values of 0.44 and 0.53 for drag and lift coefficients, respectively, these values do not correspond completely to the values obtained for C2: the drag coefficient there is equal to 0.55. It should be noted, that the numerical solution for C2 had a very poor convergence.

Summarizing, the fact that the lift and drag coefficients can be scaled with the velocity profile form parameter allows to write Formula 4.8 for the FST-hemisphere density as:

$$\rho_h = \rho_w \left[1 + \frac{3}{8}\frac{u_{ht}^2}{r_h\, g}\left(c_l + \frac{c_d}{\mu}\right)\right] = \rho_w \left[1 + \frac{3}{8}\frac{u_{ht}^2}{r_h\, g}\frac{u_{hc}}{u_{ht}}\left(c_{l,b} + \frac{c_{d,b}}{\mu}\right)\right]$$

$$\boxed{\rho_h = \rho_w \left[1 + \frac{3}{8}\frac{u_{ht}\, u_{hc}}{r_h\, g}\left(c_{l,b} + \frac{c_{d,b}}{\mu}\right)\right] \qquad [\mathrm{kg/m^3}] \qquad (5.13)}$$

| with | | | | |
|---|---|---|---|---|
| | $\rho_h$ | = | density of a hemisphere, | [kg/m$^3$] |
| | $\rho_w$ | = | density of water, | [kg/m$^3$] |
| | $c_{d,b}, c_{l,b}$ | = | base drag and lift coefficients, | [-] |
| | $\mu$ | = | friction coefficient, | [-] |
| | $r_h$ | = | radius of a hemisphere, | [m] |
| | $u_{hc}$ | = | velocity at the level of a hemisphere's center of mass, | [m/s] |
| | $u_{ht}$ | = | velocity at the top level of a hemisphere | [m/s] |
| | $g$ | = | acceleration due to gravity, | [m/s$^2$] |

The values of the base drag and lift coefficients are those resulting from calculations with uniform inflow velocity profile for the sub- and supercritical regimes, respectively. These are:

**Subcritical regime:** $c_{d,b} = 0.44$, $c_{l,b} = 0.53$

**Supercritical regime:** $c_{d,b} = 0.31$, $c_{l,b} = 0.76$

Application of this formula with the base coefficients is verified in Chapters 6 and 7.

## 5.5 Visualized flow features

In post-processing of the simulation results, it is also important to look, whether flow features such as horseshoe and arch vortices are captured by the model. Generally, the pressure minimum or vorticity maximum can be used for the identification of vortex structures in inviscid flows. However, in shear flows, these standard approaches can lead to improper vortex identification [95].

Nevertheless, the horseshoe flow structure is captured without applying special vortex identification methods. While the main vortex of the horseshoe is seen well through the visualization of static pressure iso-surfaces (Figures 5.22, 5.23), the minor vortices contributing to the structure are made visible through the parallel rendering of the instantaneous flow path-lines (see Figure 5.23).

Analyzing the obtained records of time dependent drag and lift coefficients for a hemisphere, no periodicity of flow quantities in the wake can be reported. Thus, there is an evidence of the vortex shedding suppression, which usually is associated with the absence of von Kármán vortex shedding. However, the symmetrical shedding of arch vortices, which theoretically does not result in a strong variation of hydrodynamic coefficients, should still take place for a hemisphere. Unfortunately, flow visualization (at least with pressure iso-surfaces) does not show the presence of arch vortices. Although the elevated vorticity is

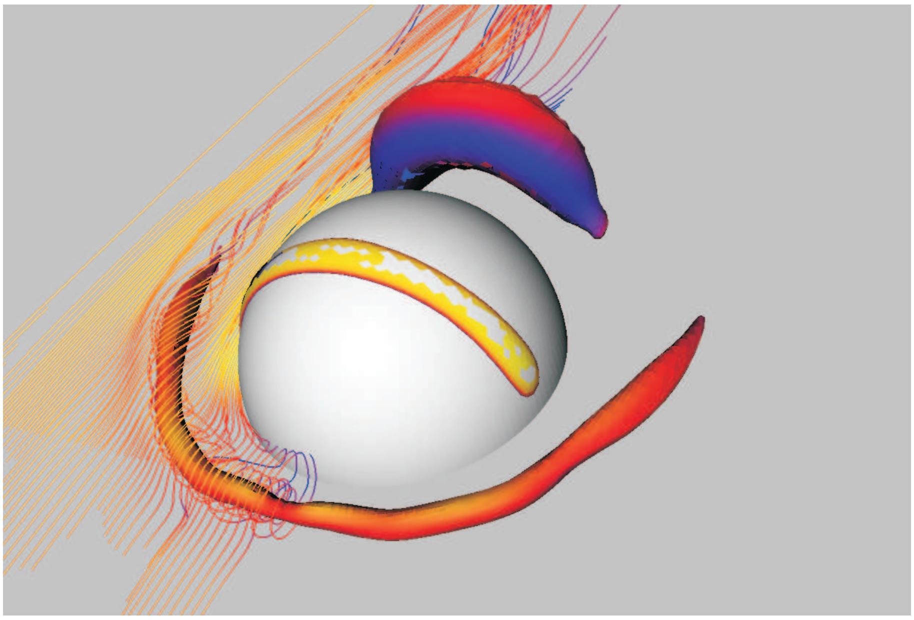

**Figure 5.22:** Bird's eye view of a horseshoe vortical structure and standing vortex behind a hemisphere in Run C2 ($I = 0.5\%$), visualized through an iso-surface of static pressure $\overline{p} =$ -9.55 Pa and flow path-lines

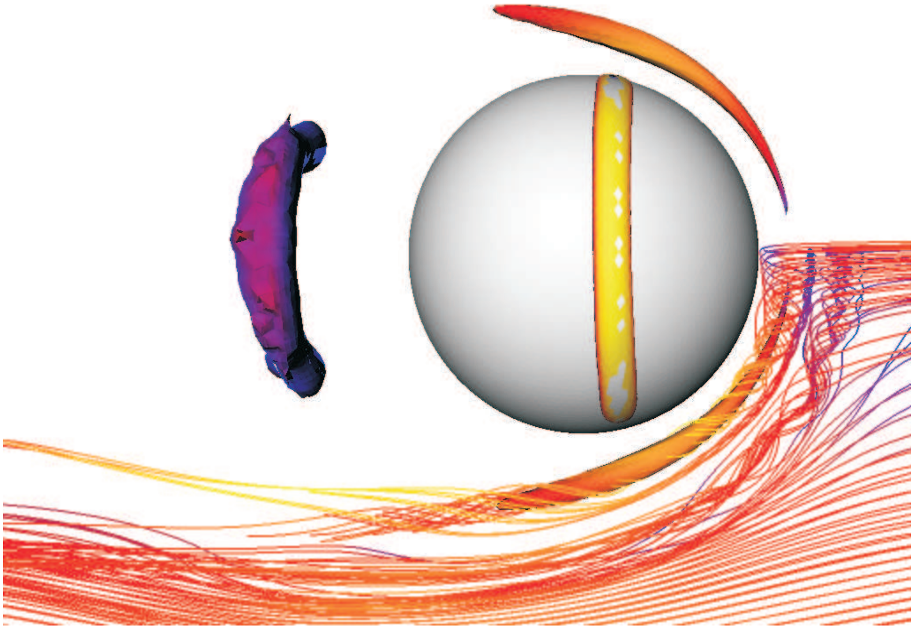

**Figure 5.23:** Top view of a horseshoe vortical structure and standing vortex behind a hemisphere in Run R-Sub1 ($I = 0.5\%$), visualized through an iso-surface of static pressure $\overline{p} =$ -7.55 Pa and flow path-lines

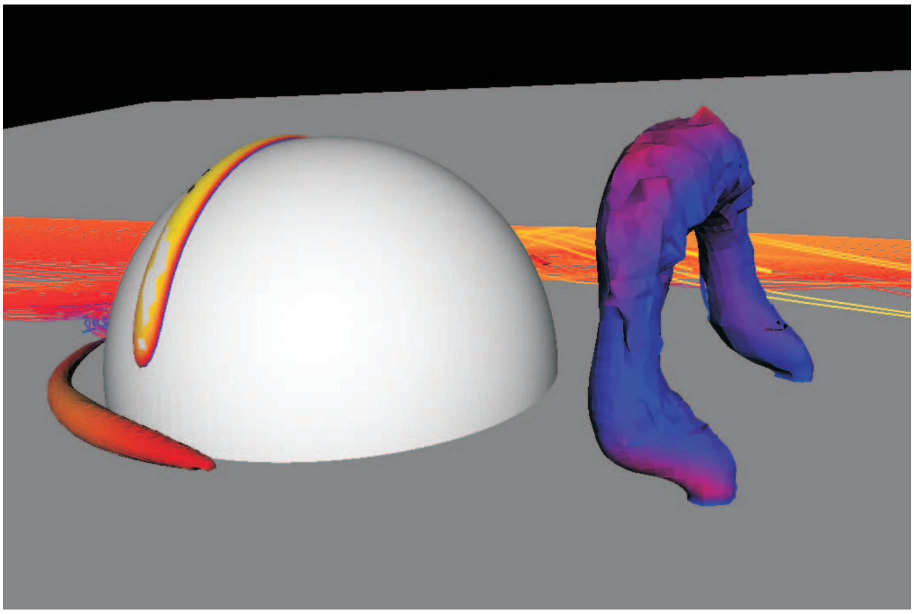

**Figure 5.24:** Side view of a standing vortex behind a hemisphere in Run R-Sub1 ($I = 0.5\%$), visualized through an iso-surface of static pressure $\overline{p}$ = -7.55 Pa

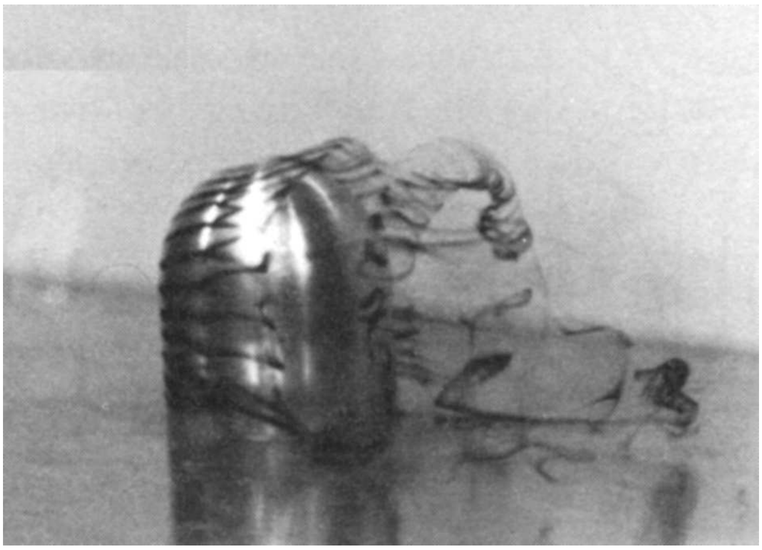

**Figure 5.25:** Arch vortices in the wake of a hemisphere-cylinder at $Re_{U_0} = 1 \times 10^3$ (side view), from Okamoto (1982) [60];

observed in the area of flow separation from the body, this does not result in the formation of vortices further downstream. It is very likely, that the applied turbulence models are not able to model this phenomena.

The structure seen behind a hemisphere in Figure 5.24 looks like an arch vortex on a first glance (compare to Figure 5.25, where arch vortex shedding in a wind tunnel is visualized through a smoke technique). However, this structure does not advance downstream with time, but just represents a standing vortex of the recirculation zone. The position and size of the standing vortex changes in simulation runs and stands in connection with the position of the flow separation from a body: in subcritical regime (earlier separation and larger recirculation zone) the core of this structure is high and positioned at a distance from the hemisphere; in supercritical regime it is not as high and positioned closer to the hemisphere. It is interesting, that in some references this structure is called arch vortex. However, arch vortices should develop in the area between the oncoming flow and a recirculation zone.

## 5.6 Summary

Analysis of references dealing with the flow around a hemisphere attached to the bottom suggests, that the flow in the body's wake is dominated by a symmetrical vortex shedding process. The arch vortices emerging here do not cause considerable fluctuations in the pressure field, thus, hydrodynamic drag and lift coefficients for a hemisphere can be assumed to be quasi constant over time. Within the range of those Reynolds numbers $\mathrm{Re}_{ht}$ from $10^4$ to $10^5$ relevant for FST-hemisphere measurements, the transition from subcritical to supercritical flow regime takes place. That means, that the laminar boundary layer separation is replaced by a turbulent one, resulting in a reduction of the drag coefficient from a value of 0.4 to 0.3. The numerical simulations described in this chapter aim to estimate the values for the lift coefficient in these regimes and to find out the influence of some important factors, such as roughness of the FST ground plate, oncoming flow turbulence intensity, and near-bed velocity profile form on the hydrodynamic coefficients.

Numerical simulations of the flow, performed with $k - \omega$ and Spalart-Allmaras turbulent models, both based on Reynolds averaging, show some restrictions in application. Firstly, these models predict the transition from subcritical to supercritical flow regime at a much lower Reynolds numbers as it occurs in reality at the same conditions. As the reduction of the drag coefficient for a hemisphere attached to the bottom encompasses a much larger range of Reynolds numbers than, for example, for the sphere in a uniform flow field, therefore, hydrodynamic coefficients cannot be estimated within this whole "transitional" regime. Only hydrodynamical coefficients corresponding to a clearly expressed subcritical or supercritical regime can be obtained, which imposes a considerable disadvantage. Secondly, no vortex shedding is reproduced with these turbulence models. Though it can be implied, that for high Reynolds number flows accompanied with high levels of turbulence intensity, the vortical structures do not persist long in the wake and do not affect the pressure field around a hemisphere. More physical experiments are desirable to clarify this. Correspondence of pressure distributions, obtained with the $k - \omega$ model, to the measured ones speaks for correctness of at least time averaged coefficients obtained in the present study.

The following can be summarized about influence of flow and equipment characteristics on the drag and lift coefficients for a hemisphere in a velocity-gradient flow field:

1. In free-surface flows, at relative submergences of a hemisphere of 4 and higher, the hydrodynamic coefficients can be assumed to be constant and independent from the Froude number. For smaller relative submergences, a considerable increase in drag is seen in laboratory measurements. In that case, the influence of the Froude number cannot be disregarded.

2. The roughness of the ground plate is of no relevance for the flow around a hemisphere. Thus, the hydrodynamical coefficients are the same for FST measurements performed with the smooth and structured ground plate.

3. The turbulence intensity of oncoming flow and the roughness of a hemisphere's surface theoretically influence the Reynolds number at which the transition from subcritical to supercritical regime occurs: elevated turbulent intensity and/or scratches on a surface lead to a lower critical Reynolds number. However, for FST measurements these effects cannot be parameterized quantitatively. For the computational method to FST-hemispheres, it is suggested to use only two kinds of coefficients: one corresponding to the subcritical and another corresponding to the supercritical flow regime. According to laboratory data, the critical Reynolds number corresponding to the switch between these regimes can be assumed to be $7 \times 10^4$. This $Re$ corresponds to the velocity at the level of a hemisphere's top $u_{ht} = 0.9$ m/s.

4. Numerical experiments allow to quantify the effect of the near-bed velocity profile form on the hydrodynamic lift and drag coefficients. Those coefficients corresponding to the uniform velocity profile are referenced further as *base coefficients*. For the subcritical regime those are $c_{d,b} = 0.44$ and $c_{l,b} = 0.53$; for the supercritical regime they are $c_{d,b} = 0.31$ and $c_{l,b} = 0.76$, respectively. Knowing the velocity at the levels of a hemisphere's top $u_{ht}$ and the center of mass $u_{hc}$, the density of a hemisphere to be moved by this flow can be evaluated with:

$$\rho_h = \rho_w \left[1 + \frac{3}{8}\frac{u_{ht}\,u_{hc}}{r_h\,g}\left(c_{l,b} + \frac{c_{d,b}}{\mu}\right)\right] \qquad [\mathrm{kg/m^3}] \qquad (5.14)$$

| with | | | | |
|---|---|---|---|---|
| | $\rho_h$ | = | density of a hemisphere, | [kg/m$^3$] |
| | $\rho_w$ | = | density of water, | [kg/m$^3$] |
| | $c_{d,b}, c_{l,b}$ | = | base drag and lift coefficients, | [-] |
| | $\mu$ | = | friction coefficient, | [-] |
| | $r_h$ | = | radius of a hemisphere, | [m] |
| | $u_{hc}$ | = | velocity at the level of a hemisphere's center of mass | [m/s] |
| | $u_{ht}$ | = | velocity at the top level of a hemisphere | [m/s] |
| | $g$ | = | acceleration due to gravity, | [m/s$^2$] |

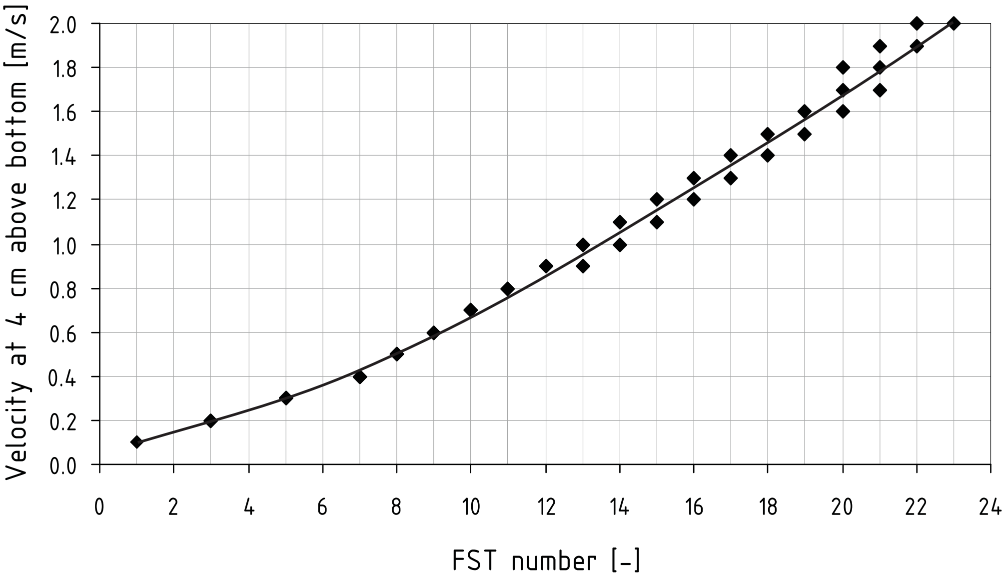

**Figure 5.26:** Relation "near-bed velocity vs. FST number", mean between curves related to sub- and supercritical flow regimes, $\mu = 0.24$, $u_{hc}/u_{ht} = 0.9$

Above given formula expresses the strict relationship between FST-hemisphere density/number and near-bed velocity (see Figure 5.26). Thus, it can be concluded that FST-hemisphere equipment measure mean (time averaged) near bottom velocity at a distance of 4 cm above the FST ground plate.

This part of the study discloses the complexity of flow over rough bottom. The picture is getting complex already by considering a flow past a single hemispherical obstacle, characterized by an interaction of the horseshoe vortex structure with the recirculation region behind the body. It is clear, that the values of the hydrodynamic drag and lift coefficients found in the numerical study rather correspond to idealized conditions. Many factors such as, for example, influence of neighbor roughness elements, a nonzero vertical velocity component, and flow between a structured plate and a hemisphere are difficult or impossible to account for. If those factors impose any problems on a numerical approach, is clarified in the next chapter.

# 6 Case studies

Two important questions should be answered by the following case studies: (1) whether it is possible to estimate, especially for field conditions, the near-bed velocity using the modified logarithmical law of Bezzola, and (2) how well FST-hemisphere densities/numbers can be calculated by means of Formula 5.14 using the values of hydrodynamic coefficients obtained in Chapter 5.

The case studies of this chapter are based on data collected in rivers of Austria, France, Belgium and Germany. The majority of material is kindly supplied by colleagues of a small scientific group for modelling of benthic habitats, organized within the COST 626 action. Thus, the calculations are done not only for rivers differing in morphology and size, but also for various equipment and FST measurements techniques.

For all case studies, a consistent methodology is applied. Where it is appropriate, the influence of parameters such as the mean substrate grain size and the thickness of the roughness sublayer, the hydrodynamic coefficients at different flow regimes, and the friction coefficient are tested and analyzed.

Detailed data tables for the case studies are not included in the printed text of the work due to their large size. They are available on request from the Institut für Wasserbau der Universität Stuttgart [45].

## 6.1 Methodology of FST-hemisphere numbers calculation

The following procedure of FST-hemisphere numbers calculation is applied in all case studies. It consists of two major steps: (1) estimation of near bed velocities (if they are not measured) and (2) calculation of FST densities and, consequentially, FST numbers itself. In Figure 6.1a, the parameters used are defined. In Figure 6.1b, possible vertical positions of an FST plate are shown. A plate put on the roughness elements is in position "very high" and with the upper surface levelled with the tops of the grains in position "high". The third position – "deep" – is rare and is found only in the laboratory experiments of Scherer (see Section 6.2).

To obtain the near-bed velocities, in particular the velocity at the top level of a hemisphere $u_{ht}$ and at the level of a hemisphere's center of mass $u_{hc}$, the logarithmical velocity distribution law after Bezzola [8] (see Section 3.6) is applied:

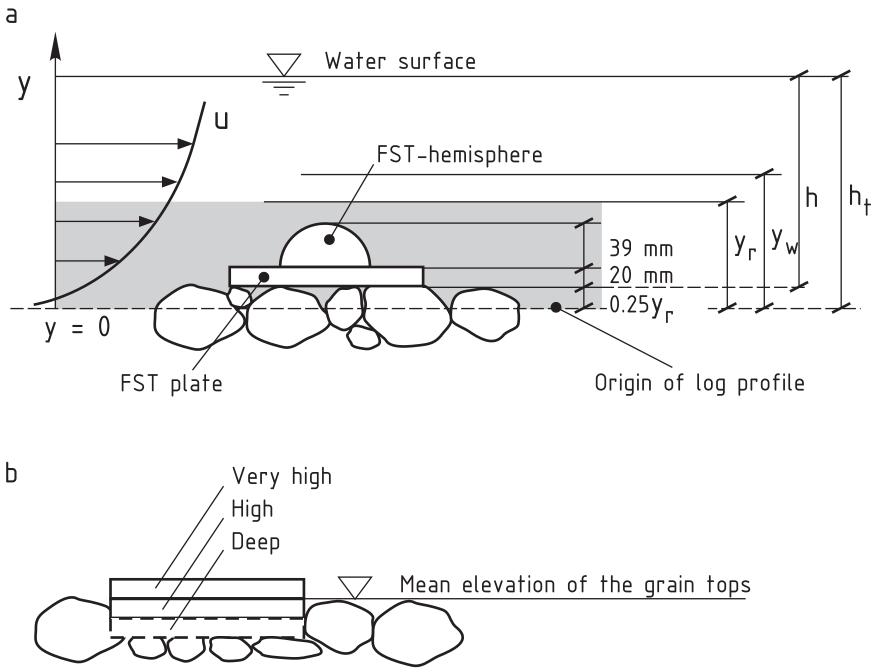

**Figure 6.1:** a. Definition of major parameters for calculation of FST-hemisphere densities; b. Vertical positions of the FST plate

1. Based on visual observations of substrate or sieve analysis data, the thickness of a roughness sublayer $y_r$ is estimated. It is described how this was done in each particular case study.

2. From the mean column velocity $u_{0.4}$, total water depth $h_t$, and the thickness of the roughness sublayer $y_r$, the shear velocity is calculated with:

$$u_* = \frac{u_{0.4}}{c_r\left(\frac{1}{\kappa}\ln\frac{0.4\,h_t}{y_r} + 8.48\right)} \qquad \text{if} \quad 0.4\,h_t \leq y_w \tag{6.1a}$$

$$u_* = \frac{u_{0.4}}{c_r\left(\frac{1}{\kappa}\ln\frac{y_w}{y_r} + 8.48\right) + \frac{2}{3}\frac{h_t}{\kappa y_w}\left[\left(1 - \frac{y_w}{h_t}\right)^{\frac{3}{2}} - 0.465\right]} \qquad \text{if} \quad 0.4\,h_t > y_w \tag{6.1b}$$

with $u_*$ = shear velocity, [m/s]
$u_{0.4}$ = mean column velocity acting at a distance of $0.4\ h_t$, [m/s]
$h_t$ = total water depth, [m]
$y_r$ = thickness of roughness sublayer, [m]
$y_w$ = thickness of the inner (wall) region, [m]
$c_r$ = damping factor, [-]
$\kappa$ = von Kármán constant, [-]

The value of the total depth $h_t$ is defined as the distance from the origin of a logarithmical velocity profile to the water surface (see Figure 6.1a). It is the sum of water depth $h$, measured from the mean elevation of substrate grain tops, and offset of the log law profile origin below roughness tops $\Delta y_0$, assumed in all cases to be $0.25 y_r$ (see Section 3.6).

In Equations 6.1a,b, the damping factor $c_r$ is defined as follows:

$$c_r^2 = \begin{cases} 1 - \frac{y_r}{h_t} & \text{for } \frac{h_t}{y_r} > 2, \\ 0.25\ \frac{h_t}{y_r} & \text{for } \frac{h_t}{y_r} \leq 2 \end{cases} \tag{6.2}$$

The thickness of the inner region is differentiated for cases of large and small relative submergence:

$$y_w = \begin{cases} h_t & \text{for } \frac{h_t}{y_r} \leq 1, \\ y_r & \text{for } 1 < \frac{h_t}{y_r} \leq 3.2, \\ 0.31\ h_t & \text{for } \frac{h_t}{y_r} > 3.2 \end{cases} \tag{6.3}$$

3. Knowing the shear velocity $u_*$, the velocities $u_{ht}$ and $u_{hc}$ acting at the levels of a hemisphere's top $y_{ht}$ and center of mass $y_{hc}$, respectively can be determined. This is done by substitution of the values $y_{ht}$ and $y_{hc}$ into Equations 6.1a,b, where $y_{ht}$ and $y_{hc}$ are defined as:

$$y_{ht} = 0.25\ y_r + r_h + h_p \tag{6.4a}$$

$$y_{hc} = 0.25\ y_r + \frac{3}{8}\ r_h + h_p \tag{6.4b}$$

with $y_{ht}$ = level at which $u_{ht}$ acts, [m]
$y_{hc}$ = level at which $u_{hc}$ acts, [m]
$y_r$ = thickness of roughness sublayer, [m]
$r_h$ = hemisphere radius, [m]
$h_p$ = thickness of the FST ground plate, [m]

$h_p$ = 0.02 m with the FST plate in position “very high”,
$h_p$ = 0 with the FST plate in position “high”.

Then, the density of an FST-hemisphere is calculated with:

$$\boxed{\rho_h = \rho_w \left[1 + \frac{3}{8}\frac{u_{ht}\,u_{hc}}{r_h\,g}\left(c_{l,b} + \frac{c_{d,b}}{\mu}\right)\right] \qquad [\mathrm{kg/m^3}] \qquad (6.5)}$$

with $\rho_h$ density of a hemisphere, $[\mathrm{kg/m^3}]$
$\rho_w$ density of water, $[\mathrm{kg/m^3}]$
$u_{ht}$ = velocity at the top level of a hemisphere, [m/s]
$u_{hc}$ = velocity at the level
of a hemisphere’s center of mass, [m/s]
$c_{l,b}$ = base lift coefficient, [-]
$c_{d,b}$ = base drag coefficient, [-]
$\mu$ = friction coefficient, [-]
$r_h$ = hemisphere radius, [m]
$g$ = acceleration due to gravity, $[\mathrm{m/s^2}]$

The values of base lift and drag coefficients are 0.53 and 0.44 for a subcritical regime, and 0.76 and 0.31 for a supercritical regime (see Section 5.6). Also, calculations in the so called “mixed” regime are performed. That is, if the velocity $u_{ht}$ is less than 0.9 m/s, the hydrodynamic coefficients corresponding to the subcritical regime are taken, and those corresponding to the supercritical regime otherwise. As 0.9 m/s is quite a large value for a near-bed velocity, results of subcritical and mixed regimes are almost identical in many cases (see Figures 6.11 and 6.12). The value of the friction coefficient is chosen according to the type of the plate (see Section 4.2.2).

Finally, the FST number corresponding to the obtained density is selected from Table 4.1. For example, the density 1005 $\mathrm{kg/m^3}$ corresponds to FST number 0, the density 2000 $\mathrm{kg/m^3}$ to FST number 10.

## 6.2 Laboratory measurements of Scherer

### 6.2.1 Data description

The only set of laboratory measurements within the case studies originates from the work of Scherer [69]. These experiments aimed to show the performance of the new, structured FST plate (see also Section 4.1.2). Of particular value is, that the measurements were conducted on a number of artificial "substrates", characterized not only by a specific grain diameter, but also by a distinct arrangement and density of roughness elements.

FST-hemisphere measurements were done in a laboratory flume with a length of 25 m and a width of 0.6 m. In every run, normal flow conditions were established, meaning that water depth and flow velocity in the longitudinal direction in the flume did not vary.

The main experimental data, that is further verified with the calculational method, is given in Table 6.1.

| Run | Substrate material | $d$ mm | Arrangement of roughness elements | Assumed $y_r$ m | Plate position |
|---|---|---|---|---|---|
| 2 | fine gravel | 3 – 5 | random | 0.006 | deep[a] |
| 5 | coarse gravel | 20 – 65 | dense | 0.065 | high |
| 6 | coarse gravel | 20 – 65 | dense | 0.065 | very high |
| 9 | coarse gravel | 20 – 65 | loose | 0.086 | high |
| 11 | coarse gravel | 20 – 140 | dense | 0.160 | high |
| a | plate position is assumed to be of no importance | | | | |

**Table 6.1:** Substrate characteristics in the experiments of Scherer [69]

To obtain the total depth $h_t$, a zero-level displacement (0.25 $y_r$) is added to the mean water depth $h$ registered in experiments(see Figure 6.1).

Unfortunately, vertical velocity distributions were not acquired. The mean flow velocity, which is calculated here through the ratio of discharge to cross-sectional area, is assumed to be equal to the mean column velocity at 0.4 of the total water depth $h_t$.

The thickness of the roughness sublayer is calculated upon recommendations of Bezzola: the mean diameter of substrate material, estimated for every run from the description in Table 6.1, is multiplied by a factor of 1.5 for homogeneous and densely ordered (Runs 2, 5, 6), and by a factor of 2 for loosely arranged (Run 9) or inhomogeneous (Run 11) substrates.

### 6.2.2 Results

Three cases were generally calculated with drag and lift coefficients corresponding to sub-, supercritical and mixed hydrodynamic regimes. But, due to the absence of a near bottom velocity larger than 0.9 m/s, the results for subcritical and mixed cases are identical.

The best correlation between calculated and measured FST numbers is obtained for Run 2, characterized by a very fine substrate material (see Figure 6.2[1]). The difference between measured and calculated FSTs is no larger than one for the whole range of values. Numbers of lighter FST-hemispheres are slightly overestimated by the computation. The average difference between calculated and measured FST numbers, estimated with:

$$\overline{\Delta}_{FST} = \frac{1}{N}\sum_{n=1}^{N}(FST_c - FST_m) \qquad [-] \qquad (6.6)$$

with $\overline{\Delta}_{FST}$ = average difference between calculated and measured FST numbers, [-]
$N$ = number of measurements, [-]
$FST_c$ = calculated FST number, [-]
$FST_m$ = measured FST number, [-]

for the supercritical and mixed regimes is -0.15 and +0.31, respectively.

With growing mean substrate diameter, the differences between calculated and measured FST numbers become larger. Runs 5 and 6, which differ only by the vertical position of the plate, show a similar degree of correlation between computed and measured values (see Figures 6.3 and 6.4). In these runs, FST numbers higher than 5 and 7 respectively, are underestimated by the computational method. In Run 5, the worst mean difference value between calculated and measured FSTs among all runs is obtained for the mixed calculation procedure (-0.89). In Run 6, the mean difference equals -0.74.

Run 9 differs from Run 5 in the arrangement of roughness elements. Here, a maximum in difference between calculated and measured values is found for heavy FST hemispheres (-3), but the mean difference $\overline{\Delta}_{FST}$ is comparable to Runs 5 and 6 and comprises to a value of -0.77 (see Figure 6.5).

In Run 11, characterized by the coarsest substrate, the maximum difference between measured and calculated values is two FST numbers. A similar trend like in previous runs can be seen: large FST numbers (7 an higher) are underestimated. Low FST numbers are, in contrast, overestimated. Despite of a coarse substrate, the mean difference $\overline{\Delta}_{FST}$ is -0.38 and, thus, less than in Run 5, 6 and 9.

It can be concluded, that despite the absence of measured near-bottom velocity data, FST numbers are relatively well estimated from those velocities computed through the mean

---

[1] Some points in this and similar diagrams are on top of each other.

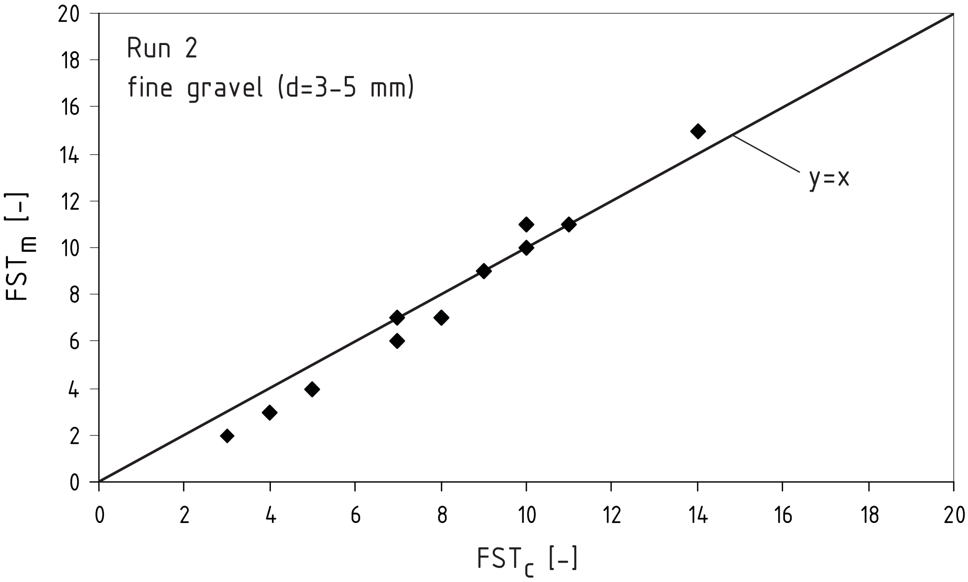

**Figure 6.2:** Calculated vs. measured FST numbers for Run 2, mixed flow regime

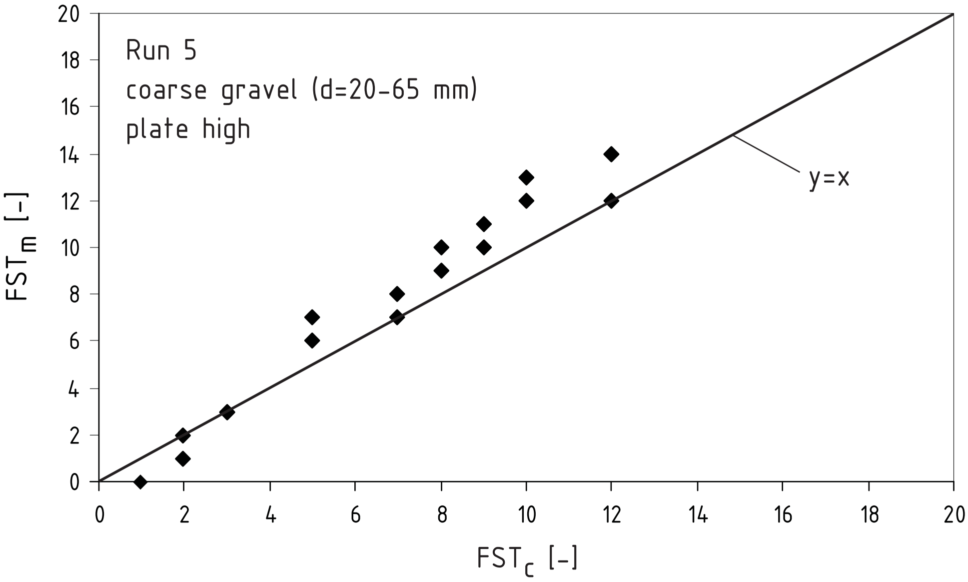

**Figure 6.3:** Calculated vs. measured FST numbers for Run 5, mixed flow regime

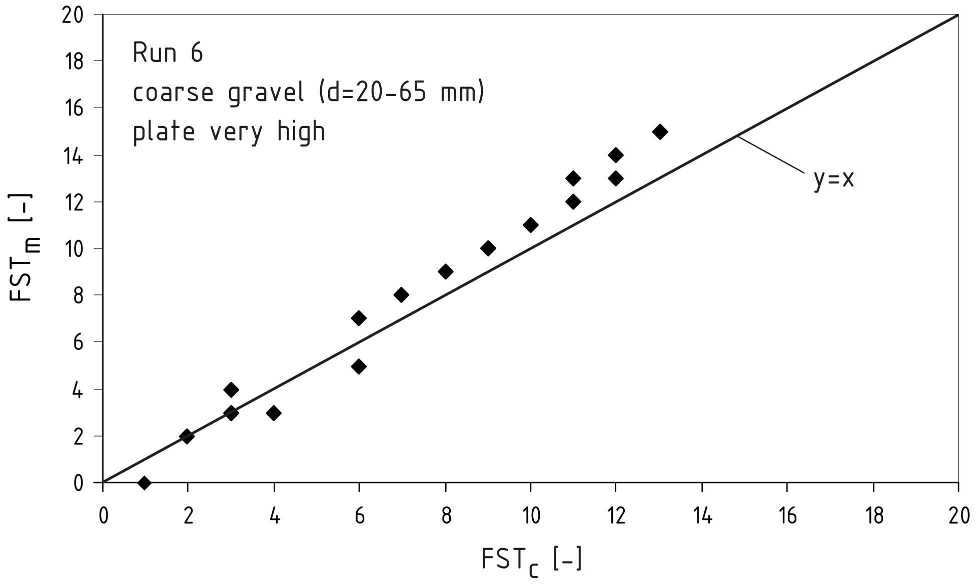

**Figure 6.4:** Calculated vs. measured FST numbers for Run 6, mixed flow regime

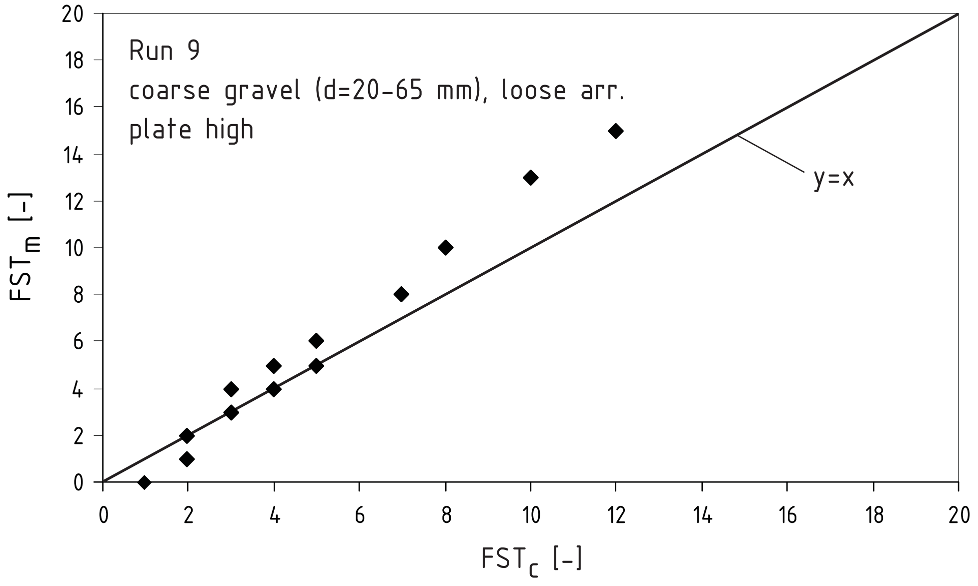

**Figure 6.5:** Calculated vs. measured FST numbers for Run 9, mixed flow regime

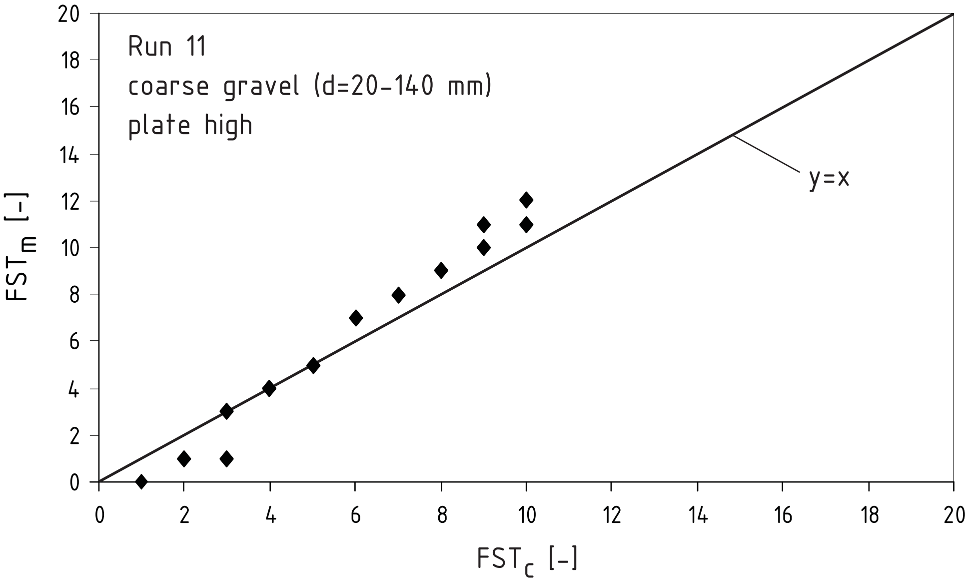

**Figure 6.6:** Calculated vs. measured FST numbers for Run 11, mixed flow regime

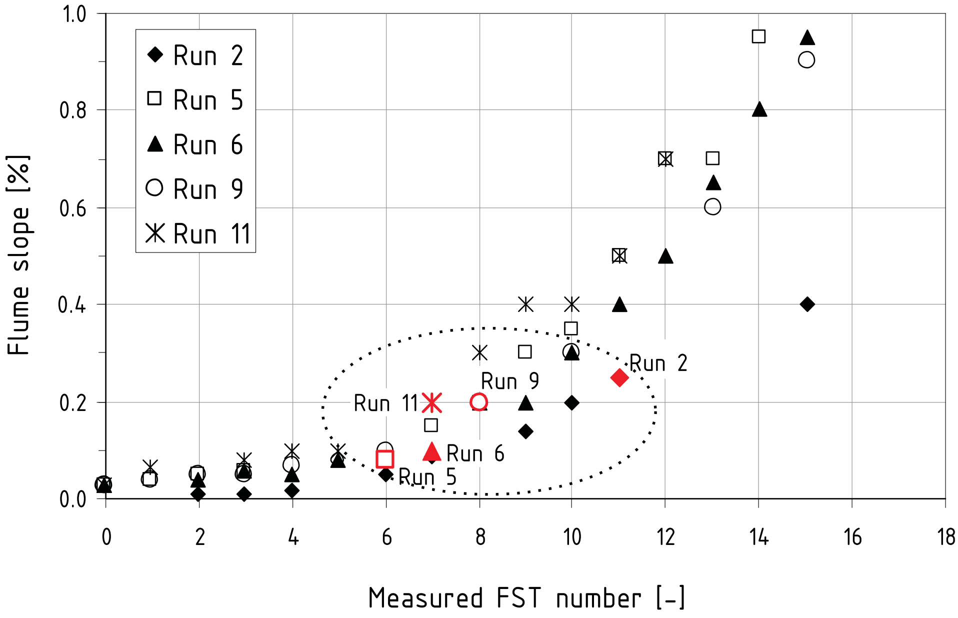

**Figure 6.7:** Measured FST numbers vs. flume slope in Runs 2, 5, 6, 9 and 11, mixed flow regime

column velocity by application of the logarithmical velocity distribution law. In most runs, the difference between calculated and measured values is no larger than two FST numbers. The mean difference $\overline{\Delta}_{\mathrm{FST}}$ is worst for Run 5 (-0.89) for the mixed regime.

The systematic underestimation of heavy hemispheres is difficult to explain. One hint can give a comparison of the measured FST numbers and the slope of the flume bottom shown in Figure 6.7. The area marked with a dotted circle shows, when the underestimation of calculated FST numbers starts. It can be seen, that for all runs a bottom slope larger than 0.1 to 0.3 % appears to be a threshold at which the computational method starts to underestimate FST numbers. Run 2, with the best correlation of values, is characterized by the lowest flume slopes. It remains unclear, whether the horizontal plate position was adjusted after the slope of a flume had been changed in the experiment. By the inclined ground plate, a part of the weight force acts in the same direction as the drag force. This could result in increased FST numbers at larger flume slopes.

## 6.3 Field case: River Schwechat, Austria

### 6.3.1 Data description

Collection of this data was initiated through the work of a small scientific group for modelling of benthic habitats, organized within the COST 626 action, and is kindly supplied by H. Mader and M. Pedersen for the present study.

**Figure 6.8:** Measurement reach at river Schwechat, photo H. Mader

FST-hemisphere and simultaneous velocity measurements were conveyed on the Lower Austria river Schwechat. Schwechat, a south-west tributary of Danube, is 62 km long in total and is characterized by a yearly mean flow discharge of 1.55 $m^3/s$ at the measurement site [50]. Measurements, in total 299 FST and velocity samples, were done at flow rates of 0.39 and 0.33 $m^3/s$. The mean river width at these discharges is about 9 m, the energy slope of a reach is 5 ‰. Measurements were conducted in transects; in every transect, 5 points were recorded. The distance between transects equals to about one river width. Composition of the substrate in the river reach is given in Table 6.2.

FST measurements were conducted the following way: the FST plate (new standard structured) was placed on the river bottom with the upper surface levelled with the roughness tops. Thus, the definition of total water depth $h_t$ and roughness sublayer thickness is the same as in Section 6.2.1 with the plate put into the position "high" (see methodology in Section 6.1). After the FST number was noted, velocity measurements with the 2D P-EMS (Programmable 4-Quad Velocity Meter) of Delft Hydraulics at distances of 1 and 4 cm above the plate followed. Also, the mean column flow velocity (at 40 % of water depth $h$) was measured with a P-EMS and a propeller type velocity meter with a diameter of 35 mm.

| Substrate class | Diameter range mm | Mean grain diameter mm | Percentage in the sample % |
|---|---|---|---|
| Silt | $< 0.063$ | - | 0.4 |
| Sand | 0.063 - 2 | 1 | 3.6 |
| Gravel | 2 - 63 | 33 | 45.1 |
| Stones | 63 - 200 | 132 | 49.3 |
| Blocks | $> 200$ | - | 1.6 |

**Table 6.2:** Substrate composition at the measurement reach, river Schwechat, from [50]

This data set allows application of the calculational method for FST-hemispheres in two ways. First, from measured near bottom velocities at distances of 1 and 4 cm from a plate, direct calculations of FST densities with Formula 6.5 are possible. Second, from mean column velocities, an estimation of near bottom velocities is done using the procedure described in Section 6.1. After this, FST densities are calculated through the use of Equation 6.5.

Characteristic diameter of substrate material is assumed to be the same for the whole reach. The mean grain diameter is estimated upon data from Table 6.2, using the following expression [83]:

$$d = \frac{a_1\, d_1 + a_2\, d_2 + a_3\, d_3}{9} \tag{6.7}$$

with $d_1, d_2, d_3$ = mean diameters of the first, second and third most abundant substratum classes in the sample, respectively, [m]

$a_1, a_2, a_3$ = weight coefficients, [-]

In [83], for the weight coefficients $a_1$, $a_2$, $a_3$ values of 5, 3 and 1 are given. As at Schwechat the first and second most abundant substrate classes have almost the same percentage in the sample, coefficients $a_1$ and $a_2$ are both taken equal to 4. Thus, the mean grain diameter calculated with above formula is equal to 7.3 cm. The thickness of the roughness sublayer $y_r$ is calculated by multiplying the mean grain diameter $d$ by a factor of 1.5 (see recommendations in Section 3.6) and is equal to 11 cm. Also, mean grain diameters of 6 cm and 8.6 cm with values of $y_r = 9$ cm and 12.9 cm, respectively, which correspond to almost a 20 % decrease and increase in mean value, are considered to investigate the sensitivity of the methodology to this parameter.

### 6.3.2 Results

First of all, computed and measured near-bed velocities are compared. It can be seen from Figures 6.9 and 6.10, that, with the help of the logarithmical law, velocity at a distance of 1 and 4 cm from the plate is estimated well, even with an assumed equal mean grain diameter of 7.3 cm for the whole reach. Most points lie within a ±10 cm/s distance from the $y = x$ line. It seems, that velocities at a distance of 4 cm are better estimated than those at 1 cm. Variation of the mean substrate diameter does not change the correlations considerably.

Also, mean column velocities measured with P-EMS (2D vector) and the propeller velocity-meter (1D component) are compared. Most values are close to each other, but there are more points where the P-EMS velocity is larger than the 1D velocity measured with the propeller. This fact can be explained that way, that it is not always possible to find the direction of the maximum velocity with a propeller meter. There are a few points where large P-EMS velocity and, at the same time, a zero propeller velocity was registered, probably showing problems measuring near-bottom velocities with the propeller.

In Figure 6.11, the cumulative curves of FST numbers estimated through measured near-bottom velocities are shown. The three curves correspond to sub-, supercritical and mixed regimes with the values for drag and lift coefficients taken as recommended in Section 6.1. It can be seen, that although the mixed method gives the best correlation of measured and computed FST numbers, the differences obtained in sub- and supercritical regimes are also not large, the curves are quite close to each other. The mean differences between computed and measured values $\overline{\Delta}_{\mathrm{FST}}$ for sub-, supercritical and mixed cases are +0.15, -0.29 and +0.11, respectively. As can be seen from Figure 6.13, most computed values (85.9 % from a total of 299) have a difference of ±2 to the measured ones. 27.5 % of the points in the sample have the same computed FST number like the measured ones.

Cumulative curves of FST numbers estimated through near-bed velocities computed with the help of the log law have also a good correlation to the measured curve (see Figure 6.12). These match the measurements even slightly better than those obtained from the measured near-bed velocities. Subcritical calculation method gives slightly better results than the mixed one, but again all three curves lie very close to each other. The mean differences between computed and measured FST numbers $\overline{\Delta}_{\mathrm{FST}}$ are +0.01, -0.34 and -0.04 for sub-, supercritical and mixed methods, respectively. 89.3 % and 32.8 % of the points have a difference of ±2 respectively zero to the measured FSTs. The differences are distributed more symmetrical to the zero deviation than in case of measured near-bed velocities (see Figure 6.13).

Comparing the curves in Figures 6.11 and 6.12, it can be noticed, that in the range of large FST numbers, the supercritical regime shows a better correlation to the measured values. It

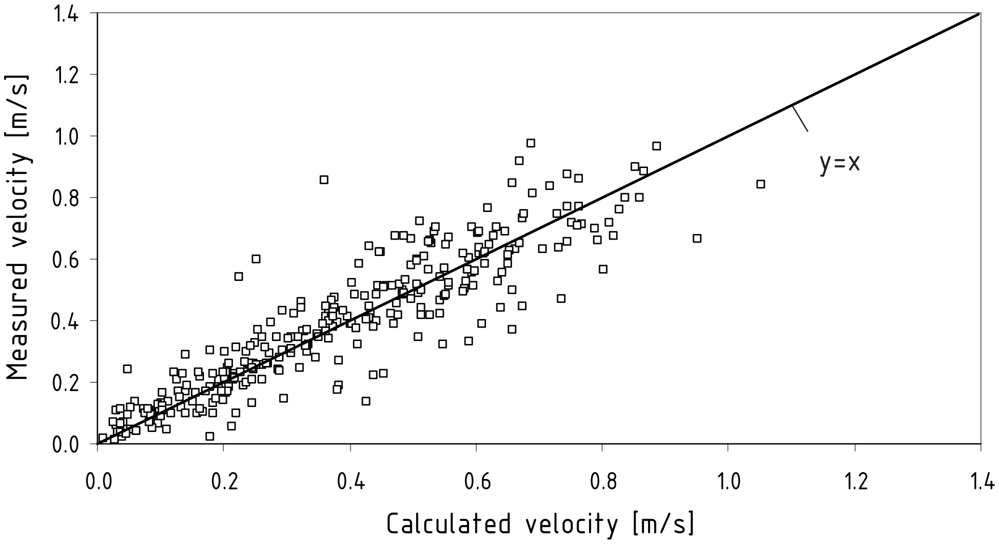

**Figure 6.9:** Calculated vs. measured velocity at 1 cm above the plate, d = 7.3 cm

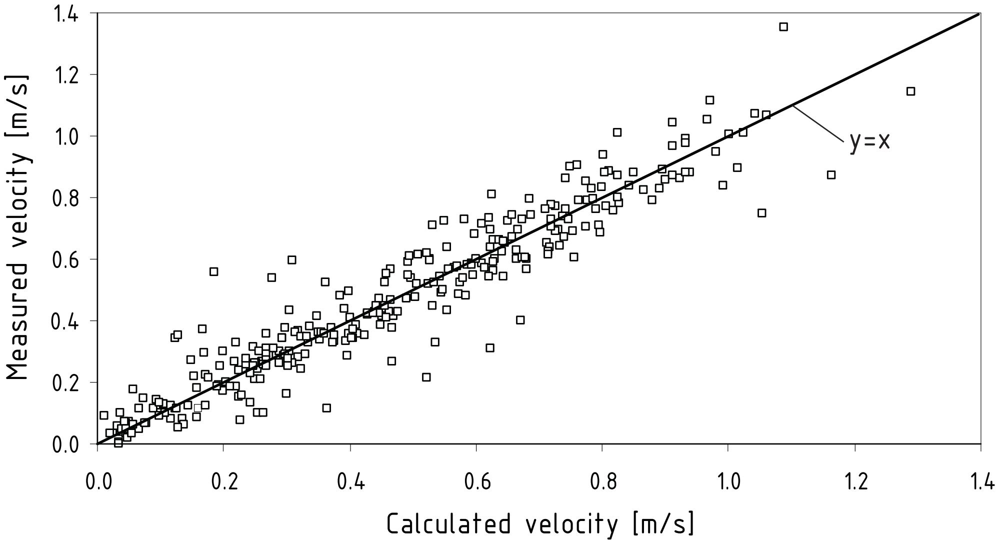

**Figure 6.10:** Calculated vs. measured velocity at 4 cm above the plate, d = 7.3 cm

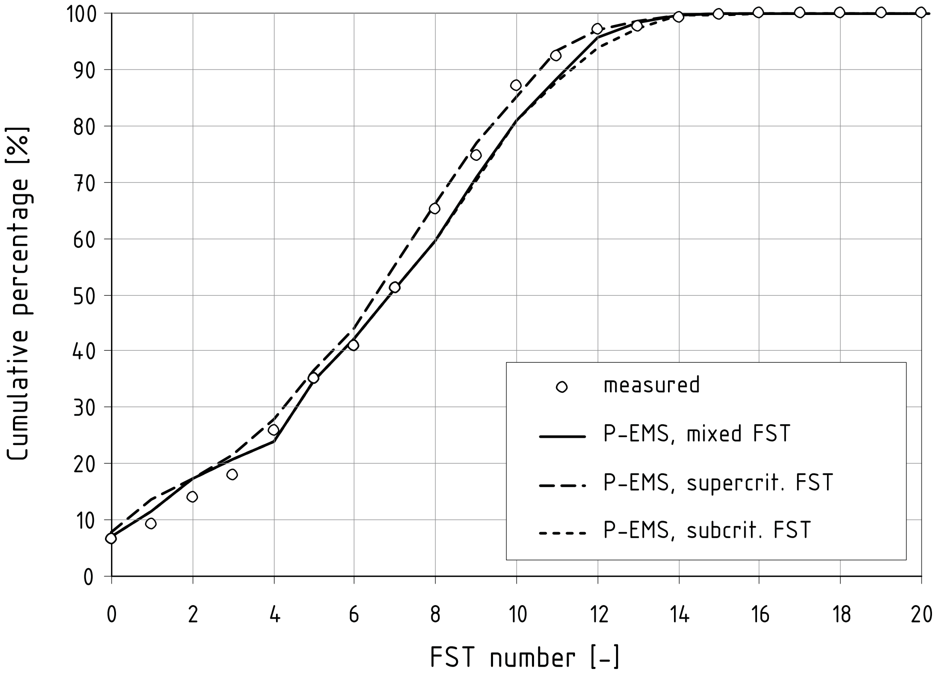

**Figure 6.11:** Cumulative curves of FST numbers: measured and computed from P-EMS near-bed velocities

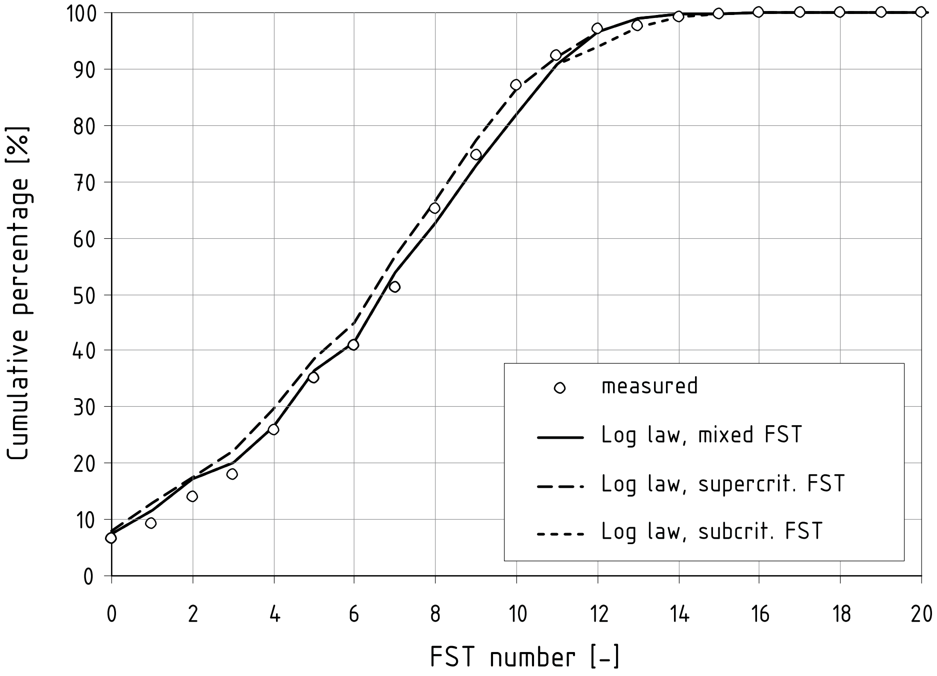

**Figure 6.12:** Cumulative curves of FST numbers: measured and computed from log law near-bed velocities, d = 7.3 cm

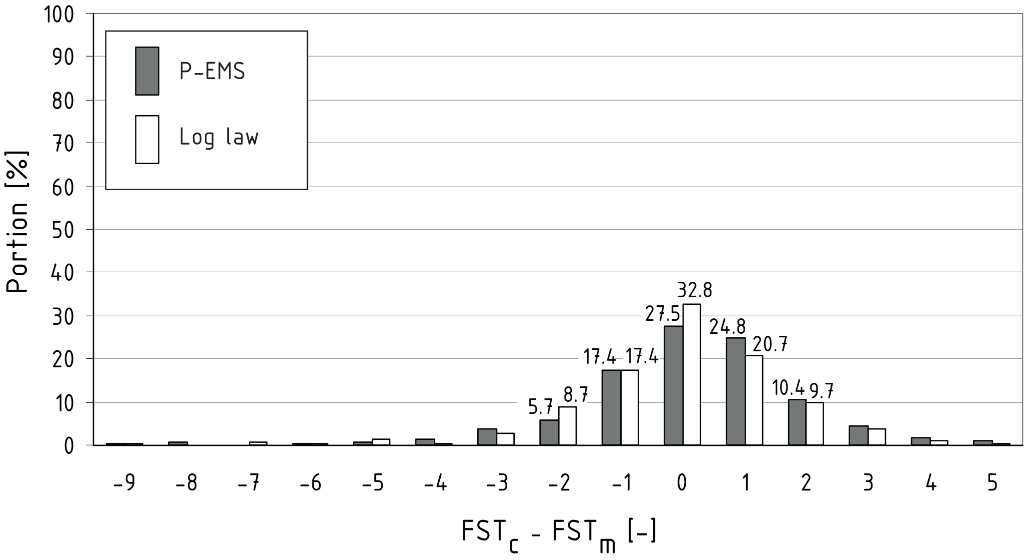

**Figure 6.13:** Comparison of differences in computed and measured FST numbers for P-EMS and log law, mixed flow regime

appears to be possible, that the transition to the supercritical regime takes place earlier than at the assumed velocity of 0.9 m/s (see methodology in Section 6.1).

Considering the influence of substrate, we can say that the representative mean diameter of 7.3 cm for this reach is a bit too high. Calculations in the mixed regime with the mean substrate diameter equal to 6 cm gives the best values of zero and ±2 FST number differences – 33.4 % and 90.3 %. Also, the distribution of differences is pure symmetrical. In contrast, the calculation with a mean grain diameter of 8.6 cm gives worse result than with 7.3 cm. The values of zero and ±2 FST differences are 29.4 % and 88.3 %, respectively.

## 6.4 Field case: River Rhône, France

### 6.4.1 Data description

This data set originates from studies within the framework of the Decennial Rhône Hydraulics and Ecological Rehabilitation Plan (2000) for the river Rhône in France [80]. It is kindly supplied by the COST 626 member Sylvie Mérigoux for the present evaluation.

River Rhône originates out of snow and ice melt from the Rhône Glacier in Switzerland and flows into the Mediterranean Sea. The average annual discharge from Lake Léman is 570 $m^3/s$, and at Beaucaire, upstream Arles near the end of the river course, it is 2300 $m^3/s$. The river has a relative high gradient and respectively a large hydroelectric potential. Nowadays, one third of the total river length consists of bypass sections (old Rhône channel), from which water is taken for the needs of navigation and hydropower production. The 19 Rhône hydro-power stations account for 20–25 % of the French hydroelectric production [80]. In the bypass sections, only a small portion of the total discharge is flowing, resulting in considerable changes in the physical habitat for many species. Major deficits are the reduction of ground water levels and, consequentially, degradation of the riparian vegetation, cutoff of side branches, and a general decline of biodiversity.

Within the framework of a restoration program aimed on discharge augmentation in the bypass sections and cut-off channels rehabilitation, biological investigations of benthos fauna were conducted. For the assessment of the physical habitat, FST-hemispheres and flow velocities were measured at four bypass river sections. As a standard, measurement spots were randomly distributed over a river reach of a total length comprising 15 to 30 widths of the river (containing at least one pool-riffle succession), resulting in total about 240 random samples. Additionally, in one bypass section, 60 spots were measured. These were not randomly distributed, but an attempt to get the whole spectrum of FST numbers (from 0 to 17) was made [56].

The measurement procedure was as follows: the old (smooth) plexiglass plate was placed on the substrate (position "very high" according to the scheme in Figure 6.1b) and the FST number was obtained using Statzner's standard placement procedure (see Section 4.1.1). Then, the plate was removed and the mean column velocity (at a distance of 40 % of the water depth from the bottom) was measured with the propeller type Ott current meter. At every spot, substrate probes were taken (also for biological analysis) and a sieve analysis was performed to obtain the percentage of every substrate fraction in the sample.

In the present work, for calculation of FST numbers, near-bed velocities are estimated with the logarithmical velocity distribution law (see methodology in Section 6.1). After this, Formula 6.5 is used for the estimation of FST densities. Again calculations in sub-, supercritical and mixed hydrodynamic regimes with respective drag and lift coefficients are performed.

The roughness sublayer thickness $y_r$ is calculated as follows. Upon the substrate composition data [45], the mean diameter $d$ of every sample is estimated by Formula 6.7 (with coefficients $a_1 = 5$, $a_2 = 3$ and $a_3 = 1$). To obtain $y_r$, the value of the mean grain diameter is multiplied by a factor of 1.5.

The largest uncertainty in this field case is connected to the selection of the friction coefficient $\mu$. Disregarding the fact of different materials tested for the determination of the friction coefficient for the smooth plate (see Table 4.3: Heilmair and Strobl [36]: plexiglas, Scherer [69]: PVC, own: steel), the largest influence on the $\mu$ value has the FST placement method. Using the "drop" method, the friction coefficient can be as small as 0.05, meaning that a very small velocity is required to move heavy hemispheres. Using the "press" method, this coefficient is as large as 0.5–0.7.

After analysis of the Rhône river data, it becomes clear that the friction coefficient here is larger than 0.24. That is, the particular FST-hemisphere in the river Rhône case is moved at a much higher flow velocity than in previous case studies (using the new structured plate). That means, that the placement method was more close to the variant “press” using the old smooth plate. That also means, that the transferability formula recommended in [20] (see Section 4.1.3) is not applicable in this case. According to it, the FST number corresponding to the equipment with a structured plate has to be increased by 1 to obtain the values corresponding to a smooth plate. However, the opposite – a mean decrease by 1–2 FST numbers – has to be done to obtain the measured values. Thus, for this case the FST numbers are computed with the two friction coefficients corresponding to the “press” method using the smooth plate: 0.601 and 0.506 (see Table 4.3). Also, calculations with $\mu = 0.24$ and a subsequent increase of FST numbers by one are done.

### 6.4.2 Results

In Figure 6.14, the cumulative curves of FST numbers are shown. It is clear that calculations using a friction coefficient of 0.24 with a subsequent increase of FST numbers by one give no acceptable result – measured FST numbers are much lower than those calculated. The mean difference between computed and measured values is +2.64.

The curves obtained with $\mu = 0.506$ and 0.601 do not differ considerably from each other. They match the measured distribution better than the first curve, but considerable differences up to 8 % are seen for FST numbers 3, 4 and 10 to 14. The mean differences $\overline{\Delta}_{\mathrm{FST}}$ are -0.03 and -0.34, respectively, which are comparable to the results of previous studies. Unfortunately, the percentage of computed values with a zero difference to the measured ones is only 24.5 % and 22.8 %, respectively (see Figure 6.15). These are at least by 8 % lower than those for the Schwechat river. Nevertheless, the number of values which differ from the measured ones by less or equal than $\pm 2$ is high (87.2 % and 88.9 %).

Even with the relative good results achieved by a calculation with a friction coefficient of $\mu = 0.506$, it is difficult to believe, that the measurements of the team lead by B. Statzner could be conducted with such a discrepancy to the original FST placement technique. We have to allow the influence of other, not accounted for factors on the measurements, for example, a possible wrong calibration of the Ott current meter. Also, wear of the FST equipment (hemispheres and a plate) could be a reason for the increase in the friction coefficient.

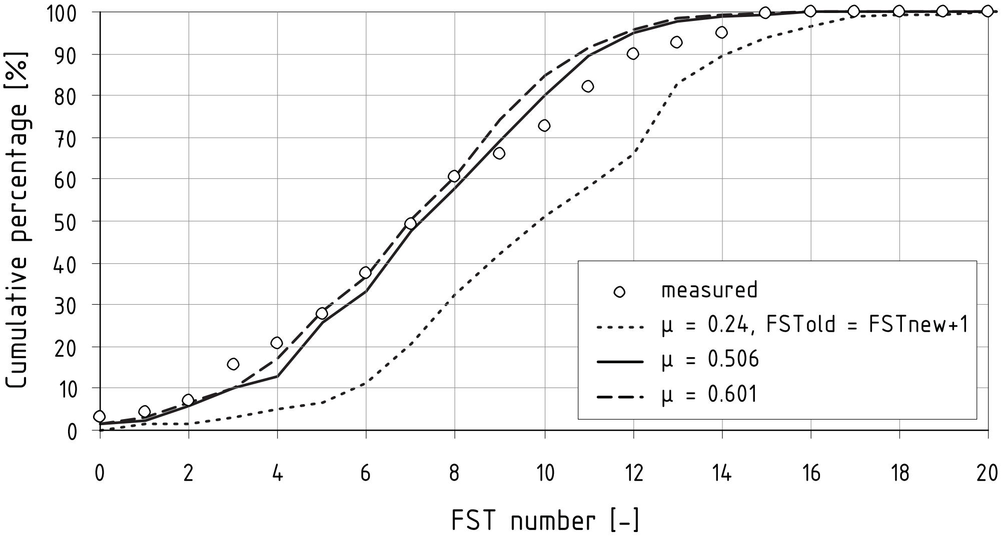

**Figure 6.14:** Cumulative curves of FST numbers for Rhône: measured and computed from log law near-bed velocities, mixed flow regime

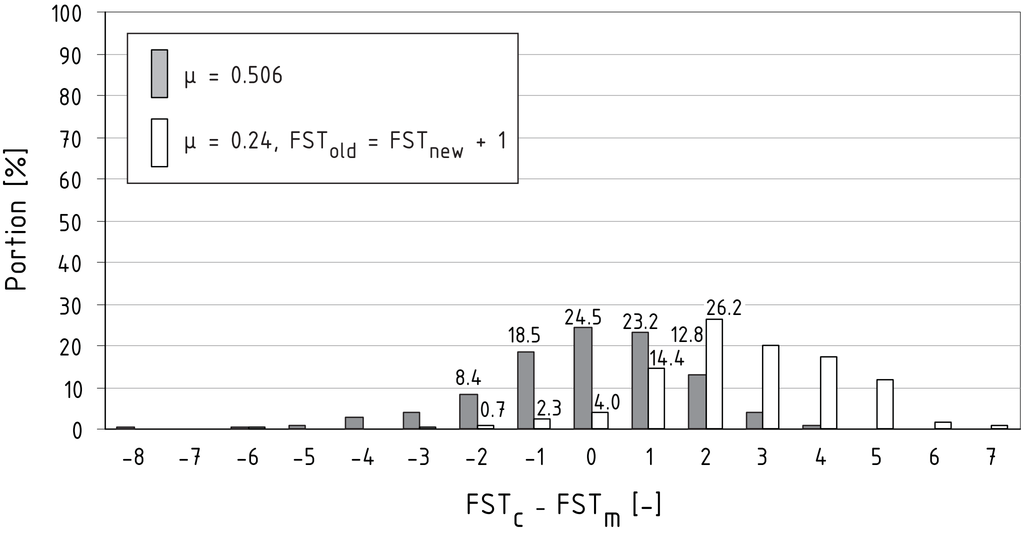

**Figure 6.15:** Comparison of differences in computed and measured FST numbers for $\mu = 0.506$ and 0.24, mixed flow regime

## 6.5 Field case Rheinau, Germany

### 6.5.1 Data description

Since the construction of the river power plant Rheinau in 1956, the discharge in the old Rhine meander around Rheinau does not surpass 5 $m^3/s$ more than half of a year. Because of this reduction in discharge, and additionally the impoundment caused by two weirs (see Figure 6.16), the living conditions for fish and benthos are heavily impacted. The weirs were constructed to maintain the impression of an intact river dimension to the casual observer. On the occasion of a technical turbine revision in summer 2001, a study was conducted on behalf of the Rheinaubund to assess the ecological situation within the Rheinau diversion reach and model the effects of discharge augmentation (15–160 $m^3/s$) and the reduction of the impounding levels on habitat availability for benthos and fish [77].

As described in Section 2.5.2, the standard FST-hemisphere survey program supposes, that at every flow situation 100 measurements randomly distributed over the river reach should be made. Due to large water depths in the diversion reach, such a measurement program could only be carried out by divers, thereby incurring immense survey costs. Thus, an alternative approach, based on the velocity vs. FST number correlation was applied.

In total, 67 FST measurements were conducted near the river banks where water depths allowed it. These were intended to cover a large as possible spectrum of FST numbers, getting at least some measurements for every number. The structured FST plate was placed over the substrate (position "very high", see Figure 6.1b) and the FST number was determined. The water depth was measured over the plate. Then, the near-bottom flow velocity $u_b$ at a distance of 2 cm above the plate and also the mean column velocity $u_{0.4}$ at approx. 40 % of the water depth from the bottom were measured with a micro-propeller MiniAir of the Schiltknecht Messtechnik AG. The polynomial trend lines for dependencies "$u_b$ vs. FST number" and "$u_{0.4}$ vs. FST number" showed very high coefficients of determination $R^2$ (0.92 and 0.95 respectively). Flow velocity distributions obtained with the two-dimensional hydraulic model were combined with the curve "$u_{0.4}$ vs. FST number" for obtaining the FST number distributions.

Substrate was noted visually in every measurement spot. The distinguished substrate classes with corresponding mean grain diameters are given in Table 6.3.

FST numbers are estimated using the methodology of Section 6.1 and obtaining near-bed velocities by application of the logarithmical velocity distribution law. The total water depth is recalculated by adding the thickness of the plate (2 cm) and a zero level displacement equal to $0.25y_r$ to the measured water depth. For every spot, $y_r$ is estimated by multiplying the mean grain diameter $d$ by a factor of 1.5.

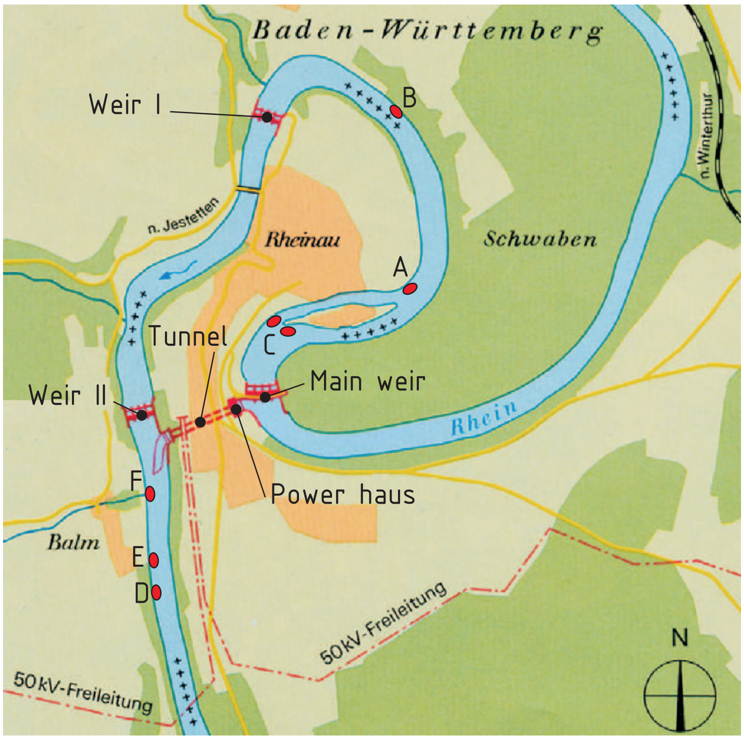

**Figure 6.16:** Diversion reach at the hydropower station Rheinau with FST measurement sites (A-F)

| Substrate class | d [mm] |
|---|---|
| Sand – fine gravel | 5 |
| Medium gravel | 40 |
| Coarse gravel | 60 |
| Coarse gravel – stones | 100 |

**Table 6.3:** Substrate classes and assumed mean grain diameters for Rheinau

### 6.5.2 Results

Comparing velocities at a distance of 2 cm above the plate (Figure 6.17), we can say, that up to a value of 0.6 m/s, the numbers computed through the log law are quite close to the measured ones, but are all in all slightly overestimated. Above 0.6 m/s, the overestimation is stronger, and for about 20 % of the total points, the difference to the measured values reaches 0.3–0.4 m/s. This can be explained partly by the fact, that it is easier to detect the main flow direction at a level of 40 % of the water depth than close to the river bottom when a using propeller meter. Computing the near-bed velocity through the mean column velocity, we get larger values than measured in field.

It can be seen from Figure 6.18, that computed FST numbers are close to the measured ones within the whole range of measurements with maximum absolute deviations of +2 and -3. This is the best correlation among all field cases, but we should not forget the relatively small number of measurements. In Figure 6.19, the cumulative curves of measured and computed FST-hemispheres are shown. The curves computed with sub-, supercritical and mixed regimes are very close to each other and also to the measured curve. The best approximation to the measured data is achieved by the subcritical regime calculation. The mean differences $\overline{\Delta}_{\mathrm{FST}}$ for sub-, supercritical and mixed regimes are -0.22, -0.58 and -0.34, respectively. Also in this field case, the highest percentage of computed FST numbers with zero deviation to the measured ones (50.7 %) is reached for both subcritical and mixed regimes (see Figure 6.20 for the latter). This distribution is slightly biased in the direction of negative values.

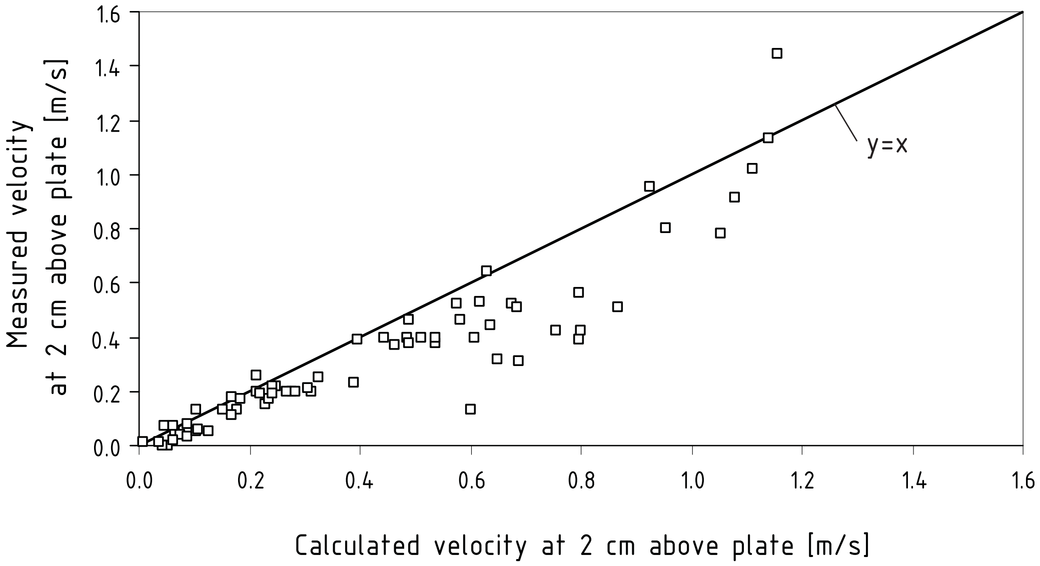

**Figure 6.17:** Calculated and measured velocities at a distance of 2 cm above the plate

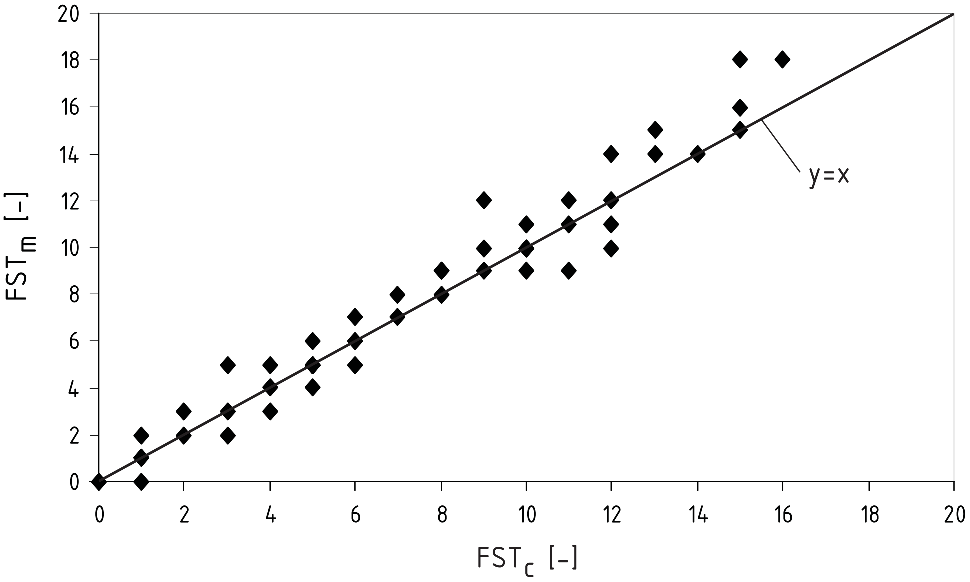

**Figure 6.18:** Calculated and measured FST numbers, mixed flow regime

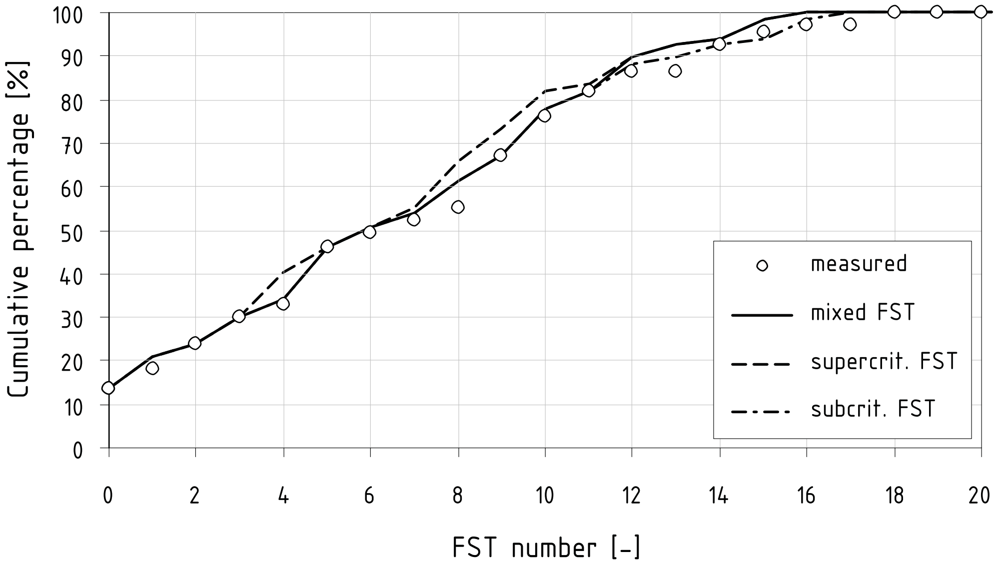

**Figure 6.19:** Cumulative curves of FST numbers for Rheinau, measured and computed in sub-, supercritical and mixed flow regimes

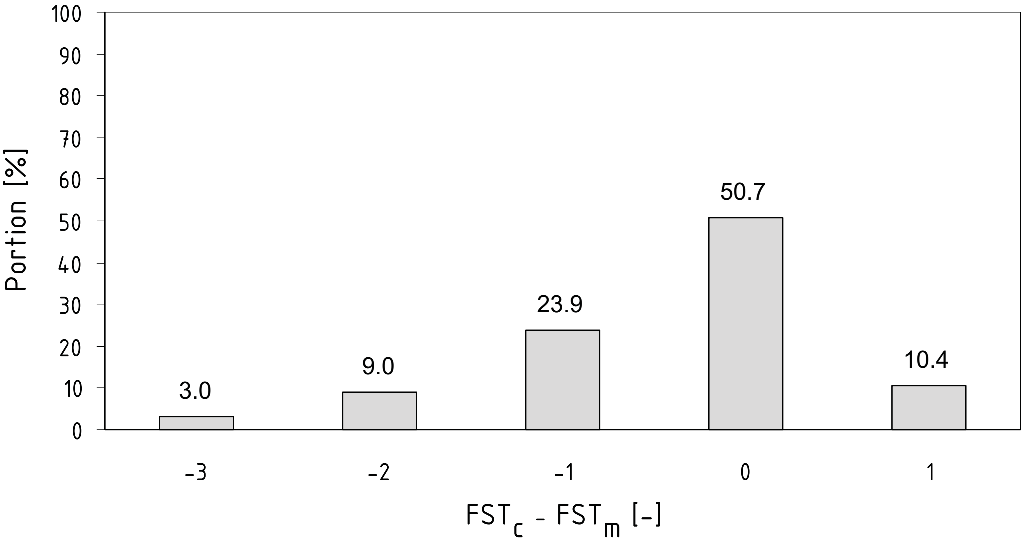

**Figure 6.20:** Comparison of differences in computed and measured FST numbers for Rheinau, mixed flow regime

## 6.6 Case study: River Zwalm, Belgium

### 6.6.1 Data description

This data is also provided by a contact within the COST action. Ans Mouton from Gent University works on habitat modelling for benthos species as well, and thus was interested in the application of the FST hemispheres on river Zwalm in Belgium. This data set is of particular interest, as all measurements are done with the instrumentary of the Institut für Wasserbau of Universität Stuttgart like in the case study at river Körsch.

River Zwalm flows in Flanders and is 22 km long. It has an irregular hydrological regime with an average water flow (at Nederzwalm) of about 1 $m^3/s$. The low flow minima is less than 0.3 $m^3/s$, and discharges in rainy periods are up to 4.7 $m^3/s$. Despite the investments in sewer systems and wastewater treatment plants since 1999, most parts of the river are still polluted by untreated urban wastewater discharges and by diffuse pollution originating from agricultural activities. The structural quality of the river is also heavily impacted. Numerous fish migration barriers are one of the most important ecological problems in the river basin. Although Flanders is in general rather flat, the Zwalm River basin is characterized by a number of differences in altitude, making it a quite unique river ecosystem within the Flemish Region. Some of the upper reaches of the watercourses in the Zwalm River basin are colonized by very rare species such as Bullhead (*Cottus gobio*), Brook Lamprey (*Lampetra planeri*) and several vulnerable macroinvertebrates [30].

**Figure 6.21:** River Zwalm at the FST measurement site, photo A. Mouton

The FST study reach also shows structural deficits, the banks are protected against erosion with stones or wood, the river channel is straightened (see Photo 6.21). The substrate is quite coarse. The measurement reach, 80 m long with a mean channel width of about 3 to 5 m, includes two distinct hydromorphological units: a 30 m fast-flowing, shallow riffle and a 30 m long slower-flowing and deeper glide. 14 transects were equally distributed within the riffle and glide units, with a 5 m interval between them. In every transect three sampling points were recorded.

In the measurements conducted in March 2005, the structured FST plate was placed on the substrate (position "very high" - see Figure 6.1b) and the FST number was recorded. After measuring the water depth, the plate was removed. At the same spot, velocity profiles were taken with a Höntsch micro-propeller and a Sontek 3D FlowTracker Handheld ADV [1]. The averaging period was set to 60 seconds, producing mean values of 600 and 60 repetitions, based on the measuring frequency of the ADV (10 Hz) and the propeller velocity meter (1 Hz), respectively. Velocity was measured at different depths with a larger density of samples near the bottom. Common distances from the bottom during velocity measurements were 3, 4, 6, 8, 10, 12, 16 cm and so on. Also, the water depth from the same reference level as velocity profile measurements (without a ground plate) was noted.

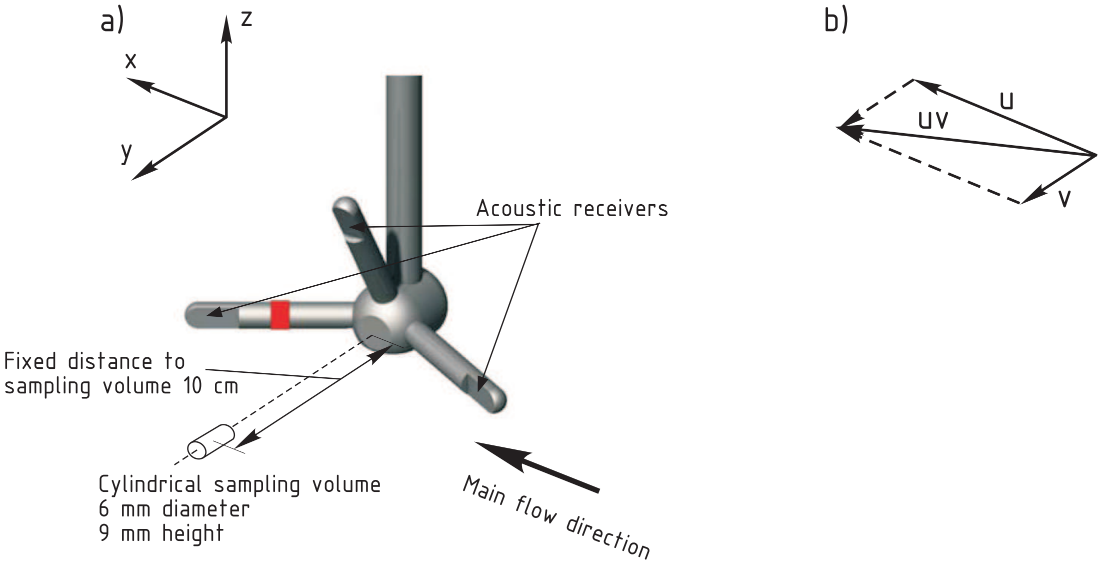

**Figure 6.22:** a) Sontek ADV: 2D/3D Side-Looking Probe with the sampling volume; b) definition of velocity components

As substrate characteristics were not recorded in this case and, therefore, the thickness of the roughness sublayer cannot be deduced, calculations of FST densities are performed upon measured near-bed velocities using Formula 6.5 with standard values of the hydrodynamic coefficients (see methodology in Section 6.1). For the calculation, the velocity profile values with a vertical position corresponding to the elevations of 4 and 1.5 cm above the FST plate are taken. From the ADV data, the scalar value of a vector resulting from the two horizontal components $u$ and $v$ is used (see Figure 6.22b). Here, the $u$-component is in longitudinal flow direction, the $v$-component in the transverse and $w$ in the vertical direction. While measuring with the micro-propeller in the field, it was attempted to find the direction with the highest velocity. Thus, its values should correspond to the $u - v$ vector.

## 6.6.2 Results

Measurements with FST-hemispheres in parallel to velocity profiles are quite lengthy, especially in the cold period of a year. Only 40 FST points could be surveyed within 3 days.

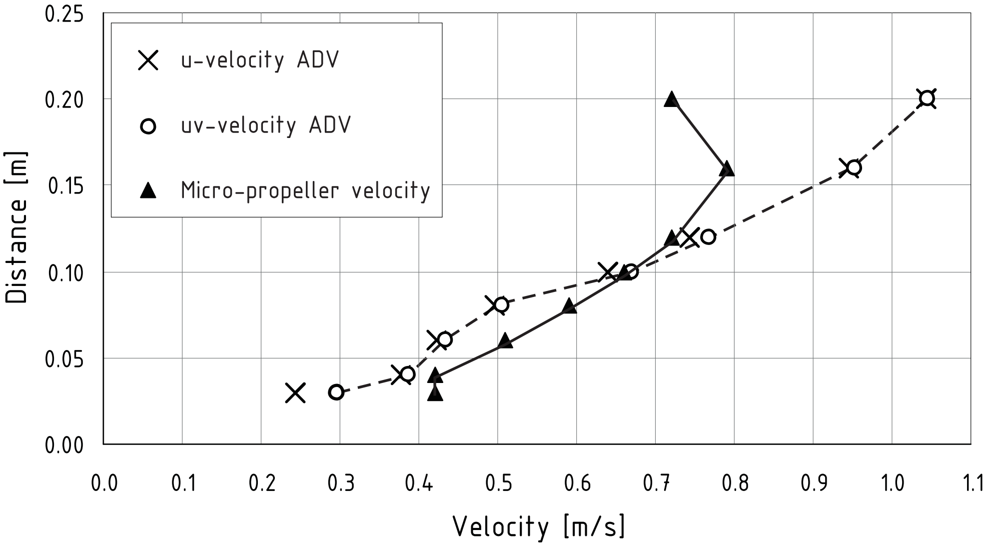

**Figure 6.23:** Typical velocity profiles measured at Zwalm with ADV and Höntsch micro-propeller

As very important appears to be the parallel measurements with two flow velocity measuring devices. A striking fact is: velocities taken with an ADV near the bottom (hereafter, $u - v$ vector values are used) are much lower than those taken with a micro-propeller. In Figure 6.23, an example of velocity profiles taken at Zwalm is shown. The profile measured with the Höntsch velocity meter looks quite typical compared to the classical one from text-books on hydrometry: an already considerable velocity value very close to the bottom, a gradual rise with the depth and reduction of the velocity near the water surface. On contrary, the ADV profile shows a different behavior: a slow increase in velocity from zero near the bottom and no reduction near the free surface. Almost all profiles look the same for the River Zwalm.

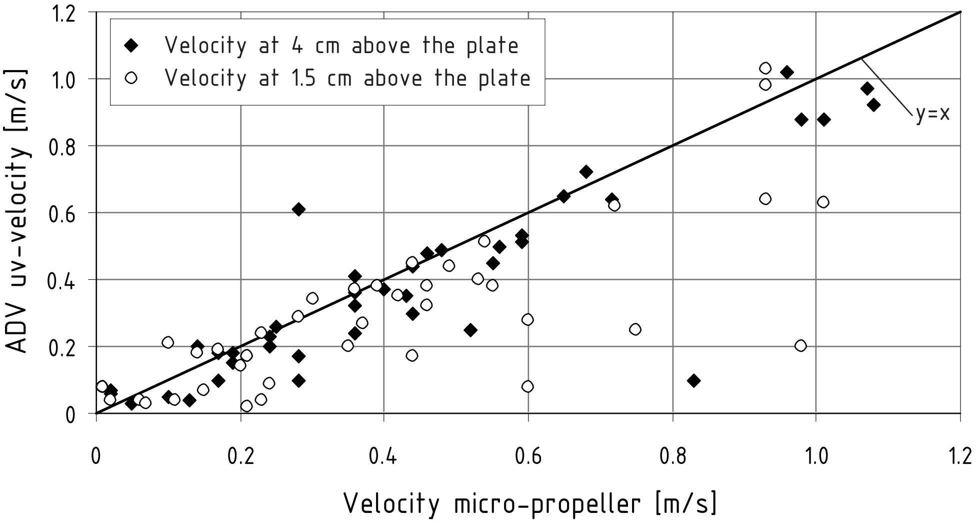

**Figure 6.24:** Velocities measured with the FlowTracker ADV and Höntsch micro-propeller at levels of 1.5 and 4 cm above the FST plate

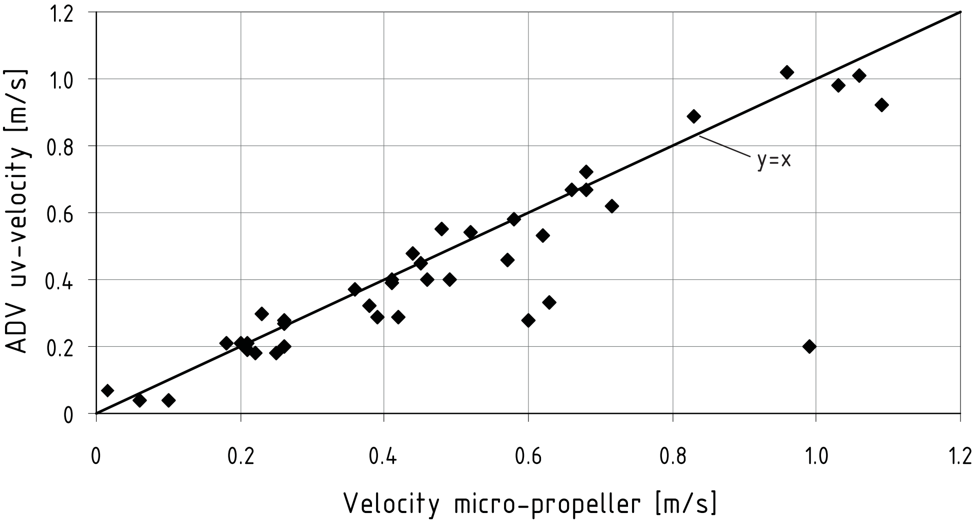

**Figure 6.25:** Mean column velocities measured with the FlowTracker ADV and the Höntsch micro-propeller

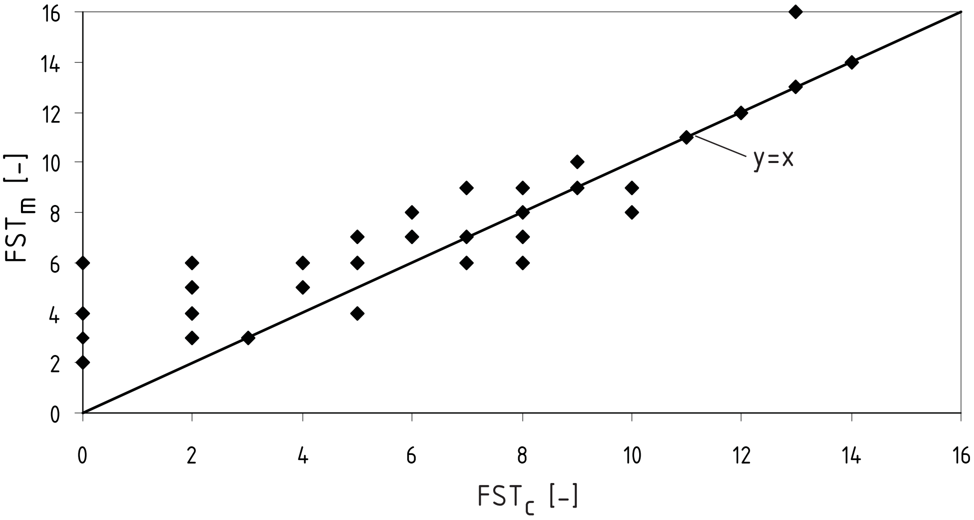

**Figure 6.26:** FST numbers calculated from near-bed velocities measured with the Höntsch micro-propeller, mixed flow regime

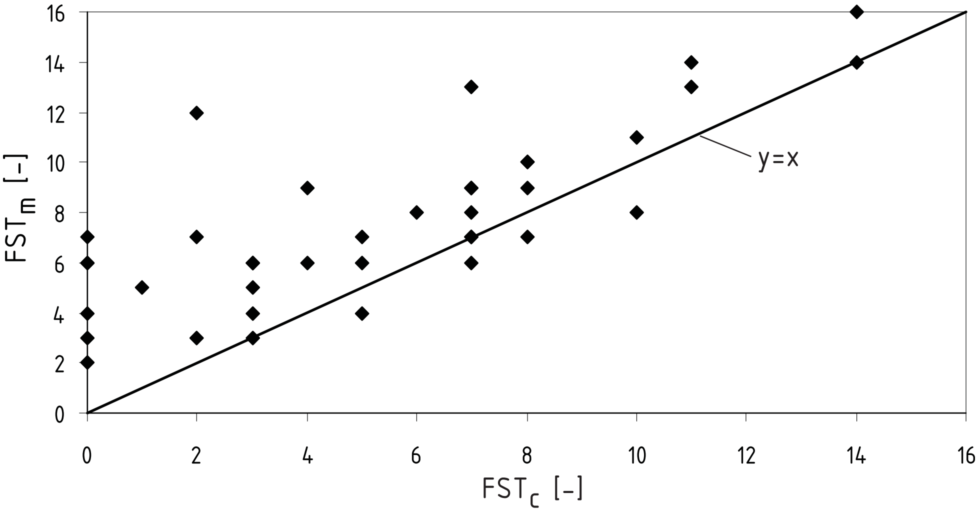

**Figure 6.27:** FST numbers calculated from near-bed velocities measured with the FlowTracker ADV, mixed flow regime

Own measurements, performed on two reaches of the river Körsch in Baden-Württemberg were also done with the Sontek FlowTracker ADV (see Section 6.7). A strong discrepancy between the measurements of the Höntsch and Sontek devices makes the results of velocity measurements for the Körsch suspect, and questions the comparison of measured and computed FST numbers. Trying to find a reason for the discrepancy, the user manual of the Sontek device was consulted [1]. Although FlowTracker is designed for field applications and is supplied with a special correction procedure to account for the presence of a solid boundary, the user manual states, that flow interferences can appear when working in very shallow water or near underwater obstacles situated within a distance of 15 cm from the tip of the probe. Acoustic reflections can potentially affect the measurements, resulting in a lower maximum velocity. ADV tries to correct for the presence of obstacles, and the degree of correction is documented in the data protocol. It was noticed in own measurements, though, that not in every case of suspicious low velocities a correction was documented.

Another reason for the reduced velocities in near-bed areas can be a wrong positioning of the ADV in a coarse substrate: as for the ADV's 2D/3D Side-Looking Probe the sampling volume is situated approximately 10 cm away from the tip of the probe (Figure 6.22a), and as the FST ground plate would normally be placed between the roughness elements, it is quite difficult to ensure, that the sample volume is situated exactly there where the FST number is measured. Usually, the device is put in the area where the ground plate was placed, so the sample volume is 10 cm to the right of the FST-hemisphere position, with a large chance of interference from neighboring stones in the sampling volume. On the other hand, as measurements with the Höntsch propeller-meter can be performed exactly at the place of a ground plate, there is no reason to distrust them.

For a demonstration of the discrepancies between the measurements of the two velocity meters, and to track possible consequences for the calculation of FST numbers, velocity comparisons at the levels of 4 and 1.5 cm above the FST plate are shown in Figure 6.24. It can be seen, that ADV velocities are considerably lower than those taken with a micro-propeller, especially accounting for, that a 2D ADV velocity is compared to a 1D propeller velocity. The same but less pronounced effect can be seen in Figure 6.25, where mean column velocities are compared.

The above mentioned means, that FST numbers calculated from ADV near-bed velocities are potentially lower than those from the Höntsch device. This can be seen in Figures 6.26 and 6.27, where FST numbers via Höntsch measurements match the measured values considerably better than those via ADV.

The large differences between computed FST numbers obtained from velocities measured with two different devices can be also seen in Figure 6.28. The percentage of calculated FST numbers with a zero difference to the measured ones is high (30.8 %) for velocities from

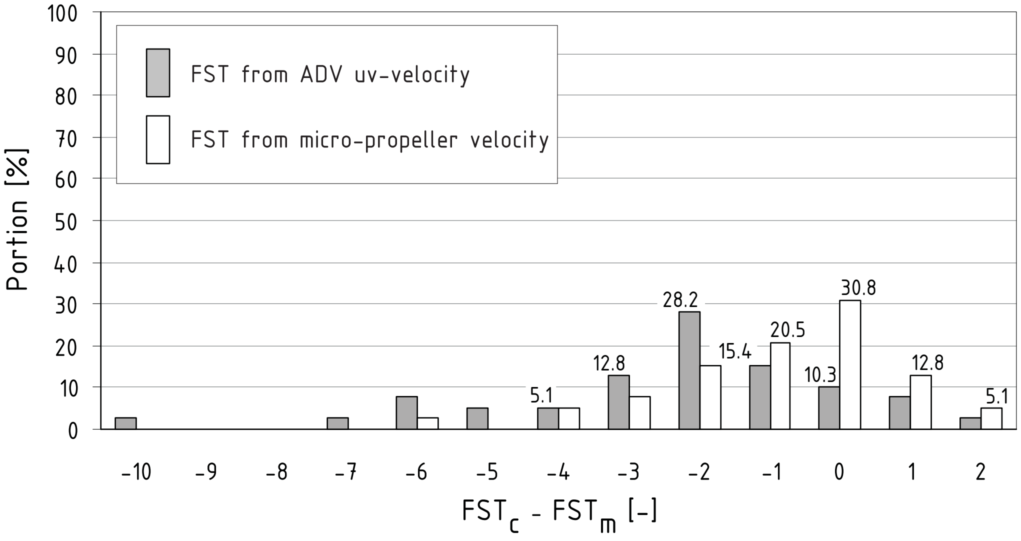

**Figure 6.28:** Comparison of differences in computed and measured FST numbers calculated from velocities obtained by the ADV and Höntsch micro-propeller, mixed flow regime

the Höntsch and comparable to the previous case studies. The part of correctly determined FST numbers from ADV velocities is only 10.3 % in contrast.

## 6.7 Case study: River Körsch, Germany

### 6.7.1 Data description

This data set was obtained by own measurements on the river Körsch in Baden-Württemberg, Germany. River Körsch is a left tributary of Neckar with a total length of 26.3 km. It joins Neckar near Esslingen, draining an area of 127 km$^2$. The mean yearly discharge of Körsch in the low river course is 1.8 m$^3$/s. Measurements were conducted in February and June of 2005 at two selected river reaches:

**Reach I** is situated between the towns Denkendorf and Deizisau, approximately 1 kilometer upstream from the point where Körsch joins Neckar. The river course is straightened there with a mean channel width of about 6 m (see Photo 6.29). The banks are protected against erosion with large stones and the bottom substrate is also quite coarse, not natural, but more or less homogeneous, with a mean diameter of 8–13 cm. In total 35 FST-hemisphere and vertical velocity profile samples were taken in this reach in February 2005. The survey program was interrupted by a flood event, which, although not extreme in terms of discharge, did increase the turbidity considerably, so the FST-hemisphere equipment was not visible in the water anymore.

Measurements were conducted as follows. The FST ground plate was placed on the bottom (position "very high", see methodology in Section 6.1) and the FST number was registered. Water depth was measured from a plate to water surface. The size of the dominating substrate fraction was estimated visually and special point features (such as presence of large stones around the point, wavy water surface and so on) were noted. Then, the velocity profile (with approx. 10 points) was measured with the Sontek FlowTracker ADV [1]. The first point in the profile was usually 3 cm above the plate, measurements were more densely spaced near the bottom. FST measurements were performed in transects, with 5 measurement points within.

**Reach II** is situated approximately 6 km upstream of Reach I, to the south of the town Nellingen. It shows a little more natural flow course and the width of the channel is more variable, ranging from 3 to 6 m, but substrate is still unnaturally coarse due to erosion protection measures (see Photo 6.30) and also highly inhomogeneous. In the upstream part of the reach, large rock blocks (up to 1 m in diameter) are placed in the river.

The strategy of survey had been changed, as it was noticed from the measurements at Reach I, that the points close to the plate (at 3, 4 cm above) had a systematically conspicuous low velocity, and at first it was believed, that the ground plate contributes some disturbance. Thus, after the FST-hemisphere number (again with the plate in position "very high") was noted, the plate was removed and the velocity profile was measured with the ADV placed directly over the substrate. Four water depths were recorded: depth over the plate, depth corresponding to the ADV velocity profile, and minimum and maximum depths around the measurement spot, aiming at the estimation of substrate roughness. Also, like for Reach I, the size of the dominating substrate fraction was estimated visually. FST measurements were performed again in transects, with 4 to 5 measurement points within every transect.

For FST-hemisphere number calculations, the methodology outlined in Section 6.1 is used. The specific construction of the ADV support restricts the first measurement point to be at a distance of at least 3 cm above the ground. Thus, for Reach I, the velocity at 1.5 cm above the ground plate is assumed to be 0.9 of the velocity at a level of 4 cm. Two types of calculations – via measured near-bed velocities and via application of the log law – are evolved. The thickness of the roughness sublayer is taken as a visually estimated mean grain diameter multiplied by a factor of 1.5.

**Figure 6.29:** Study Reach I, river Körsch

**Figure 6.30:** Study Reach II, river Körsch

## 6.7.2 Results

### 6.7.2.1 Reach I

Looking at the calculation of FST-hemisphere numbers using the measured near-bed velocities, it can be seen from Figure 6.31, that the computed numbers show a very poor correspondence to the measured ones. In total, for 20 of 35 points the computed value is generally underestimated. For 11 points of the 35, special conditions such as the presence of large stones around the spot or situation of the spot in a local depression of the river bed were noted. In 9 cases from these 11, the FST-hemisphere number is underestimated. The mean difference between calculated and measured FSTs $\overline{\Delta}_{\mathrm{FST}}$ for Reach I is -1.36 (mixed flow regime). It is believed, that these discrepancies have the same origin as those in River Zwalm – the ADV measured too low velocities near the bottom. If only the points without special conditions are considered, the mean difference between calculated and measured values $\overline{\Delta}_{\mathrm{FST}}$ increases to the value of -0.4.

FST-hemisphere numbers calculated using the log law correspond better to the measured ones (see Figure 6.32). This can be explained that way, that the ADV velocity meter measures more realistic velocities at some distance from the bottom. The mean difference between computed and measured FST-hemisphere numbers in this case is -0.57 and it can be seen, that some points with “special” conditions could recover from the wrong velocity measurements by the ADV.

Considering the deviations from the measured FSTs in Figure 6.33 for both types of calculation for Reach I, we can say, that the log law performs a little better as the distribution is more symmetrical around the point of zero difference. The percentage of points with zero deviation, however, is low for both calculations (25.7 %).

### 6.7.2.2 Reach II

It is not surprising, that for Reach II a poor correlation between computed and measured FST-hemisphere numbers is found also. The mean differences $\overline{\Delta}_{\mathrm{FST}}$ in a mixed regime are -1.88 and -1.23 for calculations via measured and log law estimated near-bed velocities, respectively. The correlation is even worse than that for Reach I, probably due to the fact, that the FST plate was removed before the ADV measurements, therefore, increasing this way the chance of loosing the exact measurement point. Also, the substrate in Reach II was sometimes much coarser than at Reach I. For very poor correlation speaks Figure 6.34, where can be seen, that the percentage of points with a zero difference to the measured values is less than those with a difference of -1.

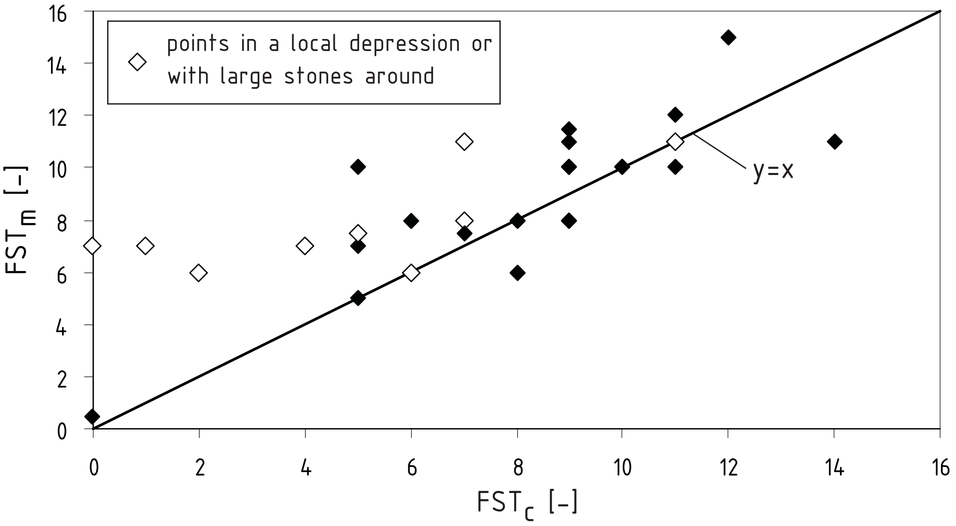

**Figure 6.31:** FST numbers calculated from near-bed velocities measured by the ADV in Körsch, Reach I, mixed flow regime

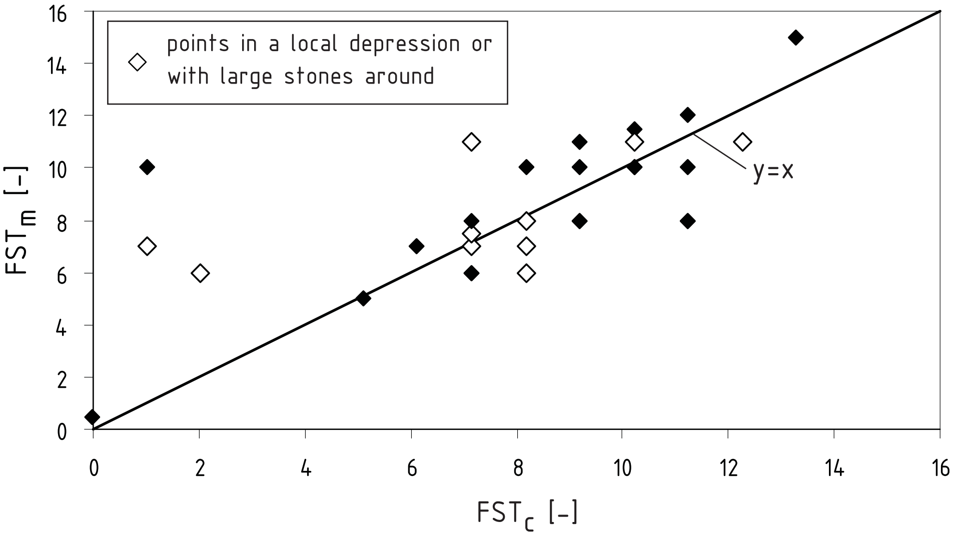

**Figure 6.32:** FST numbers calculated via application of log law in Körsch, Reach I, mixed flow regime

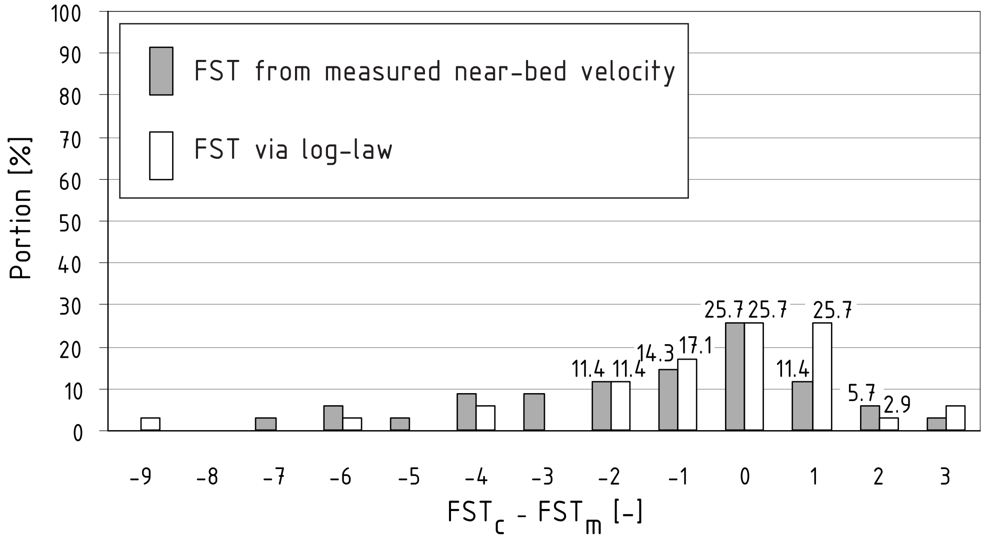

**Figure 6.33:** Comparison of differences in computed and measured FST numbers calculated from velocities obtained by the ADV and log law in Körsch, Reach I, mixed flow regime

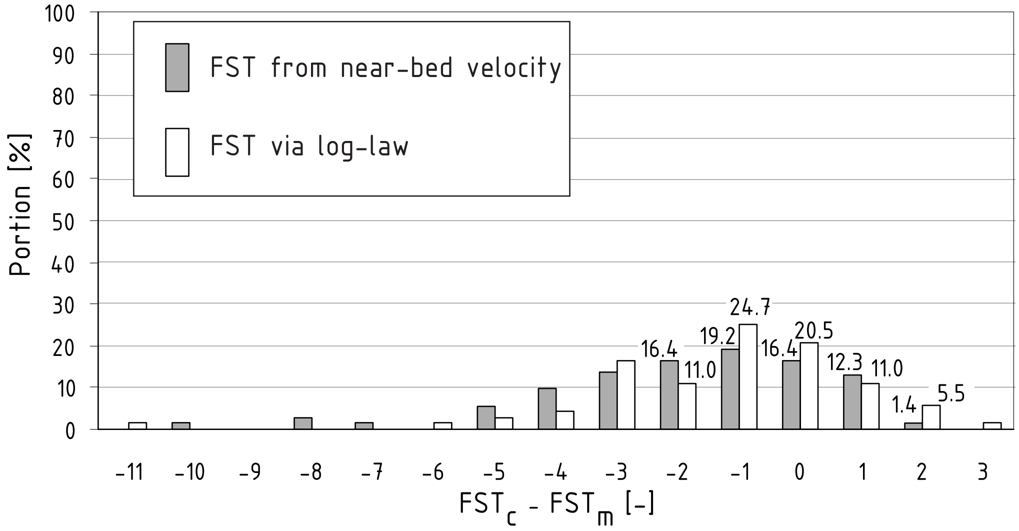

**Figure 6.34:** Comparison of differences in computed and measured FST numbers calculated from velocities obtained by the ADV and log law in Körsch, Reach II, mixed flow regime

## 6.8 Summary

Application of the force balance based formula for the estimation of FST-hemisphere density shows controversial results in the case studies. In some studies FST-hemisphere numbers estimated from measured near-bed velocities match quite well those FST numbers measured in the field. In others, there is a big scatter between computed and measured FST numbers. In general, FST numbers calculated upon near-bed velocities determined via application of Bezzola's logarithmical velocity distribution are more close to the measured ones than the FST-numbers calculated through measured near-bed velocities. This fact can be related to the different measurement volumes of FST-hemispheres and velocity-meters as pointed out in Section 4.3.1. In most studies, the average amount of correctly determined FST numbers in a sample is about 25–30 %, and 80–90 % of values deviate no more than ±2 FST numbers from the measured ones.

The newly developed methodology performs well for the laboratory study of Scherer. FST-hemisphere numbers estimated through the application of the log law are in good agreement to the measured ones. This proves to be true for the different vertical positions of the FST ground plate, as well as for the substrates consisting of grains with various mean diameters and with different arrangements of roughness elements.

The least satisfactory results are obtained for the river Rhône, where FST measurements were performed with a smooth plexiglass plate. Application of the new method together with the transferability Formula 4.1 recommended in [20] and resulting in a difference of 1 FST number between measurements with an old and a new structured plate, leads to a mean overestimation of the computed values by 2 to 3 FST numbers. A better correspondence to the measured values is obtained using a higher friction coefficient. A possible explanation is, that the measurements were not performed according to the standard placement procedure of Statzner, but more likely by pressing the FST hemispheres to the ground plate.

Field studies of the German Rheinau and Austrian Schwechat rivers completely support the new method for the calculation of FST-hemisphere numbers. Here, with the help of the log law, it is possible to estimate with good accuracy the near bottom velocities and further to calculate FST numbers. The results for Rheinau are the best among all studies, with 50 % of correctly determined FST numbers and 97 % values with a maximum deviation of ± 2 numbers from the measured ones. The Austrian case shows a little poorer performance, but at the same time, the data set is larger (300 vs. 67 FST measurement points for Rheinau) and, also, the substrate is assumed to be of the same size for the whole reach.

The river Zwalm study is very interesting as it shows, through a large discrepancy between the ADV and micro-propeller measurements, that quite a large uncertainty exists in velocity measurements. The ADV possibly registers too low near-bed velocities, what has a pronounced effect on the calculation of FST numbers, resulting in a strong underestimation of calculated values. It is likely, that acoustic reflections from roughness elements result in low flow velocities. And, as usually water depths are not large during FST measurements, this effect is present even in the mean column velocity, suggesting that FST numbers calculated by the application of the log law are also slightly underestimated. This also allows to judge the results obtained for the river Körsch. In this light, they are not that bad as they look at first glance, as for the velocity measurements also the ADV was used. This deficiency of ADV measurements hindered the initially planned detailed investigation of Bezzola's log law applicability for natural flows over rough beds with small relative submergences.

# 7 Computational approach to FST-hemispheres in benthos habitat modelling

It is shown in Chapter 5, that FST-hemisphere density can be estimated using Formula 5.14, knowing the friction coefficient between a plate and a hemisphere and the local near bed velocities. Case studies in Chapter 6 prove, that this approach gives satisfactory results, no matter whether the near bottom velocities are measured in the field or estimated using Bezzola's modified logarithmical velocity distribution formula described in Section 3.6. For application of the log law, only three parameters are needed: mean column velocity $u_{0.4}$, water depth $h_t$ and thickness of the roughness sublayer $y_r$. Although distributions of these parameters for a particular river reach can be acquired in field at flow rates/situations of interest, a real saving of time and work in habitat modelling can be achieved through the application of a hydrodynamic model to obtain distributions of $u_{0.4}$ and $h_t$.

In this chapter, a computational approach to FST-hemisphere number distributions using a two-dimensional hydrodynamic model is described. Further, the application of this new approach for habitat modelling is shown.

## 7.1 Calculation of FST distributions

### 7.1.1 Outline of the approach

The proposed approach for calculating FST-hemisphere number distributions consists of the following steps:

**Field survey** serves as a basis for the hydrodynamic modelling of a river reach. The geometry of the river reach, texture of the bottom and data for calibration and validation of a numerical model are obtained in this step. Data on the river bottom texture – substrate composition – is also used later for the calculation of FST distributions.

**Hydrodynamic modelling** is performed to obtain mean column velocities and water depths at a number of flow situations relevant for the habitat availability assessment.

**Computing the FST number distributions** is done upon the results of numerical modelling. Using mean column velocities and water depths, combined with the substrate characteristics, near-bed velocities are computed. Then, the corresponding FST density/number is calculated for every cell of a numerical model. The last step is obtaining the integral distribution of FST-hemisphere numbers expressed as the percentages of the wetted areas with a specific FST number. This procedure is repeated for every flow situation.

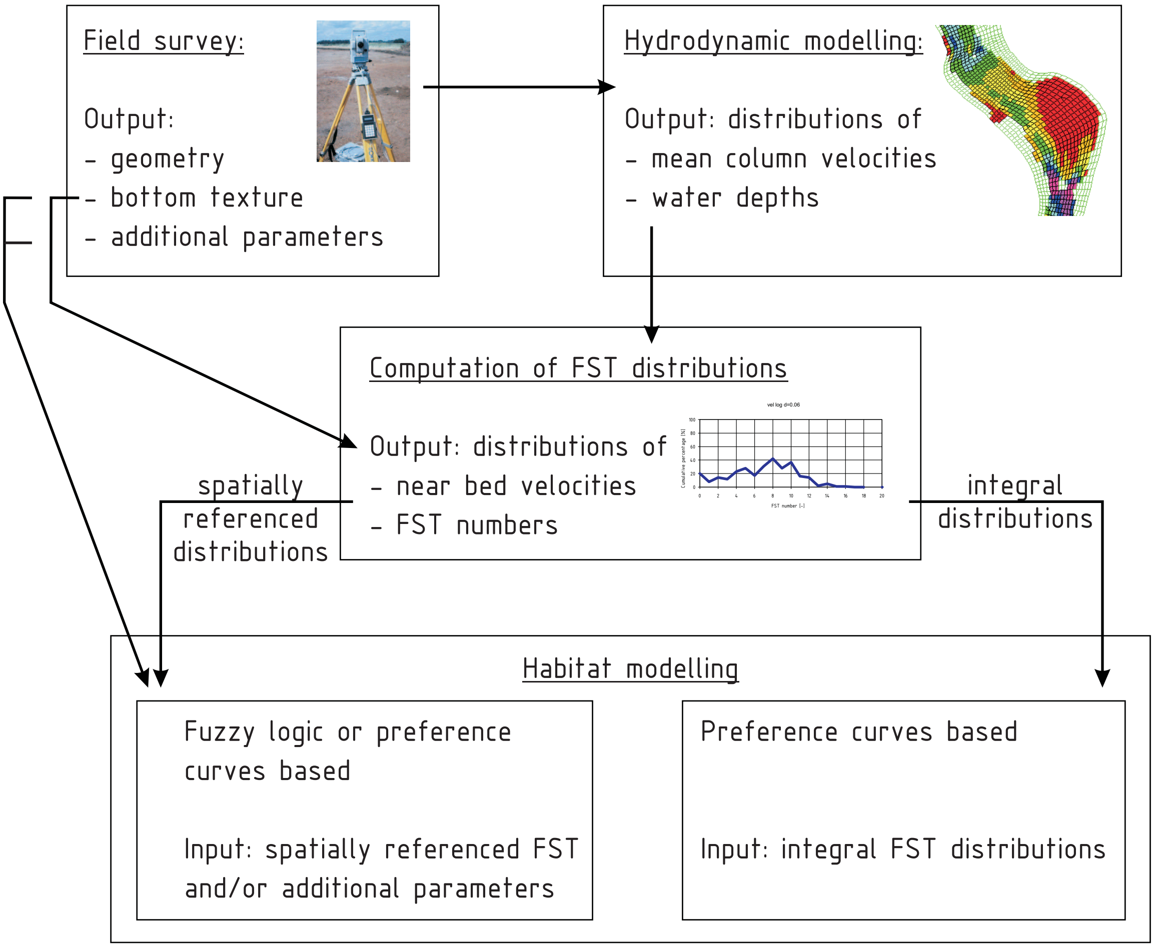

**Figure 7.1:** Data processing steps in benthos habitat modelling using the proposed computational approach to FST-hemisphere numbers

The outlined procedure replaces the laborious FST-hemisphere measurements in the field described in 2.5.2. Integral FST distributions obtained this way can be processed later, as is implemented in the BHABIM module of the simulation model CASiMiR (see Section 7.2.1). Moreover, the first two steps in this approach are basically the same as those presently used in CASiMiR in modelling for fish habitat assessment. Thus, in future, fish and benthos modelling can be performed on the same base data. Like it is shown in Figure 7.1, the new approach allows also alternative habitat modelling for benthic species based on spatially referenced FST distributions. Linking up additional parameters, such as substrate (as living space or food source), water depth (in terms of light availability) or others, which can be mapped or modelled for the reach, appears to be straightforward. This multivariate modelling can be performed using either conventional preference curves or a fuzzy logic approach (see Section 7.2.2). Integration of other parameters was hindered until now, as coverage of the whole study reach with FST-measurement points (even if the positions of the spots are geo-referenced) has been simply not feasible.

In the next sections, three steps for obtaining FST distributions are described in detail. Also, an application example using a two-dimensional hydrodynamic model for the river Körsch is given (see Section 7.1.2). Field survey and hydraulic modelling recommendations are based mainly on experience with the habitat simulation strategy using the CASiMiR model [73], [74].

#### 7.1.1.1 Field survey

The main two types of data constituting to the morphology of a river reach are surveyed in this step:

- digital elevation data, and
- bottom texture data.

The strategy how digital elevation data of a river bottom can be acquired depends on the channel form, and, consequentially, on the requirements of the hydrodynamic model used for flow simulations. If a river channel is of simple form and flow can be modelled by means of a one-dimensional hydrodynamic model, the geometry is usually surveyed on a profile basis. The original CASiMiR hydraulic model, for example, a so called 1.5-dimensional model [74], requires a profile-oriented input of points with specified $x$, $y$ and $z$ coordinates. For complex river reaches requiring the application of a two-dimensional flow model, profile points have to be enriched with additional ones reflecting geometry specialities to insure a high quality mesh for modelling. The density of survey points should satisfy the accuracy which is required for habitat modelling.

The tachymeter is a common equipment for geometry survey in small rivers and creeks, especially with heavily vegetated banks. Together with a communication device, used for work coordination and transmitting substrate data and other habitat specific parameters from the person carrying the reflector to the person operating the tachymeter, it allows fast and high precision acquisition. As an alternative, a Differential GPS (DGPS) can be used, which allows to reach a surveying accuracy in the range of 1 cm in horizontal and 2 cm in vertical directions at best. This is a very promising, but nowadays very expensive, approach. In larger and deeper rivers, it is feasible to use a combination of an echo-sounder and a DGPS or an automated tachymeter. The echo sounder can provide additional information on structure and consistency of the river bed material [74].

Attention should be given to how the vertical position of geometry points (z-coordinate) is defined. With rough substrates and at low flow rates, it can play an important role whether the reflector is systematically over or between the stones. This fact should be taken into account during mesh generation for flow simulations, and also for computing FST numbers.

As is shown in the case studies of Chapter 6, a visual estimation of the substrate class and/or the mean grain diameter at the geometry points is generally sufficient for further use in the FST computational approach for the calculation of near-bed velocities. From this information, also the roughness parameter (commonly Manning coefficient) for the hydraulic model can be deduced.

For calibration of the hydrodynamic model, water surface elevations at particular flow rates are needed. These have to be measured preferably at three discharges which have to cover the whole range in the spectrum of studied flow situations. If no river gauge is situated close to the study reach, parallel discharge measurements should be done, either with conventional flow meters or salt tracer equipment for small rivers. Some mean column velocity measurements (at 40 % of the water depth) are very helpful for the calibration of the numerical model. Selecting the river reach for investigation, the researcher should always have in mind, which boundary conditions will be applied further in modelling. It is recommended, that the inflow and outflow boundaries for the numerical model are always situated at some distance outside from the borders of the reach for which habitat modelling will be performed.

A few FST-hemisphere measurements with recorded positions can serve for validation of the FST distributions obtained by the computational approach.

#### 7.1.1.2 Hydrodynamic modelling

In recent times, it became routine to apply two-dimensional hydrodynamic models in habitat studies, also in CASiMiR. This is not only due to an extended range of applications (from short rest-water stretches at small rivers to large reaches at Rhine, Aare), but also due to the continuously growing robustness and user friendliness of such models and, last but not least, computer capacities. A number of simulation packages for the calculation of water depths and mean column velocities have been applied in CASiMiR studies, including such models as FESWMS, Mike21 and HydroAS-2D.

In general, the two-dimensional hydraulic modelling of a river reach comprises following steps:

- mesh generation, definition of boundary conditions and bottom roughness coefficients;
- calibration of the model;
- validation of the model;
- calculation of flow situations and analysis of results.

If the river channel has a simple form, the original CASiMiR 1.5 hydraulics approach can be used [74].

Application of 1.5- and 2-dimensional models for small rivers and creeks is sometimes at the fringe of their capabilities. Dimensions of the channels (relation of water depth to width) and large roughness elements do not allow a strict application of these models, as the assumption of the two-dimensionality of the flow is not valid. In alpine streams characterized by steep slopes, coarse substrates and specific bottom forms (see Section 3.1.1), application of these models is very questionable, also. Only direct near-bed flow velocity measurements can help to resolve this problem.

#### 7.1.1.3 Calculation of FST distributions

For the calculation of FST number distributions, a small application implemented as an extension to ArcView GIS 3.3 was written by the author. It allows:

- Import of the hydrodynamic simulation results obtained with the two-dimensional hydraulic model (presently HydroAS-2D) into ArcView GIS in form of a shape file;
- calculation of FST numbers for every cell of the numerical model;
- calculation of integral distributions of FST-hemisphere numbers.

Extension functions can be launched out of the menu “FST” from the View window in ArcView. Prior to this, the add-on has to be activated in the menu “Extensions”.

The import function reads the output files of HydroAS-2D (mesh file “Hydro_as-2d.2dm”, result files “depth.dat” and “veloc.dat”) and converts the data into the ArcView shape format.

A computational cell in HydroAS-2D is built from three (triangular cell) or four (quadrilateral cell) nodes (see Figure 7.2). For every node, among the $x$, $y$, and $z$ coordinates, two components of the mean column velocity and the water depth are known after calculation.

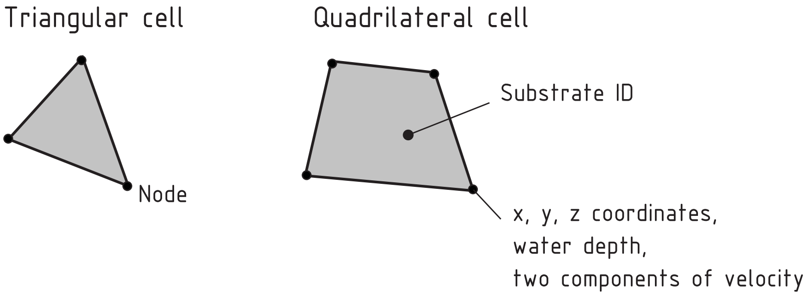

**Figure 7.2:** Cell types and definition of computational variables used for the HydroAs-2D hydrodynamic model

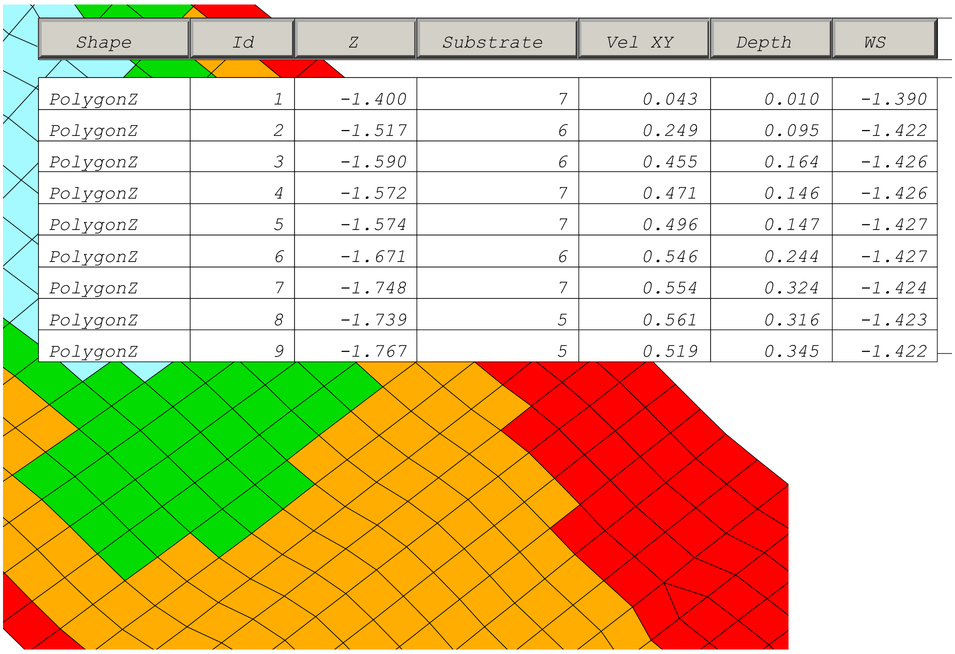

| Shape | Id | Z | Substrate | Vel XY | Depth | WS |
|---|---|---|---|---|---|---|
| PolygonZ | 1 | -1.400 | 7 | 0.043 | 0.010 | -1.390 |
| PolygonZ | 2 | -1.517 | 6 | 0.249 | 0.095 | -1.422 |
| PolygonZ | 3 | -1.590 | 6 | 0.455 | 0.164 | -1.426 |
| PolygonZ | 4 | -1.572 | 7 | 0.471 | 0.146 | -1.426 |
| PolygonZ | 5 | -1.574 | 7 | 0.496 | 0.147 | -1.427 |
| PolygonZ | 6 | -1.671 | 6 | 0.546 | 0.244 | -1.427 |
| PolygonZ | 7 | -1.748 | 7 | 0.554 | 0.324 | -1.424 |
| PolygonZ | 8 | -1.739 | 5 | 0.561 | 0.316 | -1.423 |
| PolygonZ | 9 | -1.767 | 5 | 0.519 | 0.345 | -1.422 |

**Figure 7.3:** An example of the polygon shape and the attribute table with cells from the HydroAS-2D model

The substrate ID is defined for the cell area. As a substrate parameter (in form of the thickness of the roughness sublayer) is needed for the calculation, FST numbers are estimated not for a node but at a cell basis. The import function of the extension creates a polygon shape file, in which every cell is represented by a separate polygon. Then the new file can be loaded into the ArcView project. This shape file (*.shp) is accompanied by an attribute table (*.dbf), in which the water depth, flow velocity vector, and substrate ID is saved for every cell (see Figure 7.3). To obtain the representative velocity and depth for the cell, these parameters are averaged from the node values.

After import of the HydroAS-2D model into ArcView, the next function can be run for the calculation of FST numbers upon the detailed hydrodynamic data. Using the input form, which appears after starting the function, the user has to:

- Select the name of the attribute table for the calculation from a list of tables in the project;
- specify the columns of the attribute table where mean column velocity, depth, and substrate ID are stored;
- specify the transformation table where is defined, which substrate ID corresponds to which mean grain diameter;
- define the parameters of calculation, in particular: factor for the thickness of the roughness sublayer (1.5 by default), friction coefficient between plate and FST-hemisphere, hydrodynamic coefficients (for sub-, supercritical or mixed regimes) and the vertical position of a plate (high or very high).

In the present version of the application, it is assumed that the water depth is measured from the mean elevation of the roughness elements tops. Thus, a length of zero level displacement equal to $0.25y_r$ is added to $h$ to obtain the total depth $h_t$ during calculation. FST numbers are calculated only for cells with a water depth larger than 12 cm (instead of the theoretically required 16 cm), as it was noticed in the case studies, that up to this value the correlation is not noticeably affected. In general, the calculation follows exactly the methodology described in Section 6.1. The result – FST-hemisphere number for every cell-polygon – is written into a new field in the attribute table.

The last function of the extension summarizes the results of the previous calculation. It iterates through cell-polygons and sums up the areas with a particular FST number. As the total wetted area or, more precisely, the area with depths over the roughness tops larger than 12 cm, is also computed here, the proportionate contribution of every FST number $\delta_{FST_i}$ can be calculated through:

$$\delta_{FST_i} = \frac{\sum_{n=1}^{N} A_{FST_i}}{A_{tot}} \cdot 100 \qquad [\%] \qquad (7.1)$$

with $\delta_{FST_i}$ = contribution of i-th FST number in the sample, [%]
$A_{FST_i}$ = area of the cell with $FST = i$, [$m^2$]
$N$ = number of cells with $FST = i$, [-]
$A_{tot}$ = total wetted area of a river reach with water depth $> 12$ cm, [$m^2$]

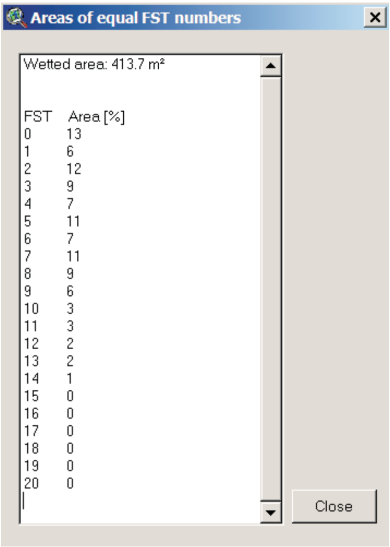

```
Wetted area: 413.7 m²


FST   Area [%]
0     13
1     6
2     12
3     9
4     7
5     11
6     7
7     11
8     9
9     6
10    3
11    3
12    2
13    2
14    1
15    0
16    0
17    0
18    0
19    0
20    0
```

**Figure 7.4:** Report for an integral FST-hemisphere numbers distribution

The function generates a report like it is shown in Figure 7.4. The left column contains the FST number, the right – the percentage of the river reach area which has this FST number. The function processes only one flow situation at a time, but an improvement to support multiple is planned. This data can be copied and pasted into an Excel spreadsheet to create an input file for the BHABIM module and, subsequently, for habitat modelling (see Section 7.2.1).

Alternatively, Suitability Indexes (SI) for particular benthic species can be calculated within ArcView GIS using the fuzzy logic based extension "FuzzySI" (see Section 7.2.2).

### 7.1.2 Example of FST-hemispheres distribution calculation

This example is based on data from the river Körsch, study Reach II (see Section 6.7).

#### 7.1.2.1 Field survey

A tachymeter was used for the geometry survey of the study reach with a total length of 95 m and a mean width of 6 m. A local coordinate system was assumed. Geometry points were taken in transects, spaced with a distance of 2.5 to 3.5 m. In every transect, the points where the water surface crossed the bank line were measured, giving the water surface width for validation of the hydrodynamic model. The downstream profile was selected at the step in the longitudinal profile to insure an uncomplicated outflow boundary condition. During geometry survey, the reflector's end point was put consistently at the estimated mean level of the roughness tops. In total, 73 FST points and parallel velocity profiles distributed within 15 transects with normally 5 points per transect were taken.

In Figure 7.5, a study reach map with marked positions for geometry, water surface, and FST measurement points is shown. The FST profile names are also given there.

During survey, the ID of the representative substrate class was registered for every point. The substrate classes with the corresponding assumed mean grain diameters d and values of the Manning coefficient are given in Table 7.1.

| ID<br>- | Substrate class | d<br>m | Manning n<br>- |
|---|---|---|---|
| 1 | silt | 0.001 | 0.020 |
| 2 | sand | 0.002 | 0.022 |
| 3 | fine gravel (1–2 cm) | 0.015 | 0.024 |
| 4 | medium gravel (2–5 cm) | 0.035 | 0.030 |
| 5 | coarse gravel (2–10 cm) | 0.060 | 0.035 |
| 6 | stones (10–20 cm) | 0.150 | 0.045 |
| 7 | stones (20–30 cm) | 0.250 | 0.055 |

**Table 7.1:** Substrate classes, assumed mean grain diameters and Manning coefficients for Körsch, Reach II

During field measurements, the Körsch had an almost constant flow rate, checked with a temporary water level gauge installed in cross-section P2. The discharge was measured in the cross-section with a regular form (situated 100 m downstream of the the study reach) two times and was 438 and 504 l/s, respectively. The mean of the two values (470 l/s) is taken as an input for the modelling.

#### 7.1.2.2 Hydrodynamic modelling

HydroAS-2D [59] is used for the flow simulation. The mesh is generated with the SMS software package and consists of 3868 triangular and quadrilateral cells with a linear size of about 0.4 m, built from 4074 nodes. For the mesh generation, at first, the border of the model

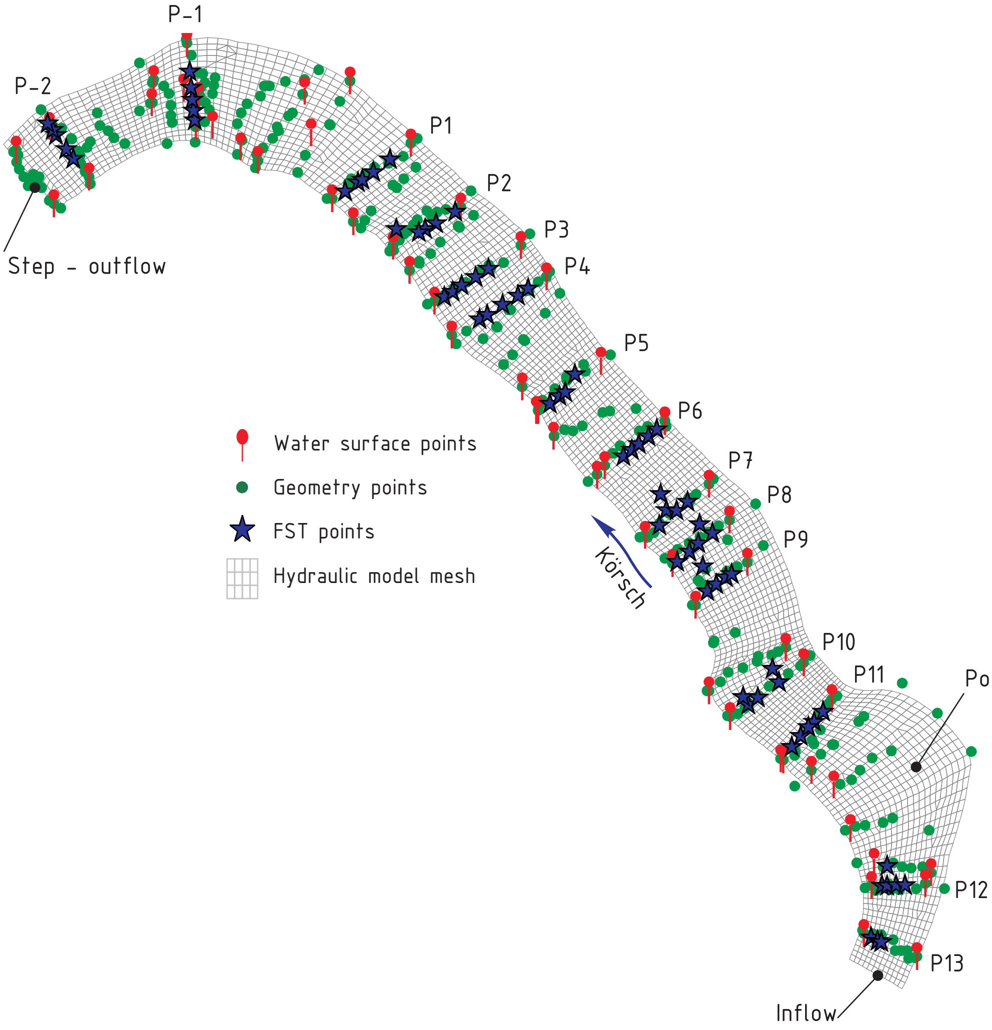

**Figure 7.5:** Mesh of the numerical model; FST-hemisphere, geometry and water surface survey points for Körsch, Reach II

domain is defined, then it is subdivided into smaller polygons, which are meshed with the mesh type "patch". Measured geometry points are triangulated and the obtained surface is interpolated to the nodes of the previously created mesh.

The flow simulation is run in an unsteady regime (standard HydroAS-2D option) increasing the inflow from zero to 470 l/s and continuing with this flow rate until a steady state condition in the river reach is achieved. At the downstream boundary, a very large energy slope is specified, equivalent to the transition from sub- to supercritical flow regime at the step.

The result of hydraulic modelling is loaded into an ArcView project for analysis and further computation of FST distributions. In Figure 7.6, the distribution of computed water depths is shown. It can be seen, that the inundated area computed by the model corresponds well to the wetted widths of transects acquired in the field. Water surface elevations also match quite well the measured ones, what was achieved by minor Manning coefficient adjustments.

In contrast to water surface elevations, a very big scatter – up to 25 cm (!) – between computed and measured water depths at the locations of the FST points is found (see Figure 7.7). One of the major reasons for this discrepancy is the way the FST measurements are performed: according to the methodology, the ground plate has to be put over the substrate. At such rough substrates like in the Körsch study reach, to put the plate "over substrate" is difficult: either the plate is put over a larger stone or stone group, or between stones. It is possible, that the mean elevation of river bottom, assumed during the geometry survey, does not coincide with the bottom elevation registered during FST-hemisphere measurements. Additionally, insufficient density of geometry survey points for an appropriate characterization of this complex river geometry can be claimed. Other possible reasons are:

- Possible wrong triangulation of the neighboring geometry points during mesh generation.
- Wrong geo-referencing of FST measurement points, as their locations were defined not with a tachymeter but later in ArcView, measuring distances from the left bank within the corresponding transects.
- Errors due to imperfect calibration of the model.
- Averaging of node values for z-coordinates within cells of the hydrodynamic model for the FST-hemisphere density calculation in ArcView.

Only for 6 out of 14 cases, in which the position of the geometry point was very close to the one of the FST point, the difference between computed and measured water depths is less than ±3 cm. The largest discrepancies are found in FST transects P11 and P-2. These are

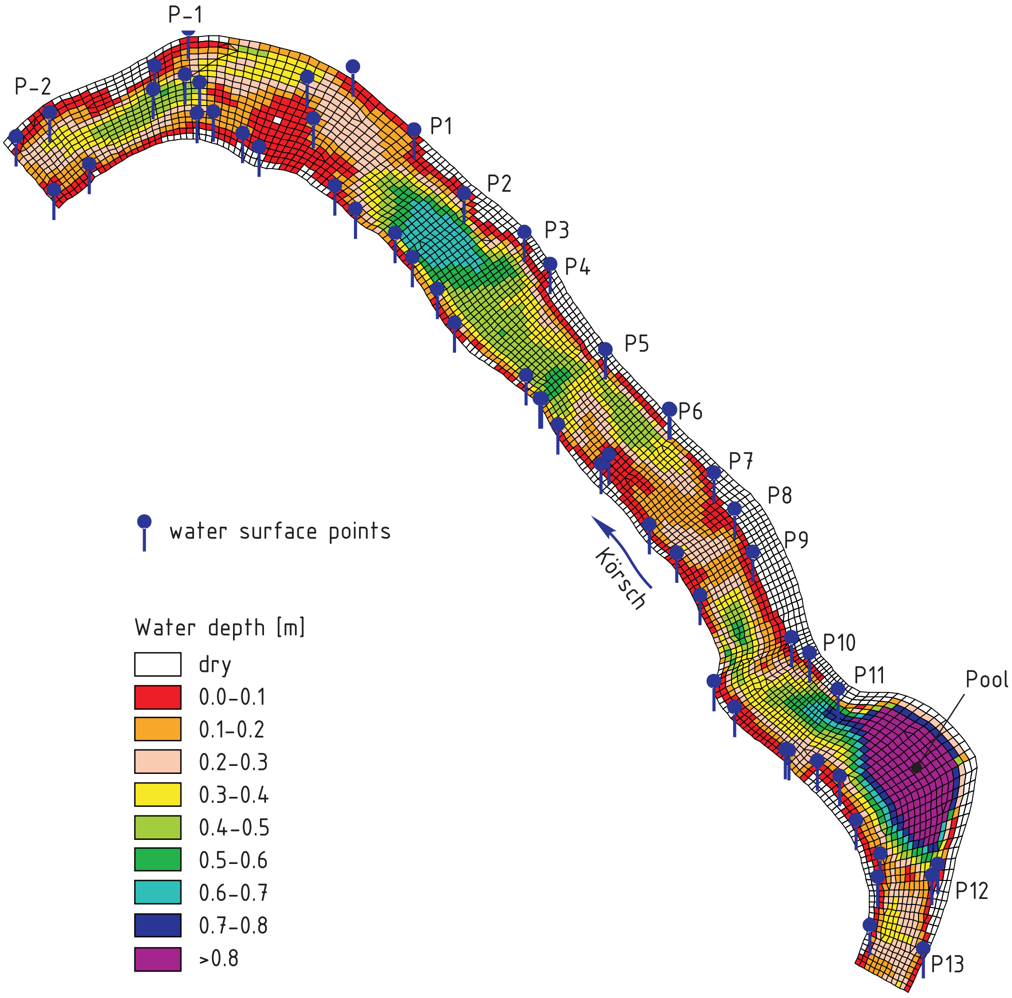

**Figure 7.6:** Plan view of computed water depths for Körsch, Reach II

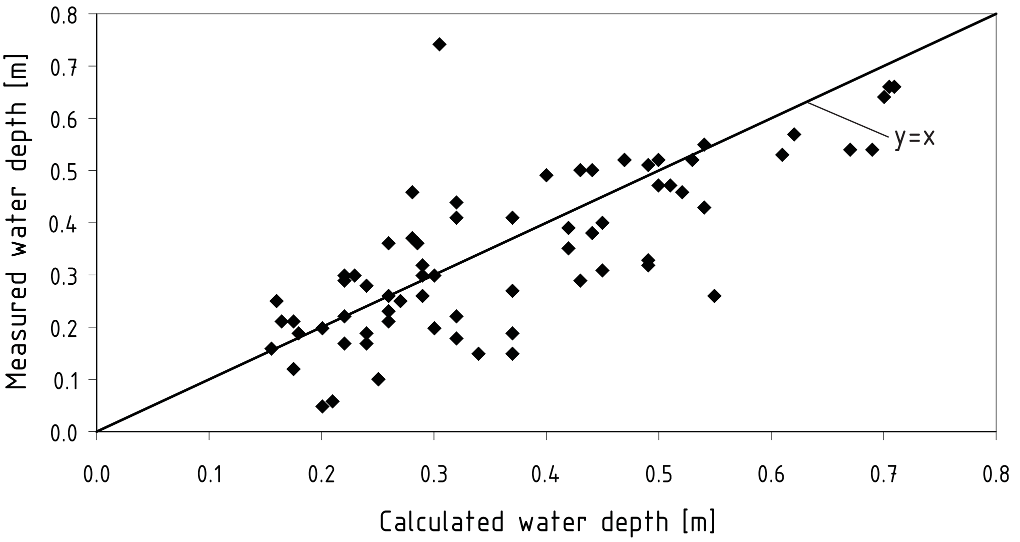

**Figure 7.7:** Comparison of computed and measured water depths (over the roughness tops) at locations of FST sample points for Körsch, Reach II

characterized by a very rough substrate with the presence of boulders with diameters up to 50–70 cm.

Finally, it should be stressed, that the flow of the river is not strictly two-dimensional in some profiles. Therefore, this Körsch example can be considered as a marginal case for the application of a two-dimensional hydrodynamic model. Large stone blocks, especially in the upstream part of the reach, and considerable water depths (up to 70–80 cm) together with relatively small river widths, as well as the presence of steep banks result in a complex, three-dimensional flow.

#### 7.1.2.3 Calculation of FST-hemisphere numbers

The FST-hemisphere numbers are calculated using the hydrodynamic data and compared to the measured ones.

Comparison shows some transects with accurately predicted FST numbers (P1, P4, P5 and P6) and some with large differences between computed and measured values (P7, P11, P-1 and P-2). It is remarkable, that for transects P11 and P-2 also the largest differences in computed and measured water depths are found, but there is no correlation between the absolute values of differences in FST numbers and water depths.

The cumulative curves of FST numbers, measured and computed via the new approach, are shown in Figure 7.8. The computational model captures quite well the trend of the FST-hemisphere numbers' distribution within the reach. Although the percentage of points with

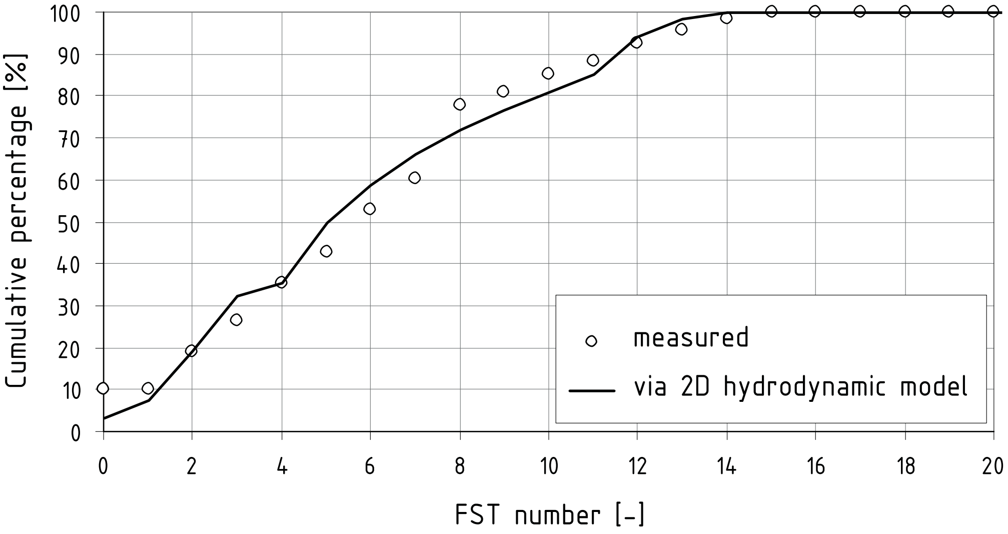

**Figure 7.8:** Cumulative curves of FST numbers: measured and computed via new approach, mixed flow regime

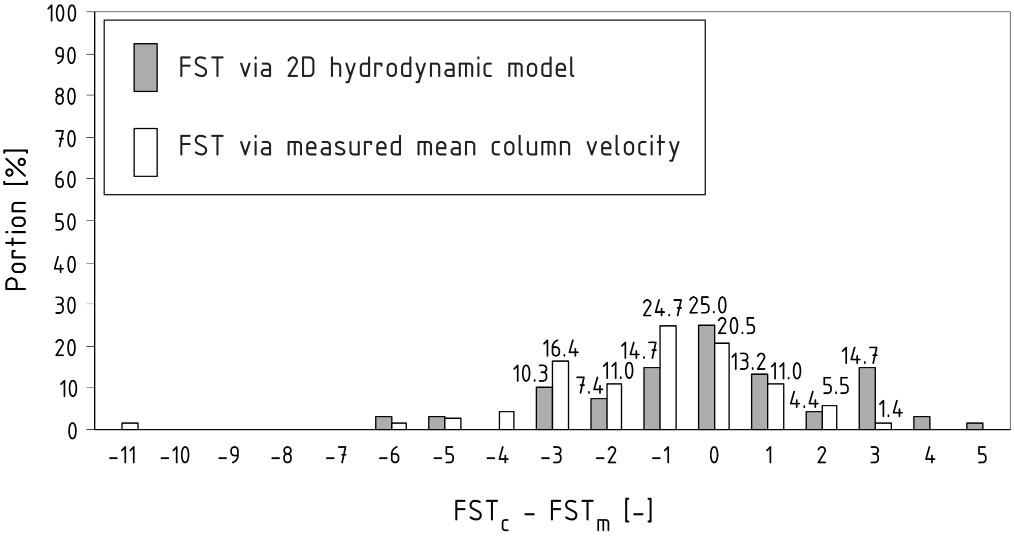

**Figure 7.9:** Comparison of differences in computed and measured FST numbers, mixed flow regime

a zero difference between computed and measured FST numbers is not high (only 25 %), the distribution obtained with the new method is almost symmetrical and is better than that obtained through measured mean column velocities in Section 6.7.2.2 (Figure 7.9).

## 7.2 Habitat suitability modelling with the new approach

### 7.2.1 One-parametrical approach using FST preference curves

The conventional approach using FST preference curves is essentially the same as the one explained in Section 2.5.2, as with the new computational method to FST-hemispheres it is possible to produce distributions that are equivalent to those obtained by field measurements. Integral distributions of FST-hemispheres at different flow rates/situations combined with species preference curves give the information necessary for the analysis, how physical habitat availability is changing with flow. A prerequisite for the use of this method is the availability of preference curves for species that show an exclusive dependency on this parameter. At least 53 benthic species have been proven to show such demands for their physical habitat [20].

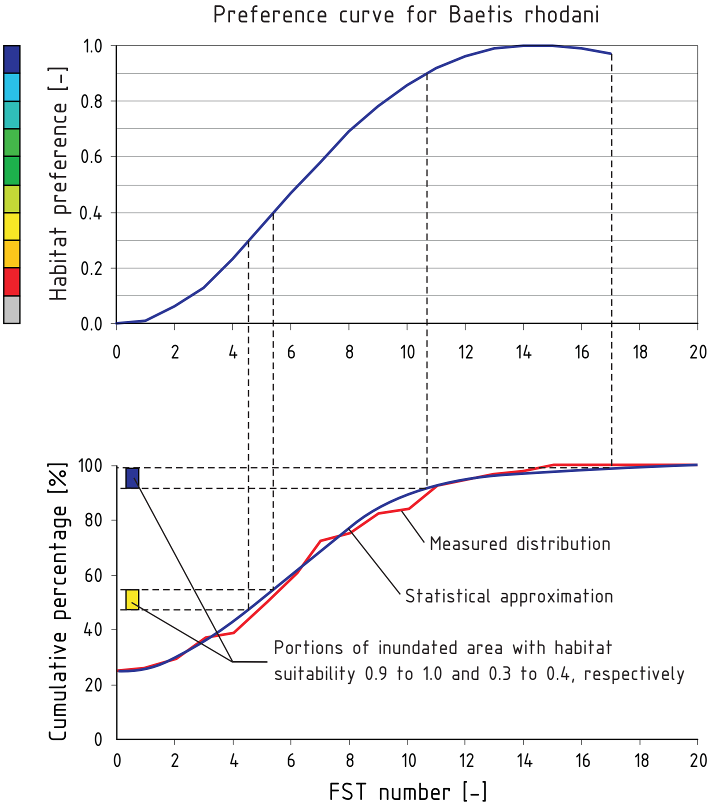

**Figure 7.10:** Combination of a preference curve with an integral FST-hemisphere distribution in BHABIM model

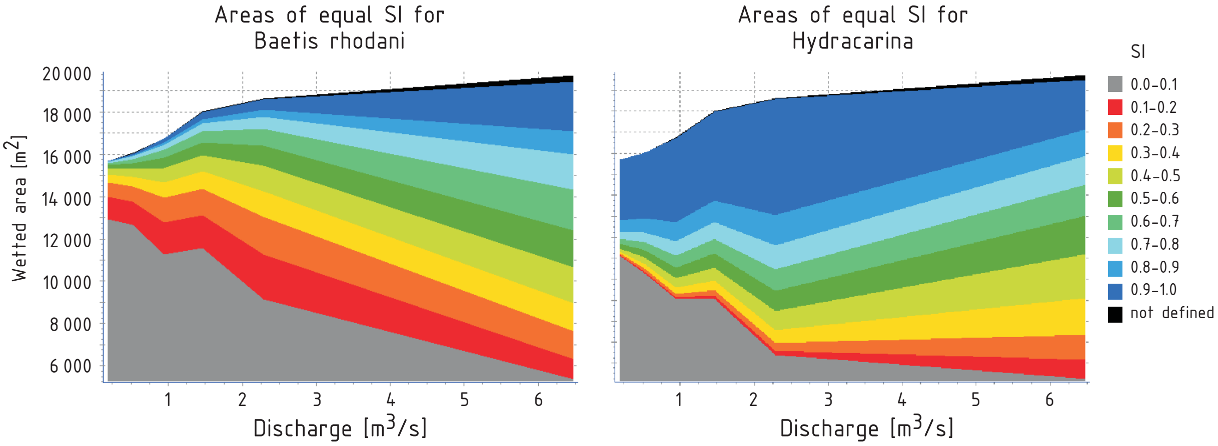

**Figure 7.11:** Examples of graphical representations of the modelling results in BHABIM: absolute areas of equal SI for *Baetis rhodani* and *Hydracarina*

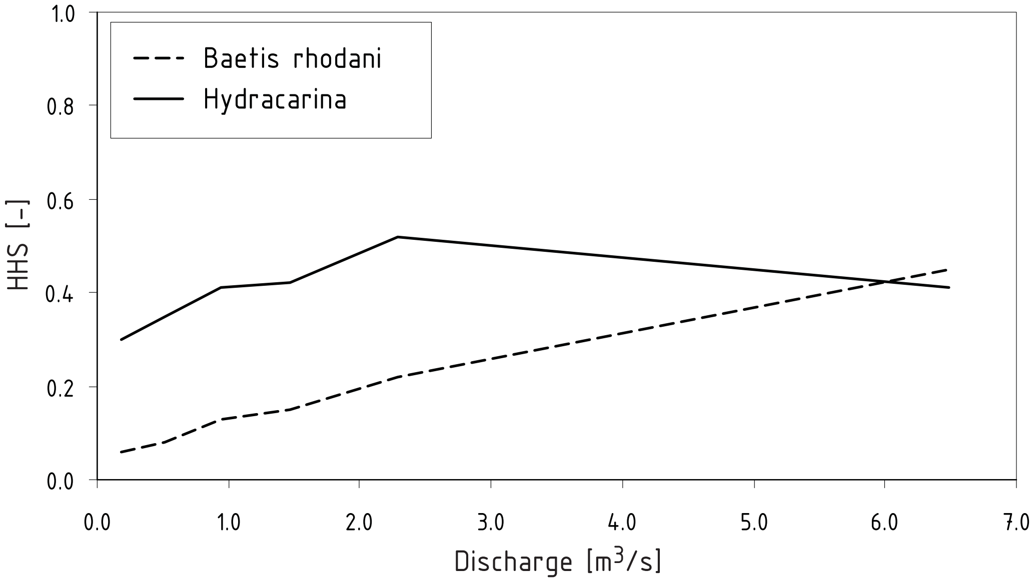

**Figure 7.12:** Example of BHABIM modelling results: curves of HHS linearly changing with flow rate for *Baetis rhodani* and *Hydracarina*

The principle of combining FST-hemisphere distributions with species preference curves is implemented in CASiMiR's application BHABIM [28], [74] (see Figure 7.10). The cumulative frequency distribution of FST-hemispheres shows, which portions of a river reach possess a particular FST number. In turn, in a preference curve, every FST number is associated with a range of Suitability Indexes (SI) which reflect the species requirements for near-bed flow conditions. The program analyzes this information and calculates the areal portions for every SI range. Contributions from the ascending as well as descending parts of the preference function are summed up.

The obtained information can be analyzed in BHABIM in many ways to produce minimum flow recommendations. Integrated graphical representation of the results, for example, diagrams depicting the change of areas of an equal SI with linearly increasing (see Figure 7.11) or naturally varying flow rate, helps a researcher to comprehend the influence of discharge on the physical habitat availability. WUA and HHS for indicator species calculated with Formula 2.1 and 2.2, respectively, and their change with discharge give the quantitative basis for decision making in habitat studies (see Figure 7.12). Additionally, input data and computed results can be viewed as text and exported into standard applications (for example, Microsoft Excel) for further processing.

It should be mentioned here, that in the original approach of Jorde [41] implemented in BHABIM, measured FST-hemisphere distributions are approximated by statistical distributions (for example, log normal). This results in a monotone increasing curve for a cumulative frequency distribution of FST numbers. However, it is questionable, whether measured data should follow a statistical distribution. It seems to be possible, that for some river reaches at specific flow rates, a distribution can exist, at which some FST numbers or even a range of them do not appear in the measured values, resulting in a flat plateau in the cumulative curve and therefore problematic application of statistics.

### 7.2.2 Fuzzy logic based approach, integration of additional parameters

The new approach for the calculation of FST-numbers opens up new perspectives for benthos habitat modelling. It is possible now to obtain spatially referenced FST distributions, thus, the combination of FST with other parameters defining the physical habitat of benthic species becomes straightforward. A multiparametrical benthos habitat simulation can be done the same way as for fish in CASiMiR using the conventional preference curves or fuzzy logic based approach. As the latter is the more promising approach, it is pursued further here.

The integral components of fuzzy logic based modelling are fuzzy sets and fuzzy rules (see Section 2.3.2). Fuzzy sets have to be defined for all (ordinal) parameters, including output parameters – in CASiMiR, conventionally, the habitat suitability. For example, we want to expand the modelling for *Baetis rhodani* with another parameter – shadow. It can be accounted for in fuzzy rules as a conditional (nominal) parameter (like a cover parameter for fish), and, therefore, only fuzzy sets for FST-hemisphere numbers and SI should be constructed.

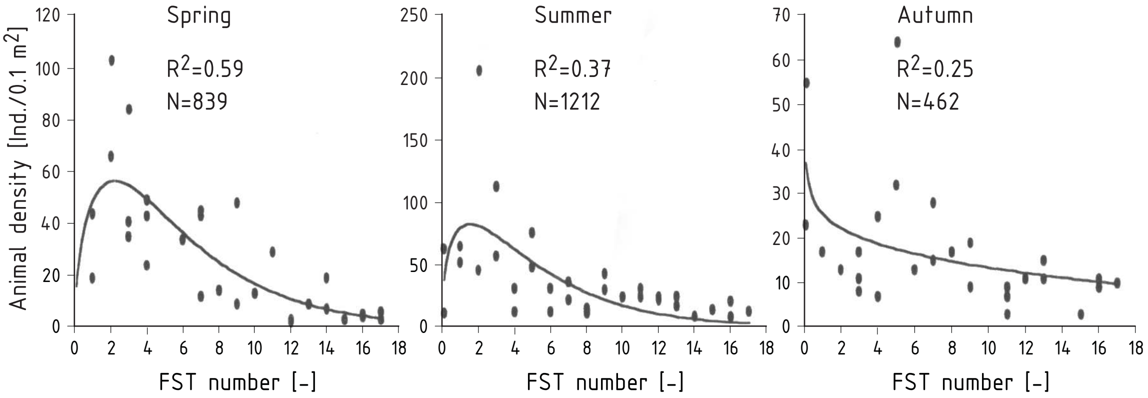

**Figure 7.13:** Sample data for *Hydracarina* in spring, summer and autumn and derived preference curves, river Prien, from Schmedtje (1995) [71]

An important advantage of the fuzzy approach is, that it allows to use imprecise information for habitat modelling. Although, the standard preference curves are taken for granted in the conventional BHABIM approach, the researcher has to recognize, that these are obtained by a statistical procedure and are therefore uncertain. This is clearly seen from the example in Figure 7.13, where the FST preference curves together with biological sample data collected for *Hydracarina* in spring, summer and autumn at the river Prien in Bavaria are shown. It looks rather unjustified, that with decreasing FST numbers for spring and summer samples the curves go to zero, but the autumn curve increases to infinity. This proves, that generation of preference curves is a rather subjective process. On contrary, for all the three samples we can say, that this species prefers low flow velocities associated with FST numbers 0 to 4, and its abundance decreases with increasing FST numbers. Such kind of information is already suitable for the fuzzy logic approach.

Using the sample data for *Baetis rhodani*, we can try to produce fuzzy sets defining the ranges of FST numbers. From Figure 7.14a, we can say, that this species avoids low flow (FST 0 to 5), tolerates medium flow (FST 5 to 11) and prefers high near-bed flow velocities (FST 11 to 18), allowing us to define three fuzzy sets for FST numbers: low, medium and high, as shown in Figure 7.14b. Fuzzy sets should be defined in cooperation with a biologist and not only account for the species preferences, but also for the conditions in the considered river reach.

It can be difficult for somebody unexperienced to order FST numbers into sets. The dia-

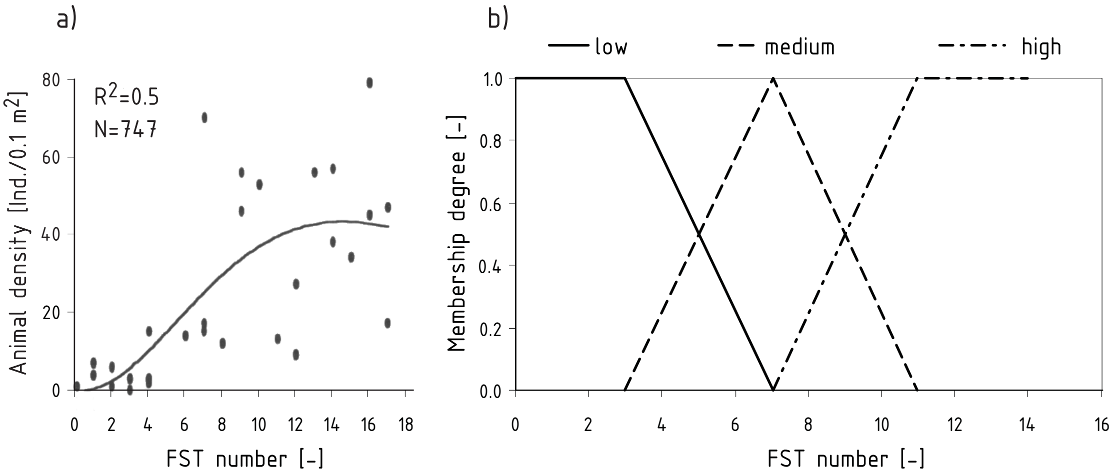

**Figure 7.14:** a) Sample data in summer and derived preference curve for *Baetis rhodani*, river Prien, from Schmedtje (1995) [71]; b) example of FST fuzzy sets for *Baetis rhodani*

gram in Figure 7.15, which shows the relation between near-bed velocity (at 4 cm above the plate) and FST-number, can help in this process. The diagram is obtained by the application of the force balance based formula of Section 5.6 using the corresponding base drag and lift coefficients.

The next step would be the definition of fuzzy rules, which should be created by or also under guidance of a biologist. In Table 7.2, fuzzy rules like they could be formulated for *Baetis rhodani* are given. They are based on information described in Section 2.4, upon which this species prefers unshaded areas due to its feeding customs.

To obtain SI distributions, now spatially oriented, the newly developed extension "FuzzySI" for ArcView GIS 3.3 can be used. It comprises of the fuzzy logic block used in the conventional CASiMiR software, but now allows habitat modelling upon arbitrary number of custom-defined parameters.

For the use of the extension, the input files – fuzzy sets and fuzzy rules in CASiMiR formats – have to be specified by the user. Generally, the program uses the data from the shape's attribute table in an ArcView project, but it is also possible to perform calculations on the basis of a single dbf-table without a data connection to geometrical entities in ArcView. The programm analyzes the present parameters in fuzzy sets and fuzzy rule files, and the user has to specify the columns corresponding to these parameters in the attribute table in order to supply data for a calculation. At last, the extension creates a new column in the attribute table, where the computed values of the SI are stored.

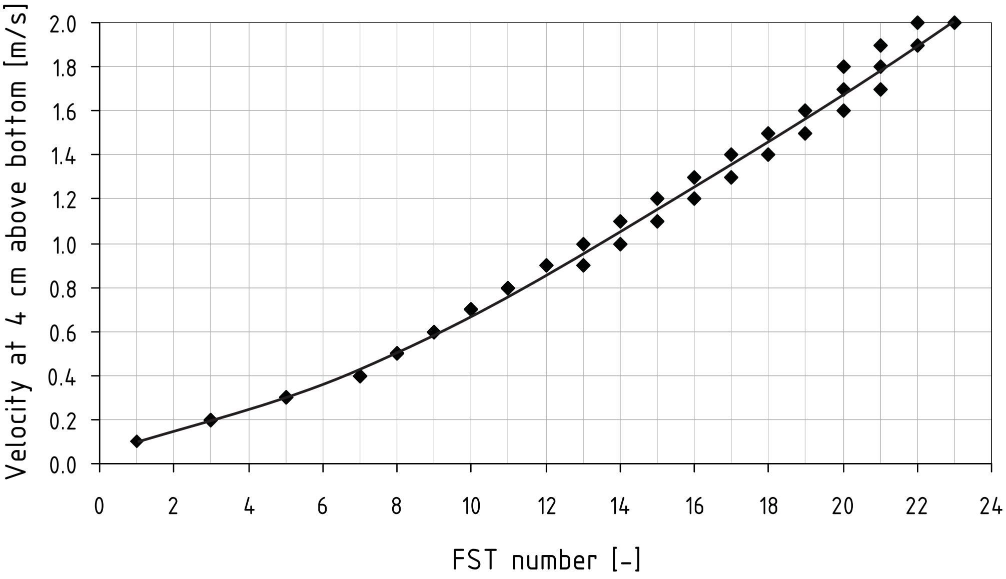

**Figure 7.15:** Relation "near-bed velocity vs. FST number", mean between curves related to sub- and supercritical flow regimes, $\mu = 0.24$, $u_{hc}/u_{ht} = 0.9$

| FST-hemisphere number | Shadow degree | Habitat suitability |
|---|---|---|
| L | L | L |
| L | M | L |
| L | H | M |
| M | L | L |
| M | M | M |
| M | H | H |
| H | L | M |
| H | M | H |
| H | H | VH |

L – low, M – medium, H – high, VH – very high.

**Table 7.2:** Fuzzy rules for *Baetis rhodani* based on FST-hemisphere and shadow parameters

## 7.3 Summary

The application of a new computational approach to FST-hemispheres for habitat modelling is shown in this part. The input data for the new approach – mean column velocities and water depths – can be obtained using a two-dimensional hydrodynamic model. Thus, in future, habitat modelling for fish and benthos can be done on the same data basis: No FST-hemisphere measurements at flow situations of interest have to be performed, but a geometry survey with a subsequent hydrodynamic modelling of a river reach is sufficient, like in the common CASiMiR study procedure for fish.

The given example for the river Körsch depicts all necessary steps for obtaining the FST-hemisphere distribution at a particular flow situation. The validation of the approach was partly hindered however by the apparently wrong measurements of the Acoustic Doppler Velocitymeter.

The new approach allows obtaining integral as well as spatially referenced FST-hemisphere distributions. Thus, two kinds of benthos habitat modelling can be performed. The conventional, one-parametric, based only on integral FST distributions, is one of them. Using this approach becomes now considerably less expensive as survey costs can be saved. More promising, however, is the modelling with spatially referenced FST-hemisphere distributions which allows:

1. Combination of FST data with other important parameters such as substrate or water depth, for example. These additional parameters can be mapped during a field survey or computed using hydrodynamic model.

2. Expansion of the model applicability range, especially for renaturation studies, where parameters in parts of a river reach can be modified and the influence on the habitat quality can be investigated.

3. If done using a fuzzy logic approach, the biological data on FST-hemisphere preferences of benthos species can be used in a more efficient way: no need for the generation of subjectivity prone “preference curves”, but introduction of fuzzy rules.

The new approach is implemented as an extension to ArcView GIS 3.3 and uses the native graphical and statistical capabilities of this program. The other, newly developed fuzzy logic extension to ArcView allows a flexible involvement of additional modelling parameters. The two-dimensional hydrodynamic data is loaded into GIS without any mesh modifications through an additionally created, easily extendable for other hydrodynamic models interface. This is a large advantage, as until now it was possible to integrate two-dimensional data into CASiMiR only through less convenient equal step grid generation and subsequent data interpolation from the original mesh onto the grid.

# 8 Summary of the work and outlook

Benthos – the community of organisms living in or at the bottom sediments – is an important constituent of flowing water ecosystems. Besides playing a major role as a food supply for aquatic vertebrates, the adaptation of many benthic animals to specific physical conditions makes them a valuable target in environmental impact assessment studies. Therefore, existing habitat modelling approaches have to be adjusted or developed further to be able to incorporate the specific parameters that influence the habitat of these animals.

The importance of flow for benthos is unquestionable. Two of the most popular benthos habitat modelling approaches in the past – PHABSIM and FST-hemisphere based – incorporate this parameter in one or another form (Section 2.5). However, these models possess strong deficiencies. The PHABSIM approach incorporates the mean column velocity, which has no one-to-one relation to the near-bed flow conditions. Additionally, conceptual problems concerning the use of preference curves and their univariate processing make this model less attractive in application. The FST-hemisphere method of Statzner and Müller appears to be more suitable than the mean column velocity for the characterization of flow conditions near the bottom. However, the original FST based habitat modelling approach requires extensive field work and does not allow direct incorporation of other parameters into the analysis. These other parameters, for example substrate or food availability, can affect the habitat quality of some benthos species at the same or even higher degree as flow velocity (Section 2.4). Hence, a state-of-the-art modelling approach should provide options for a flexible incorporation of these.

The present study can be considered as an advancement in the FST-hemisphere based habitat modelling approach. An important role in the choice of the model base for the improvement plays the existing large data collection reflecting the near-bed flow preferences of benthos species sampled with FST-hemisphere equipment. The development goals were: (1) Clarifying the FST-hemisphere method´s physical rationale; (2) elaborating a calculational approach to FST-hemispheres based on hydrodynamic and morphological parameters usually acquired in fish habitat studies; (3) verifying the new approach upon field data; (4) extending the FST based habitat modelling approach for the incorporation of additional parameters and allowing a spatially referenced analysis of river reaches.

## 8.1 Theoretical basis for computational approach to FST-hemispheres

Force balance analysis reveals, that the density of the heaviest hemisphere just moved away from atop the plate by a given flow is proportional to the square of the near-bed velocity and the combination of the corresponding lift and drag coefficients (Section 4.2). It also depends on the friction coefficient $\mu$ between hemisphere and ground plate, which is FST equipment specific. For a new standard structured ground plate in combination with a new FST-hemisphere set, a friction coefficient of 0.24 is found. For the old smooth ground plate, the friction coefficient additionally depends on the FST-hemisphere placement method and ranges considerably from values of 0.6–0.7 for the “press” method to 0.05–0.1 for the “drop” method.

During measurements in a river, the FST-hemisphere is submerged in a near-bed flow field. The knowledge of the latter is necessary for the application of the force balance based formula for the FST-hemisphere density estimation. A feasible way for determining near-bed velocities and their gradients offers the modified logarithmical velocity distribution of Bezzola (Section 3.6). Based on the mixing length theory of Prandtl, it proposes, that mainly the turbulent shear stress defines the mean flow characteristics. Bezzola’s modified log law accounts for the specific distribution of the turbulent shear stresses over rough beds in flows with small relative submergences expressed in the presence of a so called roughness sublayer. Within this roughness sublayer, the turbulent shear stress is constant or even reduces towards the roughness tops (Section 3.5). Using Bezzola’s log law, the vertical velocity distribution can be completely described upon only three parameters: mean column velocity $u_{0.4}$, water depth $h_t$, and thickness of the roughness sublayer $y_r$. The first two parameters $u_{0.4}$ and $h_t$ are commonly used in fish habitat studies and can be obtained through application of hydrodynamic models. The big advantage is, that the thickness of the roughness sublayer $y_r$, unlike the equivalent roughness height $k_s$ used in the Nikuradse’s formula, is an unique characteristic of the particular substrate grain size and arrangement and is independent from relative submergence.

Concurrent application of Bezzola’s logarithmical velocity distribution law and the force based formula allows to prove, that no unique relation between FST-hemisphere numbers/densities and bottom shear stress $\tau_0$ exists. At every particular substrate condition this correlation, although, linear according to theory, has a different slope (Section 4.3.2).

## 8.2 Numerical simulation of flow past a hemisphere

Review of literature devoted to so called junction flows – flow phenomena around obstacles on a wall – allows to suggest the appropriate choice of the object form in FST equipment. In contrast to high obstacles exhibiting a von Kármán vortex shedding in their wakes, the flow around a hemisphere is characterized by shedding of weaker arch vortices, which do not produce considerable pressure field fluctuations. Therefore, the hydrodynamic coefficients for a hemisphere can be assumed to be constant over time (Section 5.1). FST-hemisphere measurements cover a wide range of Reynolds numbers wherein a transition from sub- to supercritical flow regime takes place. The transition for a hemisphere is characterized by the reduction of the drag coefficient and an increase in the lift coefficient. Numerical investigations have shown, that the drag $c_{d,b}$ and lift $c_{l,b}$ coefficients for the uniform flow around a hemisphere are 0.44 and 0.53 for the subcritical regime. For the supercritical regime they are 0.31 and 0.76, respectively (Sections 5.3, 5.4). The critical Reynolds number at which the transition takes place generally depends on the inflow turbulence intensity and the roughness of a hemisphere's surface, and is therefore not quantifiable for the FST-hemisphere equipment. For a smooth hemisphere in a low turbulence flow, it can be assumed to be at $7\times10^4$, corresponding to the velocity at the level of a hemisphere's top $u_{ht}$ =0.9 m/s. Knowing the velocities at the levels of a hemisphere's top $u_{ht}$ and its center of mass $u_{hc}$, the force balance based formula for the estimation of a hemisphere's density takes a form:

$$\rho_h = \rho_w \left[1 + \frac{3}{8}\frac{u_{ht}\,u_{hc}}{r_h\,g}\left(c_{l,b} + \frac{c_{d,b}}{\mu}\right)\right]$$

Numerical simulations also show, that the FST ground plate does not have any influence on the values of the hydrodynamical coefficients. From this point of view, it does not matter whether the measurements are performed with the old smooth or new structured plate and the influence of the ground plate is only expressed through the friction coefficient.

## 8.3 Validation of the computational approach to FST-hemispheres

The validation of the new approach to FST-hemispheres consists of the two main tasks: (1) Verification of Bezzola's log law for the estimation of near-bed velocities and (2) exploring the applicability of the force-balance based formula for the estimation of FST-hemisphere densities. A consistent methodology is applied in six case studies, comprising laboratory as well as field measurements (Chapter 6). The method performs to a varying degree in these examples. Very good results are obtained for rivers Schwechat and Rhine, in which an FST equipment with the new structured plate was used. For the laboratory data of Scherer, the method also gives satisfactory results. The least satisfying predictions are obtained for the river Rhône, where measurements were done with the old smooth plate and an uncertainty exists which FST-hemisphere placement method was applied. Justification of the methods's performance for the rivers Zwalm and Körsch is complicated by the possibly wrong velocity measurements done with 3D ADV velocity meter. However, it is not clear, whether the new method is inapplicable due to the conditions present in these rivers, in particular very coarse substrates, or if the discrepancies between measured and computed FST-hemisphere numbers can be completely related to the errors in the velocity measurements.

## 8.4 Application of the new approach for benthos habitat modelling

Application of the new approach for benthos habitat modelling requires in general three steps. These are demonstrated for the example of the river Körsch and consist of (Section 7.1):

1. Calculation of the mean column flow velocity and water depth distributions with a hydrodynamic model at particular flow situations;
2. Estimation of near-bed flow conditions using Bezzola's log law;
3. Calculation of FST-hemisphere density distributions with the force balance based formula.

After FST-hemisphere distributions are obtained for the particular flow situations, they can be used either in a one-parametrical, FST-hemispheres only based or in a multi-parametrical benthos habitat model (Section 7.2). The first kind of application is similar to the "statistical" one implemented in the CASiMiR submodel BHABIM. The second one mimics the spatially referenced CASiMiR approach used presently for fish. The use of fuzzy logic for the latter is especially recommended, as it allows to avoid the difficulties of preference curves generation from field data. The fuzzy logic approach also offers a convenient way of multi-parametrical modelling.

Implemented as an extension to ArcView GIS 3.3, the approach is supported by the powerful analysis and visualization tools provided by this application.

## 8.5 Limitations of the FST-hemisphere based habitat modelling approach

First, it is important to have in mind, that presently the large data pool of FST-based biological data does not contain any additional information on the local sample conditions. Especially the dominating substrates, which can be as important as flow, are presently not in the data base. Some other parameters such as dominating water depths, algae presence or shadow can also be important. For this reason, the authors of the data sets should be consulted for the purpose of recovering this information. According to this additional information, the data on FST-hemisphere preferences of animals should be filtered before their use in the habitat model.

Second, there is a conceptual problem to apply the new approach for river reaches with very coarse substrates. These are for example mountain reaches, characterized by the presence of large single boulders and/or morphological structures like waterfalls and cascades. For these cases, a two-dimensional flow approximation cannot be applied anymore. Additionally, it is questionable whether the existing biological data can be used here. Proper positioning of the FST ground plate with the dimensions of 13×18 cm over substrates with mean diameters larger than 30 cm, but also application of biological sampling methods commonly used for finer substrates would be hindered.

Third, the method allows to estimate the FST-hemisphere number distribution for a river reach based on the mean elevation of the river bottom. Local peculiarities, such as large stones or dead trees, cannot be accounted for. In reality, the presence of an obstacle in front of or behind an FST measurement spot would result in a complete altering of the hydrodynamic lift and drag coefficients for a hemisphere. The logarithmical distribution law for the estimation of the near-bed velocity is not applicable at such conditions also.

## 8.6 Further research

The logarithmical velocity distribution law used for the estimation of near-bed velocities is generally only applicable for uniform flows. It is of large interest to apply Bezzola's model for gradually varying (accelerating and decelerating) flows and to implement modifications if needed. Also, additional efforts should be undertaken for the elaboration of a robust and more reliable estimation method for the roughness sublayer thickness. The estimate for the latter was based upon the mean grain diameter in the present work. One method could be to evaluate the vertical profiles of turbulent intensities for the representative substrates. This goal was set actually for the present work but its realization was hindered by the problems resulting from the ADV velocity measurements. Also, the question of an appropriate selection for the logarithmical velocity profile origin should be clarified.

Of large practical importance is the implementation of a roughness sublayer thickness concept in hydrodynamical models. This parameter allows to characterize the bottom roughness and thus energy losses independently from relative submergence. The common use of the Manning coefficient is critical for the application in the range of low discharges and, consequentially, small relative submergences, as it is known to change with the latter. The profit here shows itself not only for hydrodynamical but also for sediment transport models.

There is an urgent need to test the performance of the new approach to FST-hemispheres together with the validation via biological sampling. Application of the one-parametrical FST-based approach for habitat modelling for those species possessing a standardized preference curve would be a first step in this direction. The next step would be the incorporation of additional parameters using the fuzzy logic approach.

Taking into account the effects from isolated, large substrate elements would also be of interest for the habitat modelling for some species. For example, it is known, that recirculation zones behind large boulders represent preferential habitats for some collectors. Newly appearing methods for the estimation of flow conditions near such peculiarities would improve benthos habitat models considerably.

Another important development can be undertaken in the direction of large scale benthos habitat modelling. First attempts of "meso-scale" CASiMiR modelling for fish are very promising. At larger scales, the incorporation of other parameters like water quality appears to be important for benthos species.

**With the present work, some important steps towards a state-of-the-art benthos habitat model are made. First, the physical rationale of the FST-hemisphere method is clarified implying the large value of the existing biological information collected with this method. Second, the new computational approach to FST-hemispheres eliminates the previously needed extensive field survey work and brings habitat modelling for benthos to the same base as that for fish. At last, the now possible spatially oriented multi-parametrical benthos habitat modelling approach widens the application spectrum, for example, for restoration studies.**

# Bibliography

[1] (2004). *FlowTracker Handheld ADV. Operation Manual. Firmware Version 2.5. Software Version 1.30*. SonTek/YSI, Inc.

[2] Acalar, M. and Smith, C. (1987). A study of hairpin vortices in a laminar boundary layer: Part I, hairpin vortices generated by a hemisphere protuberance. *Journal of Fluid Mechanics*, 175:1–40.

[3] Ambühl, H. (1960). *Die Bedeutung der Strömung als ökologischer Faktor*. PhD thesis, Eidgenössische Technische Hochschule in Zürich. Buchdruckerei Birkhäuser AG., Basel.

[4] Arthington, A. (2003). Environmental flow assessment with emphasis on holistic methodologies. In *IPENZ Proceedings of Technical Groups*, volume 30.

[5] Arthington, A., Tharme, R., Brizga, S., Pusey, B., and Kennard, M. (2004). Environmental flow assessment with emphasis on holistic methodologies. In *Proceedings of the Second International Symposium on the Management of Large Rivers for Fisheries*, volume II of *RAP Publication*, pages 37–65.

[6] Ballio, F., Bettoni, G., and Franzetti, S. (1998). A survey of time-averaged characteristics of laminar and turbulent horseshoe vortices. *Journal of Fluids Engineering*, 120:233–242.

[7] Bathurst, J. C. (1985). Flow resistance estimation in mountain rivers. *Journal of Hydraulic Engineering. Proceedings of ASCE*, 111(4):625–643.

[8] Bezzola, G. R. (2002). *Fliesswiderstand und Sohlenstabilität natürlicher Gerinne unter besonderer Berücksichtigung des Einflusses der relativen Überdeckung*. PhD thesis, Mitteilungen der Versuchsanstalt für Wasserbau, Hydrologie und Glaziologie, Eidgenössische Technische Hochschule Zürich.

[9] Bovee, K., Lamb, B., Bartholow, J., Stalnaker, C., Taylor, J., and Henriksen, J. (1998). Stream habitat analysis using the Instream Flow Incremental Methodology. Technical report, Information and Technology Report USGS/BRD- 1998- 0004. US Geological Survey, Biological Research Division, Washington, DC.

[10] Coles, D. (1956). The law of the wake in the turbulent boundary layer. *Journal of Fluid Mechanics*, 1:191–226.

[11] Constantinescu, G. and Squires, K. (2004). Numerical investigations of flow over a sphere in the subcritical and supercritical regimes. *Physics of Fluids*, 16(5):1449–1466.

[12] COST Action 626 (March 2004). State-of-the-art in data sampling, modelling analysis and applications of river habitat modelling. Technical report, COST Action 626 European Aquatic Modelling Network.

[13] Cummins, K. W. (1975). *River Ecology*, volume 2 of *Studies in Ecology*, chapter Macroinvertebrates, pages 170–198. Oxford, Blackwell.

[14] Dittrich, A. (1998). *Wechselwirkung Morphologie/Strömung naturnaher Fliessgewässer*. Mitteilungen des Institutes für Wasserwirtschaft und Kulturtechnik der Universität Karlsruhe (TH), Heft 198.

[15] Dittrich, A. and Koch, W. (1994). Bestimmung des Bewegungsbeginns der Fließwasserstammtisch-Halbkugeln (FST). Gutachten im Auftrag Bayerischen Landesamts für Wasserwirtschaft. Technical report, Institut für Wasserbau und Kulturtechnik, Universität Karlsruhe.

[16] Dittrich, A. and Schmedtje, U. (1995). Indicating shear stress with FST-hemispheres - effects of stream-bottom topography and water depth. *Freshwater Biology*, 34:107–121.

[17] Dong, Z., Wang, J., Chen, C., and Xia, Z. (1991). Turbulence characteristics of open-channel flows over rough beds. In *Proceedings of 24th IAHR Congress Refined Flows, Modelling*, pages C33–C40.

[18] Dürr, A. (1999). Auswirkungen von Abflußvariationen auf das aquatische Habitatangebot in der Teststrecke Kraiburg/Inn. Diplomarbeit, Institut für Wasserbau und Wasserwirtschaft, Universität Stuttgart.

[19] DVWK (1996). Gesichtspunkte zum Abfluß in Ausleitungsstrecken kleiner Wasserkraftanlagen. Schriftenreihe des Deutschen Verbandes für Wasserwirtschaft und Kulturbau e.V.; Heft 114.

[20] DVWK (1999). Ermittlung einer ökologisch begründeten Mindestwasserführung mittels Halbkugelmethode und Habitat-Prognose-Modell. Schriftenreihe des Deutschen Verbandes für Wasserwirtschaft und Kulturbau e.V.; Heft 123.

[21] Flammer, G. H., Tullis, J. P., and Mason, E. S. (1970). Free surface, velocity gradient flow past hemisphere. *Journal of the Hydraulics Division. Proceedings of the American Society of Civil Engineers*, 96(7):1485–1502.

[22] Fluent (2003). *FLUENT 6.1 User's Guide*. Fluent Inc., Centerra Resource Park, 10 Cavendish Court, Lebanon, NH 03766.

[23] Frissell, C. A., Liss, W. J., Warren, C. E., and Hurley, M. D. (1986). A hierarchical framework for stream habitat classification: viewing streams in a watershed context. *Environmental Management*, 10(2):199–214.

[24] Frutiger, A. and Schib, J.-L. (1993). Limitations of FST hemispheres in lotic benthos research. *Freshwater Biology*, 30:463–474.

[25] Fuchs, U. (1994). *Ökologische Grundlagen zur wasserwirtschaftlichen Planung von Abfluß und Morphologie kleinerer Fließgewässer*. PhD thesis, Universität Karlsruhe.

[26] Giesecke, J. and Jorde, K. (1997a). Ansätze zur ökologischen Optimierung von Mindestabflußregelungen in Ausleitungsstrecken. *Wasserwirtschaft*, 87(5):232–237.

[27] Giesecke, J. and Jorde, K. (1997b). Approaches towards an ecological optimization of minimum flow regulations in diverted streams. In *Environmental and Coastal Hydraulics: Protecting the Aquatic Habitat*, volume 1, pages 528–533. IAHR.

[28] Giesecke, J. and Jorde, K. (1998). Simulation and assessment of hydraulic habitat in rivers. In *Modelling, Testing and Monitoring for Hydro Powerplants - III*, pages 71–82. International Journal on Hydropower and Dams.

[29] Giesecke, J. and Mosonyi, E. (2005). *Wasserkraftanlagen – Planung, Bau und Betrieb*. Spinger, 4 edition.

[30] Goethals, P. and Pauw, N. D. (2001). Development of a concept for integrated ecological river assessment in Flanders, Belgium. *Journal of Limnology*, 60(Suppl. 1):7–16.

[31] Gordon, N. D., McMahon, T. A., and Finlayson, B. L. (1992). *Stream Hydrology: An Introduction for Ecologists*. Wiley Chichester.

[32] Gore, J. A. and Judy, R. D. (1981). Predictive models of benthic macroinvertebrate density for use in Instream Flow studies and regulated flow management. *Canadian Journal of Fisheries and Aquatic Sciences*, 38:1363–1370.

[33] Gore, J. A., Layzer, J. B., and Mead, J. (2001). Macroinvertebrate instream flow studies after 20 years: a role in stream management and restoration. *Regulated Rivers: Research and Management*, 17:527–542.

[34] Gunkel, G. (1996). *Renaturierung kleiner Fließgewässer*. Gustav Fischer Verlag.

[35] Hart, D., Clark, B., and Jasentuliyana, A. (1996). Fine scale field measurement of benthic flow environments inhabited by stream invertebrates. *Limnology and Oceanography*, 41(2):297–308.

[36] Heilmair, T. and Strobl, T. (1994). Erfassung der sohlnahen Strömungen in Ausleitungsstrecken mit FST-Halbkugeln und Mikro-Flowmeter – ein Vergleich der Methoden. Berichte der Versuchanstalt Obernach und des Lehrstuhls für Wasserbau und Wassermengenwirtschaft der Technischen Universität München.

[37] Hinze, J. O. (1975). *Turbulence*. McGraw-Hill.

[38] Horne, A. J. and Goldman, C. R. (1994). *Limnology*. McGraw-Hill, Inc.

[39] Hudson, H. R., Byrom, A. E., and Chadderton, W. L. (2003). *A critique of IFIM-instream habitat simulation in the New Zealand context*. Number 231 in Science for Conservation. New Zealand Department of Conservation.

[40] Hynes, H. B. N. (1972). *The Ecology of Running Waters*. Liverpool University Press.

[41] Jorde, K. (1997). *Ökologisch begründete, dynamische Mindestwasserregelungen bei Ausleitungskraftwerken*. PhD thesis, Mitteilungen des Institutes für Wasserbau, Universität Stuttgart, Heft 90.

[42] Jowett, I. G. and Richardson, J. (1990). Microhabitat preferences of benthic invertebrates in a New Zealand river and the development of in-stream flow-habitat models for Deleatidium spp. *New Zealand Journal of Marine and Freshwater Research*, 24:19–30.

[43] King, J., Tharme, R., and Brown, C. (1999). Definition and Implementation of Instream Flows. Technical report, Thematic Report for World Commission on Dams.

[44] Koll, K. (2002). *Feststofftransport und Geschwindigkeitsverteilung in Raugerinnen*. PhD thesis, Fakultät für Bauingenieur- und Vermessungswesen der Universität Fridericiana zu Karlsruhe (TH).

[45] Kopecki, I. (2007). Data tables for the case studies. Addendum to the Dissertation "Calculational Approach to FST-Hemispheres for Multiparametrical Benthos Habitat Modelling".

[46] Lampert, W. and Sommer, U. (1997). *Limnoecology: The Ecology of Lakes and Streams*. Oxford University Press.

[47] Lancaster, J. (1999). Small-scale movements of lotic macroinvertebrates with variations in flow. *Freshwater Biology*, 45:605–619.

[48] Leder, A. (1992). *Abgelöste Strömungen: physikalische Grundlagen (Grundlagen und Fortschritte der Ingenieurwissenschaften)*. Braunschweig; Wiesbaden: Vieweg.

[49] Mader, H. and Meixner, H. (1995). Messung sohlnaher Fließgeschwindigkeit – ein Methodenvergleich. *Österreichische Wasser- und Abfallwirtschaft*, Sonderabdruck aus Jahrgang 47, Heft 11/12:289–299.

[50] Mader, H. and Pedersen, M. (to be published). Comparison of measuring near bed velocities by FST and 2D or 3D current meters.

[51] Manhart, M. (1998). Vortex shedding from a hemisphere in a turbulent boundary layer. *Theoretical and Computational Fluid Dynamics*, 12(1):1–28.

[52] Martinuzzi, R. J. and AbuOmar, M. (2003). Study of the flow around surface-mounted pyramids. *Experiments in Fluids*, 34:379–389.

[53] Menter, F. R. (1994). Two-equation eddy-viscosity turbulence models for engineering applications. *AIAA Journal*, 32(8):1598–1605.

[54] Minshall, G. W. (1984). *The Ecology of Aquatic Insects*, chapter Aquatic Insect-Substratum Relationships, pages 358–400. Praeger Publishers, New York.

[55] Morris, H. M. (1959). Design methods for flow in rough conduits. *Journal of the Hydraulics Division. Proceedings of the American Society of Civil Engineers*, 85(7):43–62.

[56] Mérigoux, S. (2004). Effects of hydraulic changes on invertebrates: predictions at the reach scale from local observations. Presentation. `http://folk.ntnu.no/borsanyi/eamn-web/documents/ghent/presentations/merigoux_gent.pdf`.

[57] Nezu, I. and Nakagawa, H. (1993). *Turbulence in Open Channel Flows*. Balkema Rotterdam.

[58] Nikuradse, J. (1933). Strömungsgesetze in rauhen Rohren. *VDI-Verlag, Forschungsheft*, 361.

[59] Nujic, M. (2003). HydroAS-2D. Ein zweidimensionales Strömungsmodell für die wasserwirtschaftliche Praxis. Benutzerhandbuch. Privatverlag Nujic.

[60] Okamoto, S. (1982). Turbulent shear flow behind hemisphere-cylinder placed on ground plane. In *Turbulent Shear Flows 3*, pages 171–185.

[61] Poff, N., Allan, J., Bain, M., Karr, J., Prestegaard, K., Richter, B., Sparks, R., and Stromberg, J. (1997). The natural flow regime: A paradigm for river conservation and restoration. *BioScience*, 47:769–784.

[62] Prandtl, L. (1925). Über die ausgebildete Turbulenz. *ZAMM*, 5:136–139.

[63] Prandtl, L. and Tietjens, O. G. (1957). *Applied Hydro- and Aeromechanics*. Dover Publications, Inc. New York.

[64] Raudkivi, A. J. (1990). *Loose Boundary Hydraulics*. Pergamon Press.

[65] Restle, E. (1992). Veränderung des hydraulischen Musters im Gerinne infolge morphologischer Umgestaltung. Diplomarbeit, Institut für Wasserbau, Universität Stuttgart.

[66] Sakamoto, H. and Arie, M. (1983). Vortex shedding from a rectangular prism and a circular cylinder placed vertically in a turbulent boundary layer. *ASME Journal of Fluid Mechanics*, 126:147–165.

[67] Savory, E. and Toy, N. (1986). Hemispheres and hemisphere-cylinders in turbulent boundary layers. *Journal of Wind Engineering and Industrial Aerodynamics*, 23:345–364.

[68] Savory, E. and Toy, N. (1988). The separated shear layers associated with hemispherical bodies in turbulent boundary layers. *Journal of Wind Engineering and Industrial Aerodynamics*, 28:291–300.

[69] Scherer, M. (1999). *Typisierungskonzept zur Festlegung einer ökologisch begründeten Mindestwassermenge*. PhD thesis, Mitteilungen des Institutes für Wasserwirtschaft und Kulturtechnik der Universität Karlsruhe.

[70] Schlichting, H. (1975). *Grenzschicht-Theorie*. Verlag G.Braun, Karlsruhe.

[71] Schmedtje, U. (1995). Beziehungen zwischen der sohlnahen Strömung, dem Gewässerbett und dem Makrozoobenthos in Fließgewässern. Schriftenreihe des Bayerischen Landesamtes für Wasserwirtschaft, Band 25.

[72] Schneider, M. (2001). *Habitat- und Abflussmodellierung für Fließgewässer mit unscharfen Berechnungsansätzen*. PhD thesis, Mitteilungen des Institutes für Wasserbau, Universität Stuttgart, Heft 108.

[73] Schneider, M. (2002). *Kurzanleitung für das Simulationsmodell CASiMiR, Modul SORAS. Gewässermodellierung und Fischhabitatsimulation*. `http://www.sjeweb.de/pdf/handb_demo_nov02.pdf`.

[74] Schneider, M. (2006). *Fish and Benthic Habitat Modeling using the simulation model CASiMiR. Manuscript*.

[75] Schneider, M., Giesecke, J., and Zöllner, F. (2001). CASIMIR – Hilfsmittel zur Mindestwasserfestlegung unter Berücksichtigung von Ökologie und Ökonomie. *Wasserwirtschaft*, 91(10):486–490.

[76] Schneider, M. and Jorde, K. (2005). Use of fuzzy logic in fish habitat modelling: A new approach incorporating imprecise expert knowledge. Submitted to River Research and Applications.

[77] Schneider, M. and Ortlepp, J. (2003). Zustand und Entwicklungspotenzial der Restwasserstrecke beim Kraftwerk Rheinau. Technical report, Rheinaubund Schaffhausen.

[78] Shamloo, H., Rajaratnam, N., and Katopodis, C. (2001). Hydraulics of simple habitat structures. *Journal of Hydraulic Research*, 39(4):351–366.

[79] Shields, A. (1936). *Anwendung der Ähnlichkeitsmechanik und der Turbulenzforschung auf die Geschiebebewegung*. PhD thesis, Mitteilungen der Preußischen Versuchsanstalt für Wasserbau und Schiffbau, 26, Berlin NW 87.

[80] Souchon, Y. (2004). Mediterranean case study: The Rhône river: Hydromorphological and ecological rehabilitation of a heavely man-used hydrosystem. In *Assessment and Provision of Environmental Flows in Mediterranean Watercourses: Basic Concepts, Methodologies and Emerging Practice*, pages 3–11. I.U.C.N. Mediterranean Office: Water and Nature Initiative.

[81] Spalart, P. and Allmaras, S. (1992). A one-equation turbulence model for aerodynamic flows. Technical Report AIAA-92-0439, American Institute of Aeronautics and Astronautics.

[82] Stalnaker, C., Lamb, B. L., Henriksen, J., Bovee, K., and Bartholow, J. (1995). The Instream Flow Incremental Methodology: A Primer for IFIM. Biological Report 29. United States National Biological Service, Fort Collins, Colorado.

[83] Statzner, B., Gore, J. A., and Resh, V. H. (1988). Hydraulic stream ecology: observed patterns and potential applications. *Journal of the North American Benthological Society*, 7:307–360.

[84] Statzner, B. and Holm, T. (1982). Morphological adaptations of benthic invertebrates to stream flow – an old question studied by means of a new technique (Laser Doppler Anemometry). *Oecologia*, 53:290–292.

[85] Statzner, B. and Holm, T. (1989). Morphological adaptations of shapes to flow: microcurrents around lotic macroinvertebrates with known Reynolds numbers at quasi-natural flow conditions. *Oecologia*, 78:145–157.

[86] Statzner, B., Kohmann, F., and Hildrew, A. (1991). Calibration of FST-hemispheres against bottom shear stress in a laboratory flume. *Freshwater Biology*, 26:227–231.

[87] Statzner, B., Kohmann, F., and Schmedtje, U. (1990). A method of ecological appraisal for determining instream flow requirements in diverted streams. *Wasserwirtschaft*, 80:248–254. In German.

[88] Statzner, B. and Müller, R. (1989). Standard hemispheres as indicators of flow characteristics in lotic benthos research. *Freshwater Biology*, 21:445–459.

[89] Statzner, B. and Mérigoux, S. (2005). Mineral grains in caddisfly pupal cases and streambed sediments: Resource use and its limitation through conflicting resource requirements. *Limnology and Oceanography*, 50(2):713–721.

[90] Taniguchi, S. and Sakamoto, H. (1982). Time-averaged aerodynamic forces acting on a hemisphere immerced in a turbulent boundary. *Journal of Wind Engineering and Industrial Aerodynamics*, 9:257–273.

[91] Tharme, R. E. (2003). Global perspective on environmental flow assessment: emerging trends in the development and applications of environmental flow methodologies for rivers. *River Research and Applications*, 19:397–441.

[92] The Council of the European Union (2000). Directive of the European Parliament and of the Council 2000/60/EC: establishing a framework for community action in the field of water policy.

[93] Thompson, N. (2003). Fluid forces on non-streamline bodies – background notes and description of the flow phenomena. Data Item 71012. `http://www2.mech.kth.se/courses/5C1211/ESDU71012.pdf`.

[94] Travin, A., Shur, M., Strelets, M., and Spalart, P. (1999). Detached-eddy simulations past a circular cylinder. *Flow, Turbulence and Combustion*, 63:293–313.

[95] Tufo, H. M., Fischer, P. F., Papka, M. E., and Blom, K. (1999). Numerical simulation and immersive visualization of hairpin vortices. In *Supercomputing '99: Proceedings of the 1999 ACM/IEEE Conference on Supercomputing (CDROM)*, page 62, New York, NY, USA. ACM Press.

[96] Ulfstrand, S. (1967). Microdistribution of benthic species (Ephemeroptera, Plecoptera, Trichoptera, Diptera: Simuliidae) in Lapland streams. *Oikos*, 18:293–310.

[97] Wang, H., Zhou, Y., Chan, C., Wong, W., and Lam, K. (2004). Flow structure around a finite-length square prism. In *15th Australasian Fluid Mechanics Conference, The University of Sydney, Australia*.

[98] Welcomme, R. L. (1985). *River Fisheries T262*. FAO Fisheries Technical Papers.

[99] Wilcox, D. C. (1998). *Turbulence Modeling for CFD*. La Cañada, Calif.: DCW Industries.

[100] Zanke, U. C. E. (1996). Lösungen für das universelle Geschwindigkeitverteilungsgesetz und die Schields-Kurve. *Wasser und Boden*, (9).

[101] Zanke, U. C. E. (2001). *Zum Einfluß der Turbulenz auf den Beginn der Sedimentbewegung*. Mitteilungen des Institutes für Wasserbau und Wasserwirtschaft der Technische Universität Darmstadt, Heft 120.

[102] Zanke, U. C. E. (2003). On the Influence of Turbulence on the Initiation of Sediment Motion. *International Journal of Sediment Research*, 18(1).

**Institut für Wasserbau**
**Universität Stuttgart**

Pfaffenwaldring 61
70569 Stuttgart (Vaihingen)
Telefon (0711) 685 - 64717/64749/64752/64679
Telefax (0711) 685 - 67020 o. 64746 o. 64681
E-Mail: iws@iws.uni-stuttgart.de
http://www.iws.uni-stuttgart.de

**Direktoren**
Prof. Dr. rer. nat. Dr.-Ing. András Bárdossy
Prof. Dr.-Ing. Rainer Helmig
Prof. Dr.-Ing. Silke Wieprecht

**Vorstand** *(Stand 1.2.2008)*
Prof. Dr. rer. nat. Dr.-Ing. A. Bárdossy
Prof. Dr.-Ing. R. Helmig
Prof. Dr.-Ing. S. Wieprecht
Prof. Dr.-Ing. habil. B. Westrich
Jürgen Braun, PhD
Dr.-Ing. H. Class
Dr.-Ing. S. Hartmann
Dr.-Ing. H.-P. Koschitzky
PD Dr.-Ing. W. Marx
Dr. rer. nat. J. Seidel

**Emeriti**
Prof. Dr.-Ing. Dr.-Ing. E.h. Jürgen Giesecke
Prof. Dr.h.c. Dr.-Ing. E.h. Helmut Kobus, PhD

**Lehrstuhl für Wasserbau und Wassermengenwirtschaft**
Leiter: Prof. Dr.-Ing. Silke Wieprecht
Stellv.: PD Dr.-Ing. Walter Marx, AOR

**Lehrstuhl für Hydrologie und Geohydrologie**
Leiter: Prof. Dr. rer. nat. Dr.-Ing. András Bárdossy
Stellv.: Dr.-Ing. Arne Färber

**Lehrstuhl für Hydromechanik und Hydrosystemmodellierung**
Leiter: Prof. Dr.-Ing. Rainer Helmig
Stellv.: Dr.-Ing. Holger Class, AOR

***VEGAS,* Versuchseinrichtung zur Grundwasser- und Altlastensanierung**
Leitung: Jürgen Braun, PhD
Dr.-Ing. Hans-Peter Koschitzky, AD

**Versuchsanstalt für Wasserbau**
Leiter: apl. Prof. Dr.-Ing. Bernhard Westrich

# Verzeichnis der Mitteilungshefte

1 Röhnisch, Arthur: *Die Bemühungen um eine Wasserbauliche Versuchsanstalt an der Technischen Hochschule Stuttgart*,
und
Fattah Abouleid, Abdel: *Beitrag zur Berechnung einer in lockeren Sand gerammten, zweifach verankerten Spundwand*, 1963

2 Marotz, Günter: *Beitrag zur Frage der Standfestigkeit von dichten Asphaltbelägen im Großwasserbau*, 1964

3 Gurr, Siegfried: *Beitrag zur Berechnung zusammengesetzter ebener Flächentragwerke unter besonderer Berücksichtigung ebener Stauwände, mit Hilfe von Randwert- und Lastwertmatrizen*, 1965

4 Plica, Peter: *Ein Beitrag zur Anwendung von Schalenkonstruktionen im Stahlwasserbau*, und Petrikat, Kurt: *Möglichkeiten und Grenzen des wasserbaulichen Versuchswesens*, 1966

5 Plate, Erich: *Beitrag zur Bestimmung der Windgeschwindigkeitsverteilung in der durch eine Wand gestörten bodennahen Luftschicht*,
und
Röhnisch, Arthur; Marotz, Günter: *Neue Baustoffe und Bauausführungen für den Schutz der Böschungen und der Sohle von Kanälen, Flüssen und Häfen; Gestehungskosten und jeweilige Vorteile*, sowie Unny, T.E.: *Schwingungsuntersuchungen am Kegelstrahlschieber*, 1967

6 Seiler, Erich: *Die Ermittlung des Anlagenwertes der bundeseigenen Binnenschiffahrtsstraßen und Talsperren und des Anteils der Binnenschiffahrt an diesem Wert*, 1967

7 *Sonderheft anläßlich des 65. Geburtstages von Prof. Arthur Röhnisch mit Beiträgen von* Benk, Dieter; Breitling, J.; Gurr, Siegfried; Haberhauer, Robert; Honekamp, Hermann; Kuz, Klaus Dieter; Marotz, Günter; Mayer-Vorfelder, Hans-Jörg; Miller, Rudolf; Plate, Erich J.; Radomski, Helge; Schwarz, Helmut; Vollmer, Ernst; Wildenhahn, Eberhard; 1967

8 Jumikis, Alfred: *Beitrag zur experimentellen Untersuchung des Wassernachschubs in einem gefrierenden Boden und die Beurteilung der Ergebnisse*, 1968

9 Marotz, Günter: *Technische Grundlagen einer Wasserspeicherung im natürlichen Untergrund*, 1968

10 Radomski, Helge: *Untersuchungen über den Einfluß der Querschnittsform wellenförmiger Spundwände auf die statischen und rammtechnischen Eigenschaften*, 1968

11 Schwarz, Helmut: *Die Grenztragfähigkeit des Baugrundes bei Einwirkung vertikal gezogener Ankerplatten als zweidimensionales Bruchproblem*, 1969

12 Erbel, Klaus: *Ein Beitrag zur Untersuchung der Metamorphose von Mittelgebirgsschneedecken unter besonderer Berücksichtigung eines Verfahrens zur Bestimmung der thermischen Schneequalität*, 1969

13 Westhaus, Karl-Heinz: *Der Strukturwandel in der Binnenschiffahrt und sein Einfluß auf den Ausbau der Binnenschiffskanäle*, 1969

14 Mayer-Vorfelder, Hans-Jörg: *Ein Beitrag zur Berechnung des Erdwiderstandes unter Ansatz der logarithmischen Spirale als Gleitflächenfunktion*, 1970

15 Schulz, Manfred: *Berechnung des räumlichen Erddruckes auf die Wandung kreiszylindrischer Körper*, 1970

16 Mobasseri, Manoutschehr: *Die Rippenstützmauer. Konstruktion und Grenzen ihrer Standsicherheit*, 1970

17 Benk, Dieter: *Ein Beitrag zum Betrieb und zur Bemessung von Hochwasserrückhaltebecken*, 1970

18 Gàl, Attila: *Bestimmung der mitschwingenden Wassermasse bei überströmten Fischbauchklappen mit kreiszylindrischem Staublech*, 1971, vergriffen

19 Kuz, Klaus Dieter: *Ein Beitrag zur Frage des Einsetzens von Kavitationserscheinungen in einer Düsenströmung bei Berücksichtigung der im Wasser gelösten Gase*, 1971, vergriffen

20 Schaak, Hartmut: *Verteilleitungen von Wasserkraftanlagen*, 1971

21 *Sonderheft zur Eröffnung der neuen Versuchsanstalt des Instituts für Wasserbau der Universität Stuttgart mit Beiträgen von* Brombach, Hansjörg; Dirksen, Wolfram; Gàl, Attila; Gerlach, Reinhard; Giesecke, Jürgen; Holthoff, Franz-Josef; Kuz, Klaus Dieter; Marotz, Günter; Minor, Hans-Erwin; Petrikat, Kurt; Röhnisch, Arthur; Rueff, Helge; Schwarz, Helmut; Vollmer, Ernst; Wildenhahn, Eberhard; 1972

22 Wang, Chung-su: *Ein Beitrag zur Berechnung der Schwingungen an Kegelstrahlschiebern*, 1972

23 Mayer-Vorfelder, Hans-Jörg: *Erdwiderstandsbeiwerte nach dem Ohde-Variationsverfahren*, 1972

24 Minor, Hans-Erwin: *Beitrag zur Bestimmung der Schwingungsanfachungsfunktionen überströmter Stauklappen*, 1972, vergriffen

25 Brombach, Hansjörg: *Untersuchung strömungsmechanischer Elemente (Fluidik) und die Möglichkeit der Anwendung von Wirbelkammerelementen im Wasserbau*, 1972, vergriffen

26 Wildenhahn, Eberhard: *Beitrag zur Berechnung von Horizontalfilterbrunnen*, 1972

27 Steinlein, Helmut: *Die Eliminierung der Schwebstoffe aus Flußwasser zum Zweck der unterirdischen Wasserspeicherung, gezeigt am Beispiel der Iller*, 1972

28 Holthoff, Franz Josef: *Die Überwindung großer Hubhöhen in der Binnenschiffahrt durch Schwimmerhebewerke*, 1973

29 Röder, Karl: *Einwirkungen aus Baugrundbewegungen auf trog- und kastenförmige Konstruktionen des Wasser- und Tunnelbaues*, 1973

30 Kretschmer, Heinz: *Die Bemessung von Bogenstaumauern in Abhängigkeit von der Talform*, 1973

31 Honekamp, Hermann: *Beitrag zur Berechnung der Montage von Unterwasserpipelines*, 1973

32 Giesecke, Jürgen: *Die Wirbelkammertriode als neuartiges Steuerorgan im Wasserbau*, und Brombach, Hansjörg: *Entwicklung, Bauformen, Wirkungsweise und Steuereigenschaften von Wirbelkammerverstärkern*, 1974

33 Rueff, Helge: *Untersuchung der schwingungserregenden Kräfte an zwei hintereinander angeordneten Tiefschützen unter besonderer Berücksichtigung von Kavitation*, 1974

34 Röhnisch, Arthur: *Einpreßversuche mit Zementmörtel für Spannbeton - Vergleich der Ergebnisse von Modellversuchen mit Ausführungen in Hüllwellrohren*, 1975

35 *Sonderheft anläßlich des 65. Geburtstages von Prof. Dr.-Ing. Kurt Petrikat mit Beiträgen von*: Brombach, Hansjörg; Erbel, Klaus; Flinspach, Dieter; Fischer jr., Richard; Gàl, Attila; Gerlach, Reinhard; Giesecke, Jürgen; Haberhauer, Robert; Hafner Edzard; Hausenblas, Bernhard; Horlacher, Hans-Burkhard; Hutarew, Andreas; Knoll, Manfred; Krummet, Ralph; Marotz, Günter; Merkle, Theodor; Miller, Christoph; Minor, Hans-Erwin; Neumayer, Hans; Rao, Syamala; Rath, Paul; Rueff, Helge; Ruppert, Jürgen; Schwarz, Wolfgang; Topal-Gökceli, Mehmet; Vollmer, Ernst; Wang, Chung-su; Weber, Hans-Georg; 1975

36 Berger, Jochum: *Beitrag zur Berechnung des Spannungszustandes in rotationssymmetrisch belasteten Kugelschalen veränderlicher Wandstärke unter Gas- und Flüssigkeitsdruck durch Integration schwach singulärer Differentialgleichungen*, 1975

37 Dirksen, Wolfram: *Berechnung instationärer Abflußvorgänge in gestauten Gerinnen mittels Differenzenverfahren und die Anwendung auf Hochwasserrückhaltebecken*, 1976

38 Horlacher, Hans-Burkhard: *Berechnung instationärer Temperatur- und Wärmespannungsfelder in langen mehrschichtigen Hohlzylindern*, 1976

39 Hafner, Edzard: *Untersuchung der hydrodynamischen Kräfte auf Baukörper im Tiefwasserbereich des Meeres*, 1977, ISBN 3-921694-39-6

40 Ruppert, Jürgen: *Über den Axialwirbelkammerverstärker für den Einsatz im Wasserbau*, 1977, ISBN 3-921694-40-X

41 Hutarew, Andreas: *Beitrag zur Beeinflußbarkeit des Sauerstoffgehalts in Fließgewässern an Abstürzen und Wehren*, 1977, ISBN 3-921694-41-8, vergriffen

42 Miller, Christoph: *Ein Beitrag zur Bestimmung der schwingungserregenden Kräfte an unterströmten Wehren*, 1977, ISBN 3-921694-42-6

43 Schwarz, Wolfgang: *Druckstoßberechnung unter Berücksichtigung der Radial- und Längsverschiebungen der Rohrwandung*, 1978, ISBN 3-921694-43-4

44 Kinzelbach, Wolfgang: *Numerische Untersuchungen über den optimalen Einsatz variabler Kühlsysteme einer Kraftwerkskette am Beispiel Oberrhein*, 1978, ISBN 3-921694-44-2

45 Barczewski, Baldur: *Neue Meßmethoden für Wasser-Luftgemische und deren Anwendung auf zweiphasige Auftriebsstrahlen*, 1979, ISBN 3-921694-45-0

46 Neumayer, Hans: *Untersuchung der Strömungsvorgänge in radialen Wirbelkammerverstärkern*, 1979, ISBN 3-921694-46-9

47 Elalfy, Youssef-Elhassan: *Untersuchung der Strömungsvorgänge in Wirbelkammerdioden und -drosseln*, 1979, ISBN 3-921694-47-7

48 Brombach, Hansjörg: *Automatisierung der Bewirtschaftung von Wasserspeichern*, 1981, ISBN 3-921694-48-5

49 Geldner, Peter: *Deterministische und stochastische Methoden zur Bestimmung der Selbstdichtung von Gewässern*, 1981, ISBN 3-921694-49-3, vergriffen

50 Mehlhorn, Hans: *Temperaturveränderungen im Grundwasser durch Brauchwassereinleitungen*, 1982, ISBN 3-921694-50-7, vergriffen

51 Hafner, Edzard: *Rohrleitungen und Behälter im Meer*, 1983, ISBN 3-921694-51-5

52 Rinnert, Bernd: *Hydrodynamische Dispersion in porösen Medien: Einfluß von Dichteunterschieden auf die Vertikalvermischung in horizontaler Strömung*, 1983, ISBN 3-921694-52-3, vergriffen

53 Lindner, Wulf: *Steuerung von Grundwasserentnahmen unter Einhaltung ökologischer Kriterien*, 1983, ISBN 3-921694-53-1, vergriffen

54 Herr, Michael; Herzer, Jörg; Kinzelbach, Wolfgang; Kobus, Helmut; Rinnert, Bernd: *Methoden zur rechnerischen Erfassung und hydraulischen Sanierung von Grundwasserkontaminationen*, 1983, ISBN 3-921694-54-X

55 Schmitt, Paul: *Wege zur Automatisierung der Niederschlagsermittlung*, 1984, ISBN 3-921694-55-8, vergriffen

56 Müller, Peter: *Transport und selektive Sedimentation von Schwebstoffen bei gestautem Abfluß*, 1985, ISBN 3-921694-56-6

57 El-Qawasmeh, Fuad: *Möglichkeiten und Grenzen der Tropfbewässerung unter besonderer Berücksichtigung der Verstopfungsanfälligkeit der Tropfelemente*, 1985, ISBN 3-921694-57-4, vergriffen

58 Kirchenbaur, Klaus: *Mikroprozessorgesteuerte Erfassung instationärer Druckfelder am Beispiel seegangsbelasteter Baukörper*, 1985, ISBN 3-921694-58-2

59 Kobus, Helmut (Hrsg.): *Modellierung des großräumigen Wärme- und Schadstofftransports im Grundwasser*, Tätigkeitsbericht 1984/85 (DFG-Forschergruppe an den Universitäten Hohenheim, Karlsruhe und Stuttgart), 1985, ISBN 3-921694-59-0, vergriffen

60 Spitz, Karlheinz: *Dispersion in porösen Medien: Einfluß von Inhomogenitäten und Dichteunterschieden*, 1985, ISBN 3-921694-60-4, vergriffen

61 Kobus, Helmut: *An Introduction to Air-Water Flows in Hydraulics*, 1985, ISBN 3-921694-61-2

62 Kaleris, Vassilios: *Erfassung des Austausches von Oberflächen- und Grundwasser in horizontalebenen Grundwassermodellen*, 1986, ISBN 3-921694-62-0

63 Herr, Michael: *Grundlagen der hydraulischen Sanierung verunreinigter Porengrundwasserleiter*, 1987, ISBN 3-921694-63-9

64 Marx, Walter: *Berechnung von Temperatur und Spannung in Massenbeton infolge Hydratation*, 1987, ISBN 3-921694-64-7

65 Koschitzky, Hans-Peter: *Dimensionierungskonzept für Sohlbelüfter in Schußrinnen zur Vermeidung von Kavitationsschäden*, 1987, ISBN 3-921694-65-5

66 Kobus, Helmut (Hrsg.): *Modellierung des großräumigen Wärme- und Schadstofftransports im Grundwasser*, Tätigkeitsbericht 1986/87 (DFG-Forschergruppe an den Universitäten Hohenheim, Karlsruhe und Stuttgart) 1987, ISBN 3-921694-66-3

67 Söll, Thomas: *Berechnungsverfahren zur Abschätzung anthropogener Temperaturanomalien im Grundwasser*, 1988, ISBN 3-921694-67-1

68 Dittrich, Andreas; Westrich, Bernd: *Bodenseeufererosion, Bestandsaufnahme und Bewertung*, 1988, ISBN 3-921694-68-X, vergriffen

69 Huwe, Bernd; van der Ploeg, Rienk R.: *Modelle zur Simulation des Stickstoffhaushaltes von Standorten mit unterschiedlicher landwirtschaftlicher Nutzung*, 1988, ISBN 3-921694-69-8, vergriffen

70 Stephan, Karl: *Integration elliptischer Funktionen*, 1988, ISBN 3-921694-70-1

71 Kobus, Helmut; Zilliox, Lothaire (Hrsg.): *Nitratbelastung des Grundwassers, Auswirkungen der Landwirtschaft auf die Grundwasser- und Rohwasserbeschaffenheit und Maßnahmen zum Schutz des Grundwassers*. Vorträge des deutsch-französischen Kolloquiums am 6. Oktober 1988, Universitäten Stuttgart und Louis Pasteur Strasbourg (Vorträge in deutsch oder französisch, Kurzfassungen zweisprachig), 1988, ISBN 3-921694-71-X

72 Soyeaux, Renald: *Unterströmung von Stauanlagen auf klüftigem Untergrund unter Berücksichtigung laminarer und turbulenter Fließzustände*,1991,
ISBN 3-921694-72-8

73 Kohane, Roberto: *Berechnungsmethoden für Hochwasserabfluß in Fließgewässern mit überströmten Vorländern*, 1991, ISBN 3-921694-73-6

74 Hassinger, Reinhard: *Beitrag zur Hydraulik und Bemessung von Blocksteinrampen in flexibler Bauweise*, 1991, ISBN 3-921694-74-4, vergriffen

75 Schäfer, Gerhard: *Einfluß von Schichtenstrukturen und lokalen Einlagerungen auf die Längsdispersion in Porengrundwasserleitern*, 1991, ISBN 3-921694-75-2

76 Giesecke, Jürgen: *Vorträge, Wasserwirtschaft in stark besiedelten Regionen; Umweltforschung mit Schwerpunkt Wasserwirtschaft*, 1991, ISBN 3-921694-76-0

77 Huwe, Bernd: *Deterministische und stochastische Ansätze zur Modellierung des Stickstoffhaushalts landwirtschaftlich genutzter Flächen auf unterschiedlichem Skalenniveau*, 1992, ISBN 3-921694-77-9, vergriffen

78 Rommel, Michael: *Verwendung von Kluftdaten zur realitätsnahen Generierung von Kluftnetzen mit anschließender laminar-turbulenter Strömungsberechnung*, 1993, ISBN 3-92 1694-78-7

79 Marschall, Paul: *Die Ermittlung lokaler Stofffrachten im Grundwasser mit Hilfe von Einbohrloch-Meßverfahren*, 1993, ISBN 3-921694-79-5, vergriffen

80 Ptak, Thomas: *Stofftransport in heterogenen Porenaquiferen: Felduntersuchungen und stochastische Modellierung*, 1993, ISBN 3-921694-80-9, vergriffen

81 Haakh, Frieder: *Transientes Strömungsverhalten in Wirbelkammern,* 1993, ISBN 3-921694-81-7

82 Kobus, Helmut; Cirpka, Olaf; Barczewski, Baldur; Koschitzky, Hans-Peter: *Versucheinrichtung zur Grundwasser und Altlastensanierung VEGAS, Konzeption und Programmrahmen*, 1993, ISBN 3-921694-82-5

83 Zang, Weidong: *Optimaler Echtzeit-Betrieb eines Speichers mit aktueller Abflußregenerierung*, 1994, ISBN 3-921694-83-3, vergriffen

84 Franke, Hans-Jörg: *Stochastische Modellierung eines flächenhaften Stoffeintrages und Transports in Grundwasser am Beispiel der Pflanzenschutzmittelproblematik*, 1995, ISBN 3-921694-84-1

85 Lang, Ulrich: *Simulation regionaler Strömungs- und Transportvorgänge in Karstaquiferen mit Hilfe des Doppelkontinuum-Ansatzes: Methodenentwicklung und Parameteridentifikation*, 1995, ISBN 3-921694-85-X, vergriffen

86 Helmig, Rainer: *Einführung in die Numerischen Methoden der Hydromechanik*, 1996, ISBN 3-921694-86-8, vergriffen

87 Cirpka, Olaf: *CONTRACT: A Numerical Tool for Contaminant Transport and Chemical Transformations - Theory and Program Documentation* -, 1996, ISBN 3-921694-87-6

88 Haberlandt, Uwe: *Stochastische Synthese und Regionalisierung des Niederschlages für Schmutzfrachtberechnungen*, 1996, ISBN 3-921694-88-4

89 Croisé, Jean: *Extraktion von flüchtigen Chemikalien aus natürlichen Lockergesteinen mittels erzwungener Luftströmung*, 1996, ISBN 3-921694-89-2, vergriffen

90 Jorde, Klaus: *Ökologisch begründete, dynamische Mindestwasserregelungen bei Ausleitungskraftwerken*, 1997, ISBN 3-921694-90-6, vergriffen

91 Helmig, Rainer: *Gekoppelte Strömungs- und Transportprozesse im Untergrund - Ein Beitrag zur Hydrosystemmodellierung-*, 1998, ISBN 3-921694-91-4

92 Emmert, Martin: *Numerische Modellierung nichtisothermer Gas-Wasser Systeme in porösen Medien*, 1997, ISBN 3-921694-92-2

93 Kern, Ulrich: *Transport von Schweb- und Schadstoffen in staugeregelten Fließgewässern am Beispiel des Neckars*, 1997, ISBN 3-921694-93-0, vergriffen

94 Förster, Georg: *Druckstoßdämpfung durch große Luftblasen in Hochpunkten von Rohrleitungen 1997*, ISBN 3-921694-94-9

95 Cirpka, Olaf: *Numerische Methoden zur Simulation des reaktiven Mehrkomponententransports im Grundwasser*, 1997, ISBN 3-921694-95-7, vergriffen

96 Färber, Arne: *Wärmetransport in der ungesättigten Bodenzone: Entwicklung einer thermischen In-situ-Sanierungstechnologie*, 1997, ISBN 3-921694-96-5

97 Betz, Christoph: *Wasserdampfdestillation von Schadstoffen im porösen Medium: Entwicklung einer thermischen In-situ-Sanierungstechnologie*, 1998, ISBN 3-921694-97-3

98 Xu, Yichun: *Numerical Modeling of Suspended Sediment Transport in Rivers*, 1998, ISBN 3-921694-98-1, vergriffen

99 Wüst, Wolfgang: *Geochemische Untersuchungen zur Sanierung CKW-kontaminierter Aquifere mit Fe(0)-Reaktionswänden,* 2000, ISBN 3-933761-02-2

100 Sheta, Hussam: *Simulation von Mehrphasenvorgängen in porösen Medien unter Einbeziehung von Hysterese-Effekten*, 2000, ISBN 3-933761-03-4

101 Ayros, Edwin: *Regionalisierung extremer Abflüsse auf der Grundlage statistischer Verfahren*, 2000, ISBN 3-933761-04-2, vergriffen

102 Huber, Ralf: *Compositional Multiphase Flow and Transport in Heterogeneous Porous Media*, 2000, ISBN 3-933761-05-0

103 Braun, Christopherus: *Ein Upscaling-Verfahren für Mehrphasenströmungen in porösen Medien*, 2000, ISBN 3-933761-06-9

104 Hofmann, Bernd: *Entwicklung eines rechnergestützten Managementsystems zur Beurteilung von Grundwasserschadensfällen*, 2000, ISBN 3-933761-07-7

105 Class, Holger: *Theorie und numerische Modellierung nichtisothermer Mehrphasenprozesse in NAPL-kontaminierten porösen Medien,* 2001, ISBN 3-933761-08-5

106 Schmidt, Reinhard: *Wasserdampf- und Heißluftinjektion zur thermischen Sanierung kontaminierter Standorte*, 2001, ISBN 3-933761-09-3

107 Josef, Reinhold:, *Schadstoffextraktion mit hydraulischen Sanierungsverfahren unter Anwendung von grenzflächenaktiven Stoffen*, 2001, ISBN 3-933761-10-7

108 Schneider, Matthias: *Habitat- und Abflussmodellierung für Fließgewässer mit unscharfen Berechnungsansätzen*, 2001, ISBN 3-933761-11-5

109 Rathgeb, Andreas: *Hydrodynamische Bemessungsgrundlagen für Lockerdeckwerke an überströmbaren Erddämmen*, 2001, ISBN 3-933761-12-3

110 Lang, Stefan: *Parallele numerische Simulation instätionärer Probleme mit adaptiven Methoden auf unstrukturierten Gittern*, 2001, ISBN 3-933761-13-1

111 Appt, Jochen; Stumpp Simone: *Die Bodensee-Messkampagne 2001, IWS/CWR Lake Constance Measurement Program 2001*, 2002, ISBN 3-933761-14-X

112 Heimerl, Stephan: *Systematische Beurteilung von Wasserkraftprojekten,* 2002, ISBN 3-933761-15-8

113 Iqbal, Amin: *On the Management and Salinity Control of Drip Irrigation,* 2002, ISBN 3-933761-16-6

114 Silberhorn-Hemminger, Annette: *Modellierung von Kluftaquifersystemen: Geostatistische Analyse und deterministisch-stochastische Kluftgenerierung,* 2002, ISBN 3-933761-17-4

115 Winkler, Angela: *Prozesse des Wärme- und Stofftransports bei der In-situ-Sanierung mit festen Wärmequellen,* 2003, ISBN 3-933761-18-2

116 Marx, Walter: *Wasserkraft, Bewässerung, Umwelt - Planungs- und Bewertungsschwerpunkte der Wasserbewirtschaftung,* 2003, ISBN 3-933761-19-0

117 Hinkelmann, Reinhard: *Efficient Numerical Methods and Information-Processing Techniques in Environment Water,* 2003, ISBN 3-933761-20-4

118 Samaniego-Eguiguren, Luis Eduardo: *Hydrological Consequences of Land Use / Land Cover and Climatic Changes in Mesoscale Catchments*, 2003, ISBN 3-933761-21-2

119 Neunhäuserer, Lina: *Diskretisierungsansätze zur Modellierung von Strömungs- und Transportprozessen in geklüftet-porösen Medien*, 2003, ISBN 3-933761-22-0

120 Paul, Maren: *Simulation of Two-Phase Flow in Heterogeneous Poros Media with Adaptive Methods*, 2003, ISBN 3-933761-23-9

121 Ehret, Uwe: *Rainfall and Flood Nowcasting in Small Catchments using Weather Radar*, 2003, ISBN 3-933761-24-7

122 Haag, Ingo: *Der Sauerstoffhaushalt staugeregelter Flüsse am Beispiel des Neckars - Analysen, Experimente, Simulationen -,* 2003, ISBN 3-933761-25-5

123 Appt, Jochen: *Analysis of Basin-Scale Internal Waves in Upper Lake Constance,* 2003, ISBN 3-933761-26-3

124 Hrsg.: Schrenk, Volker; Batereau, Katrin; Barczewski, Baldur; Weber, Karolin und Koschitzky, Hans-Peter: *Symposium Ressource Fläche und VEGAS - Statuskolloquium 2003, 30. September und 1. Oktober 2003,* 2003, ISBN 3-933761-27-1

125 Omar Khalil Ouda: *Optimisation of Agricultural Water Use: A Decision Support System for the Gaza Strip,* 2003, ISBN 3-933761-28-0

126 Batereau, Katrin: *Sensorbasierte Bodenluftmessung zur Vor-Ort-Erkundung von Schadensherden im Untergrund*, 2004, ISBN 3-933761-29-8

127 Witt, Oliver: *Erosionsstabilität von Gewässersedimenten mit Auswirkung auf den Stofftransport bei Hochwasser am Beispiel ausgewählter Stauhaltungen des Oberrheins*, 2004, ISBN 3-933761-30-1

128 Jakobs, Hartmut: *Simulation nicht-isothermer Gas-Wasser-Prozesse in komplexen Kluft-Matrix-Systemen*, 2004, ISBN 3-933761-31-X

129 Li, Chen-Chien: *Deterministisch-stochastisches Berechnungskonzept zur Beurteilung der Auswirkungen erosiver Hochwasserereignisse in Flussstauhaltungen,* 2004, ISBN 3-933761-32-8

130 Reichenberger, Volker; Helmig, Rainer; Jakobs, Hartmut; Bastian, Peter; Niessner, Jennifer: *Complex Gas-Water Processes in Discrete Fracture-Matrix Systems: Upscaling, Mass-Conservative Discretization and Efficient Multilevel Solution,* 2004, ISBN 3-933761-33-6

131 Hrsg.: Barczewski, Baldur; Koschitzky, Hans-Peter; Weber, Karolin; Wege, Ralf: *VEGAS - Statuskolloquium 2004,* Tagungsband zur Veranstaltung am 05. Oktober 2004 an der Universität Stuttgart, Campus Stuttgart-Vaihingen, 2004, ISBN 3-933761-34-4

132 Asie, Kemal Jabir: *Finite Volume Models for Multiphase Multicomponent Flow through Porous Media*. 2005, ISBN 3-933761-35-2

133 Jacoub, George: *Development of a 2-D Numerical Module for Particulate Contaminant Transport in Flood Retention Reservoirs and Impounded Rivers,* 2004, ISBN 3-933761-36-0

134 Nowak, Wolfgang: *Geostatistical Methods for the Identification of Flow and Transport Parameters in the Subsurface,* 2005, ISBN 3-933761-37-9

135 Süß, Mia: *Analysis of the influence of structures and boundaries on flow and transport processes in fractured porous media*, 2005, ISBN 3-933761-38-7

136 Jose, Surabhin Chackiath: *Experimental Investigations on Longitudinal Dispersive Mixing in Heterogeneous Aquifers,* 2005, ISBN: 3-933761-39-5

137 Filiz, Fulya: *Linking Large-Scale Meteorological Conditions to Floods in Mesoscale Catchments,* 2005, ISBN 3-933761-40-9

138 Qin, Minghao: *Wirklichkeitsnahe und recheneffiziente Ermittlung von Temperatur und Spannungen bei großen RCC-Staumauern*, 2005, ISBN 3-933761-41-7

139 Kobayashi, Kenichiro: *Optimization Methods for Multiphase Systems in the Subsurface - Application to Methane Migration in Coal Mining Areas*, 2005, ISBN 3-933761-42-5

140 Rahman, Md. Arifur: *Experimental Investigations on Transverse Dispersive Mixing in Heterogeneous Porous Media,* 2005, ISBN 3-933761-43-3

141 Schrenk, Volker: *Ökobilanzen zur Bewertung von Altlastensanierungsmaßnahmen,* 2005, ISBN 3-933761-44-1

142 Hundecha, Hirpa Yeshewatesfa: *Regionalization of Parameters of a Conceptual Rainfall-Runoff Model*, 2005, ISBN: 3-933761-45-X

143 Wege, Ralf: *Untersuchungs- und Überwachungsmethoden für die Beurteilung natürlicher Selbstreinigungsprozesse im Grundwasser,* 2005, ISBN 3-933761-46-8

144 Breiting, Thomas: *Techniken und Methoden der Hydroinformatik - Modellierung von komplexen Hydrosystemen im Untergrund*, 2006, 3-933761-47-6

145 Hrsg.: Braun, Jürgen; Koschitzky, Hans-Peter; Müller, Martin: *Ressource Untergrund: 10 Jahre VEGAS: Forschung und Technologieentwicklung zum Schutz von Grundwasser und Boden,* Tagungsband zur Veranstaltung am 28. und 29. September 2005 an der Universität Stuttgart, Campus Stuttgart-Vaihingen, 2005, ISBN 3-933761-48-4

146 Rojanschi, Vlad: *Abflusskonzentration in mesoskaligen Einzugsgebieten unter Berücksichtigung des Sickerraumes,* 2006, ISBN 3-933761-49-2

147 Winkler, Nina Simone: *Optimierung der Steuerung von Hochwasserrückhaltebecken-systemen,* 2006, ISBN 3-933761-50-6

148 Wolf, Jens: *Räumlich differenzierte Modellierung der Grundwasserströmung alluvialer Aquifere für mesoskalige Einzugsgebiete*, 2006, ISBN: 3-933761-51-4

149 Kohler, Beate: *Externe Effekte der Laufwasserkraftnutzung*, 2006, ISBN 3-933761-52-2

150 Hrsg.: Braun, Jürgen; Koschitzky, Hans-Peter; Stuhrmann, Matthias: *VEGAS-Statuskolloquium 2006,* Tagungsband zur Veranstaltung am 28. September 2006 an der Universität Stuttgart, Campus Stuttgart-Vaihingen, 2006, ISBN 3-933761-53-0

151 Niessner, Jennifer: *Multi-Scale Modeling of Multi-Phase - Multi-Component Processes in Heterogeneous Porous Media*, 2006, ISBN 3-933761-54-9

152 Fischer, Markus: *Beanspruchung eingeerdeter Rohrleitungen infolge Austrocknung bindiger Böden,* 2006, ISBN 3-933761-55-7

153 Schneck, Alexander: *Optimierung der Grundwasserbewirtschaftung unter Berücksichtigung der Belange der Wasserversorgung, der Landwirtschaft und des Naturschutzes*, 2006, ISBN 3-933761-56-5

154 Das, Tapash: *The Impact of Spatial Variability of Precipitation on the Predictive Uncertainty of Hydrological Models,* 2006, ISBN 3-933761-57-3

155 Bielinski, Andreas: *Numerical Simulation of* $CO_2$ *sequestration in geological formations*, 2007, ISBN 3-933761-58-1

156 Mödinger, Jens: *Entwicklung eines Bewertungs- und Entscheidungsunterstützungssystems für eine nachhaltige regionale Grundwasserbewirtschaftung*, 2006, ISBN 3-933761-60-3

157 Manthey, Sabine: *Two-phase flow processes with dynamic effects in porous media - parameter estimation and simulation,* 2007, ISBN 3-933761-61-1

158 Pozos Estrada, Oscar: *Investigation on the Effects of Entrained Air in Pipelines,* 2007, ISBN 3-933761-62-X

159 Ochs, Steffen Oliver: *Steam injection into saturated porous media – process analysis including experimental and numerical investigations*, 2007, ISBN 3-933761-63-8

160 Marx, Andreas: *Einsatz gekoppelter Modelle und Wetterradar zur Abschätzung von Niederschlagsintensitäten und zur Abflussvorhersage, 2007,* ISBN 3-933761-64-6

161 Hartmann, Gabriele Maria: *Investigation of Evapotranspiration Concepts in Hydrological Modelling for Climate Change Impact Assessment*, 2007, ISBN 3-933761-65-4

162 Kebede Gurmessa, Tesfaye: *Numerical Investigation on Flow and Transport Characteristics to Improve Long-Term Simulation of Reservoir Sedimentation*, 2007, ISBN 3-933761-66-2

163 Trifković, Aleksandar: *Multi-objective and Risk-based Modelling Methodology for Planning, Design and Operation of Water Supply Systems*, 2007, ISBN 3-933761-67-0

164 Götzinger, Jens: *Distributed Conceptual Hydrological Modelling - Simulation of Climate, Land Use Change Impact and Uncertainty Analysis*, 2007, ISBN 3-933761-68-9

165 Hrsg.: Braun, Jürgen; Koschitzky, Hans-Peter; Stuhrmann, Matthias: *VEGAS – Kolloquium 2007,* Tagungsband zur Veranstaltung am 26. September 2007 an der Universität Stuttgart, Campus Stuttgart-Vaihingen, 2007, ISBN 3-933761-69-7

166 Freeman, Beau: *Modernization Criteria Assessment for Water Resources Planning; Klamath Irrigation Project, U.S.*, 2008, ISBN 3-933761-70-0

167 Dreher, Thomas: *Selektive Sedimentation von Feinstschwebstoffen in Wechselwirkung mit wandnahen turbulenten Strömungsbedingungen*, 2008, ISBN 3-933761-71-9

168 Yang, Wei: *Discrete-continuous Downscaling Model for Generating Daily Precipitation Time Series*, 2008, ISBN 3-933761-72-7

169 Kopecki, Ianina: *Calculational Approach to FST-Hemispheres for Multiparametrical Benthos Habitat Modelling,* 2008*,* ISBN 3-933761-73-5

*Die Mitteilungshefte ab dem Jahr 2005 stehen als pdf-Datei über die Homepage des Instituts: www.iws.uni-stuttgart.de zur Verfügung.*